

THE MINISTRY OF SCIENCE AND HIGHER EDUCATION OF THE RUSSIAN FEDERATION



ST. PETERSBURG STATE
POLYTECHNICAL UNIVERSITY
JOURNAL

Physics
and Mathematics

**VOLUME 15, No.2,
2022**

Peter the Great St. Petersburg
Polytechnic University
2022

ST. PETERSBURG STATE POLYTECHNICAL UNIVERSITY JOURNAL. PHYSICS AND MATHEMATICS

JOURNAL EDITORIAL COUNCIL

A.I. Borovkov – vice-rector for perspective projects;
V.A. Glukhikh – full member of RAS;
D.A. Indeitsev – corresponding member of RAS;
V.K. Ivanov – Dr. Sci.(phys.-math.), prof.;
A.I. Rudskoy – full member of RAS, deputy head of the editorial council;
R.A. Suris – full member of RAS;
A.E. Zhukov – corresponding member of RAS, deputy head of the editorial council.

JOURNAL EDITORIAL BOARD

V.K. Ivanov – Dr. Sci. (phys.-math.), prof., SPbPU, St. Petersburg, Russia, – editor-in-chief;
A.E. Fotiadi – Dr. Sci. (phys.-math.), prof., SPbPU, St. Petersburg, Russia, – deputy editor-in-chief;
V.M. Kapralova – Candidate of Phys.-Math. Sci., associate prof., SPbPU, St. Petersburg, Russia, – executive secretary;
V.I. Antonov – Dr. Sci. (phys.-math.), prof., SPbPU, St. Petersburg, Russia;
I.B. Bezprozvanny – Dr. Sci. (biology), prof., The University of Texas Southwestern Medical Center, Dallas, TX, USA;
A.V. Blinov – Dr. Sci. (phys.-math.), prof., SPbPU, St. Petersburg, Russia;
A.S. Cherepanov – Dr. Sci. (phys.-math.), prof., SPbPU, St. Petersburg, Russia;
D.V. Donetski – Dr. Sci. (phys.-math.), prof., State University of New York at Stony Brook, NY, USA;
D.A. Firsov – Dr. Sci. (phys.-math.), prof., SPbPU, St. Petersburg, Russia;
A.S. Kheifets – Ph.D., prof., Australian National University, Canberra, Australia;
O.S. Loboda – Candidate of Phys.-Math. Sci., associate prof., SPbPU, St. Petersburg, Russia;
J.B. Malherbe – Dr. Sci. (physics), prof., University of Pretoria, Republic of South Africa;
V.M. Ostryakov – Dr. Sci. (phys.-math.), prof., SPbPU, St. Petersburg, Russia;
V.E. Privalov – Dr. Sci. (phys.-math.), prof., SPbPU, St. Petersburg, Russia;
E.M. Smirnov – Dr. Sci. (phys.-math.), prof., SPbPU, St. Petersburg, Russia;
A.V. Solov'yov – Dr. Sci. (phys.-math.), prof., MBN Research Center, Frankfurt am Main, Germany;
A.K. Tagantsev – Dr. Sci. (phys.-math.), prof., Swiss Federal Institute of Technology, Lausanne, Switzerland;
I.N. Toptygin – Dr. Sci. (phys.-math.), prof., SPbPU, St. Petersburg, Russia.

The journal is included in the List of leading peer-reviewed scientific journals and other editions to publish major findings of theses for the research degrees of Doctor of Sciences and Candidate of Sciences.

The publications are presented in the VINITI RAS Abstract Journal and Ulrich's Periodical Directory International Database.

The journal is published since 2008 as part of the periodical edition 'Nauchno-tekhnicheskie vedomosti SPb-GPU'.

The journal is registered with the Federal Service for Supervision in the Sphere of Telecom, Information Technologies and Mass Communications (ROSKOMNADZOR). Certificate ПИ № ФС77-52144 issued December 11, 2012.

The journal is distributed through the CIS countries catalogue, the «Press of Russia» joint catalogue and the «Press by subscription» Internet catalogue. The subscription index is **71823**.

The journal is in the **Web of Science** (Emerging Sources Citation Index), **Scopus**, the **Russian Science Citation Index** (RSCI) and the **Directory of Open Access Journals** (DOAJ) databases.

© Scientific Electronic Library (<http://www.elibrary.ru>).

No part of this publication may be reproduced without clear reference to the source.

The views of the authors may not represent the views of the Editorial Board.

Address: 195251 Politekhnikeskaya St. 29, St. Petersburg, Russia.

Phone: (812) 294-22-85.

<http://ntv.spbstu.ru/physics>

© Peter the Great St. Petersburg Polytechnic University, 2022



НАУЧНО-ТЕХНИЧЕСКИЕ ВЕДОМОСТИ

САНКТ-ПЕТЕРБУРГСКОГО ГОСУДАРСТВЕННОГО
ПОЛИТЕХНИЧЕСКОГО УНИВЕРСИТЕТА

Физико-математические
науки

ТОМ 15, №2
2022

НАУЧНО-ТЕХНИЧЕСКИЕ ВЕДОМОСТИ САНКТ-ПЕТЕРБУРГСКОГО ГОСУДАРСТВЕННОГО ПОЛИТЕХНИЧЕСКОГО УНИВЕРСИТЕТА. ФИЗИКО-МАТЕМАТИЧЕСКИЕ НАУКИ

РЕДАКЦИОННЫЙ СОВЕТ ЖУРНАЛА

Боровков А.И., проректор по перспективным проектам;
Глухих В.А., академик РАН;
Жуков А.Е., чл.-кор. РАН – зам. председателя;
Иванов В.К., д-р физ.-мат. наук, профессор;
Индейцев Д.А., чл.-кор. РАН;
Рудской А.И., академик РАН – зам. председателя;
Сурис Р.А., академик РАН.

РЕДАКЦИОННАЯ КОЛЛЕГИЯ ЖУРНАЛА

Иванов В.К., д-р физ.-мат. наук, профессор, СПбПУ, СПб., Россия, – главный редактор;
Фотиади А.Э., д-р физ.-мат. наук, профессор, СПбПУ, СПб., Россия, – зам. главного редактора;
Капралова В.М., канд. физ.-мат. наук, доцент, СПбПУ, СПб., Россия, – ответственный секретарь;
Антонов В.И., д-р физ.-мат. наук, профессор, СПбПУ, СПб., Россия;
Безпрозванный И.Б., д-р биол. наук, профессор, Юго-Западный медицинский центр
Техасского университета, Даллас, США;
Блинов А.В., д-р физ.-мат. наук, профессор, СПбПУ, СПб., Россия;
Донецкий Д.В., д-р физ.-мат. наук, профессор, университет штата Нью-Йорк в Стоуни-Брук, США;
Лобода О.С., канд. физ.-мат. наук, доцент, СПбПУ, СПб., Россия;
Малерб Й.Б., Dr.Sc. (Physics), профессор, университет Претории, ЮАР;
Остряков В.М., д-р физ.-мат. наук, профессор, СПбПУ, СПб., Россия;
Привалов В.Е., д-р физ.-мат. наук, профессор, СПбПУ, СПб., Россия;
Смирнов Е.М., д-р физ.-мат. наук, профессор, СПбПУ, СПб., Россия;
Соловьёв А.В., д-р физ.-мат. наук, профессор, Научно-исследовательский центр мезобионаносистем (MBN),
Франкфурт-на-Майне, Германия;
Таганцев А.К., д-р физ.-мат. наук, профессор, Швейцарский федеральный институт технологий,
Лозанна, Швейцария;
Топтыгин И.Н., д-р физ.-мат. наук, профессор, СПбПУ, СПб., Россия;
Фирсов Д.А., д-р физ.-мат. наук, профессор, СПбПУ, СПб., Россия;
Хейфец А.С., Ph.D. (Physics), профессор, Австралийский национальный университет,
Канберра, Австралия;
Черепанов А.С., д-р физ.-мат. наук, профессор, СПбПУ, СПб., Россия.

Журнал с 2002 г. входит в Перечень ведущих рецензируемых научных журналов и изданий, в которых должны быть опубликованы основные результаты диссертаций на соискание ученых степеней доктора и кандидата наук.

Сведения о публикациях представлены в Реферативном журнале ВИНТИ РАН, в международной справочной системе «Ulrich's Periodical Directory».

С 2008 года выпускается в составе сериального периодического издания «Научно-технические ведомости СПбГПУ».

Журнал зарегистрирован Федеральной службой по надзору в сфере информационных технологий и массовых коммуникаций (Роскомнадзор). Свидетельство о регистрации ПИ № ФС77-52144 от 11 декабря 2012 г.

Распространяется по Каталогу стран СНГ, Объединенному каталогу «Пресса России» и по Интернет-каталогу «Пресса по подписке». Подписной индекс **71823**.

Журнал индексируется в базе данных **Web of Science** (Emerging Sources Citation Index), **Scopus**, а также включен в базы данных **«Российский индекс научного цитирования»** (РИНЦ), размещенную на платформе Научной электронной библиотеки на сайте <http://www.elibrary.ru>, и **«Directory of Open Access Journals»** (DOAJ)

При перепечатке материалов ссылка на журнал обязательна. Точка зрения редакции может не совпадать с мнением авторов статей.

Адрес редакции и издательства:

Россия, 195251, Санкт-Петербург, ул. Политехническая, д. 29.
Тел. редакции (812) 294-22-85.
<http://ntv.spbstu.ru/physics>

© Санкт-Петербургский политехнический университет Петра Великого, 2022

Contents

Condensed Matter Physics

- Sotova Yu. I., Gorokhovatsky Yu. A., Temnov D. E.** *The role of the electret effect in the formation of the piezoelectric state in the polyvinylidene fluoride-tetrafluoroethylene copolymer films*..... 8

Physical Electronics

- Filimonov A. V., Bondarenko V. B., Kumar Ravi.** *A chaotic potential of charged dislocations in the III-nitride heterojunctions at high temperatures* 16
- Berdnikov A. S., Krasnova N. K., Masyukevich S. V., Solovyev K. V.** *Visualization of the 3D stability zone of a quadrupole mass filter in the static longitudinal magnetic field*..... 26

Physical Materials Technology

- Tereshina I. S., Politova G. A., Kaminskaya T. P., Popov V. V., Gunderov D. V., Filimonov A. V., Pelevin I. A.** *Features of the nanostructure formation in the Nd-Pr-Fe-B-system alloys: a study by AFM and MFM*..... 35

Biophysics and Medical Physics

- Antonova D. A., Zotova A. D., Usatykh A. A., Morozova N. E., Yakunina M. V.** *Characterization of fluorescent proteins for studying the morphological rearrangements inside single bacterial cells during infection with phiKZ bacteriophage* 46

Nuclear Physics

- Tiba A., Karaseov P. A., Berdnikov Ya. A., Egorov A. Yu., Mironova S. Yu.** *Features of the copper-64 isotope production using the MGC-20 cyclotron at St. Petersburg Polytechnical University*..... 56
- Ekinci F., Bostanci E., Güzel M. S., Dağlı Ö.** *Analysing the effect of a cranium thickness on a Bragg peak range in the proton therapy: a TRIM and GEANT4 based study*..... 64

Theoretical Physics

- Mahanta C. R., Das M. P.** *Reconstructing quintessence scalar field model from new holographic dark energy in Bianchi type I universe*..... 79

Mathematics

- Yurova N. V.** *On conjugacy classes of the F_4 group over a field q with characteristic 2*..... 93

Mechanics

- Savikovskii A. V., Semenov A. S.** *Calculation of mixed-mode stress intensity factors for orthotropic materials in the plane stress state*..... 102
- Smirnov A. S., Suvorov S. V.** *Two-factor optimization in the brachistochrone problem*..... 124
- Lavrov Yu. A.** *The response of a round plate and a cylindrical water-filled volume underneath to a point load moving periodically* 140

Содержание

Физика конденсированного состояния

- Сотова Ю. И., Гороховатский Ю. А., Темнов Д. Э. Роль электростатического эффекта в формировании пьезоэлектрического состояния в пленках сополимера поливинилиденфторида с тетрафторэтиленом 8

Физическая электроника

- Филимонов А. В., Бондаренко В. Б., Кумар Рави. Хаотический потенциал заряженных дислокаций в гетероконтактах III-нитридов при высоких температурах..... 16
- Бердников А. С., Краснова Н. К., Масюкевич С. В., Соловьев К. В. Визуализация трехмерной зоны устойчивости квадрупольного фильтра масс в постоянном продольном магнитном поле..... 26

Физическое материаловедение

- Терёшина И. С., Политова Г. А., Каминская Т. П., Попов В. В., Гундеров Д. В., Филимонов А. В., Пелевин И. А. Особенности формирования наноструктуры в сплавах системы Nd-Pr-Fe-B, исследованные методами атомно-силовой и магнитно-силовой микроскопии..... 35

Биофизика и медицинская физика

- Антонова Д. А., Зотова А. Д., Усатых А. А., Морозова Н. Е., Якунина М. В. Характеризация флуоресцентных белков для изучения морфологических перестроек внутри одиночных бактериальных клеток при инфекции бактериофагом ϕ KZ с помощью оптической микроскопии 46

Ядерная физика

- Тиба А., Карасев П. А., Бердников Я. А., Егоров А. Ю., Миронова С. Ю. Особенности получения изотопа меди-64 на циклотроне МГЦ-20 Санкт-Петербургского политехнического университета 56
- Экинджи Ф., Бостанджи Э., Гузель М. С., Дагли О. Анализ влияния толщины тканей человеческого черепа на диапазон пиков Брэгга при протонной терапии с помощью программ TRIM и GEANT4 (статья на английском языке) 64

Теоретическая физика

- Маханта Ч. Р., Дас М. П. Реконструкция модели скалярного поля квинтэссенции для новой голографической модели темной энергии во Вселенной Бианки типа I (статья на английском языке)..... 79

Математика

- Юрова Н. В. О классах сопряженности в группе F_4 над роле q с характеристикой 2..... 93

Механика

- Савиковский А. В., Семенов А. С. Вычисление коэффициентов интенсивности напряжений в ортотропных материалах при смешанной моде разрушения в плоском напряженном состоянии 102

Смирнов А. С., Суворов С. В. *Двухфакторная оптимизация в задаче о брахистохроне* 124

Лавров Ю. А. *Действие периодически движущейся точечной нагрузки на круглую пластину и находящийся под ней цилиндрический водозаполненный объем.....* 140


Original article

DOI: <https://doi.org/10.18721/JPM.15201>

THE ROLE OF THE ELECTRET EFFECT IN THE FORMATION OF THE PIEZOELECTRIC STATE IN THE POLYVINYLIDENE FLUORIDE-TETRAFLUOROETHYLENE COPOLYMER FILMS

Yu. I. Sotova , *Yu. A. Gorokhovatsky*, *D. E. Temnov*

Herzen State Pedagogical University of Russia, St. Petersburg, Russia

 juliasotova1992@mail.ru

Abstract: In this work, the phenomenon of polarization of polyvinylidene fluoride-tetrafluoroethylene copolymer (P(VDF-TFE)) polymer films in the field of a corona discharge at elevated temperatures has been studied in order to elucidate the mechanism of formation of the piezoelectric state. The TSD spectroscopy was used to analyze the charge accumulation and relaxation processes occurring in the (P(VDF-TFE)) films during polarization. The results obtained made it possible to reveal an interrelationship of forming the electret and piezoelectric states in the (P(VDF-TFE)) as well as to explain the mentioned mechanism. On this basis a polarization procedure in the field of the corona discharge was developed and tested. This procedure permitted reducing the probability of electrical breakdown leading to mechanical damage of the films and allowed improving key characteristics of the objects under question.

Keywords: electret state, polyvinylidene fluoride, tetrafluoroethylene, piezoelectric effect, TSD spectroscopy

Funding: The research was supported by the Ministry of Education of Russian Federation as a part of a state task (project No. FSZN-2020-0026).

Citation: Sotova Yu. I., Gorokhovatsky Yu. A., Temnov D. E., The role of the electret effect in the formation of the piezoelectric state in polyvinylidene fluoride-tetrafluoroethylene copolymer films, St. Petersburg Polytechnical State University Journal. Physics and Mathematics. 15 (2) (2022) 8–16. DOI: <https://doi.org/10.18721/JPM.15201>

This is an open access article under the CC BY-NC 4.0 license (<https://creativecommons.org/licenses/by-nc/4.0/>)



Научная статья

УДК 538.9

DOI: <https://doi.org/10.18721/JPM.15201>

РОЛЬ ЭЛЕКТРЕТНОГО ЭФФЕКТА В ФОРМИРОВАНИИ ПЬЕЗОЭЛЕКТРИЧЕСКОГО СОСТОЯНИЯ В ПЛЕНКАХ СОПОЛИМЕРА ПОЛИВИНИЛИДЕНФТОРИДА С ТЕТРАФТОРЭТИЛЕНОМ

Ю. И. Сотова[✉], Ю. А. Гороховатский, Д. Э. Темнов

Российский государственный педагогический университет им. А. И. Герцена, Санкт-Петербург, Россия

[✉] juliasotova1992@mail.ru

Аннотация. С целью выяснения механизма формирования пьезоэлектрического состояния, в работе изучено явление поляризации полимерных пленок сополимера поливинилиденфторида с тетрафторэтиленом (П(ВДФ-ТФЭ)) в поле коронного разряда при повышенной температуре. Для анализа процессов накопления и релаксации зарядов, происходящих в П(ВДФ-ТФЭ) при поляризации, применялась спектроскопия токов термостимулированной деполяризации. Полученные результаты позволили обнаружить взаимосвязь процессов формирования электретного и пьезоэлектрического состояний в П(ВДФ-ТФЭ), а также объяснить указанный механизм. На этой основе была разработана и опробована методика поляризации в поле коронного разряда, позволяющая снизить вероятность электрического пробоя, приводящего к механическим повреждениям пленок, а также улучшить ключевые характеристики исследованных объектов.

Ключевые слова: электретное состояние, поливинилиденфторид, тетрафторэтилен, пьезоэлектрический эффект, спектроскопия токов термостимулированной деполяризации

Финансирование: работа выполнена при финансовой поддержке Государственного задания Минобрнауки Российской Федерации (проект № FSZN0026-2020-).

Для цитирования: Сотова Ю. И., Гороховатский Ю. А., Темнов Д. Э. Роль электретного эффекта в формировании пьезоэлектрического состояния в пленках сополимера поливинилиденфторида с тетрафторэтиленом // Научно-технические ведомости СПбГПУ. Физико-математические науки. 2022. Т. 15. № 2. С 8–16. DOI: <https://doi.org/10.18721/JPM.15201>

Статья открытого доступа, распространяемая по лицензии CC BY-NC 4.0 (<https://creativecommons.org/licenses/by-nc/4.0/>)

Introduction

The piezoelectric properties were first discovered in polyvinylidene fluoride (PVDF) by Heiji Kawai in 1969. However, producing piezoelectric films from the PVDF homopolymer comes with challenges due to a high coercive field (of the order of 10^8 V/m, which is two orders of magnitude higher than that of piezoceramics) [2], so piezoelectric polymers with lower coercive fields are commonly used as piezoelectric elements: these are composites based on vinylidene fluoride copolymers with trifluoroethylene, P(VDF-TrFE), and with tetrafluoroethylene, P(VDF-TFE). Notably, both the PVDF homopolymer and its copolymers only exhibit piezoelectric properties after repeated pre-stretching, causing the sample to extend by several times compared to the initial length [3, 4].

PVDF displays polymorphism, existing in five different crystalline modifications, denoted as α -, β -, γ -, δ - and ϵ -phases [5]. The β -phase has attracted the greatest attention from researchers due to its piezoelectric properties [6].

There are several approaches to generating a piezoelectric state in PVDF-based polymer films. A traditional method is film polarization by a corona discharge at elevated temperatures. This method is popular because larger field strengths can be achieved under corona polarization (compared to those obtained by the direct contact method) [7]. However, corona polarization at elevated temperatures induces electrical aging in polymer films: the probability of electrical breakdown increases with increasing polarization temperature, leading in turn to mechanical damage to the polymer films.

The goal of this study consisted in establishing the relationship between the electret and piezoelectric states generated in P(VDF-TFE) films, as well as in modifying the technology for inducing a piezoelectric state in PVDF-based polymer films, which can serve to decrease the probability of electrical breakdown in the given sample, preserving or even improving its key characteristics.

Experimental samples and procedure

The experimental sample was a mechanically pre-stretched F2ME-type P(VDF-TFE) copolymer film with a thickness of 20 μm . A piezoelectric state was induced in the samples with a corona discharge but under different polarization conditions.

The accumulation and relaxation of charges in P(VDF-TFE) under polarization was studied by the method of thermally stimulated depolarization currents (TSDC). TSDC measurements were carried out with a TSC II thermal analyzer (from Setaram, Lyon, France).

The piezoelectric coefficient d_{33} was measured by the dynamic method using a D33 test meter (Yangzhou, China).

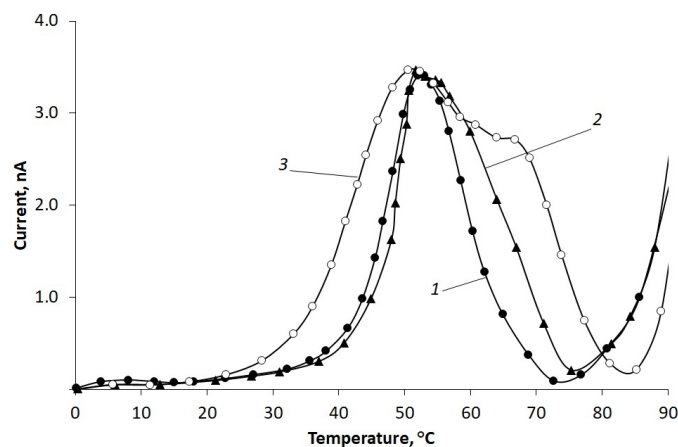


Fig. 1. Thermally stimulated depolarization currents in P(VDF-TFE) films polarized by negative corona discharge at different polarization temperatures, °C: 50 (1), 70 (2) and 80 (3)



Experimental results and discussion

The traditional procedure for inducing a piezoelectric state in the P(VDF-TPE) copolymer by a corona discharge field is as follows: the sample is placed in the given field at an elevated temperature, held in it for 10 minutes (maintaining a constant temperature), and then cooled to room temperature in the same field. It was experimentally established in earlier studies that polarization must be carried out with a negative corona discharge to achieve better electret characteristics [8].

The electric field strength required to obtain a high piezoelectric coefficient d_{33} is equal to 1.2 MV/cm [9]. We varied the polarization temperature from 50 to 80 °C.

Fig. 1 shows the TSDC curves in P(VDF-TPE) films polarized by negative corona discharge at different polarization temperatures. As evident from the data obtained, a single peak is observed on the TSDC curves for low polarization temperatures (50–60 °C) at about 50 °C, while two strongly overlapping peaks appear on the curves (near 40–70 °C) with increased polarization temperatures (70 and 80 °C). A possible explanation for this difference is that the homocharge is captured by deep near-surface traps in films polarized by the negative corona discharge. The actual homocharge in the P(VDF-TPE) sample does not contribute to the piezoelectric effect, but orientation of the polar structures occurs in the internal electric field generated by the homocharge (constituting the piezoelectric β -phase of PVDF). Apparently, there are two classes of polar structures with different activation energies. Polar structures of only one type (with lower activation energies, their current peak is located at about 50 °C) are oriented in the internal electric field of the homocharge under corona polarization at 50–70 °C, while increasing the polarization temperature to 80 °C produces orientation in both types of polar structures, which is manifested as two strongly overlapping peaks on the TSDC curves (in the temperature range of 40–70 °C).

In this case, it is possible to estimate the activation energies and the frequency factors for the polar structures in the P(VDF-TPE) samples, characterized by lower activation energies (Table 1); the samples were subjected to polarization at different temperatures. The calculations were performed by two methods: initial current rise and heating rate variation [10].

We also estimated the activation energy of the homocharge for a negatively polarized corona electrode (the release of the homocharge from the near-surface traps shown in Fig. 1 appears as an increase in current above 80 °C) by the initial rise method. The resulting value amounted to (1.90 ± 0.09) eV. A similar calculation for a positively polarized corona electrode gave an activation energy of the homocharge equal to (1.20 ± 0.06) eV.

Analyzing the dependence of the piezoelectric coefficient d_{33} on the polarization temperature (Fig. 2), we can conclude that the values of the piezoelectric coefficient are high (in the range of 24–26 pC/N) immediately after polarization (curve 1) and only slightly depend on the polarization temperature. However, it is not only the actual magnitude of the piezoelectric coefficient but also its thermal stability that is an important characteristic of the piezoelectric properties.

Table 1

**Key characteristics of polar structures
in P(VDF-TPE) films
polarized at different temperatures**

Method for determining W	Activation energy W , eV, for polarization temperature		
	50 °C	70 °C	80 °C
Initial rise method	0.82 ± 0.04	0.82 ± 0.04	0.83 ± 0.04
Heating rate variation method	0.84 ± 0.03	0.83 ± 0.03	0.83 ± 0.03
The frequency factor found by varying the heating rate was equal to $\omega = 10^{10} \text{ s}^{-1}$ for the three polarization temperatures			

Notes. 1. The results are given for polar structures characterized by lower activation energies (see Fig. 1 and explanations in the text). 2. The values of ω were determined up to a half decade.

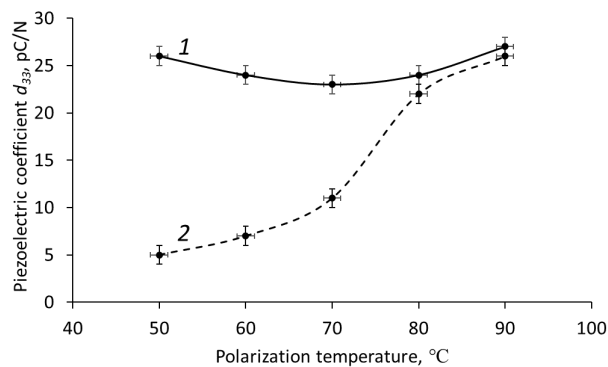


Fig. 2. Dependences of the piezoelectric coefficient d_{33} in P(VDF-TPE) films on the polarization temperature, obtained immediately after polarization (1) and after 2.5 hours of subsequent annealing at 70°C (2)

To test the thermal stability of the values obtained for the piezoelectric coefficient d_{33} , P(VDF-TFE) films were kept in a thermostat at 70 °C for two and a half hours. We then discovered that the piezoelectric coefficient in P(VDF-TFE) films polarized at a low temperature (50–70 °C) decreased considerably after exposure in a thermostat (see curve 2 in Fig. 2).

Thus, this quantity turns out to be unstable at polarization temperatures below 70 °C. On the other hand, polarization at 80–90 °C yields stable values of the piezoelectric coefficient.

As noted above, exposing the film to the corona discharge at elevated temperatures often leads to electrical breakdowns, mechanically damaging the film as a result. We used polarization in the internal field of the homocharge to reduce the risk of electrical breakdown: P(VDF-TPE) films were first subjected to polarization at room temperature under negative corona discharge for 10 minutes (the electric field strength was 1.2 MV/cm), then heated (the sample was in the open state, i.e., in the absence of an external electric field) to a different temperature, and finally cooled to room temperature. Fig. 3 shows the TSDC curves in P(VDF-TPE) films polarized by this method.

It can be seen from the TSDC curves in Fig. 3 that the peak on the curve rises with increasing heating temperature, and the area under the curve increases. We should note that the TSDC curves have a similar appearance to low-temperature equivalents in Fig. 1 (in terms of their shape and the positions of the peaks on the temperature axis), suggesting that the homocharge is held in deep near-surface traps in this case, while orientation of the polar structures occurs in the generated internal electric field. Thus, the mobility of polar structures increases with increasing heating temperature, more of them have time to orient themselves, so both the maximum value and the area under the curve grow.

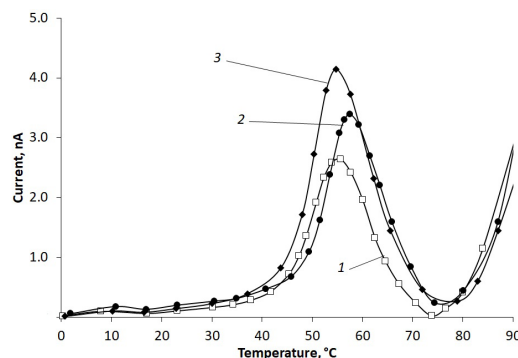


Fig. 3. Thermally stimulated depolarization currents in P(VDF-TPE) films polarized under negative corona discharge at room temperature, followed by heating (in the absence of an electric field) to different temperatures, °C: 50 (1), 70 (2) and 80 (3)



Table 2 gives the activation energies and frequency factors (with an accuracy up to half a decade) of polar structures in P(VDF-TFE) films polarized at room temperature, subsequently subjected to heating to different temperatures and further cooling to room temperature (in the open state, i.e., in the absence of an electric field), calculated by methods of initial rise and variation of the heating rate.

Table 2

**Key characteristics of polar structures in P(VDF-TPE) films
heated to different temperatures after polarization**

Method for determining W	Activation energy W , eV, at heating temperature	
	70 °C	90 °C
Initial rise	0.81 ± 0.04	0.83 ± 0.04
Heating rate variation	0.83 ± 0.03	0.84 ± 0.03
The frequency factor found by varying the heating rate was equal to $\omega = 10^{10} \text{ s}^{-1}$ for the two heating temperatures		

Notes. 1. Film samples were heated after polarization under negative corona discharge at room temperature. 2. The values of ω were determined up to a half decade.

We estimated the activation energy of the homocharge; in this case, the homocharge release from near-surface traps was manifested as an increase in depolarization current after it reaches 80 °C. (see Fig. 3). The value obtained by the initial rise method was $(1.90 \pm 0.09) \text{ eV}$, as in the case of the traditional polarization method.

Fig. 4 shows the dependence of the piezoelectric coefficient d_{33} on the heating temperature measured immediately after polarization (curve 1) and after two and a half hours of exposure in a thermostat at 70 °C (curve 2). Apparently, in the first case, the piezoelectric coefficient measured immediately after following the steps of the procedure (including polarization at room temperature, heating to a given temperature, then cooling to room temperature) increases with increasing heating temperature, reaching a maximum (25 mC/N) at a heating temperature of 90 °C. However, in the second case, when the procedure includes exposure in a thermostat after heating to a given temperature, the piezoelectric coefficient in P(VDF-TFE) samples, heated to 50–70 °C, decreased significantly, while the piezoelectric coefficient of the samples heated to 80–90 °C practically did not change. The optimal heating temperature was 90 °C, yielding the maximum value of the piezoelectric coefficient d_{33} (25 pC/N). On the other hand, heating to a higher temperature led to mechanical deformation of the samples.

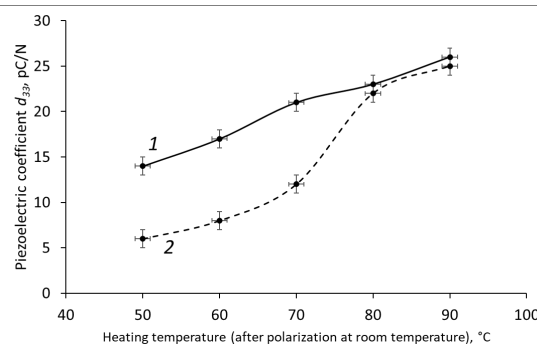


Fig. 4. Dependences of the piezoelectric coefficient d_{33} in polarized P(VDF-TPE) films on further heating temperature, obtained without subsequent annealing (1) and after 2.5 hours of subsequent annealing at 70 °C (2)
The films were polarized at room temperature

We can therefore argue that the technique proposed for inducing a piezoelectric state allows achieving the value of the piezoelectric coefficient comparable to that obtained by the traditional method in P(VDF-TFE) films; moreover, the probability of electrical breakdown (and mechanical damage to the sample) is significantly reduced.

Conclusion

As a result of the studies carried out by the method of thermal activation spectroscopy, we have proposed a mechanism for polarization in polymer films of the copolymer P(VDP-TPE): a homocharge is trapped by deep near-surface traps during polarization in corona discharge field, which itself does not contribute to the magnitude of the piezoelectric coefficient. However, orientation occurs in the internal electric field of the homocharge and the oriented state of the polar structures is preserved. Increasing the polarization temperature increases the contribution of dipoles with higher activation energies (this appears as two strongly overlapping peaks on the TSDC curves). Thus, homo and hetero charges coexist under corona discharge for polarized P(VDP-TPE) films. The activation energy of polar structures amounts to (0.82 ± 0.03) eV, and the frequency factor to 10^{10} s^{-1} (up to half a decade). The activation energy of the homocharge for a negatively polarized corona electrode is much higher than that for polar structures and amounts to (1.90 ± 0.09) eV. A similar calculation for a positively charged corona electrode gives an activation energy of the homocharge equal to (1.20 ± 0.06) eV.

Thus, we have established that the electret and piezoelectric states emerging in P(VDF-TPE) films are interconnected. Inducing an electret state in these samples is necessary to produce and preserve piezoelectric properties.

The traditional method of polarization in the corona field at elevated temperature often leads to electrical breakdowns, and, consequently, to mechanical damage to polymer films. The method for polarization in the internal field of the homocharge proposed in this study significantly reduces the risk electrical breakdown; furthermore, the values of the piezoelectric coefficient d_{33} obtained by this method in P(VDF-TPE) films are not inferior in their level and thermal stability to the piezoelectric coefficient d_{33} obtained in the samples by polarization using the traditional approach.

REFERENCES

1. Kawai H., The piezoelectricity of poly (vinylidene fluoride), Jap. J. Appl. Phys. 8 (6) (1969) 975–983.
2. Lushcheykin G. A., New polymer-containing piezoelectric materials, Physics of the Solid State. 48 (6) (2006) 1023–1025.
3. Ting Y., Suprpto Y., Chiu C.-W., Gunawan H., Characteristic analysis of biaxially stretched PVDF thin films, J. Appl. Polym. Sci. 135 (36) (2018) 46677.
4. Marandi M., Tarbuton J., Additive manufacturing of single- and double-layer piezoelectric PVDF-TrFE copolymer sensors, Procedia Manuf. 34 (2019) 666–671.
5. Begum S., Ullah H., Kausar A., et al., Fabrication of epoxy functionalized MWCNTs reinforced PVDF nanocomposites with high dielectric permittivity, low dielectric loss and high electrical conductivity, Comp. Sci. Technol. 167 (20 October) (2018) 497–506.
6. Kalimuldina G., Turdakyn N., Abay I., et al., A review of piezoelectric PVDF film by electrospinning and its applications, Sensors. 20 (18) (2020) 5214.
7. Sukumaran S., Chatbouri S., Rouxel D., et al., Recent advances in flexible PVDF based piezoelectric polymer devices for energy harvesting applications, J. Intell. Mater. Syst. Struct. 32 (7) (2021) 746–780.
8. Gorokhovatskiy Yu. A., Temnov D. E., Sotova Yu. I., Rheological parameters effect on the electric properties of polyvinylidene fluoride, St. Petersburg State Polytechnical University Journal: Physics and Mathematics. 13 (4) (2020) 39–46 (in Russian).
9. Mahadeva S. K., Berring J., Walus K., Stoeber B., Effect of poling time and grid voltage on phase transition and piezoelectricity of poly(vinylidene fluoride) thin films using corona poling, J. Phys. D: Appl. Phys. 2013. Vol. 46 (28) (2013) 285305.
10. Gorokhovatskiy Yu. A., Bordovskiy G. A., Termoaktivatsionnaya tokovaya spektroskopiya vysokomnykh poluprovodnikov i dielektrikov [Thermal activation spectroscopy of high-resistance semiconductors and dielectrics], Nauka, Moscow, 1991 (in Russian).



СПИСОК ЛИТЕРАТУРЫ

1. **Kawai H.** The piezoelectricity of poly (vinylidene fluoride) // Japanese Journal of Applied Physics. 1969. Vol. 8. No. 6. Pp. 975–983.
2. **Лучейкин Г. А.** Новые полимерсодержащие пьезоэлектрические материалы // Физика твердого тела. 2006. Т. 48. № 6. С. 963–964.
3. **Ting Y., Suprpto Y., Chiu C.-W., Gunawan H.** Characteristic analysis of biaxially stretched PVDF thin films // Journal of Applied Polymer Science. 2018. Vol. 135. No. 36. P. 46677.
4. **Marandi M., Tarbutton J.** Additive manufacturing of single- and double-layer piezoelectric PVDF-TrFE copolymer sensors // Procedia Manufacturing. 2019. Vol. 34. Pp. 666–671.
5. **Begum S., Ullah H., Kausar A., Siddiq M., Aleem M. A.** Fabrication of epoxy functionalized MWCNTs reinforced PVDF nanocomposites with high dielectric permittivity, low dielectric loss and high electrical conductivity // Composites Science and Technology. 2018. Vol. 167. 20 October. Pp. 497–506.
6. **Kalimuldina G., Turdakyn N., Abay I., Medeubayev A., Nurpeissova A., Adair D., Bakenov Z.** A review of piezoelectric PVDF film by electrospinning and its applications // Sensors. 2020. Vol. 20. No. 18. P. 5214.
7. **Sukumaran S., Chatbouri S., Rouxel D., Tisserand E., Thiebaud F., Ben Zineb T.** Recent advances in flexible PVDF based piezoelectric polymer devices for energy harvesting applications // Journal of Intelligent Material Systems and Structures. 2021. Vol. 32. No. 7. Pp. 746–780.
8. **Гороховатский Ю. А., Темнов Д. Э., Сотова Ю. И.** Влияние реологических параметров на электретные свойства поливинилиденфторида // Научно-технические ведомости СПбГПУ. Физико-математические науки. 2020. Т. 13. № 4. С. 39–46.
9. **Mahadeva S. K., Berring J., Walus K., Stoeber B.** Effect of poling time and grid voltage on phase transition and piezoelectricity of poly(vinylidene fluoride) thin films using corona poling // Journal of Physics D: Applied Physics. 2013. Vol. 46. No. 28. P. 285305.
10. **Гороховатский Ю. А., Бордовский Г. А.** Термоактивационная токовая спектроскопия высокоомных полупроводников и диэлектриков. М.: Наука. Гл. ред. физ.-мат. лит.-ры, 1991. 248 с.

THE AUTHORS

SOTOVA Yulia I.

Herzen State Pedagogical University of Russia
48 Moyka Emb., St. Petersburg, 191186, Russia
juliasotova1992@mail.ru
ORCID: 0000-0001-6792-2390

GOROKHOVATSKY Yuriy A.

Herzen State Pedagogical University of Russia
48 Moyka Emb., St. Petersburg, 191186, Russia
gorokh-yu@yandex.ru
ORCID: 0000-0001-5085-2525

TEMNOV Dmitry E.

Herzen State Pedagogical University of Russia
48 Moyka Emb., St. Petersburg, 191186, Russia
tde@herzen.spb.ru
ORCID: 0000-0002-9560-4346

СВЕДЕНИЯ ОБ АВТОРАХ

СОТОВА Юлия Ильинична — аспирантка кафедры общей и экспериментальной физики Российского государственного педагогического университета им. А. И. Герцена.

191186, Россия, г. Санкт-Петербург, наб. р. Мойки, 48

juliasotova1992@mail.ru

ORCID: 0000-0001-6792-2390

ГОРОХОВАТСКИЙ Юрий Андреевич — доктор физико-математических наук, заведующий кафедрой общей и экспериментальной физики Российского государственного педагогического университета им. А. И. Герцена.

191186, Россия, г. Санкт-Петербург, наб. р. Мойки, 48

gorokh-yu@yandex.ru

ORCID: 0000-0001-5085-2525

ТЕМНОВ Дмитрий Эдуардович — кандидат физико-математических наук, доцент кафедры общей и экспериментальной физики Российского государственного педагогического университета им. А. И. Герцена.

191186, Россия, г. Санкт-Петербург, наб. р. Мойки, 48

tde@herzen.spb.ru

ORCID: 0000-0002-9560-4346

Received 10.04.2022. Approved after reviewing 12.04.2022. Accepted 12.04.2022.

Статья поступила в редакцию 10.04.2022. Одобрена после рецензирования 12.04.2022. Принята 12.04.2022.

Original article

DOI: <https://doi.org/10.18721/JPM.15202>

A CHAOTIC POTENTIAL OF CHARGED DISLOCATIONS IN THE III-NITRIDE HETEROJUNCTIONS AT HIGH TEMPERATURES

A. V. Filimonov ¹✉, V. B. Bondarenko ¹, Ravi Kumar ²

¹ Peter the Great St. Petersburg Polytechnic University, St. Petersburg, Russia

² Indian Institute of Technology – Madras (IIT Madras), Chennai, India

✉ filimonov@rphf.spbstu.ru

Abstract. The paper studies the high-temperature structure of a chaotic potential (CP) induced in heterojunctions of the group III nitrides by the electrostatic field of charged dislocations. The CP amplitude in the junction plane has been obtained taking into account the spatial dispersion of a dielectric response of two-dimensional electron gas. The dependence of the CP properties on the parameters of the system was found. In particular, the magnitude of the CP amplitude exceeds that of the thermal energy, if the two-dimensional non-degenerate gas given in III-nitride heterojunctions and the dislocation densities being up to and over 10^{10} cm^{-2} .

Keywords: chaotic potential, natural size effect, III-nitride heterojunction, two-dimensional electron gas

Funding: The research is funded in part by the Ministry of Science and Higher Education of the Russian Federation, within the framework of strategic academic leadership “Priority 2030” (Agreement No. 075-15-2021-1333 dated September 30, 2021)

Citation: Filimonov A. V., Bondarenko V. B., A chaotic potential of charged dislocations in the III-nitride heterojunctions at high temperature, St. Petersburg Polytechnical State University Journal. Physics and Mathematics. 15 (2) (2022) 17–25. DOI: <https://doi.org/10.18721/JPM.15202>

This is an open access article under the CC BY-NC 4.0 license (<https://creativecommons.org/licenses/by-nc/4.0/>)

Научная статья

УДК 537.9

DOI: <https://doi.org/10.18721/JPM.15202>

ХАОТИЧЕСКИЙ ПОТЕНЦИАЛ ЗАРЯЖЕННЫХ ДИСЛОКАЦИЙ В ГЕТЕРОКОНТАКТАХ III- НИТРИДОВ ПРИ ВЫСОКИХ ТЕМПЕРАТУРАХ

А. В. Филимонов ¹✉, В. Б. Бондаренко ¹, Рави Кумар ²

¹ Санкт-Петербургский политехнический университет Петра Великого, Санкт-Петербург, Россия;

² Индийский технологический институт Мадраса, г. Ченнаи, Индия

✉ filimonov@rphf.spbstu.ru

Аннотация. В работе исследуется высокотемпературная структура хаотического потенциала (ХП) в гетероконтактах III-нитридов, обусловленного электростатическим полем заряженных дислокаций. С учетом пространственной дисперсии диэлектрического отклика двумерного электронного газа определена амплитуда ХП в плоскости контакта. Показана зависимость свойств ХП от параметров системы. В частности, при наличии невырожденного двумерного электронного газа в гетероконтактах III-нитридов и плотности дислокаций 10^{10} см^{-2} и более, величина амплитуды ХП превышает значение тепловой энергии.

Ключевые слова: хаотический потенциал, естественный размерный эффект, гетерокontakt III-нитридов, двумерный электронный газ

Финансирование: Исследование частично финансируется Министерством науки и высшего образования Российской Федерации в рамках программы стратегического академического лидерства «Приоритет 2030» (Договор 075-15-2021-1333 от 30.09.2021).

Для цитирования: Филимонов А. В., Бондаренко В. Б., Кумар Р. Хаотический потенциал заряженных дислокаций в гетероконтактах III-нитридов при высоких температурах // Научно-технические ведомости СПбГПУ. Физико-математические науки. 2022. Т. № 15 2. С. 25–37. DOI: <https://doi.org/10.18721/JPM.15202>

Статья открытого доступа, распространяемая по лицензии CC BY-NC 4.0 (<https://creativecommons.org/licenses/by-nc/4.0/>)



Introduction

Heterojunctions based on nitrides of Group III elements (Al, Ga, In) are finding increasing applications in solid-state devices used as high-power microwave sources [1]. While these systems offer a number of obvious advantages over the structures based on $A^{III}B^V$ compounds, certain drawbacks remain due to the specifics of the synthesis technology, affecting, for example, the parameters of high-electron-mobility transistors (HEMT) [2]. The parameter fluctuations detected for the devices are likely due to the initial defects in the materials and heterointerfaces forming. Lattice mismatch in III-nitrides and substrates used is known to generate initial misfit/threading dislocations, turning out to be electrically charged in many cases [3]. Electron scattering by charged dislocations in the 2D channel of the HEMT produces a certain decrease in electron mobility [4–7]. Moreover, the effect of this scattering can increase manifold at threshold values of the transmitted power, as the screening properties of the two-dimensional electron gas (2DEG) deteriorate at high temperatures, when this electronic subsystem ceases to be degenerate. The inhomogeneous field of charged dislocations is not averaged in these conditions, which means that fluctuations in the strength and chaotic potential are observed in the 2DEG plane. The interaction induced by the inhomogeneous electric field of the system of linearly distributed charges is in fact self-consistent, since it is primarily the density of surface states that has a finite magnitude. The chaotic potential causes tails to appear in the density of electronic states, with part of the carriers localized to the conducting channel in HEMT.

The goal of this study consisted in characterizing the chaotic potential of charged dislocations in heterojunctions of nitride semiconductor compounds at high temperatures.

Charged dislocation field

To be definite, we consider an indium-containing structure, InAlN/GaN [8], remaining stable at record high temperatures up to 1000 °C. Misfit dislocations with the surface density N_{disl} are represented by linear defects that are normally oriented to the junction plane. If the spatial arrangement of these extended defects is uncorrelated, their number follows a Poisson distribution with the parameter

$$\langle N \rangle = N_{\text{disl}} S$$

determining the mean number of these defects in the near-junction region with an area S .

Since the channel layer is formed from undoped (or compensated) GaN, the space charge in the near-junction region with band bending is generated primarily by charged dislocations. These extended defects within the space charge region can be assumed to be uniformly charged at large band bending, with a certain linear density taking the maximum value λ . If a delocalized surface charge is present in the heterojunction, the electrostatic image method can be used at a high density of surface states D_s (over $10^{14} \text{ cm}^{-2} \text{ eV}^{-1}$) to establish the parameters of a chaotic field [9]. We determine the field of an arbitrarily chosen dislocation in a cylindrical coordinate system, where ρ is the radial coordinate measuring the distance from the dislocation in the junction plane. The magnitude of the field strength for a charged dislocation is obtained by a simple calculation in the form

$$F_i(\rho) = \frac{2\lambda}{\varepsilon} \left(\frac{1}{\rho} - \frac{1}{\sqrt{\rho^2 + L_0^2}} \right), \quad (1)$$

where ε is the dielectric constant of the medium where the i th dislocation is located, L_0 is the width of the space charge region.

Assuming that 2DEG is strongly degenerate, let us now turn to analysis of expression (1), focusing on the nature of the dislocation distribution. The mean value of (1) in an area of radius R is found from the expression

$$\langle F \rangle_i(R) = \frac{4\lambda}{\varepsilon R^2} \left(R - \sqrt{R^2 + L_0^2} + L_0 \right). \quad (2)$$

As a matter of fact, Eq. (2) determines the mean contribution of one charged dislocation to the field strength. Considering the distribution of charged dislocations, we can also represent the mean fluctuations in their number in the corresponding surface region with an area $S = \pi R^2$ in the form

$$\delta N(R) = R\sqrt{\pi N_{\text{disl}}}. \quad (3)$$

The product of (2) by (3) gives an estimate for the characteristic scale of the inhomogeneities in the surface field strength

$$\delta F(R) = \frac{4\lambda}{\varepsilon R} \sqrt{\pi N_{\text{disl}}} \left(R - \sqrt{R^2 + L_0^2} + L_0 \right). \quad (4)$$

The resulting function (4) is monotonically decreasing, reaching its maximum at $R \ll L_0$. Calculating the exact upper bound of this expression (in the limit $R \rightarrow 0$), we obtain the amplitude of the chaotic field:

$$\delta F = \frac{4\lambda\sqrt{\pi N_{\text{disl}}}}{\varepsilon}. \quad (5)$$

These high densities of surface states allow to directly estimate the magnitude of the chaotic potential amplitude in the 2DEG plane. The magnitude of potential inhomogeneities can be found under these conditions in the Thomas–Fermi approximation:

$$\delta\sigma = eD_s \cdot \delta U. \quad (6)$$

It is assumed here that the potential perturbation is small in comparison with the mean electron energy in the surface zone, while the variation in the density of states is neglected. Next, taking into account the linear dependence of the surface charge on the field strength $F = 4\pi\sigma/\varepsilon$, as well as expressions (5) and (6), we can relate the quantity δU with the parameters of the system:

$$\delta U = \frac{\lambda}{eD_s} \cdot \sqrt{\frac{N_{\text{disl}}}{\pi}}. \quad (7)$$

Case of low density of electron states

The case when the densities of electron states in a heterojunction are relatively low deserves more detailed analysis of the potential fluctuations emerging, using the dielectric response function of the surface subsystem. The potential energy of a surface electron in the field of a charged dislocation without a reaction of the medium takes the form

$$V_i(\rho) = e\lambda \cdot \ln \frac{\sqrt{\rho^2 + L_0^2} + \rho}{\rho}. \quad (8)$$

In view of the Fourier–Bessel transformation (8) [10] in the space of wave vectors q , we have

$$V_i(q) = \frac{e\lambda}{q^2} \cdot [1 - \exp(-qL_0)]. \quad (9)$$

The dielectric response function has the following form in the high-temperature region (i.e., for classical statistics of two-dimensional electron gas) [11]:

$$\varepsilon(q) = \frac{\varepsilon_1 + \varepsilon_2}{2} \cdot \left(1 + \frac{q_s(q)}{q} \right), \quad (10)$$



where ε_1 and ε_2 are the dielectric constants of contacting semiconductors, $q_s(q)$ is the screening parameter in a two-dimensional electronic system. The relation $q \ll q_s$ also holds true with large band bends for most of the harmonics; in this case, the dielectric response function (10) can be approximately represented as [12]:

$$\varepsilon(q) \approx \frac{2\pi e^2 n_s}{kT \cdot q}. \quad (11)$$

Using the form of the initial potential (9), the inverse Fourier–Bessel transform, and the expression for the dielectric response of system (11), we obtain the potential electron energy in the surface plane accounting for screening:

$$U_i(\rho) = \frac{\lambda kT}{2\pi e n_s} \cdot \left(\frac{1}{\rho} - \frac{1}{\sqrt{\rho^2 + L_0^2}} \right). \quad (12)$$

The functional dependence on the radial coordinate in (12) coincides with a similar dependence in (1), allowing to repeat the previous calculation algorithm for directly finding the amplitude of the chaotic potential:

$$\delta U = \frac{\lambda kT}{e n_s} \cdot \sqrt{\frac{N_{disl}}{\pi}}. \quad (13)$$

The resulting expression may not be final, requiring in some cases to additionally find the 2DEG density in terms of the chaotic potential parameters, i.e., to establish the functional dependency $n_s = n_s(\delta U)$.

The corresponding density of electron states $D(E)$ can be obtained for a specific form of the potential energy distribution for a surface electron, characterized by the probability density $p(U)$. Since the density of surface states is initially constant if dispersion follows a parabolic law, this density takes the following form in the presence of a chaotic potential [13]:

$$D(E) = D_s \int_{-\infty}^E p(U) dU, \quad (14)$$

Calculating the integral in (14) for a Gaussian distribution with the standard deviation parameter equal to δU yields the result known from probability theory via the error function:

$$D(E) = \frac{D_s}{2} \cdot \left[1 + \operatorname{erf} \left(\frac{E}{\delta U \sqrt{2}} \right) \right]. \quad (15)$$

The density of 2DEG in the junction is determined by integration over all occupied states:

$$n_s = \int_{-\infty}^{+\infty} D(E) f(E) dE. \quad (16)$$

The Boltzmann distribution law

$$f(E) \approx \exp[\mu - E/kT]$$

should be chosen here for the high-temperature limit, where μ is the chemical potential measured from the bottom of the unperturbed surface band of electron states.

In view of the form that perturbed density (15) takes, we obtain from expression (16) [9]:

$$n_s = D_s kT \cdot \exp \left[\frac{\mu}{kT} + \frac{1}{2} \left(\frac{\delta U}{kT} \right)^2 \right]. \quad (17)$$

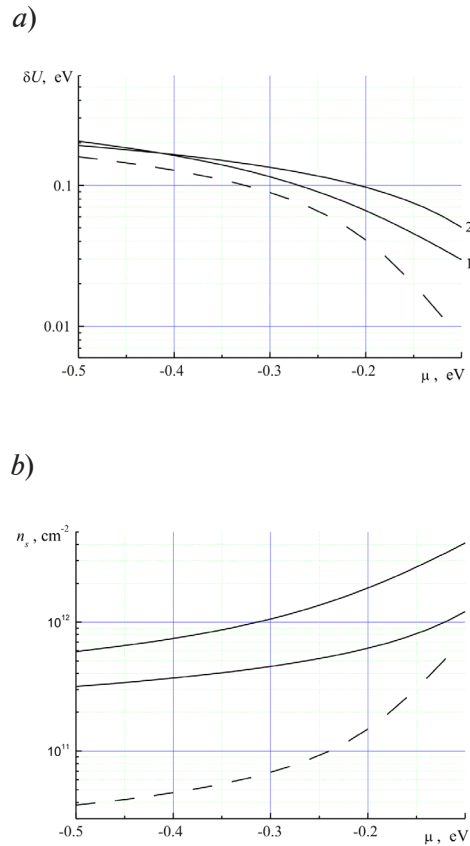


Fig. 1. Chaotic potential amplitude of charged dislocations (a) and 2DEG density (b) in a III-nitride heterojunction as functions of chemical potential for two temperatures, K: 600 K (curves 1 and dashes), 1200 K (2); $N_{\text{disl}} = 10^{10} \text{ cm}^{-2}$ (1, 2) and 10^8 cm^{-2} (dashes), $\lambda = 0.01 \text{ ESU}$, $D_s \approx 10^{14} \text{ cm}^{-2} \text{ eV}^{-1}$

Thus, to determine the magnitude of the chaotic potential amplitude, we should solve the transcendental equation obtained by substituting (17) into (13):

$$\delta U = \frac{\lambda}{eD_s} \cdot \sqrt{\frac{N_{\text{disl}}}{\pi}} \cdot \exp \left[-\frac{\mu}{kT} - \frac{1}{2} \left(\frac{\delta U}{kT} \right)^2 \right]. \quad (18)$$

The δU dependences calculated for the typical parameter values in the system are shown in Fig. 1.

Discussion

Summarizing the analysis carried out, we should note that the expression for the characteristic values of surface potential inhomogeneity at high temperatures (13) could be obtained from Eq. (7) by substituting the density of states D_s with the ratio n_s/kT . Estimating the values that δU takes for the chaotic potential parameters in heterojunctions based on III-nitrides, we adopt the effective electron mass in the surface zone $m^* \approx 0.2m$ (m is the electron rest mass) and the corresponding unperturbed density of surface states $D_s \approx 10^{14} \text{ cm}^{-2} \text{ eV}^{-1}$. Then, assuming that the dislocation density at the interface is of the order of 10^{10} cm^{-2} , carrying the maximum charge per unit length of about 0.01 ESU, δU values in non-degenerate 2DEG exceed the thermal energies kT in a wide range of negative values of the chemical potential (or electrochemical potential, if a blocking voltage is applied to the transistor gate). The chaotic potential amplitude can reach over 100 meV in HEMP operating modes close to the cutoff, even at significantly lower dislocation densities (dashed line in Fig. 1). The corresponding 2DEG densities decrease from the initial levels (about 10^{13} cm^{-2}) by one or two orders of magnitude (Fig. 2).



Conclusion

We have considered the behavior of the chaotic potential induced in heterojunctions based on III-nitrides by the electrostatic field of the dislocations present throughout the material, carrying an electric charge. The CP amplitude in the junction plane at high temperatures has been determined taking into account the spatial dispersion of the dielectric response of two-dimensional electron gas. We have analyzed the dependence of the CP properties on the system parameters. Our main finding is that the CP amplitude exceeds the thermal energy level for non-degenerate 2DEG in III-nitride heterojunctions at dislocation densities of 10^{10} cm^{-2} or higher. This can lay the groundwork for future applications in semiconductor devices.

REFERENCES

1. Aleksandrov S. B., Baranov D.A., Kaydash A.P., et al., Microwave field-effect transistors based on group-III nitrides, *Semiconductors*. 38 (10) (2004) 1235–1239.
2. Emtsev V. V., Zavarin E. E., Oganessian G. A., et al., Relationship between the reliability of transistors with 2D AlGaIn/GaN channel and organization type of nanomaterial, *Techn. Phys. Lett.* 42 (7) (2016) 701–703.
3. Shikin V. B., Shikina Yu. V., Charged dislocations in semiconductor crystals, *Phys. Usp.* 38 (8) (1995) 845–875.
4. Weimann N. G., Eastman L. F., Doppalapudi D., et al., Scattering of electrons at threading dislocations in GaN, *J. Appl. Phys.* 83 (7) (1998) 3656–3659.
5. Debdeep J., Gossard A. C., Mishra U. K., Dislocation scattering in a two-dimensional electron gas, *Appl. Phys. Lett.* 76 (13) (2000) 1707–1709.
6. Protasov D. Y., Malin T. V., Tikhonov A. V., et al., Electron scattering in AlGaIn/GaN heterostructures with a two-dimensional electron gas, *Semiconductors*. 47 (1) (2013) 33–44.
7. Bondarenko V. B., Davydov S. N., Nacke B., Filimonov A. V., Chaotic potential on the degenerated semiconductor surface, *Key Eng. Mater.* 806 (2019) 17–23.
8. Medjdoub F., Carlin J. F., Gaquiere C., et al., Status of the emerging InAlIn/GaN power HEMT technology, *Open Electr. Electron. Eng. J.* 2 (2008) 1–7.
9. Bondarenko V. B., Filimonov A. V., Kumar R., A chaotic potential of charged dislocations in group III-nitride heterojunctions, *Techn. Phys. Lett.* 47 (1) (2021) 8–10.
10. Gradshteyn I. S., Ryzhik I.M., Table of integrals, series, and products, 17-th edition, Ed. by A. Jeffrey, D. Zwillinger, Academic Press; Amsterdam, Boston, Heidelberg, London, 2007.
11. Ando T., Fowler A. B., Stern F., Electronic properties of two-dimensional systems, *Rev. Mod. Phys.* 54 (2) (1982) 437– 672.
12. Bondarenko V. B., Davydov S. N., Filimonov A. V., Inherent potential inhomogeneity on the semiconductor surface for equilibrium impurity distribution, *Semiconductors*. 44 (1) (2010) 41–44.
13. Bondarenko V. B., Filimonov A. V., Criterion for strong localization on a semiconductor surface in the Thomas – Fermi approximation, *Semiconductors*. 51 (10) (2017) 1321–1325.

СПИСОК ЛИТЕРАТУРЫ

1. Александров С. Б., Баранов Д. А., Кайдаш А. П. и др. Сверхвысокочастотные полевые транзисторы на основе нитридов III группы // *Физика и техника полупроводников*. 2004. Т. 10 № 38. С. 1275–1279.
2. Емцев В.В., Заварин Е. Е., Оганесян Г. А. и др. Взаимосвязь надежности AlGaIn/GaN транзисторов с характером организации наноматериала // *Письма в Журнал технической физики*. 2016. Т. 42. № 13. С. 80–86.
3. Шикин В. Б., Шикина Ю. В. Заряженные дислокации в полупроводниковых кристаллах // *Успехи физических наук*. 1995. Т. 165. № 8. С. 887–917.
4. Weimann N. G., Eastman L. F., Doppalapudi D., Ng H. M., Maustakus T. D. Scattering of electrons at threading dislocations in GaN // *Journal of Applied Physics*. 1998. Vol. 83. No. 7. Pp. 3656–3659.
5. Debdeep J., Gossard A. C., Mishra U. K. Dislocation scattering in a two-dimensional electron gas // *Applied Physics Letters*. 2000. Vol. 76. No. 13. Pp. 1707–1709.

6. Протасов Д. Ю., Малин Т. В., Тихонов А. В., Цацульников А. Ф., Журавлев К. С. Рассеяние электронов в гетероструктурах AlGaIn/GaN с двумерным электронным газом // Физика и техника полупроводников. 2013. Т. 47. № 1. С. 36–47.

7. Bondarenko V. B., Davydov S. N., Nacke B., Filimonov A. V. Chaotic potential on the degenerated semiconductor surface // Key Engineering Materials. 2019. Vol. 806. Pp. 17–23.

8. Medjdoub F., Carlin J. F., Gaquiere C., Grandjean N., Kohn E. Status of the emerging InAlN/GaN power HEMT technology // The Open Electrical and Electronic Engineering Journal. 2008. Vol. 2. No. Pp. 1–7.

9. Бондаренко В. Б., Филимонов А. В., Kumar R. Хаотический потенциал заряженных дислокаций в гетероконтактах III-нитридов // Письма в Журнал технической физики. 2021. Т. 47. № 1. С. 12–14.

10. Градштейн И. С., Рыжик И. М. Таблицы интегралов, сумм, рядов и произведений. М.: Наука, 1108 .1971 с.

11. Андо Т., Фаулер А., Стерн Ф. Электронные свойства двумерных систем. М.: Мир, 415 .1985 с.

12. Бондаренко В. Б., Давыдов С. Н., Филимонов А. В. Естественные неоднородности потенциала на поверхности полупроводника при равновесном распределении примеси // Физика и техника полупроводников. 2010. Т. 1 № .44. С. 44–47.

13. Бондаренко В. Б., Филимонов А. В. Критерий сильной локализации на поверхности полупроводника в приближении Томаса – Ферми // Физика и техника полупроводников. 2017. Т. 51. № 10. С. 1372–1375.

THE AUTHORS

FILIMONOV Alexey V.

Peter the Great St. Petersburg Polytechnic University

29 Politechnicheskaya St., St. Petersburg, 195251, Russia

filimonov@rphf.spbstu.ru

ORCID: 0000-0002-2793-5717

BONDARENKO Vyacheslav B.

Peter the Great St. Petersburg Polytechnic University

29 Politechnicheskaya St., St. Petersburg, 195251, Russia

vyacheslav.b.bondarenko@mail.ru

ORCID: 0000-0002-9357-3902

KUMAR Ravi N. V.

Indian Institute of Technology – Madras (IIT Madras)

IIT P.O., Chennai, Tami Nadu, 600036, India

nvrk@iitm.ac.in

ORCID: 0000-0001-6856-6092



СВЕДЕНИЯ ОБ АВТОРАХ

ФИЛИМОНОВ Алексей Владимирович — доктор физико-математических наук, профессор Высшей инженерно-физической школы, руководитель Научно-образовательного центра «Физика нанокompозитных материалов электронной техники» Санкт-Петербургского политехнического университета Петра Великого.

195251, Россия, г. Санкт-Петербург, Политехническая ул., 29

filimonov@rphf.spbstu.ru

ORCID: 0000-0002-2793-5717

БОНДАРЕНКО Вячеслав Борисович — кандидат физико-математических наук, доцент Высшей инженерно-физической школы Санкт-Петербургского политехнического университета Петра Великого.

195251, Россия, г. Санкт-Петербург, Политехническая ул., 29

vyacheslav.b.bondarenko@mail.ru

ORCID: 0000-0002-9357-3902

КУМАР Рави Н. В. — Ph.D., профессор, заведующий кафедрой металлургии и материаловедения Индийского технологического института Мадраса (ИТ Мадрас).

ИТ Р.О., Chennai, Tami Nadu, 600036, India

nvrk@iitm.ac.in

ORCID: 0000-0001-6856-6092

Received 11.04.2022. Approved after reviewing 13.05.2022. Accepted 13.05.2022.

Статья поступила в редакцию 11.04.2022. Одобрена после рецензирования 13.05.2022. Принята 13.05.2022.

Original article

DOI: <https://doi.org/10.18721/JPM.15203>

VISUALIZATION OF THE 3D STABILITY ZONE OF A QUADRUPOLE MASS FILTER IN THE STATIC LONGITUDINAL MAGNETIC FIELD

A. S. Berdnikov¹, N. K. Krasnova², S. V. Masyukevich¹, K. V. Solovyev²✉

¹ Institute for Analytical Instrumentation of the Russian Academy of Sciences, St. Petersburg, Russia;

² Peter the Great St. Petersburg Polytechnic University, St. Petersburg, Russia

✉ k-solovyev@mail.ru

Abstract. A new visualization method has been put forward to show the three-dimensional stability zones of a quadrupole mass filter placed in the constant uniform magnetic field directed along the quadrupole axis. The three-dimensional zone was represented by a set of two-dimensional sections each of which being an analogue of a stability two-dimensional zone of an intermittent electric quadrupole. The procedure for redetermining the boundaries of stability regions for the two-dimensional sections was applied. The results obtained can be used both in design of new mass spectrometers and in an analysis of periodic dynamic system stability.

Keywords: quadrupole mass filter, mass spectrometry, stability zone, Floquet theory

Citation: Berdnikov A. S., Krasnova N. K., Masyukevich S. V., Solovyev K. V., Visualization of the 3D stability zone of a quadrupole mass filter in the static longitudinal magnetic field, St. Petersburg Polytechnical State University Journal. Physics and Mathematics. 15 (2) (2022) 26–34. DOI: <https://doi.org/10.18721/JPM.15203>

This is an open access article under the CC BY-NC 4.0 license (<https://creativecommons.org/licenses/by-nc/4.0/>)



Научная статья

УДК 537.533.7, 537.534.7, 681.2.084

DOI: <https://doi.org/10.18721/JPM.15203>

ВИЗУАЛИЗАЦИЯ ТРЕХМЕРНОЙ ЗОНЫ УСТОЙЧИВОСТИ КВАДРУПОЛЬНОГО ФИЛЬТРА МАСС В ПОСТОЯННОМ ПРОДОЛЬНОМ МАГНИТНОМ ПОЛЕ

А. С. Бердников¹, Н. К. Краснова², С. В. Масюкевич¹, К. В. Соловьев²✉

¹ Институт аналитического приборостроения Российской академии наук, Санкт-Петербург, Россия;

² Санкт-Петербургский политехнический университет Петра Великого, Санкт-Петербург, Россия

✉ k-solovyev@mail.ru

Аннотация. Предложен новый способ визуализации трехмерной зоны устойчивости иона в квадрупольном масс-филт্রে, помещенном в однородное постоянное магнитное поле, направленное вдоль оси квадруполя. Трехмерная зона представлена набором двумерных сечений, каждое из которых является аналогом двумерной зоны устойчивости электрического квадруполя с периодическим питанием. Применен способ уточненного определения границ областей устойчивости для двумерных сечений. Результаты могут быть использованы как в ходе проектирования новых масс-спектрометрических приборов, так и для анализа устойчивости периодических динамических систем.

Ключевые слова: квадрупольный масс-филтър, масс-спектрометрия, зоны устойчивости, теория Флоке

Для цитирования: Бердников А.С., Краснова Н. К., Масюкевич С. В., Соловьев К. В. Визуализация трехмерной зоны устойчивости квадрупольного фильтра масс в постоянном продольном магнитном поле // Научно-технические ведомости СПбГПУ. Физико-математические науки. 2022. Т. 2 № 15. С. 26–34. DOI: <https://doi.org/10.18721/JPM.15203>

Статья открытого доступа, распространяемая по лицензии CC BY-NC 4.0 (<https://creativecommons.org/licenses/by-nc/4.0/>)

Introduction

The quadrupole mass spectrometer, first proposed by Wolfgang Paul back in 1953 [1], is still in much demand for several applications. Different approaches to improving its characteristics include, in particular, placing the device in a magnetic field that is constant homogeneous in the simplest configuration. Finding the conditions for the stability of a charged particle in the field combination produced is pivotal for understanding the operating principles of the device. A number of studies have explored the stability of the ion in a system with a static homogeneous magnetic field directed normal to the quadrupole axis [2, 3]; the authors tend to rely on the data on the stability regions of the Mathieu equation (see, for example, monographs [7, 8]). However, most works (see, for example, [4–6]) do not provide preliminary analysis of ion stability of ions, choosing to focus directly on the transmission of an idealized device with the magnetic field vector pointing in different directions by numerically analyzing the motion of a large number of charged particles. Meanwhile, the nature of ion motion can be explored by analytical techniques from Floquet's theory [8–10, 15], since the equations of motion remain linear for the given system comprising the quadrupole with a static homogeneous magnetic field. The approach based on this theory allows to clarify the specific issues related to stability of ion motion and, accordingly, facilitate analysis of the system, formulating assumptions about its optimal operating modes.

The standard approach to analyzing the stability of ion motion in systems with an AC power supply, described by linear differential equations of motion, consists of separating the motion with respect to the coordinates, followed by analysis of the Hill equations for each of the resulting coordinates and combining (overlapping) the stability regions for all the directions of motion considered (see, for example, [9–12]). The dimension of the stability region is determined by the number of parameters affecting the stability of the ion motion. The parameters are typically related to the electrical power supply of the ion-optical system.

The goal of this study is to construct a three-dimensional stability region for the equations of transverse ion motion in the electric field of a quadrupole with an AC power supply and a static longitudinal magnetic field.

Finding the sections of the three-dimensional stability region of the system

Let us consider as an example the case that is not reduced to a situation with separated one-dimensional motion, specifically, the case of a quadrupole in a homogeneous magnetic field. Notably, the approach used here was first applied in our earlier study [16]. We have now managed to both improve the quality with which the boundaries of two-dimensional stability regions are approximated (relying on the algorithm proposed in [17]), and better understand the required operating principle of the device by representing the three-dimensional stability regions as a set of plane sections with angular sampling between the planes.

To simplify further presentation, we introduce dimensionless units of measurement [16], assuming that the dimensional coordinates $\mathbf{R} = (X, Y, Z)$ and time t are connected to the corresponding dimensionless coordinates $\mathbf{r} = (x, y, z)$ and time τ by the following relations:

$$\mathbf{R} = \ell \mathbf{r}, t = T \tau, \quad (1)$$

where ℓ, T are the selected linear and time scales.

A particle with charge e and mass m moves in a static homogeneous magnetic field

$$\mathbf{B} = B_0(b_1, b_2, b_3), \quad b_1^2 + b_2^2 + b_3^2 = 1, \quad (2)$$

and in an electric field with an AC power supply

$$U = (U_0 - U_1 f(\omega t)) \frac{X^2 - Y^2}{\ell^2}, \quad f(\omega(t + \alpha)) = f(\omega t). \quad (3)$$

The system of equations of motion in these fields has the following dimensionless form:



$$\begin{aligned}\ddot{x} &= -(a - 2q f(2\tau))x + \lambda (\dot{y}b_3 - \dot{z}b_2), \\ \ddot{y} &= (a - 2q f(2\tau))y + \lambda (\dot{z}b_1 - \dot{x}b_3), \\ \ddot{z} &= \lambda (\dot{x}b_2 - \dot{y}b_1),\end{aligned}\quad (4)$$

with the coefficients a , q , λ , determined by selecting the time scale $T = 2/\omega$ by the following relations:

$$a = \frac{8eU_0}{\omega^2 m \ell^2}, \quad q = \frac{4eU_1}{\omega^2 m \ell^2}, \quad \lambda = \frac{2eB_0}{\omega m}. \quad (5)$$

The dots over the variables in Eqs. (4) denote a multiple of the differentiation over time τ . System (4) has five independent parameters affecting the stability: the traditional parameters a and q , as well as new ones, the parameter λ associated with the strength of the magnetic field and the parameters associated with the direction of the magnetic field, conditionally associated with the polar and azimuthal angles of the vector \mathbf{B} relative to the coordinate system bound to the geometry of the electric quadrupole. Evidently, the five-dimensional region can only be visualized by sections whose dimensions do not exceed 3.

If the magnetic field $\mathbf{B} = B_0(0, 0, 1)$ is directed along the quadrupole axis, then system (4) is simplified:

$$\begin{aligned}\ddot{x} &= -(a - 2q f(2\tau))x + \lambda \dot{y}, \\ \ddot{y} &= (a - 2q f(2\tau))y - \lambda \dot{x},\end{aligned}\quad (6)$$

$$\ddot{z} = 0. \quad (7)$$

The number of parameters is reduced to three in this case, so it becomes possible to visualize the stability region. Eq. (8) determines the drift motion along the coordinate z . In the absence of a magnetic field ($\lambda = 0$), the two equations of system (7) are isolated from each other and are solved independently. If $\lambda \neq 0$, these equations should be solved simultaneously.

The operating principle of the mass separator based on this combination of fields uses the simultaneous stability of the solutions to Eqs. (7) for the parameters a , q , λ lying in some ranges, determining the range of masses transmitted by the device given that other quantities entering relation (5) are constant. Therefore, three-dimensional stability regions can be constructed, for example, through sequential analysis of system stability for a set of discrete values of parameters (a, q, λ) given in a certain three-dimensional domain with steps in parameters $(\Delta a, \Delta q, \Delta \lambda)$, respectively. For the zero magnetic field ($\lambda = 0$), we have a plane (a, q) with traditional two-dimensional stability diagrams.

According to Floquet's theory [8, 15], the stability of system (7) is determined through analyzing the multipliers s_i , which are the monodromy matrix eigenvalues of the normal system constructed from the equations of system (7). Since the matrix of the normal system is periodic, the stability of motion is guaranteed when each of its multipliers lies in a unit circle $|s| \leq 1$, with the multipliers lying on the circle $|s| = 1$ are not multiples of the roots of the corresponding characteristic equation [8].

Next, we construct a two-dimensional diagram of the joint stability region of Eqs. (7) with a cosine-wave power supply and a constant value of the magnetic field parameter $\lambda = 0.3$ (Fig. 1). Black dots indicate stable mesh nodes (q, a) , the bounding curves interpolate the refined boundary points. Refinement (crossed points) is performed by the algorithm given in our report [17] and consisting in analysis of the quantity

$$S(q) = \max_i |s_i(q)|$$

for the values of the parameter q adjacent to the boundary.

The stability region is characterized by the values $S(q) \leq 1$. $S(q) > 1$ and $S(q) \rightarrow 1$ outside the stability region, with q tending to the value corresponding to the boundary one for the given a and λ . The boundary can be refined both by the bisection method and by quadratic interpolation of the dependence $q(S)$ in the instability region adjacent to the boundary. The results shown in Fig. 1 are easily confirmed by directly calculating the trajectories for the parameters lying inside/outside the stability region.

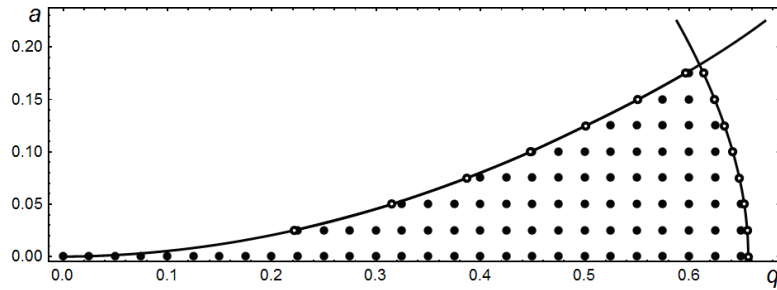


Fig. 1. Boundary of stability region for Eqs. (6) refined by analyzing the multipliers:
black dots indicate stable mesh nodes (q, a) , the bounding curves interpolate the refined boundary points

In the case of a mass analyzer based on the system defined by Eqs. (7), (8) by the traditional principle used in the quadrupole mass filter (time sweep of the electric field amplitudes), we should find the section of the three-dimensional stability region by a plane including the axis a and forming a certain angle φ with the plane $\lambda = 0$, subsequently constructing an operating line (see [9, 10]) in the given plane relating the parameters q and λ . A synchronized (with the electric quadrupole's power supply) sweep of the magnetic field should also be carried out. The purpose of this procedure is to ensure that the variation in the parameters a, q, λ is proportional to that in the filtered ion mass. Notably, the frequency sweeping is hardly possible here because the parameters depend on the frequency to varying degrees.

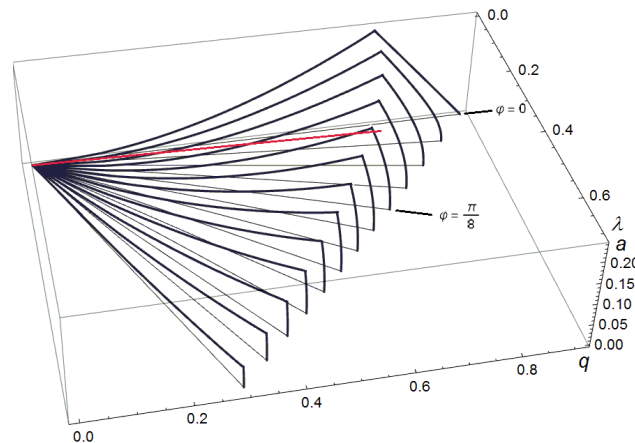


Fig. 2. Section of three-dimensional stability region of system (6)
by the planes $\varphi = \text{const}$, drawn through the axis a ; the angle φ is measured from the plane $\lambda = 0$.
(φ varies from 0 to $3\pi/8$ with a step of $\pi/32$)
The operating line is highlighted in red

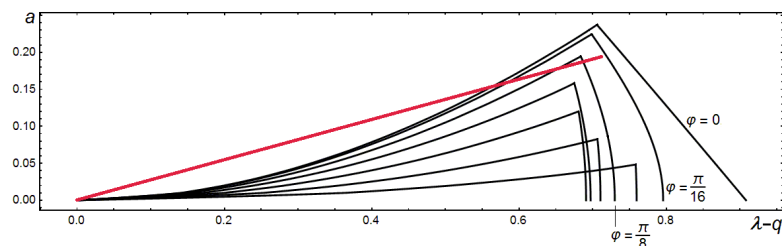


Fig. 3. Example of a comparative estimate for selecting the angle φ : the sections given
in Fig. 2 are projected on a single plane, the step with respect to φ is doubled
(φ varies from 0 to $3\pi/8$ with a step of $\pi/16$)



Visualization of the three-dimensional stability regions by a discrete set of two-dimensional projections corresponding to different angles φ is shown in Fig. 2. An operating line is located on one of the sections. Fig. 3 shows the region boundaries of all projections in a single diagram so that it is convenient to assess whether it is reasonable to select a particular angle φ . While the location proposed for the loading line is hardly optimal (we did not carry out strict optimization with respect to the parameter φ), it may serve to increase the resolution of the device by narrowing the projection of the region.

Conclusion

To summarize, the study is the first ever attempt to construct three-dimensional stability regions for a system equations of transverse ion motion in the electric field of a quadrupole with AC supply in a static magnetic field directed along the quadrupole axis. The data given have been obtained based on Floquet's theory.

The results are presented as a set of sections in the coordinates (a, q, λ) , that is, planes passing through the axis a ; the given coordinates are essentially parameters of the Mathieu equation, supplemented by the reduced strength of the magnetic field.

This allows to apply the technique for determining the range of ion masses transmitted by the filter, which is traditionally used in the two-dimensional statement, to this (three-dimensional) case.

The authors have no financial or non-financial interests to disclose.

REFERENCES

1. Paul W., Steinwedel H., Ein neues Massenspektrometer ohne Magnetfeld, Z. Naturforschung. 8a (7) (1953) 448–450.
2. Pavlenko Yu. G., Toropova A. I., A new mass-spectrometer: A quadrupole in a magnetic field, J. Commun. Technol. Electronics. 41 (5) (1996) 471–475.
3. Sarfarazi S., Sohani M., Magnetic field effect on the stability regions of a linear quadrupole, Rapid Commun. Mass Spectrom. 34 (12) (2020) e8784 (1–6).
4. Syed S. U., Sreekumar J., Brkic B., et al., Effect of an axial magnetic field on the performance of a quadrupole mass spectrometer, J. Am. Soc. Mass. Spectrom. 21 (8) (2010) 2070–2076.
5. Maher S., Syed S. U., Hughes D. M., et al., Mapping the stability diagram of a quadrupole mass spectrometer with a static transverse. Magnetic field applied, J. Am. Soc. Mass Spectrom. 24 (8) (2013) 1307–1314.
6. Syed S. U. A. H., Maher S., Taylor S., Quadrupole mass filter operation under the influence of magnetic field, J. Mass Spectrom. 48 (12) (2013) 1325–1339.
7. Kamke E., Differentialgleichungen Lösungsmethoden und Lösungen, Band 1. 10 ed. B. G. Teubner, Springer, Leipzig, 1977.
8. Demidovich B. P., Lektsii po matematicheskoy teorii ustoychivosti [Lectures on the mathematical stability theory], Nauka, Moscow, 1967 (in Russian).
9. Slobodenyuk G. I., Kvadrupolnyye mass-spektrometry [Quadrupole mass spectrometers], Atomizdat, Moscow, 1974 (in Russian).
10. Dawson P. H. (editor), Quadrupole mass spectrometry and its application, AIP Press, New York, USA, 1995.
11. March R. E., Todd J. F. J., Quadrupole ion trap mass spectrometry, 2nd ed. J. Wiley & Sons, Inc. Hoboken, New Jersey, USA, 2005.
12. Major F. G., Gheorghe V. N., Werth G., Charged particle traps, Springer-Verlag, Berlin, Heidelberg, 2005.
13. Strett M. D. O., Funktsii Lyame, Matye i rodstvennyye im v fizike i tekhnike [Lamé and Mathieu functions and related ones in physics and technology], Sci. & Techn. Publish. House of Ukraine, Kharkov, Kiev, 1935 (in Russian).
14. Pipes L. A., Matrix solution of equations of the Mathieu – Hill type, J. Appl. Phys. 24 (7) (1953) 902–910.
15. Floquet G. Sur les équations différentielles linéaires a coefficients périodiques, Ann. Sci. Éc. Norm. Supér. 2e Serie, 12 (1883) 47–88.

16. Golikov Yu. K., Krasnova N. K., Solovyev K. V., et al., Stability zones of quadrupole mass spectrometer in longitudinal magnetic field, Appl. Phys. (Prikladnaya fizika). (3) (2006) 78–81 (in Russian).

17. Berdnikov A., Kapralov V., Solovyev K., Krasnova N. Algorithm for constructing a multidimensional stability domain of a charged particle in an ion-optical system with periodic supply voltage. In: Proc. of 2021 IEEE Int. Conf. on Electrical Engineering and Photonics (EExPolytech-2021), October 14–15, 2021. St. Petersburg, Russia. (2021) 51–54.

СПИСОК ЛИТЕРАТУРЫ

1. Paul W., Steinwedel H. Ein neues Massenspektrometer ohne Magnetfeld // Zeitschrift für Naturforschung. 1953. Vol. 8a. No. 7. Pp. 448–450.

2. Павленко Ю. Г., Торопова А. И. Новый масс-спектрометр – квадруполь в магнитном поле // Радиотехника и электроника. 1996. Т. 41. № 4. С. 508–512.

3. Sarfarazi S., Sohani M. Magnetic field effect on the stability regions of a linear quadrupole // Rapid Communications in Mass Spectrometry. 2020. Vol. 34. No. 12. P. e8784 (1–6).

4. Syed S. U., Sreekumar J., Brkic B., Gibson J. R., Taylor S. Effect of an axial magnetic field on the performance of a quadrupole mass spectrometer // Journal of the American Society for Mass Spectrometry. 2010. Vol. 21. No. 8. Pp. 2070–2076.

5. Maher S., Syed S. U., Hughes D. M., Gibson J. R., Taylor S. Mapping the stability diagram of a quadrupole mass spectrometer with a static transverse. Magnetic field applied // Journal of the American Society for Mass Spectrometry. 2013. Vol. 24. No. 8. Pp. 1307–1314.

6. Syed S. U. A. H., Maher S., Taylor S. Quadrupole mass filter operation under the influence of magnetic field // Journal of Mass Spectrometry. 2013. Vol. 48. No. 12. Pp. 1325–1339.

7. Камке Э. Справочник по обыкновенным дифференциальным уравнениям. М.: Наука, 1976. 576 с.

8. Демидович Б. П. Лекции по математической теории устойчивости. М.: Наука, 1967. 471 с.

9. Слободенюк Г. И. Квадрупольные масс-спектрометры. М.: Атомиздат, 1974. 272 с.

10. Dawson P. H. (editor). Quadrupole mass spectrometry and its application. New York: AIP Press, 1995. 349 p.

11. March R. E., Todd J. F. J. Quadrupole ion trap mass spectrometry. 2nd ed. New Jersey, USA: J. Wiley & Sons, Inc. Hoboken, 2005. 346 p.

12. Major F. G., Gheorghe V. N., Werth G., Charged particle traps. Berlin, Heidelberg: Springer – Verlag, 2005. 354 p.

13. Стретт М. Д. О. Функции Ляме, Матье и родственные им в физике и технике. С приложением таблиц функций Матье, составленных Айнсом. Пер. с нем. Харьков-Киев: Научно-техническое издательство Украины, 1935. 237 с.

14. Pipes L. A. Matrix solution of equations of the Mathieu – Hill type // Journal of Applied Physics. 1953. Vol. 24. No. 7. Pp. 902–910.

15. Floquet G. Sur les équations différentielles linéaires à coefficients périodiques // Annales Scientifiques de l'École Normale Supérieure. 2e Serie, 1883. Tome 12. Pp. 47–88.

16. Голиков Ю. К., Краснова Н. К., Соловьев К. В., Елохин В. А., Николаев В. И. Зоны устойчивости квадрупольного масс-спектрометра в продольном магнитном поле // Прикладная физика. 2006. № 3. С. 78–81.

17. Berdnikov A., Kapralov V., Solovyev K., Krasnova N. Algorithm for constructing a multidimensional stability domain of a charged particle in an ion-optical system with periodic supply voltage // Proceedings of 2021 IEEE International Conference on Electrical Engineering and Photonics (EExPolytech-2021), October 14–15, 2021. St. Petersburg, Russia. Pp. 51–54.

THE AUTHORS

BERDNIKOV Alexander S.

Institute for Analytical Instrumentation of the Russian Academy of Sciences

26, Rizhsky Ave., St. Petersburg, 190103, Russia

asberd@yandex.ru

ORCID: 0000-0003-0985-5964

**KRASNOVA Nadezhda K.**

Peter the Great St. Petersburg Polytechnic University
29 Politechnicheskaya St., St. Petersburg, 195251, Russia
n.k.krasnova@mail.ru
ORCID: 0000-0002-6162-9481

MASYUKEVICH Sergey V.

Institute for Analytical Instrumentation of the Russian Academy of Sciences
26, Rizhsky Ave., St. Petersburg, 190103, Russia
serg_08@mail.ru
ORCID: 0000-0002-0873-8849

SOLOVYEV Konstantin V.

Peter the Great St. Petersburg Polytechnic University
29 Politechnicheskaya St., St. Petersburg, 195251, Russia
k-solovyev@mail.ru
ORCID: 0000-0003-3514-8577

СВЕДЕНИЯ ОБ АВТОРАХ

БЕРДНИКОВ Александр Сергеевич — доктор физико-математических наук, ведущий научный сотрудник ФГБУН «Институт аналитического приборостроения Российской академии наук». 190103, Россия, Санкт-Петербург, Рижский пр., 26
asberd@yandex.ru
ORCID: 0000-0003-0985-5964

КРАСНОВА Надежда Константиновна — доктор физико-математических наук, профессор Высшей инженерно-физической школы Санкт-Петербургского политехнического университета Петра Великого. 195251, Россия, г. Санкт-Петербург, Политехническая ул., 29
n.k.krasnova@mail.ru
ORCID: 0000-0002-6162-9481

МАСЮКЕВИЧ Сергей Владимирович — старший научный сотрудник, ФГБУН «Институт аналитического приборостроения Российской академии наук». 190103, Россия, Санкт-Петербург, Рижский пр., 26
serg_08@mail.ru
ORCID: 0000-0002-0873-8849

СОЛОВЬЕВ Константин Вячеславович — кандидат физико-математических наук, доцент Высшей инженерно-физической школы Санкт-Петербургского политехнического университета Петра Великого. 195251, Россия, г. Санкт-Петербург, Политехническая ул., 29
k-solovyev@mail.ru
ORCID: 0000-0003-3514-8577

Received 18.04.2022. Approved after reviewing 28.04.2022. Accepted 28.04.2022.

Статья поступила в редакцию 18.04.2022. Одобрена после рецензирования 28.04.2022. Принята 28.04.2022.

Original article

DOI: <https://doi.org/10.18721/JPM.15204>

FEATURES OF THE NANOSTRUCTURE FORMATION IN THE ND-PR-FE-B-SYSTEM ALLOYS: A STUDY BY AFM AND MFM

I. S. Tereshina ^{1, 5}, G. A. Politova ^{2, 4}✉, T. P. Kaminskaya ¹, V. V. Popov ¹,
D. V. Gunderov ³, A. V. Filimonov ⁴, I. A. Pelevin ⁵

¹ Lomonosov Moscow State University, Moscow, Russia;

² Baikov Institute of Metallurgy and Materials Science, RAS, Moscow, Russia;

³ Institute of Molecule and Crystal Physics – subdivision of the Ufa
Federal Research Centre of the RAS, Ufa, Russia;

⁴ Peter the Great St. Petersburg Polytechnic University, St. Petersburg, Russia;

⁵ National University of Science and Technology «MISIS» (MISIS), Moscow, Russia

✉ gpolitova@gmail.com

Abstract. In this work, polycrystalline samples of hard-magnetic materials of $(\text{Nd}_{1-x}\text{Pr}_x)_2\text{Fe}_{14}\text{B}$ general formula have been prepared and subjected to severe plastic deformation (SPD). Thereafter the features of nanostructure formation in the compounds were investigated before and after SPD using atomic force microscopy and magnetic force one (AFM & MFM). The differences in texture formation were revealed when studying the surface microstructure of both the initial and deformed samples. The initial ones prepared by the Czochralski method, exhibited the columnar structure, while the SPD samples exhibited the concentric rings containing elongated nanosized crystallites. The magnetic domain structure was visualized using the MFM that clearly demonstrated the relationship between the microstructural features and the magnetic domains' configuration.

Keywords: atomic force microscopy, magnetic force microscopy, hard-magnetic material, nanostructure

Funding: The research was supported by the Ministry of Science and Higher Education of the Russian Federation, projects No. 075-00715-22-00 and No. 0784-2020-0025. The research of I. A. Pelevin and I. S. Tereshina was funded by the Russian Science Foundation (Agreement No. 21-79-10239)

Citation: Tereshina I. S., Politova G. A., Kaminskaya T. P., Popov V. V., Gunderov D. V., Filimonov A. V., Pelevin I. A., Features of the nanostructure formation in the Nd-Pr-Fe-B-system alloys: a study by AFM and MFM, St. Petersburg Polytechnical State University Journal. Physics and Mathematics. 15 (2) (2022) 35–45. DOI: <https://doi.org/10.18721/JPM.15204>

This is an open access article under the CC BY-NC 4.0 license (<https://creativecommons.org/licenses/by-nc/4.0/>)



Научная статья

УДК 620.186: 539.378:537.622

DOI: <https://doi.org/10.18721/JPM.15203>

ОСОБЕННОСТИ ФОРМИРОВАНИЯ НАНОСТРУКТУРЫ В СПЛАВАХ СИСТЕМЫ Nd-Pr-Fe-B, ИССЛЕДОВАННЫЕ МЕТОДАМИ АТОМНО-СИЛОВОЙ И МАГНИТНО-СИЛОВОЙ МИКРОСКОПИИ

И. С. Терёшина^{1, 5}, Г. А. Политова^{2, 4}✉, Т. П. Каминская¹, В. В. Попов¹,
Д. В. Гундеров³, А. В. Филимонов⁴, И. А. Пелевин⁵

¹ Московский государственный университет им.
М. В. Ломоносова, г. Москва, Россия;

² Институт металлургии и материаловедения им. А. А. Байкова РАН, г. Москва, Россия;

³ Институт физики молекул и кристаллов Уфимского научного центра РАН, г. Уфа, Россия;

⁴ Санкт-Петербургский политехнический университет Петра Великого, г. Санкт-Петербург, Россия;

⁵ Национальный исследовательский технологический университет

«Московский институт стали и сплавов (МИСиС)», г. Москва, Россия

✉ gpolitova@gmail.com

Аннотация. В работе получены и исследованы на микро- и наноуровне поликристаллические образцы магнитотвердых материалов общей формулы $(Nd_{1-x}Pr_x)_2Fe_{14}B$, подвергнутые процедуре интенсивной пластической деформации (ИПД). Для контроля особенностей формирования наноструктуры соединений до и после ИПД использовались методы атомно-силовой и магнитно-силовой микроскопии (АСМ и МСМ). При изучении поверхностей как исходных, так и деформированных образцов были выявлены различия в текстурообразовании. Для исходных образцов, полученных с помощью метода Чохральского, оказалась характерной столбчатая структура, тогда как после процедуры ИПД структура состояла из концентрических колец, которые содержали вытянутые наноразмерные кристаллиты. Структура магнитных доменов была визуализирована с помощью метода МСМ, который четко продемонстрировал связь между особенностями микроструктуры и конфигурацией магнитных доменов.

Ключевые слова: атомно-силовая и магнитно-силовая микроскопия, магнитотвердый материал, наноструктура, доменная структура

Финансирование: работа выполнена при финансовой поддержке Министерства науки и высшего образования Российской Федерации, проекты № 00-22-00715-075 и № -0784 0025-2020. И. А. Пелевин и И. С. Терёшина выполняли исследования при поддержке гранта Российского научного фонда № 10239-79-21.

Для цитирования: Терёшина И. С., Политова Г. А., Каминская Т. П., Попов В. В., Гундеров Д. В., Филимонов А. В., Пелевин И. А. Особенности формирования наноструктуры в сплавах системы Nd-Pr-Fe-B, исследованные методами атомно-силовой и магнитно-силовой микроскопии // Научно-технические ведомости СПбГПУ. Физико-математические науки. 2022. Т. 15. № 2. С. 35–45. DOI: <https://doi.org/10.18721/JPM.15204>

Статья открытого доступа, распространяемая по лицензии CC BY-NC 4.0 (<https://creativecommons.org/licenses/by-nc/4.0/>)

Introduction

Developing new high-tech devices including computers, motors and generators, magnetic resonance imaging, etc. [1–3] generates great demand for high-energy hard magnetic materials capable of operating stably at various temperatures. Special attention is focused on $(\text{Nd,Pr})_2\text{Fe}_{14}\text{B}$ materials [1–3]. It is known that permanent magnets based on $\text{Nd}_2\text{Fe}_{14}\text{B}$ compound show the best properties in the narrow temperature range of 150–400 K [4, 5]. The highest experimentally obtained energy product is 475 kJ/m³ (59.6 MGsOe) [9], which is close to the predicted theoretical limit $(BH)_{\text{max}}$ for the $\text{Nd}_2\text{Fe}_{14}\text{B}$ compound. Moreover, at $T = 135$ K, the magnetic anisotropy type of $\text{Nd}_2\text{Fe}_{14}\text{B}$ compound changes from “easy axis” to “cone of easy magnetization axes”, in other words, a spontaneous spin-reorientation transition (SRT) occurs with decreasing temperature [6, 7]. The observed SRT leads to remanence and energy product decreasing, which limits the applicability of the material based on the $\text{Nd}_2\text{Fe}_{14}\text{B}$ compound at low temperatures. Partial substitution of Nd by Pr allows decreasing of SRT temperature expanding working temperature range of the magnets based on $(\text{Nd,Pr})_2\text{Fe}_{14}\text{B}$ compounds. It should be noted that the level of properties of magnets strongly depends on microstructure peculiarities. For example, it is known that magnetic properties can be increased by nanostructure formation [8,9]. Alloys with nanocrystalline structure could be obtained by various methods, both conventional (powder metallurgy [10,11] strip casting [12, 13], severe plastic deformation [14–18], etc., and their combination [9, 14, 19–21]). There are also new modern additive methods for the production of highly efficient magnetic materials, including magnetic materials [22–24]. Regardless of the chosen method, the mechanisms of magnetic properties formation and their dependence on structural features are mostly the same. Thus, the methods of structural analysis of nanostructured materials can be applied to samples obtained by any of the above methods, including modern advanced methods, such as selective laser melting (SLM) of Nd-Fe-B materials [25–27]. The SLM process is characterized by high cooling rates (10⁶ K/s [28]) and rapid solidification, which can lead to the formation of nanostructures.

It should be noted that the development of the modern high-energy permanent magnets based on $R\text{-Fe-B}$ ($R = \text{Nd, Pr}$) is possible in case of proper distribution of rare-earth reach phase along with optimal microstructure and texture formation. The presence of random oriented or elongated grains within the microstructure, as a rule, decreases final magnetic characteristics. That is why deep analysis and understanding of microstructure formation is needed to reach new results in the Nd-Fe-B system qualitatively.

The present work aims to investigate $(\text{Nd,Pr})_2\text{Fe}_{14}\text{B}$ nanostructure formation peculiarities during severe plastic deformation (SPD) using atomic and magnetic force microscopy. The work is carried out as a continuation of early studies [18, 29], which develop methods and approaches to the analysis of nanostructured magnetic materials. These approaches are planned to be applied in further studies for Nd-Pr-Fe-B samples obtained, for example, by selective laser melting.

Experimental details

$(\text{Nd}_{1-x}\text{Pr}_x)_2\text{Fe}_{14}\text{B}$ ($x = 0.5$ and 0.75) alloys were synthesized by a modified Czochralski method in a tri-arc furnace under an inert atmosphere [30]. As a result, polycrystalline samples with a directed crystal structure, as well as small single crystals, were obtained. It is polycrystals that we used in this work for further research. The SPD process was performed using Bridgman anvils under 6 GPa pressure and anvils' rotation (3 full turns). SMENA-A scanning probe microscope on the Solver platform (by NT-MDT, Russia) was used for atomic and magnetic force microscopy (AFM and MFM, respectively) investigations. Samples were investigated in the semi-contact method at room temperature using HA_NC ETALON standard silicon cantilevers with resonance frequencies from 110 to 235 kHz and 10 nm radius of curvature of the tip of the needle. MFM was performed using MFM 01 cantilevers with Co coating with 50–85 kHz frequencies. Elemental analysis was performed using scanning electron microscopy (SEM) TESCAN Vega 3 (Tescan Analytics, Fuveau, France).



Results

Previous investigation [30] showed that $(\text{Nd}_{1-x}\text{Pr}_x)_2\text{Fe}_{14}\text{B}$ solidifies with tetragonal crystal structure ($P4_2/mnm$ space group) with $\text{Nd}_2\text{Fe}_{14}\text{B}$ type. The main phase in samples varied from 86 to 98 %. The high content of α -Fe (up to 13 %) was found in alloy with $x = 0.75$. Content of iron within grains was around 70.41 wt.% which corresponds to the $\text{Nd}_2\text{Fe}_{14}\text{B}$ phase, while iron content at grain boundaries was far lower (30–130 times less). Elements such as Cu and Ni were present mainly at the grain boundaries and were considered by us as impurities in the boundary region, while oxygen was present mainly in the inclusions. Thus, a small amount of oxygen found in inclusions rich in iron indicates the presence of oxides in the alloy structure.

Fig. 1 shows surface structures of $(\text{Nd}_{1-x}\text{Pr}_x)_2\text{Fe}_{14}\text{B}$ with $x = 0.5$ before and after the SPD procedure. These samples contain a minimum amount of the second phase thus are the most interesting for research. The columnar structure may be seen in Fig. 1,a associated with the samples' synthesis method. This method is usually used to grow large single crystals; however, in this work, as noted above, the single crystal structure was not predominant. However, the directional heat dissipation inherent in this method has led to the formation of some uniaxial texture, which may appear as a columnar structure. The columns had a width of about $0.8\text{ }\mu\text{m}$ and were primarily perpendicular to the investigated surface. The surface structure of the initial sample consisted of slightly elongated subgrains (with an aspect ratio of about 1.5) with the size of 100 - 200 nm order. It is the high temperature gradient (and hence the high rates of cooling and crystallization) that can explain the formation of such small structural elements on the surface of the initial sample during synthesis. It should also be noted that the observed inclusions, which consist mainly of iron atoms, should crystallize first due to the higher melting point. Thus, iron inclusions act as nucleation centers for main phase grains.

The surface microstructure of $\text{Nd}_1\text{Pr}_1\text{Fe}_{14}\text{B}$ after the SPD procedure differs significantly (see Fig. 1,b). Crystallite agglomerations with a „swirling vortex“ shape are seen wherein the columnar structure still exists. It is better observed in Fig. 1,c, which shows another surface area of the same sample.

Similar microstructure peculiarities in $(\text{Nd},\text{Pr})_2\text{Fe}_{14}\text{B}$ -type alloys after strip casting were mentioned in [31]. To better visualize the vortex structure in direction perpendicular to the surface and detect its shape and typical sizes and typical sizes of the main structural elements, the samples were polished and etched using a 5% solution of nitric acid in ethyl alcohol. Images of such polished and etched surfaces are shown in Fig. 2. It can be seen that the swirling vortex consists of concentric rings set with a 150–300 nm thick (in one layer of crystallites) closely adjacent to each other. One can see crystallites of various sizes and shapes, oriented mainly along the vortex circumferences.

Possible reasons for such a swirling vortex structure are different deformation speeds and uneven heating of sample parts during the SPD procedure. Observed microstructure peculiarities may also be considered as a rounded induced texture because of deformation.

MFM method was applied to visualize magnetic domain structure on the samples' surface. Fig. 3 shows the MFM image of the $\text{Nd}_1\text{Pr}_1\text{Fe}_{14}\text{B}$ sample surface before and after the SPD procedure to show the difference arising from the deformation. A double domain structure was observed: striped domains with 5–10 μm width on the surface of the sample before SPD (Fig. 3,a) and with 5–7 μm width in case of the sample after SPD (Fig. 3,b); superimposed on these stripes a classical homogeneous branched domain structure on the alloy surface before SPD with a domain width of 1–3 μm (Fig. 3,c) and a more complex homogeneous structure on the alloy surface after SPD (Fig. 3,d) with a domain width of 1–2 μm are seen.

The observed complex domain structure of the sample after SPD (Fig 3,b and d) could arise because of a much more inhomogeneous microstructure and the possible presence of some amount of amorphous phase. Amorphous phase existence after SPD procedure was shown in [9,14] severe plastic deformation (SPD, and its volume content may exceed 50%, making it the dominant phase in the structure. The observed “dimple” domain structure means that the basal plane of most crystallites coincides with the surface of the sample before the SPD procedure confirms the texture. The initial sample shows mostly equiaxed domains (dark areas in Fig. 3,a), and the evenly dark fill of rounded domains means the single domain state of the corresponding crystallites.

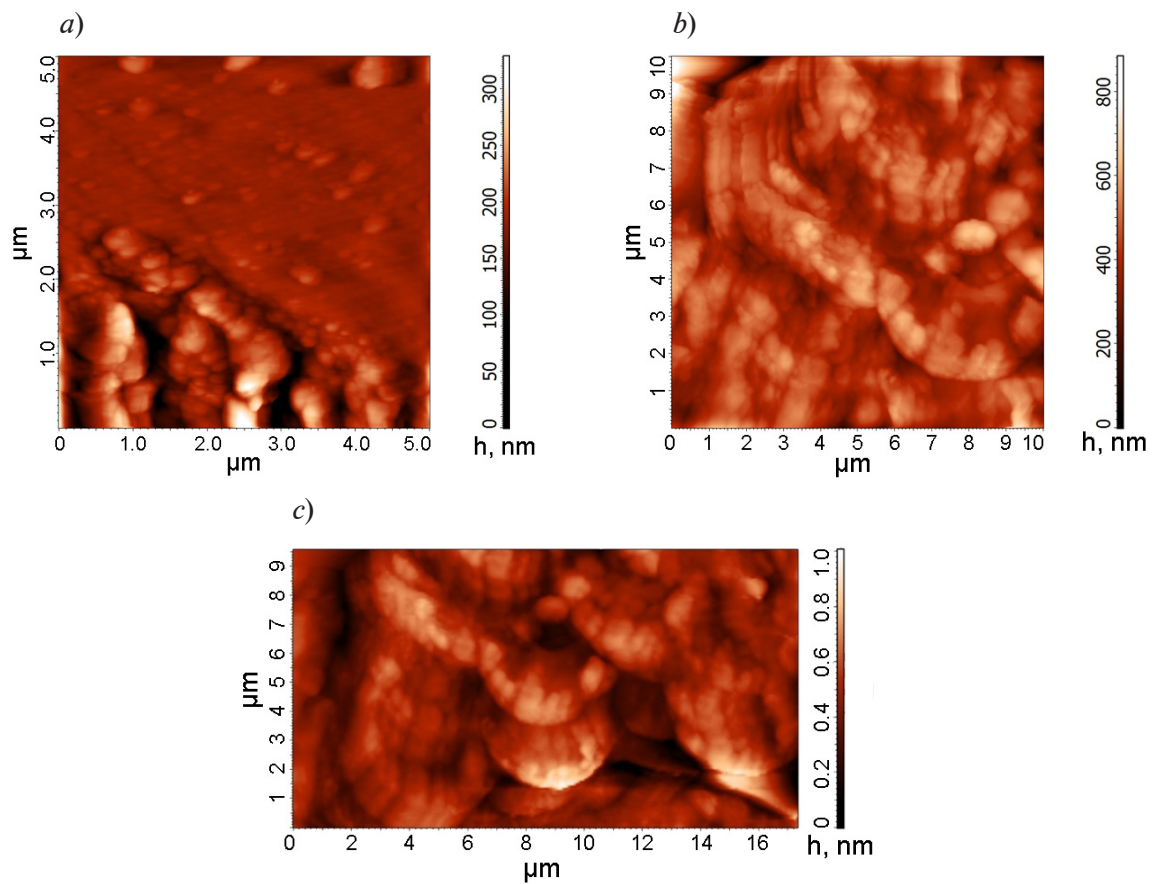


Fig. 1. AFM image for surface microstructure of $\text{Nd}_1\text{Pr}_1\text{Fe}_{14}\text{B}$ before (a) and after (b, c) severe plastic deformation; c shows another fragment of the sample surface (b) where swirling vortex structures are the most pronounced

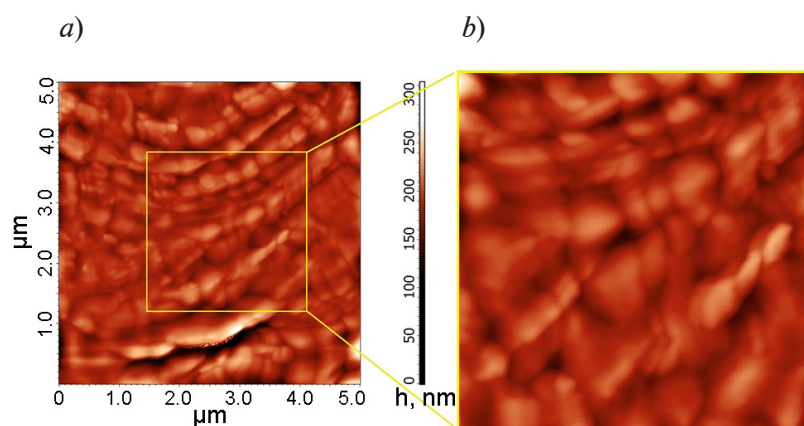


Fig. 2. AFM image for surface microstructure of $\text{Nd}_1\text{Pr}_1\text{Fe}_{14}\text{B}$ after SPD (see Fig. 1, c), surface polishing and acid etching (a); enlarged fragment (b)



Analysis of MFM images of samples after the SPD procedure does not give the same unambiguously interpretable domain structure as in the case of initial samples, which makes it difficult to describe the shape of crystallites, to identify foreign phases, inclusions, etc. However, it is quite obvious that the SPD procedure violates the texture of the initial samples and, most importantly, disorients the structural elements.

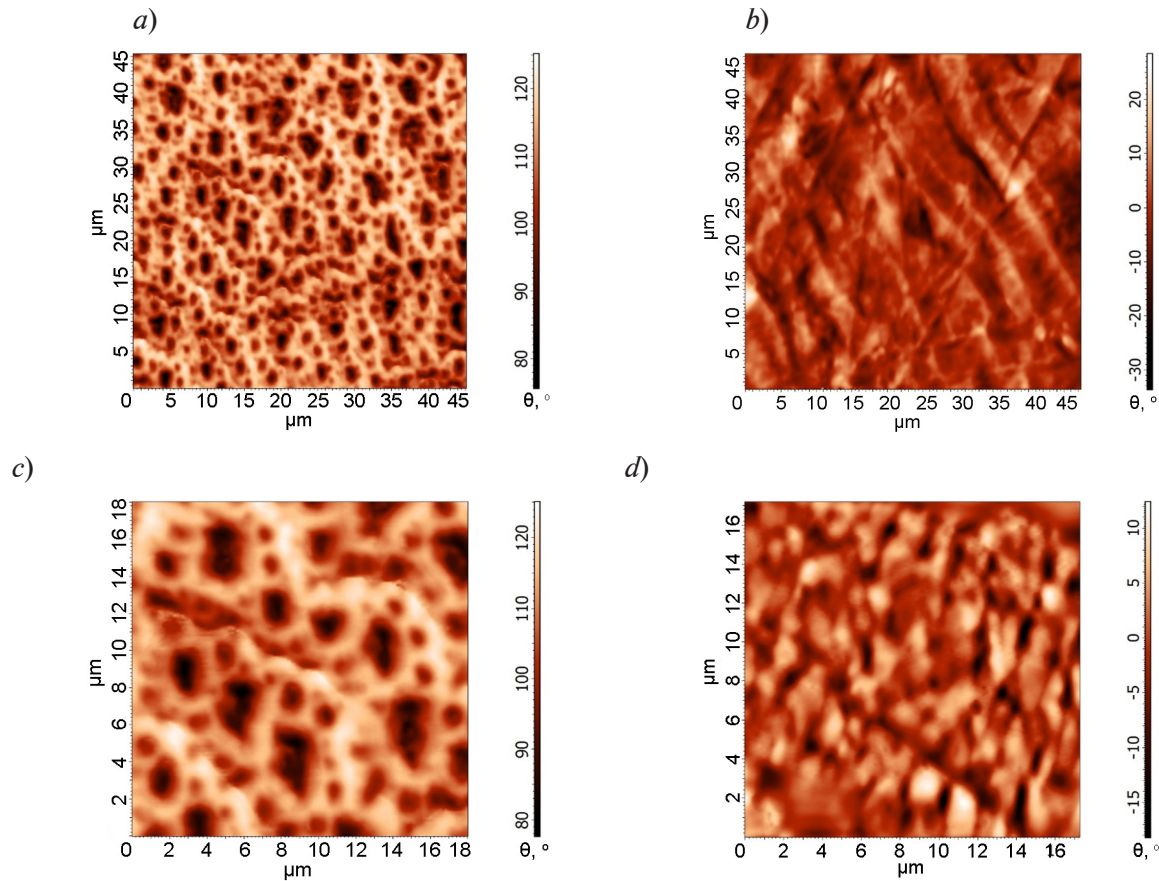


Fig. 3. MFM images for double domain structure of $\text{Nd}_1\text{Pr}_1\text{Fe}_{14}\text{B}$ sample surface before (a, c) and after SPD (b, d); the figure shows striped domains (a, b), classical branched domain structure (c) and more complex homogeneous structure (d)

Conclusions

Samples of the $(\text{Nd,Pr})_2\text{Fe}_{14}\text{B}$ type were synthesized to study the formation of their surface morphology in the initial state and after severe plastic deformation. The main phase of the initial samples was a tetragonal phase of the $\text{Nd}_2\text{Fe}_{14}\text{B}$ type with a certain amount of $\alpha\text{-Fe}$, which is typical for the materials under study. The lowest content of $\alpha\text{-Fe}$ (up to 2%) was found in the $\text{Nd}_1\text{Pr}_1\text{Fe}_{14}\text{B}$ alloy, while in the $\text{Nd}_{0.5}\text{Pr}_{1.75}\text{Fe}_{14}\text{B}$ alloy the amount of the second phase reached 13%. The columnar structure (consisting, in turn, of rounded grains about 100–200 nm in size) was characteristic of the original $\text{Nd}_1\text{Pr}_1\text{Fe}_{14}\text{B}$ sample. On the contrary, for the samples after the SPD procedure, agglomerations in the form of a “swirling vortex” (sets of concentric rings 150–300 nm thick, consisting of elongated nanosized crystallites) were found.

Conducting the MFM study and domain structure visualization, on the one hand, confirmed the AFM analysis of the microstructure; on the other hand, they demonstrated the main features of the emerging structure of magnetic domains. While the original sample has a classical “dimple” domain structure with single-domain crystallites, the sample after the SPD procedure has a complex “smeared” domain structure, which can be explained both by the features of the microstructure and the appearance of an amorphous phase after severe plastic deformation.

The study demonstrates the convenience and informativeness of using the AFM and MFM methods in studying the surface of nanocrystalline hard magnetic materials, in particular, the $(\text{Nd,Pr})_2\text{Fe}_{14}\text{B}$ materials considered in this work, and also makes it possible to reveal the main features of the formation of their structure before and after severe plastic deformation. AFM and MFM studies of the surface morphology of alloys make it possible to obtain information about the sizes of all the main structural elements and their shape at the nanolevel, about the domain structure, and make it possible to reveal differences in texture formation depending on the methods of obtaining alloys and their further processing, which is extremely important for the production of highly efficient magnetically hard materials and products from them for various functional purposes.

REFERENCES

1. Hara T., Tanaka T., Kitamura H., et al., Cryogenic permanent magnet undulators, *Phys. Rev. ST. Accel. Beams*. 7 (5) (2004) 050702.
2. Huang J. C., Kitamura H., Yang C. K., et al., Challenges of in-vacuum and cryogenic permanent magnet undulator technologies, *Phys. Rev. ST. Accel. Beams*. 20 (6) (2017) 064801.
3. Neznakhin D. S., Politova G. A., Ivanov L. A., et al., Low-temperature magnetic hysteresis in $\text{Nd}(\text{Pr})\text{-Fe-B}$ nanostructured alloys with $\text{Nd}_2\text{Fe}_{14}\text{B}$ type main phase composition, *Defect Diffus. Forum*. 386 (2018) 125–130.
4. Herbst J. F., $\text{R}_2\text{Fe}_{14}\text{B}$ materials: Intrinsic properties and technological aspects, *Rev. Mod. Phys.* 63 (4) (1991) 819–898.
5. Benabderrahmane C., Berteaud P., Valliau M., et al., $\text{Nd}_2\text{Fe}_{14}\text{B}$ and $\text{Pr}_2\text{Fe}_{14}\text{B}$ magnets characterisation and modelling for cryogenic permanent magnet undulator applications, *Nucl. Instruments Methods Phys. Res. A*. 669 (21 March) (2012) 1–6.
6. Kim Y. B., Kim M. J., Han-Mina J., Kim T. K., Spin reorientation and magnetocrystalline anisotropy of $(\text{Nd}_{1-x}\text{Pr}_x)_2\text{Fe}_{14}\text{B}$, *J. Magn. Magn. Mater.* 191 (1–2) (1999) 133–136.
7. Politova G. A., Tereshina I. S., Gorbunov D. I., et al., Magnetic and magnetocaloric properties of single crystal $(\text{Nd}_{0.5}\text{Pr}_{0.5})_2\text{Fe}_{14}\text{B}$, *J. Alloys Compd.* 751 (30 June) (2018) 283–288.
8. Lewis L. H., Panchanathan V., Wang J. Y., Technical magnetic properties of melt-spun $(\text{Nd}_{1-x}\text{Pr}_x)_2\text{Fe}_{14}\text{B}$ at low temperature, *J. Magn. Magn. Mater.* 176 (2–3) (1997) 288–296.
9. Tereshina I. S., Pelevin I. A., Tereshina E. A., et al., Magnetic hysteresis properties of nanocrystalline $(\text{Nd,Ho})\text{-(Fe,Co)-B}$ alloy after melt spinning, severe plastic deformation and subsequent heat treatment, *J. Alloys Compd.* 681 (5 October) (2016) 555–560.
10. Gutfleisch O., Harris I. R., Fundamental and practical aspects of the hydrogenation, disproportionate, desorption and recombination process, *J. Phys. D*. 29 (9) (1996) 2255–2265.
11. Gutfleisch O., Willard M. A., Brück E., et al., Magnetic materials and devices for the 21st century: Stronger, lighter, and more energy efficient, *Adv. Mater.* 23 (7) (2011) 821–842.
12. Croat J. J., Manufacture of NdFeB permanent magnets by rapid solidification, *J. Less-Common Met.* 148 (1–2) (1989) 7–15.
13. Gabay A. M., Popov A. G., Gaviko V. S., et al., The structure and magnetic properties of rapidly quenched and annealed multi-phase nanocrystalline $\text{Nd}_5\text{Fe}_{91-x}\text{B}_x$ ribbons, *J. Alloys Compd.* 245 (1–2) (1996) 119–124.
14. Straumal B. B., Kilmametov A. R., Mazilkin A. A., et al., Amorphization of Nd-Fe-B alloy under the action of high-pressure torsion, *Mater. Lett.* 145 (15 April) (2015) 63–66.
15. Li H., Li W., Zhang Y., et al., Phase evolution, microstructure and magnetic properties of bulk $\alpha\text{-Fe/Nd}_2\text{Fe}_{14}\text{B}$ nanocomposite magnets prepared by severe plastic deformation and thermal annealing, *J. Alloys Compd.* 651 (15 December) (2015) 434–439.
16. Hosokawa A., Takagi K., Kuriwa T., et al., Severe plastic deformation of Nd-Fe-B nanocomposite magnets at room temperature, *J. Magn. Magn. Mater.* 473 (1 March) (2019) Pp. 51–60.
17. Tereshina-Chitrova E. A., Korneeva Y. V., Ozherelkov D. Y., et al., Enhanced magnetocaloric effect in distilled terbium and emergence of novel properties after severe plastic deformation, *Scr. Mater.* 187 (October) (2020) 340–344.
18. Pelevin I. A., Ozherelkov D. Y., Kaminskaya T. P., Tereshina I. S., Surface morphology investigations of nanocrystalline $\text{R}_2\text{Fe}_{14}\text{B}$ ($\text{R} = \text{Y, Nd, Gd, Er}$) by atomic force microscopy, *Mater. Res. Proc.* 21 (2022) 81–87.



19. Yagodkin Y. D., Lileev A. S., Lyubina J. V., et al., Structure and magnetic properties of nanocrystalline alloys based on $\text{Nd}_2\text{Fe}_{14}\text{B}$ obtained by various techniques, *J. Magn. Magn. Mater. Journal of Magnetism and Magnetic Materials*. 258–259 (March) (2003) 586–589.
20. Dempsey N. M., Walther A., May F., et al., High performance hard magnetic NdFeB thick films for integration into micro-electro-mechanical systems, *Appl. Phys. Lett.* 90 (9) (2007) 092509.
21. Politova G. A., Tereshina I. S., Kaminskaya T. P., et al., Atomic-force microscopic study of the surface morphology of the $\text{Nd}_2\text{Fe}_{14}\text{B}$ alloys prepared by various techniques, *Russian Metallurgy (Metally)*. 2018 (9) (2018) 859–866.
22. Li L., Tirado A., Nlebedim I. C., et al., Big area additive manufacturing of high performance bonded NdFeB magnets, *Sci. Rep.* 6 (2016) 36212.
23. Paranthaman M. P., Shafer C. S., Elliott A. M., et al., Binder jetting: A novel NdFeB bonded magnet fabrication process, *J. Min. Met. Mater.* 68 (7) (2016) 1978–1982.
24. Li L., Post B., Kunc V., et al., Additive manufacturing of near-net-shape bonded magnets: Prospects and challenges, *Scr. Mater.* 135 (1 July) (2017) 100–104.
25. Bittner F., Thielsch J., Drossel W. G., Microstructure and magnetic properties of Nd-Fe-B permanent magnets produced by laser powder bed fusion, *Scr. Mater.* 201 (August) (2021) 113921.
26. Jaćimović J., Binda F., Herrmann L. G., et al., Net shape 3D printed NdFeB permanent magnet, *Adv. Eng. Mater.* 19 (8) (2017) 1700098.
27. Huber C., Sepehri-Amin H., Goertler M., et al., Coercivity enhancement of selective laser sintered NdFeB magnets by grain boundary infiltration, *Acta Mater.* 172 (15 June) (2019) 66–71.
28. Pelevin I. A., Nalivaiko A. Y., Ozherelkov D. Y., et al., Selective laser melting of Al-based matrix composites with Al_2O_3 reinforcement: Features and advantages, *Materials*. 2021. Vol. 14 (10) (2021) 2648.
29. Andreeva N. V., Filimonov A. V., Rudskoi A. I., et al., A study of nanostructure magnetosolid Nd-Ho-Fe-Co-B materials via atomic force microscopy and magnetic force microscopy, *Phys. Solid State*. 58 (9) (2016) 1862–1869.
30. Politova G. A., Tereshina I. S., Kaminskaya T. P., et al., Substituted $(\text{Nd,Pr})_2\text{Fe}_{14}\text{B}$ alloys: Structural features and magnetic properties, *J. Phys. Conf. Ser.* 1236 (2019) 012016.
31. Kolchugina N. B., Lukin A. A., Kaminskaya T. P., et al. Morphological peculiarities of R-Fe-B (R = Nd, Pr) alloys formed upon solidification by strip-casting, *Phys. Met. Metallogr.* 121 (8) (2020) 772–782.

СПИСОК ЛИТЕРАТУРЫ

1. Hara T., Tanaka T., Kitamura H., Bizen T., Maréchal X., Seike T., Kohda T., Matsuura Y. Cryogenic permanent magnet undulators // *Physical Review. ST. Accelerators and Beams*. 2004. Vol. 7. No. 5. P. 050702.
2. Huang J. C., Kitamura H., Yang C. K., Chang C. H., Chang C. H., Hwang C. S. Challenges of in-vacuum and cryogenic permanent magnet undulator technologies // *Physical Review. ST. Accelerators and Beams*. 2017. Vol. 20. No. 6. P. 064801.
3. Neznakhin D. S., Politova G. A., Ivanov L. A., Volegov A. S., Gorbunov D. I., Tereshina I. S., Kudrevatykh N. V. Low-temperature magnetic hysteresis in Nd(Pr)-Fe-B nanostructured alloys with $\text{Nd}_2\text{Fe}_{14}\text{B}$ type main phase composition // *Defect and Diffusion Forum*. 2018. Vol. 386. Pp. 125–130.
4. Herbst J. F. $\text{R}_2\text{Fe}_{14}\text{B}$ materials: Intrinsic properties and technological aspects // *Review of the Modern Physics*. 1991. Vol. 63. No. 4. Pp. 819–898.
5. Benabderrahmane C., Berteaud P., Valli  au M., Kitegi C., Tavakoli K., B  chu N., Mary A., Filhol J. M., Couprie M. E. $\text{Nd}_2\text{Fe}_{14}\text{B}$ and $\text{Pr}_2\text{Fe}_{14}\text{B}$ magnets characterisation and modelling for cryogenic permanent magnet undulator applications // *Nuclear Instruments & Methods in Physics Research A*. 2012. Vol. 669. 21 March. Pp. 1–6.
6. Kim Y. B., Kim M. J., Han-Mina J., Kim T. K. Spin reorientation and magnetocrystalline anisotropy of $(\text{Nd}_{1-x}\text{Pr}_x)_2\text{Fe}_{14}\text{B}$ // *Journal of Magnetism and Magnetic Materials*. 1999. Vol. 191. No. 1–2. Pp. 133–136.
7. Politova G. A., Tereshina I. S., Gorbunov D. I., Paukov, Andreev A. V., Grechishkin R. M., Rogacki K. Magnetic and magnetocaloric properties of single crystal $(\text{Nd}_{0.5}\text{Pr}_{0.5})_2\text{Fe}_{14}\text{B}$ // *Journal of Alloys and Compounds*. 2018. Vol. 751. 30 June. Pp. 283–288.

8. **Lewis L. H., Panchanathan V., Wang J. Y.** Technical magnetic properties of melt-spun $(\text{Nd}_{1-x}\text{Pr}_x)_2\text{Fe}_{14}\text{B}$ at low temperature // *Journal of Magnetism and Magnetic Materials*. 1997. Vol. 176. No. 2–3. Pp. 288–296.
9. **Tereshina I. S., Pelevin I. A., Tereshina E. A., et al.** Magnetic hysteresis properties of nanocrystalline $(\text{Nd}, \text{Ho})-(\text{Fe}, \text{Co})-\text{B}$ alloy after melt spinning, severe plastic deformation and subsequent heat treatment // *Journal of Alloys and Compounds*. 2016. Vol. 681. 5 October. Pp. 555–560.
10. **Gutfleisch O., Harris I. R.** Fundamental and practical aspects of the hydrogenation, disproportionate, desorption and recombination process // *Journal of Physics D*. 1996. Vol. 29. No. 9. P. 2255–2265.
11. **Gutfleisch O., Willard M. A., Brück E., Chen C. H., Sankar S. G., Liu J. P.** Magnetic materials and devices for the 21st century: Stronger, lighter, and more energy efficient // *Advanced Materials*. 2011. Vol. 23. No. 7. Pp. 821–842.
12. **Croat J. J.** Manufacture of NdFeB permanent magnets by rapid solidification // *Journal of the Less-Common Metals*. 1989. Vol. 148. No. 1–2. Pp. 7–15.
13. **Gabay A. M., Popov A. G., Gaviko V. S., Belozarov Y. V., Yermolenko A. S.** The structure and magnetic properties of rapidly quenched and annealed multi-phase nanocrystalline $\text{Nd}_9\text{Fe}_{91-x}\text{B}_x$ ribbons // *Journal of Alloys and Compounds*. 1996. Vol. 245. No. 1–2. Pp. 119–124.
14. **Straumal B. B., Kilmametov A. R., Mazilkin A. A., Protasova S. G., Kolesnikova K. I., Straumal P. B., Baretzky B.** Amorphization of Nd-Fe-B alloy under the action of high-pressure torsion // *Materials Letters*. 2015. Vol. 145. 15 April. Pp. 63–66.
15. **Li H., Li W., Zhang Y., Gunderov D. V., Zhang X.** Phase evolution, microstructure and magnetic properties of bulk $\alpha\text{-Fe}/\text{Nd}_2\text{Fe}_{14}\text{B}$ nanocomposite magnets prepared by severe plastic deformation and thermal annealing // *Journal of Alloys and Compounds*. 2015. Vol. 651. 15 December. Pp. 434–439.
16. **Hosokawa A., Takagi K., Kuriwa T., Inoue Y., Ozaki K.** Severe plastic deformation of Nd-Fe-B nanocomposite magnets at room temperature // *Journal of Magnetism and Magnetic Materials*. 2019. Vol. 473. 1 March. Pp. 51–60.
17. **Tereshina-Chitrova E. A., Korneeva Y. V., Ozherelkov D. Y., Doležal P., Tereshina I. S., Kaminskaya T. P., Gorbunov D. I., Dobatkin S. V., Minárik P.** Enhanced magnetocaloric effect in distilled terbium and emergence of novel properties after severe plastic deformation // *Scripta Materialia*. 2020. Vol. 187. October. Pp. 340–344.
18. **Pelevin I. A., Ozherelkov D. Y., Kaminskaya T. P., Tereshina I. S.** Surface morphology investigations of nanocrystalline $\text{R}_2\text{Fe}_{14}\text{B}$ ($\text{R} = \text{Y}, \text{Nd}, \text{Gd}, \text{Er}$) by atomic force microscopy // *Materials Research Proceedings*. 2022. Vol. 21. Pp. 81–87.
19. **Yagodkin Y. D., Lileev A. S., Lyubina J. V., Shingarev E. N., Glebov V. A., Nefedov V. S.** Structure and magnetic properties of nanocrystalline alloys based on $\text{Nd}_2\text{Fe}_{14}\text{B}$ obtained by various techniques // *Journal of Magnetism and Magnetic Materials*. 2003. Vol. 258–259. March. Pp. 586–589.
20. **Dempsey N. M., Walther A., May F., Givord D., Khlopkov K., Gutfleisch O.** High performance hard magnetic NdFeB thick films for integration into micro-electro-mechanical systems // *Applied Physics Letters*. 2007. Vol. 90. No. 9. P. 092509.
21. **Политова Г. А., Терешина И. С., Каминская Т. П., Пауков М. А., Добаткин С. В.** Исследование методом атомно-силовой микроскопии морфологии поверхности сплавов $\text{Nd}_2\text{Fe}_{14}\text{B}$, полученных с помощью различных технологий // *Металлы*. 2018. № 5. С. 75–82.
22. **Li L., Tirado A., Nlebedim I. C., et al.** Big area additive manufacturing of high performance bonded NdFeB magnets // *Scientific Reports*. 2016. Vol. 6. P. 36212.
23. **Paranthaman M. P., Shafer C. S., Elliott A. M., Siddel D. H., McGuire M. A., Springfield R. M., Martin J., Fredette R., Ormerod J.** Binder jetting: A novel NdFeB bonded magnet fabrication process // *Journal of Minerals, Metals and Materials*. 2016. Vol. 68. No. 7. Pp. 1978–1982.
24. **Li L., Post B., Kunc V., Elliott A. M., Paranthaman M. P.** Additive manufacturing of near-net-shape bonded magnets: Prospects and challenges // *Scripta Materialia*. 2017. Vol. 135. 1 July. Pp. 100–104.
25. **Bittner F., Thielsch J., Drossel W. G.** Microstructure and magnetic properties of Nd-Fe-B permanent magnets produced by laser powder bed fusion // *Scripta Materialia*. 2021. Vol. 201. August. P. 113921.
26. **Jaćimović J., Binda F., Herrmann L. G., Greuter F., Genta J., Calvo M., Tomše T., Simon R. A.** Net shape 3D printed NdFeB permanent magnet // *Adv. Eng. Mater.* 2017. 2017. Vol. 19. No. 8. P. 1700098.



27. Huber C., Sepehri-Amin H., Goertler M., Groenefeld M., Teliban I., Hono K., Suess D. Coercivity enhancement of selective laser sintered NdFeB magnets by grain boundary infiltration // *Acta Materialia*. 2019. Vol. 172. 15 June. Pp. 66–71.
28. Pelevin I. A., Nalivaiko A. Y., Ozherelkov D. Y., Shinkaryov A. S., Chernyshikhin S. V., Arnautov A. N., Zmanovsky S. V., Gromov A. A. Selective laser melting of Al-based matrix composites with Al_2O_3 reinforcement: Features and advantages // *Materials*. 2021. Vol. 14. No. 10. P. 2648.
29. Андреева Н. В., Филимонов А. В., Рудской А. И., Бурханов Г. С., Терёшина И. С., Политова Г. А., Пелевин И. А. Исследование наноструктурированных магнитотвердых материалов системы Nd-Ho-Fe-Co-B методами атомно-силовой и магнитно-силовой микроскопии // *Физика твердого тела*. 2016. Т. 58. № 9. С. 1798–1805.
30. Politova G. A., Tereshina I. S., Kaminskaya T. P., Viryus A. A., Paukov M. A., Lukin A. A., Andreev A. V. Substituted $(Nd,Pr)_2Fe_{14}B$ alloys: Structural features and magnetic properties // *Journal of Physics. Conference Series*. 2019. Vol. 1236. P. 012016.
31. Kolchugina N. B., Lukin A. A., Kaminskaya T. P., et al. Morphological peculiarities of R-Fe-B (R = Nd, Pr) alloys formed upon solidification by strip-casting // *Phys. Met. Metallogr.* 2020. Vol. 121. No. 8. Pp. 772–782.

THE AUTHORS

TERESHINA Irina S.

*Lomonosov Moscow State University,
National University of Science and Technology "MISiS"*
1, Leninskie Gory, Moscow, 119991, Russia
irina_tereshina@mail.ru
ORCID: 0000-0003-3633-3440

POLITOVA Galina A.

*Baikov Institute of Metallurgy Materials Science, RAS, Moscow;
Peter the Great St. Petersburg Polytechnic University, St. Petersburg*
49, Leninskiy Ave., Moscow, 119334, Russia
gpolitova@gmail.com
ORCID: 0000-0003-1908-9677

KAMINSKAYA Tatiana P.

Lomonosov Moscow State University
1, Leninskie Gory, Moscow, 119991, Russia
ktp53@mail.ru
ORCID: 0000-0002-3667-0837

POPOV Vladimir V.

Lomonosov Moscow State University
1, Leninskie Gory, Moscow, 119991, Russia
vvpopov@physics.msu.ru
ORCID: 0000-0003-1191-3860

GUNDEROV Dmitry V.

*Institute of Molecule and Crystal Physic of the Ufa Federal Research Centre,
RAS*
151, Oktyabr Ave., Ufa, 450075, Russia
dimagun@mail.ru
ORCID: 0000-0001-5925-4513

FILIMONOV Alexey V.

Peter the Great St. Petersburg Polytechnic University
29 Politechnicheskaya St., St. Petersburg, 195251, Russia
filimonov@rphf.spbstu.ru
ORCID: 0000-0002-2793-5717

PELEVIN Ivan A.

National University of Science and Technology "MISiS"
4, Leninskiy Ave., Moscow, 119049, Russia
pele.po4ta@yandex.ru
ORCID: 0000-0003-1592-3062

СВЕДЕНИЯ ОБ АВТОРАХ

ТЕРЁШИНА Ирина Семеновна — доктор физико-математических наук, ведущий научный сотрудник кафедры физики твердого тела Московского государственного университета имени М. В. Ломоносова; ведущий научный сотрудник Национального исследовательского технологического университета «Московский институт стали и сплавов (МИСиС)».

119991, Россия, г. Москва, ул. Ленинские Горы, 1
irina_tereshina@mail.ru
ORCID: 0000-0003-3633-3440

ПОЛИТОВА Галина Александровна — кандидат физико-математических наук, старший научный сотрудник Института металлургии и материаловедения им. А. А. Байкова Российской академии наук; старший научный сотрудник Научно-образовательного центра «Физика нанокompозитных материалов электронной техники» Санкт-Петербургского политехнического университета Петра Великого.

119334 Россия, г. Москва, Ленинский пр., 49
gpolitova@gmail.com
ORCID: 0000-0003-1908-9677

КАМИНСКАЯ Татьяна Петровна — кандидат технических наук, старший научный сотрудник кафедры общей физики Московского государственного университета имени М. В. Ломоносова.

119991, Россия, Москва, ул. Ленинские Горы, 1
ktp53@mail.ru
ORCID: 0000-0002-3667-0837

ПОПОВ Владимир Викторович — кандидат физико-математических наук, старший научный сотрудник кафедры общей физики Московского государственного университета имени М. В. Ломоносова.

119991, Россия, Москва, ул. Ленинские Горы, 1
vvpopov@physics.msu.ru
ORCID: 0000-0003-1191-3860

ГУНДЕРОВ Дмитрий Валерьевич — доктор физико-математических наук, ведущий научный сотрудник Института физики молекул и кристаллов — обособленного структурного подразделения ФГБНУ — Уфимского федерального исследовательского центра Российской академии наук.

450075, Россия, г. Уфа, пр. Октября, 151
dimagun@mail.ru
ORCID: 0000-0001-5925-4513



ФИЛИМОНОВ Алексей Владимирович — доктор физико-математических наук, профессор Высшей инженерно-физической школы, руководитель Научно-образовательного центра «Физика нанокompозитных материалов электронной техники» Санкт-Петербургского политехнического университета Петра Великого.

195251, Россия, г. Санкт-Петербург, Политехническая ул., 29

filimonov@rphf.spbstu.ru

ORCID: 0000-0002-2793-5717

ПЕЛЕВИН Иван Алексеевич — кандидат физико-математических наук, научный сотрудник Национального исследовательского технологического университета «Московский институт стали и сплавов (МИСиС)».

119049, Россия, г. Москва, Ленинский пр., 4

pele.po4ta@yandex.ru

ORCID: 0000-0003-1592-3062

Received 19.04.2022. Approved after reviewing 11.05.2022. Accepted 11.05.2022.

Статья поступила в редакцию 19.04.2022. Одобрена после рецензирования 11.05.2022. Принята 11.05.2022.

Original article

DOI: <https://doi.org/10.18721/JPM.15205>

CHARACTERIZATION OF FLUORESCENT PROTEINS FOR STUDYING THE MORPHOLOGICAL REARRANGEMENTS INSIDE SINGLE BACTERIAL CELLS DURING INFECTION WITH **phiKZ** BACTERIOPHAGE

D. A. Antonova, A. D. Zotova, A. A. Usatykh,

N. E. Morozova, M. V. Yakunina ✉

Peter the Great St. Petersburg Polytechnic University, St. Petersburg, Russia

✉ yakuninam@nanobio.spbstu.ru

Abstract. This work deals with evaluation of key properties of some fluorescent proteins (FPs) in order to use them for observation of redistributing the target proteins between the cytoplasm and pseudonucleus forming in bacterial cell infection by bacteriophage phiKZ. Four FPs, namely, mNeonGreen, mCherry, ECFP and EYFP, have been investigated using fluorescence microscopy. It was established that EYFP, unlike other objects, localized in the pseudonucleus during the infection. This phenomenon gave grounds to exclude EYFP from further experiments. As a result of analyzing the obtained values of FP key parameters, a set of FPs suitable for studying the process of bacterial cells infection by fluorescence microscopy was found.

Keywords: fluorescent protein, optical microscopy, bacterial cell, phiKZ bacteriophage

Funding: The reported study was funded by Russian Science Foundation (Agreement No. 19-74-10030 dated August 15, 2019)

Citation: Antonova D. A., Zotova A. D., Usatykh A. F., Morozova N. E., Yakunina M. V., Characterization of fluorescent proteins to study morphological rearrangements inside single bacterial cells. St. Petersburg Polytechnical State University Journal. Physics and Mathematics. 15 (2) (2022) 46–55. DOI: <https://doi.org/10.18721/JPM.15205>

This is an open access article under the CC BY-NC 4.0 license (<https://creativecommons.org/licenses/by-nc/4.0/>)



Научная статья

УДК 577.359

DOI: <https://doi.org/10.18721/JPM.15205>

ХАРАКТЕРИЗАЦИЯ ФЛУОРЕСЦЕНТНЫХ БЕЛКОВ ДЛЯ ИЗУЧЕНИЯ МОРФОЛОГИЧЕСКИХ ПЕРЕСТРОЕК ВНУТРИ ОДИНОЧНЫХ БАКТЕРИАЛЬНЫХ КЛЕТОК ПРИ ИНФЕКЦИИ БАКТЕРИОФАГОМ ϕ iKZ С ПОМОЩЬЮ ОПТИЧЕСКОЙ МИКРОСКОПИИ

*Д. А. Антонова, А. Д. Зотова, А. А. Усатых,
Н. Е. Морозова, М. В. Якунина* ✉

Санкт-Петербургский политехнический университет Петра Великого, Санкт-Петербург, Россия

✉ yakuninam@nanobio.spbstu.ru

Аннотация. В работе проведена оценка ключевых свойств флуоресцентных белков (ФБ) с целью их использования при наблюдении процессов перераспределения целевых белков между цитоплазмой и псевдоядром, которое образуется в ходе инфицирования бактериальной клетки бактериофагом ϕ iKZ. С помощью флуоресцентной микроскопии были изучены четыре ФБ: mNeonGreen, mCherry, ECFP и EYFP. Установлено, что белок EYFP, в отличие от остальных, локализуется в псевдоядре во время инфекции, что послужило основанием для его исключения из дальнейших опытов. В результате анализа полученных значений ключевых параметров ФБ был выявлен набор ФБ, перспективных для исследования процесса инфицирования бактериальных клеток.

Ключевые слова: флуоресцентный белок, оптическая микроскопия, бактериальная клетка, бактериофаг ϕ iKZ

Финансирование: Исследование выполнено при финансовой поддержке Российского научного фонда (соглашение № 19-74-10030 от 15.08.2019)

Для цитирования: Антонова Д. А., Зотова А. Д., Усатых А. А., Морозова Н. Е., Якунина М. В. Характеризация флуоресцентных белков для изучения морфологических перестроек внутри одиночных бактериальных клеток при инфекции бактериофагом ϕ iKZ с помощью оптической микроскопии // Научно-технические ведомости СПбГПУ. Физико-математические науки. 2022. Т. 2 № 15. С. 46–55. DOI: <https://doi.org/10.18721/JPM.15205>

Статья открытого доступа, распространяемая по лицензии CC BY-NC 4.0 (<https://creativecommons.org/licenses/by-nc/4.0/>)

Introduction

While the genomes of giant bacteriophages have a great coding potential, homologous sequences have yet to be detected in other organisms for most of the genes, so it is difficult to determine their functions. The reason for the keen interest towards phiKZ-like bacteriophages is that they form a spherical structure called the pseudonucleus in the center of the cell throughout their life cycle [1].

The pseudonucleus is coated with a protein shell shielding the bacteriophage's DNA from the defense systems of the infected cell, such as restriction-modification systems and CRISPR/Cas aimed at destroying foreign DNA [2, 3]. The pseudonucleus is localized through the phage-encoded cytoskeletal structure produced by the tubulin-like protein TubZ [1, 4]. It was established in [1] that as the infection progresses, the pseudonucleus separates not only phage DNA but also the transcription factory from the cell cytoplasm, while the translation processes are localized to the cytoplasm. Furthermore, enzyme transport into the lumen of the pseudonucleus was found to be selective: experiments with phage non-virion RNA polymerase confirmed that proteins can translocate through the proteinaceous shell post-transcriptionally, suggesting a mechanism for selective transport [5, 6].

Nuclei of eukaryotic cells have the same properties. In view of this, it can be hypothesized that the predecessors of phiKZ-like viruses, capable of assembling pseudonuclei, might have played the key role in evolutionary nucleogenesis of modern eucaryotic cells [7].

Further studies into the mechanisms behind the assembly of the phage pseudonucleus, the translocation of protein products into the lumen, selective transport and other processes of intracellular growth in bacteriophages can contribute towards drawing comparisons with the life cycle of eucaryotic cells, subsequently gaining deeper insights into the evolutionary pathways of multicellular life on Earth.

We focused on the phiKZ phage, which is the first gigantic bacteriophage ever described [8] (its genome size is 280 kilobase pairs (kbp)); this bacteriophage infects *Pseudomonas aeruginosa*-like bacteria [8]. The pseudonucleus of this phage is still poorly characterized, in contrast to its relative 201phi2-1 [5].

Fluorescent microscopy is an effective method for studying bacterial cells. Fluorescence imaging allows to monitor the changes occurring to the cell infected by a bacteriophage. A report on gigantic phages [1], fusing the red fluorescent protein (FP) mCherry to the target protein, detected that the proteinaceous shell of the pseudo-nucleus essentially consists of the Gp54 protein. This largely determined our approach to studying the proteins of the phiKZ bacteriophage throughout the cellular infection. However, it was also discovered that the mutated GFP, GFPmut1, is capable of translocating into the pseudonucleus of the phiKZ bacteriophage [3]. This means that different FPs should be selected and tested for further experiments.

We examined the expression in several FP genes taken for the experiments in bacteriophage-infected cells to select the optimal variants on the progression of the phiKZ bacteriophage in *P. aeruginosa* cells. We managed to detect one more FP (EYFP) capable of translocation through the proteinaceous shell of the pseudonucleus.

Fluorescence methods

Fluorescence techniques are widely used to study cellular compartments, proteins, and DNA. Different methods can be applied for fluorescent tagging depending on the samples considered. Organic dyes with low molecular weight are actively used for staining cell components. For example, lipophilic dyes such as Nile Red are used to stain cell membranes, MitoRed and MitoTracker Red [9] to stain mitochondrial membranes, while DAPI, Propidium Iodide, YOYO-1 and others are often used to stain DNA in the cell [1]. Some dyes can stain only dead cells, allowing to estimate the number of viable bacteria in the population. The range of dyes for particular tasks is limited, so it is impossible to selectively stain any biomolecules in most cases.

Selective fluorescent tagging is often performed with antibodies that have highly specific binding to the target. Antibodies can be modified by a fluorophore molecule, allowing to track the position of the antibody (and, respectively, its target) to in the cell via fluorescence microscopy [10]. However, this method also has limitations: in particular, the target can only be observed in fixed dead cells, antibodies specific to the molecule under consideration should be produced (the terms 'molecule of interest' (MOI) or 'protein of interest' (POI) are used for brevity from now on), and the modified antibodies are expensive.



FPs are extremely popular for imaging protein structures. There is a wide variety of FPs with different excitation and emission spectra, different brightness, maturation time, sensitivity to pH, etc. This way, researchers are able to select the proteins most appropriate for each particular experiment. To synthesize fusion proteins, FP genes are fused in a single reading frame with POI genes. Expression of such a gene produces a protein macromolecule containing both the POI and the FP. This allows to detect the location of fluorescent protein, and therefore the POI by fluorescence microscopy of living cells over long time periods. However, in the case of fusion proteins, the FP should reach the correct conformation in the cell so that it does not prevent the POI from performing its function. An important criterion for further experiments is the option for tracking the POI within living cells over long time periods, so we chose fluorescent tagging of the POI.

Selection of fluorescent proteins

To monitor synthesis and localization of proteins in real time over a long period, we had to select the FPs with the optimal characteristics that could be convenient for simultaneously tracking several proteins in a single cell.

We considered the following FPs: ECFP, EGFP, mNeonGreen, EYFP, TagRFP, mCherry, and FusionRed (Table 1); data were extracted from the FPbase fluorescent protein database [11].

The most important characteristics of the FP in our study were the *in vivo* maturation time, fluorescence brightness, and stability.

In terms of brightness, calculated as the product of the molar extinction coefficient and quantum fluorescence yield, mNeonGreen, EYFP, and TagRFP FB turned out to be the most intense. However, the red fluorescent protein TagRFP proved largely inferior to others in terms of maturation time, also serving as an essential characteristic, since cultivating bacterial colonies for excessively long periods can distort the results obtained. Another red protein, FusionRed, did not fit this requirement either, despite its high pH stability. Thus, mCherry appeared to be the best red protein, sufficiently stable and fast-maturing, even though it is still inferior to TagRFP in terms of brightness.

The proteins mNeonGreen and EYFP are better than the protein EGFP in terms of fluorescence brightness and also have comparably shorter maturation, so we excluded the green protein EGFP from analysis. Even though the yellow protein EYFP has weak pH stability (high pKa), we still decided to test it since its other parameters are at acceptable levels. The protein ECFP is a stable monomer, however, it has a rather low brightness, so it was not considered for further experiments.

Table 1

Key characteristics for several fluorescent proteins

Parameter	Parameter value for FP						
	ECFP	EGFP	mNG	EYFP	TagRFP	mCherry	FR
Excitation peak, nm	434	488	506	513	555	587	580
Emission peak, nm	477	507	517	527	584	610	608
EC, $M^{-1} \cdot cm^{-1}$	32.5	55.9	116	67.0	100	72	94.5
QY	0.40	0.60	0.80	0.67	0.48	0.22	0.19
Calculated intensity	13.00	33.54	92.80	44.89	48.00	15.84	17.95
pKa	4.7	6.0	5.7	6.9	3.8	4.5	4.6
Maturation time, min	—	60	10	9	100	15	130
<i>In vivo</i> structure	M	WD	M	WD	WD	M	M

Notations: EC is the molar extinction coefficient at maximum absorption, QY is the quantum fluorescence yield, pKa is the pH value at which the fluorescence intensity drops to 50% of the maximum, M refers to the monomer, WD to weak dimerization. Note. The brightness is calculated as the product of $EC \times QY$.

Based on this reasoning, we selected only three FPs from the list for testing: mNeonGreen, EYFP, and mCherry. We prepared gene constructs containing the genes of these FPs for subsequent expression in cells.

Experimental procedure

Fluorescent microscopy allows to visualize the locations of FPs in cells. However, a small amount of FPs may complicate subsequent image processing and analysis of protein localization in the cell. To improve image quality, cells with the above-mentioned gene constructs were grown in the presence of an inducer in a medium triggering protein synthesis in the cell. Thus, the cells already contain some amount of FP by the start of the experiment. Cells were infected with a bacteriophage, immediately placed on a slide with an agarose support containing inducer and culture medium, and sealed with a cover glass. Uninfected cells were used as controls. The sample was placed under a microscope for subsequent imaging. An inverted Nikon Eclipse Ti-E microscope (Japan) equipped with an incubator was used for fluorescence microscopy under transmitted light as well as red and yellow/green fluorescence. A set of xRed-4040C band filters was used to detect red fluorescence, YFP-2427B to detect yellow or green fluorescence (the filters were produced by Semrock (USA) in both cases). An ND8 filter (Fujimi, Japan) was used during the imaging to avoid FP destaining in cells. The exposure was the same for all proteins, selected in such a way that the signal from the FP was not too strong to prevent overshooting. Images were acquired at 1 frame per 10 min over 3 h at 37 °C using the MicroManager script.

Results and processing

The images acquired were processed in ImageJ software. First, the background was subtracted from the images, then the relative brightness intensity was measured in the cells outside the pseudonucleus (I_0) and inside it (I_1) for each FP tested. The localization of the pseudonucleus in the cells was confirmed by DNA staining with the DAPI fluorescent dye (Beckman Counter Life Sciences, USA). Since the absolute amount of FPs is individual for each cell, we calculated its relative amount as the ratio I_1/I_0 in the same infected cell. Next, we found the mean value and the standard deviation among the infected cells considered for this ratio. The computational results are summarized in Table 2.

Table 2

**Quantitative computations for the contents
of selected fluorescent proteins in infected cells**

Fluorescent protein	Number of cells considered	Mean value I_1/I_0	Standard deviation
EYFP	45	2.10	0.50
mNeonGreen	37	0.80	0.11
mCherry	50	0.66	0.14

Notation: I_1/I_0 is the ratio of relative fluorescence brightnesses in the cell inside the pseudonucleus (I_1) and outside it (I_0).

Notably, FPs are distributed uniformly in uninfected cells, while the behavior of the protein in the cell varied throughout the infection, depending on the type of protein (Fig. 1). The fluorescent protein EYFP was redistributed to the pseudonucleus throughout the infection, so that the mean fluorescence intensity inside the pseudonucleus was twice as high than that outside it. Admittedly, this behavior of EYFP limits the potential for using it in further studies. On the other hand, the proteins mNeonGreen and mCherry did not penetrate the pseudonucleus, as the fluorescence intensity inside it decreased by an average of 20–35% (depending on the protein type) under similar conditions.

Brightness of proteins in the cells is another crucial parameter for analyzing the data obtained by fluorescence microscopy. The higher the protein's fluorescence intensity, the easier it is to process and analyze the images. The mean fluorescence intensity was calculated for each FP from 80 uninfected cells, along with the corresponding standard deviation in the first frame. The results of these calculations are as follows (in relative units):

Fluorescent protein	Mean fluorescence intensity, rel. units
mNeonGreen	550 ± 390,
mCherry	210 ± 110,
EYFP	250 ± 100.

The results present clear evidence that the protein mNeonGreen best meets the requirements for further experiments, since it does not redistribute into the pseudonucleus and also exhibits the highest brightness among the proteins considered. Even though the mean fluorescence intensity of the protein EYFP was slightly higher than that of mCherry, the former, unlike the latter, was redistributed to the pseudonucleus, so it was rejected. Protein destaining in this experiment does not impose considerable limitations, since the imaging rate was fairly low (1 frame per 10 min), so it was possible to synthesize the new FP over the time between frames.

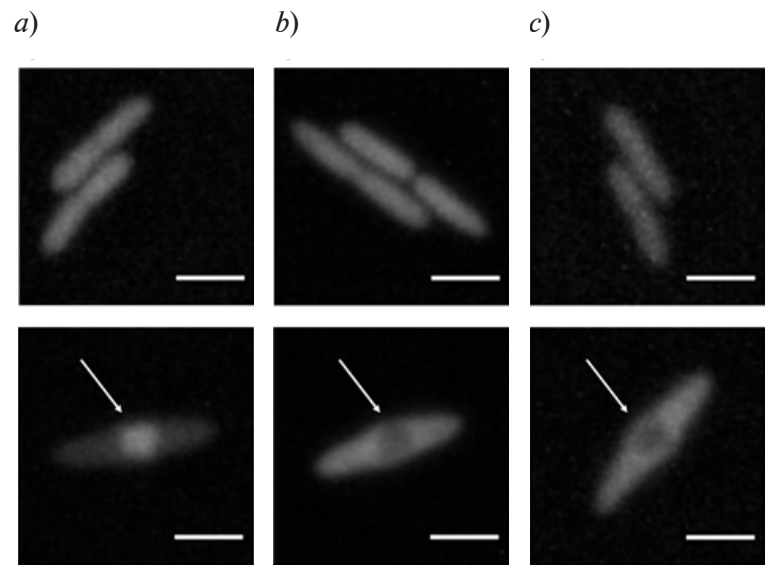


Fig. 1. Micrographs of uninfected (top row) and infected (bottom row) cells containing fluorescent proteins EYFP (a), mNeonGreen (b) and mCherry (c) 60 min after the onset of infection. The white arrows point to the pseudonuclei. The scale bars are 2 μm long

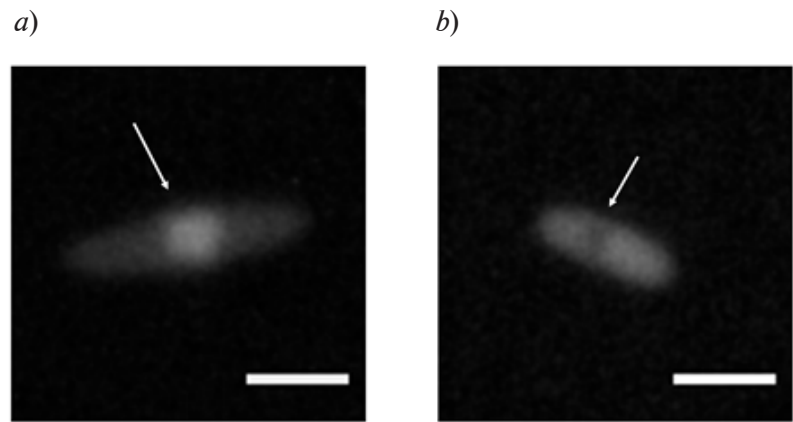


Fig. 2. Micrographs of infected cell preparations containing fluorescent proteins EYFP (a) and ECFP (b). The white arrows point to the pseudonuclei The scale bars are 2 μm long

Estimating the relationship between FP amino acid sequences and their localizations within bacteriophage-infected cells

In contrast to other types of the initial GFP (specifically, sfGFP and pMutinGFP), the protein GFPmut1 that redistributes to the pseudonucleus contains amino acid substitutions at positions 99, 153, and 163. Serine was replaced by phenylalanine (99F) at position 99, tyrosine by methionine (153m) at position 153, alanine by valine (163V) at position 163, while 99-phenylalanine and 153-methionine made the greatest contributions to redistribution to the pseudonucleus. EYFP, GFPmut1, and ECFP PBs are all derived from the same protein. As reported in [3], unlike the other two proteins, ECFP is not redistributed to the pseudonucleus. To verify this result, we prepared an expression plasmid containing the ECFP gene and analyzed its localization under the given experimental conditions. According to the data obtained, the protein ECFP indeed does not penetrate the pseudonucleus (Fig. 2). We also analyzed its amino acid sequence and aligned it with the proteins EYFP and GFPmut1 (Fig. 3).

As seen from Fig. 3, the protein EYFP contains both amino acids in its sequence; according to [3], these amino acids are responsible for redistributing the FP inside the pseudonucleus, which is in apparent agreement with our results. However, the protein ECFP, which also contains phenylalanine at position 99, does not redistribute to the pseudonucleus, remaining in the cytoplasm. The protein ECFP carries the same amino acid at position 153 as the proteins EYFP and EGFP.

EYFP	MVSKGEELFTGVVPIVLVDGVDVNGHKFSVSGEGGDATYGKLT LKFICTTGKLPVPHPT	60
ECFP	MVSKGEELFTGVVPIVLVDGVDVNGHKFSVSGEGGDATYGKLT LKFICTTGKLPVPHPT	60
GFPmut1	-MSKGEELFTGVVPIVLVDGVDVNGHKFSVSGEGGDATYGKLT LKFICTTGKLPVPHPT	59
	:*****	
EYFP	LVTTFGYGLQCFARYPDHIIKHQDFFKSAMPEGYVQERTIFFKDDGNYKTRAEVKFEGDTL	120
ECFP	LVTTLTWGVQCFSRYPDHIIKHQDFFKSAMPEGYVQERTIFFKDDGNYKTRAEVKFEGDTL	120
GFPmut1	LVTTLTYGVQCFSRYPDHIIKHQDFFKSAMPEGYVQERTIFFKDDGNYKTRAEVKFEGDTL	119
	:;*:**	
	99	
EYFP	VNRIELKGIDFKEDGNILGHKLEYNINSHNVYIADKQKNGIKVNFKIRHNIEDGGSVQLA	180
ECFP	VNRIELKGIDFKEDGNILGHKLEYNINSHNVYIADKQKNGIKVNFKIRHNIEDGGSVQLA	180
GFPmut1	VNRIELKGIDFKEDGNILGHKLEYNINSHNVYIADKQKNGIKVNFKIRHNIEDGGSVQLA	179

	153 163	
EYFP	DHYQQNTPIGDGPVLLPDNHYLSYQSALS KDPNEKRDMHVLLEFVTAAGITLGMDELYK	239
ECFP	DHYQQNTPIGDGPVLLPDNHYLSYQSALS KDPNEKRDMHVLLEFVTAAGITLGMDELYK	239
GFPmut1	DHYQQNTPIGDGPVLLPDNHYLSYQSALS KDPNEKRDMHVLLEFVTAAGITLGMDELYK	238

Fig. 3. Alignment of amino acid sequences for related fluorescent proteins EYFP, ECFP, and GFPmut1. The amino acids 99, 153 and 163 of the protein GFPmut1 are underlined and tagged. All three types have phenylalanine (F) at position 99

Thus, the data we have obtained suggest that the mechanism behind the FP distribution between the pseudonucleus and the cytoplasm does not depend on the presence of particular amino acids at certain positions, but is most likely associated with the general changes in the structure that they cause.

Conclusion

The study aimed to find fluorescent proteins (FPs) suitable for monitoring their redistribution between the cytoplasm and the pseudonucleus resulting from infection of a bacterial cell by the phiKZ bacteriophage.

In view of this, we selected FPs for the experiments on imaging living cells. The FPs were then tested for brightness levels, with distribution of FPs in infected cells subsequently constructed. The experiments indicate that the ECFP, mNeonGreen and mCherry proteins do not enter the pseudonucleus, while the protein EYFP is redistributed to the pseudonucleus during infection and is therefore unsuitable for further experiments. Moreover, further experiments allowed to disprove the traditional theory about the relationship of specific mutations in fluorescent proteins with their position relative to the pseudonucleus.



REFERENCES

1. Chaikerasak V., Nguyen K., Egan M. E., et al., The phage nucleus and tubulin spindle are conserved among large *Pseudomonas* phages, Cell Rep. 2017. Vol. 20 (7) (2017) 1563–1571.
2. Danilova Ya. A., Belousova V. V., Moiseenko A. V., et al., Maturation of pseudo-nucleus compartment in *P. aeruginosa*, infected with giant phiKZ phage, Viruses. 12 (10) (2020) 1197.
3. Nguyen K. T., Sugie J., Khanna K., et al., Selective transport of fluorescent proteins into the phage nucleus, PloS ONE. 16 (6) (2021) e0251429.
4. Chaikerasak V., Birkholz E. A., Pogliano J., The phage nucleus and PhuZ spindle: Defining features of the subcellular organization and speciation of nucleus-forming jumbo phages, Front. Microbiol. 2021. 13 July, <https://doi.org/10.3389/fmicb.2021.641317>.
5. Chaikerasak V., Nguyen K. T., Khanna K., et al., Assembly of a nucleus-like structure during viral replication in bacteria, Science. 355 (6321) (2017) 194–197.
6. Ceyssens P.-J., Minakhin L., den Bossche A.V., et al., Development of giant bacteriophage phiKZ is independent of the host transcription apparatus, J. Virol. 88 (18) (2014) 10501–10510.
7. Bell P. J. L., Evidence supporting a viral origin of the eukaryotic nucleus // Virus Research. 289 (November) (2020) 198168.
8. Krylov V., Bourkaltseva M., Pleteneva E., et al., Phage phiKZ – The first of giants, Viruses. 2021. Vol. 13 (2) (2021) 149.
9. Shibata T., Yamashita S., Hirusaki K., et al., Isolation of mitochondria by gentle cell membrane disruption, and their subsequent characterization, Biochem. Biophys. Res. Commun. 463 (4) (2015) 563–568.
10. Oakeley E. J., Podesta A., Jost J.-P., Developmental changes in DNA methylation of the two tobacco pollen nuclei during maturation, Proc. Natl. Acad. Sci. 94 (21) (1997) 11721–11725.
11. Lambert T. J., FPbase: a community-editable fluorescent protein database, Nat. Methods. 16 (4) (2019) 277–278.

СПИСОК ЛИТЕРАТУРЫ

1. Chaikerasak V., Nguyen K., Egan M. E., Erb M. L., Vavilina A., Pogliano J. The phage nucleus and tubulin spindle are conserved among large *Pseudomonas* phages // Cell Reports. 2017. Vol. 20. No. 7. Pp. 1563–1571.
2. Danilova Ya. A., Belousova V. V., Moiseenko A. V., Vishnyakov I. E., Yakunina M. V., Sokolova O. S. Maturation of pseudo-nucleus compartment in *P. aeruginosa*, infected with giant phiKZ phage // Viruses. 2020. Vol. 12. No. 10. P. 1197.
3. Nguyen K. T., Sugie J., Khanna K., Egan M. E., Birkholz E. A., Lee J., Beierschmitt C., Villa E., Pogliano J. Selective transport of fluorescent proteins into the phage nucleus // PloS ONE. 2021. Vol. 16. No. 6. P. e0251429.
4. Chaikerasak V., Birkholz E. A., Pogliano J. The phage nucleus and PhuZ spindle: Defining features of the subcellular organization and speciation of nucleus-forming jumbo phages // Frontiers in Microbiology. 2021. 13 July. <https://doi.org/10.3389/fmicb.2021.641317>.
5. Chaikerasak V., Nguyen K. T., Khanna K., et al., Assembly of a nucleus-like structure during viral replication in bacteria // Science. 2017. Vol. 355. No. 6321. Pp. 194–197.
6. Ceyssens P.-J., Minakhin L., den Bossche A.V., et al. Development of giant bacteriophage phiKZ is independent of the host transcription apparatus // Journal of Virology. 2014. Vol. 88. No. 18. Pp. 10501–10510.
7. Bell P. J. L. Evidence supporting a viral origin of the eukaryotic nucleus // Virus Research. 2020. Vol. 289. November. P. 198168.
8. Krylov V., Bourkaltseva M., Pleteneva E., Shaburova O., Krylov S., Karaulov A., Zhavoronok S., Svitich O., Zverev V. Phage phiKZ – The first of giants // Viruses. 2021. Vol. 13. No. 2. P. 149.
9. Shibata T., Yamashita S., Hirusaki K., Katoh K., Ohta Y. Isolation of mitochondria by gentle cell membrane disruption, and their subsequent characterization // Biochemical and Biophysical Research Communications. 2015. Vol. 463. No. 4. Pp. 563–568.
10. Oakeley E. J., Podesta A., Jost J.-P. Developmental changes in DNA methylation of the two tobacco pollen nuclei during maturation // Proceedings of the National Academy of Sciences. 1997. Vol. 94. No. 21. Pp. 11721–11725.
11. Lambert T. J. FPbase: a community-editable fluorescent protein database // Nature Methods. 2019. Vol. 16. No. 4. Pp. 277–278.

THE AUTHORS

ANTONOVA Daria A.

Peter the Great St. Petersburg Polytechnic University
29 Politechnicheskaya St., St. Petersburg, 195251, Russia
nasada12@mail.ru
ORCID: 0000-0002-2611-081X

ZOTOVA Anastasia D.

Peter the Great St. Petersburg Polytechnic University
29 Politechnicheskaya St., St. Petersburg, 195251, Russia
avotozana@gmail.com
ORCID: 0000-0002-0152-3220

USATYKH Andrey A.

Peter the Great St. Petersburg Polytechnic University
29 Politechnicheskaya St., St. Petersburg, 195251, Russia
andrew.usatih@yandex.ru
ORCID: 0000-0002-5377-3934

MOROZOVA Natalia E.

Peter the Great St. Petersburg Polytechnic University
29 Politechnicheskaya St., St. Petersburg, 195251, Russia
natusmorofovna@gmail.com
ORCID: 0000-0002-3001-2593

YAKUNINA Maria V.

Peter the Great St. Petersburg Polytechnic University
29 Politechnicheskaya St., St. Petersburg, 195251, Russia
yakuninam@nanobio.spbstu.ru
ORCID: 0000-0003-2083-3643

СВЕДЕНИЯ ОБ АВТОРАХ

АНТОНОВА Дарья Александровна — стажер-исследователь Лаборатории молекулярной микробиологии Санкт-Петербургского политехнического университета Петра Великого.
Санкт-Петербургский политехнический университет Петра Великого.
195251, Россия, г. Санкт-Петербург, Политехническая ул., 29
nasada12@mail.ru
ORCID: 0000-0002-2611-081X

ЗОТОВА Анастасия Дмитриевна — лаборант-исследователь Лаборатории молекулярной микробиологии Санкт-Петербургского политехнического университета Петра Великого.
195251, Россия, г. Санкт-Петербург, Политехническая ул., 29
avotozana@gmail.com
ORCID: 0000-0002-0152-3220

УСАТЫХ Андрей Алексеевич — студент Института биомедицинских систем и биотехнологий Санкт-Петербургского политехнического университета Петра Великого.
195251, Россия, г. Санкт-Петербург, Политехническая ул., 29
andrew.usatih@yandex.ru
ORCID: 0000-0002-5377-3934



МОРОЗОВА Наталия Евгеньевна — кандидат биологических наук, научный сотрудник
Лаборатории молекулярной микробиологии Санкт-Петербургского политехнического университета
Петра Великого.

195251, Россия, г. Санкт-Петербург, Политехническая ул., 29

natusmorozevna@gmail.com

ORCID: 0000-0002-3001-2593

ЯКУНИНА Мария Вячеславовна — кандидат биологических наук, научный сотрудник
Лаборатории молекулярной микробиологии Санкт-Петербургского политехнического университета
Петра Великого.

195251, Россия, г. Санкт-Петербург, Политехническая ул., 29

yakuninam@nanobio.spbstu.ru

ORCID: 0000-0003-2083-3643


Received 27.04.2022. Approved after reviewing 28.04.2022. Accepted 28.04.2022.

*Статья поступила в редакцию 27.04.2022. Одобрена после рецензирования 28.04.2022.
Принята 28.04.2022.*


Original article

DOI: <https://doi.org/10.18721/JPM.15206>

FEATURES OF THE COPPER-64 ISOTOPE PRODUCTION USING THE MGC-20 CYCLOTRON AT ST. PETERSBURG POLYTECHNICAL UNIVERSITY

*A. Tiba , P. A. Karaseov, Ya. A. Berdnikov,
A. Yu. Egorov, S. Yu. Mironova*

Peter the Great St. Petersburg Polytechnic University, St. Petersburg, Russia

 alitiba1991@gmail.com

Abstract. The article deals with the technology of ^{64}Cu isotope production by cyclotron proton irradiation of nickel foil of natural isotopic composition. In order to produce the ^{64}Cu isotope, three nickel samples were irradiated with 13 MeV protons (beam current was 4 μA) for three hours using the MGC-20 cyclotron at SPbPU. After irradiation the samples were subjected to multistage radiochemical treatment aimed at refining the chemical form suitable for measuring the activities of ^{64}Cu isotope and impurities. According to gamma spectrometric analysis, the ^{64}Cu activity value was 30 MBq. The performed calculations of induced ^{64}Cu isotope activity were based on the initial data and took into account the experimental conditions. A comparison of the experimental data with calculation results showed a good agreement between them.

Keywords: copper-64 isotope, cyclotron irradiation, natural nickel foil, comparison

Citation: Tiba A., Karaseov P. A., Berdnikov Ya. A., Egorov A. Yu., Mironova S. Yu., Features of the copper-64 isotope production using the MGC-20 cyclotron at St. Petersburg Polytechnical University, St. Petersburg Polytechnical State University Journal. Physics and Mathematics. 15 (2) (2022) 56–63. DOI: <https://doi.org/10.18721/JPM.15206>

This is an open access article under the CC BY-NC 4.0 license (<https://creativecommons.org/licenses/by-nc/4.0/>)




Научная статья


УДК 539.1.03

DOI: <https://doi.org/10.18721/JPM.15206>

ОСОБЕННОСТИ ПОЛУЧЕНИЯ ИЗОТОПА МЕДИ-64 НА ЦИКЛОТРОНЕ МГЦ-20 САНКТ-ПЕТЕРБУРГСКОГО ПОЛИТЕХНИЧЕСКОГО УНИВЕРСИТЕТА

*А. Тиба , П. А. Карасев, Я. А. Бердников,
А. Ю. Егоров, С. Ю. Миронова*

Санкт-Петербургский политехнический университет Петра Великого, Санкт-Петербург, Россия

 alitiba1991@gmail.com

Аннотация. В статье рассматривается технология получения изотопа ^{64}Cu путем циклотронного облучения протонами никелевой фольги природного изотопного состава. С целью наработки изотопа ^{64}Cu , три образца тонкой никелевой фольги в виде дисков были облучены протонами с энергией 13 МэВ (ток пучка – 4 мкА) на циклотроне МГЦ-20 СПбПУ в течение трех часов. По окончании облучения эти образцы подвергали многоэтапной радиохимической обработке, направленной на получение химической формы, удобной для измерения активности примесей и изотопа ^{64}Cu , образованных в результате облучения. По данным гамма-спектрометрического анализа значение активности этого изотопа составило 30 МБк. Сравнение данных эксперимента с результатами выполненных расчетов наведенной активности изотопа ^{64}Cu , базирующихся на исходных данных и учитывающих условия эксперимента, показало хорошее согласие между ними.

Ключевые слова: изотоп меди-64, циклотронное облучение, природные никелевые фольги, сравнение.

Для цитирования: Тиба А., Карасев П. А., Бердников Я. А., Егоров А. Ю., Миронова С. Ю. Особенности получения изотопа меди-64 на циклотроне МГЦ-20 Санкт-Петербургского политехнического университета // Научно-технические ведомости СПбГПУ. Физико-математические науки. 2022. Т. 2 № 15. С. 56–63. DOI: <https://doi.org/10.18721/JPM.15206>

Статья открытого доступа, распространяемая по лицензии CC BY-NC 4.0 (<https://creativecommons.org/licenses/by-nc/4.0/>)

Introduction

Molecular imaging has become a major tool for treating diseases such as cancer, not only providing a means for non-invasive imaging of physiological processes in living organisms at cellular and molecular levels, but also yielding valuable data for early detection and stage classification of diseases, understanding its biology, and assessing therapeutic efficacy. Different imaging techniques, such as single-photon emission computed tomography (SPECT) and positron emission tomography (PET), are used for assessing specific molecular targets in biomedical and clinical applications. In particular, among diverse molecular imaging techniques, PET imaging has flourished over the past decade, as augmenting the technology with positron-emitting radiopharmaceuticals allows to image living systems with high spatial sensitivity of measurement and accurate quantification [1].

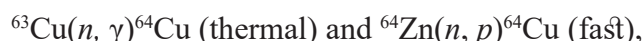
A particular radioisotope is chosen as a PET radiopharmaceutical depending on its physicochemical characteristics, availability for extraction and production, and the time scale of the biological process to be investigated. The copper-64 isotope (^{64}Cu), which has a half-life of 12.7 hours, is a radiopharmaceutical with unique properties. It can decay by three different schemes: by electron capture (EC), as well as by β^- and β^+ decays. The corresponding yields of the processes are (%): 43.5 (EC), 17.5 (β^+) and 38.4 (β^-). Because this isotope emits both β^+ and β^- particles, it can be used for both PET imaging and directed radionuclide therapy [2–4].

Increased efforts have been made over the past two decades to design new radiopharmaceuticals based on ^{64}Cu , largely thanks to the well-known copper chemistry. This isotope was attached to various molecules producing radiopharmaceuticals used for both imaging and therapy. Below we present a brief list of ^{64}Cu radiopharmaceuticals and their applications in medicine [5, 6]:

- ^{64}Cu -ATSM for imaging hypoxia and lung cancer;
- ^{64}Cu -Trastuzumab for imaging and therapy of breast cancer;
- ^{64}Cu -PSMA-617 for imaging of hypoxia and lung cancer;
- ^{64}Cu -AE105 for imaging of lung cancer, colon cancer and bladder cancer.

Another property of the isotope in question makes its ionic form ($^{64}\text{Cu}^{2+}$ ions) particularly valuable for medical applications, i.e., for PET imaging of various cancers. In contrast to most conventional radiopharmaceuticals, it is not necessary to attach the radioisotope to expensive carrier molecules in the case of $^{64}\text{Cu}^{2+}$, which greatly reduces the costs for the production technology. Bypassing the radiolabeling stage gives a unique advantage over the traditional technique, since standard radiochemical processing is sufficient after irradiating the target to obtain the composition of radiotracer acceptable for PET imaging [7, 8].

Another important characteristic of the ^{64}Cu isotope is that it can be obtained both at a cyclotron and a nuclear reactor. The latter technology is based on two nuclear reactions capturing the neutrons n :



where γ are gamma quanta, p are protons.

Large-scale production of the ^{64}Cu isotope takes advantage of the first reaction (thermal neutron capture). The main limitation of this approach is the low specific activity of the isotope against other active impurities of the target, which makes such technology unsuitable for preparing radiopharmaceuticals in practice.

The fast neutron capture reaction also has many limitations. Fast neutron flux in the reactor core is generally unavailable for isotope production. Most research reactors in the world are also limited by requirements on the target volume of the target, which, in turn, imposes restrictions on the activity of the resulting ^{64}Cu isotope [8].

However, ^{64}Cu can be produced in a cyclotron via a nuclear reaction $^{64}\text{Ni}(p, n)^{64}\text{Cu}$ through irradiation with protons of enriched or natural nickel. Automated modules are now available for rapid and highly efficient separation of ^{64}Cu from ^{64}Ni and other radioisotopes by ion-exchange chromatography. The majority of preclinical and clinical studies available have used ^{64}Cu produced in the cyclotron by this technology. When it comes to developed countries with advanced cyclotron equipment, this route is likely optimal for producing the required isotope for regular clinical practice [9, 10]. Notably, all studies on this subject concern copper production with targets from enriched nickel isotope ^{64}Ni , which is extremely expensive. Selecting a natural mixture of nickel isotopes can be considerably more cost-effective.

The goal of this study consisted in obtaining data on the activation of nickel targets with natural isotopic composition.

This was achieved by the following steps:
 foil made of natural nickel was irradiated with 13 MeV protons at the MGC-20 cyclotron of Peter the Great St. Petersburg Polytechnic University (SPbPU);
 irradiated foil was subjected to radiochemical processing to separate the resulting radioisotopes;
 activity of the ^{64}Cu isotope was measured;
 experimental data were compared with computational results.

Methods

Foil irradiation. Proton energies from 10 to 15 MeV are sufficient for obtaining ^{64}Cu [11]. We chose an energy of 13 MeV at the MGC-20 cyclotron at SPbPU. Three layers of nickel foil with natural isotopic composition (natural mixture), each 100 μm thick, were used as targets; their total thickness was 300 μm , each sample weighed 0.09 g. The samples were disc-shaped, 12 mm in diameter (with an area of 1.13 cm^2).

To additionally purify the foil prior to irradiation, it was first washed three times with heptane (C_7H_{16} , saturated hydrocarbon) and then three times with isopropyl alcohol.

The three nickel discs exposed to radiation were secured with a copper target holder (Fig. 1).

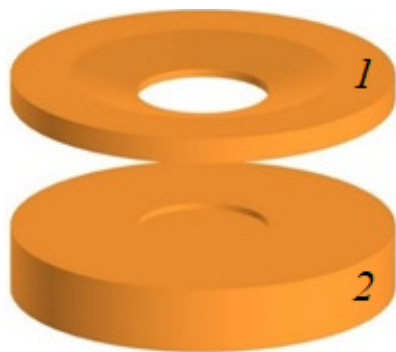


Fig. 1. Copper target holder; three foil discs attached between ring (1) and substrate (2)

Copper was chosen due to its high thermal conductivity ensuring heat removal. The diameter of the irradiated field was determined by the geometry of the holder, amounting to 10 mm. The holder was attached to a water-cooled substrate to prevent overheating of the target.

A beam of 13 MeV protons was used for irradiation, the beam current was 4 μA , the irradiation time was 3 hours.

Radiochemical processing of samples. Following irradiation, nickel foil samples were processed by the following technique to obtain the ^{64}Cu isotope:

samples were held for 12 hours to allow short-lived isotopes to decay; next, the irradiated foil was removed from the cyclotron and placed in a box with lead protection;

three foil samples were dissolved in 5 ml of aqueous HCl solution (molar concentration of the solution was 11.7 M) for 4 hours at 100 $^{\circ}\text{C}$;

solution was evaporated in a glycerol bath for 1 hour at 185–200 $^{\circ}\text{C}$ to dryness; the resulting precipitate was cooled to room temperature for 20 min; solid precipitate was dissolved in 4 ml of aqueous HCl solution (concentration of the solution was 6.0 M) for 20 min at room temperature of 25 $^{\circ}\text{C}$;

20 μl aliquot was removed from a solution of a known volume (obtained at the end of the previous stage) for gamma-spectrometric analysis.

Spectrometric analysis of the sample. Analysis was performed after another 1 hour 14 minutes via a gamma radiation spectrometer equipped with a GEM-FX5825 semiconductor detector based on ultrapure germanium and a DSPEC-50 multi-channel digital analyzer.

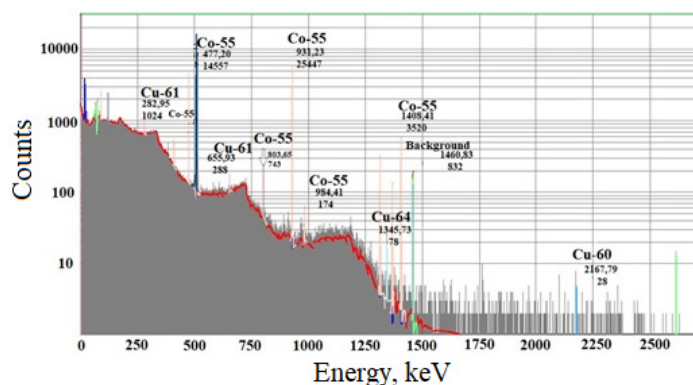


Fig. 2. Spectrum from aliquot (20 μl) obtained from the radiotracer with a natural mixture of nickel isotopes

Experimental results

A peak is observed on the energy spectrum (Fig. 2) at 1345.77 keV, corresponding to ^{64}Cu , suggesting it is present in the sample. The activity of ^{64}Cu in a 20 μl aliquot was 45 kBq (with an error of 30%), while the complete solution (4 ml) contains ^{64}Cu with an activity of 9 MBq. This activity is achieved 21 hours after irradiation. Thus, we can conclude that the activity of ^{64}Cu immediately after the end of irradiation was 30 ± 9 MBq. Further analysis of the data showed that the measurement result obtained is consistent with the computational result (see below).

Simulation of ^{64}Cu yield for natural nickel irradiated with a proton beam

The simulation was carried out using the solution to the equation for passage of protons through matter (Bethe–Bloch formula) and the equation for isotope production in a natural nickel target irradiated with protons in the cyclotron to find the yield of the reaction $^{64}\text{Ni}(p, n)^{64}\text{Cu}$ [12]. Natural nickel contains the following isotopes [13]:

^{58}Ni (68.00 %), ^{60}Ni (26.00 %), ^{61}Ni (1.14 %), ^{62}Ni (3.71 %) and ^{64}Ni (0.93 %).

Fig. 3 shows the total activity of ^{64}Cu depending on the thickness of the target made of natural nickel irradiated with protons with an initial kinetic energy of 13 MeV. The line corresponds to the dependence, and the band to its measurement error depending on the error of the reaction cross section. Evidently, the optimal target thickness for producing the maximum isotope activity at this energy is 300–350 μm .

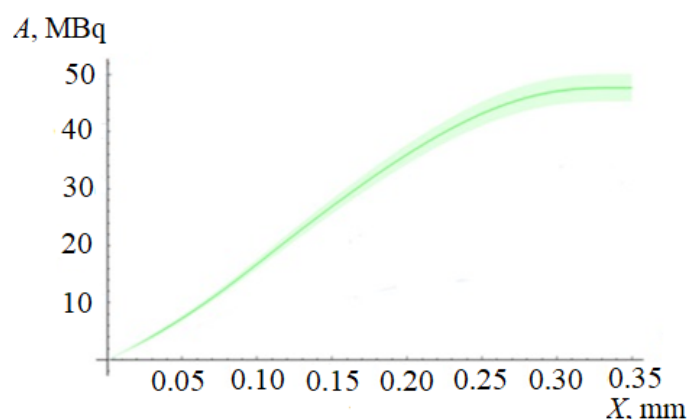


Fig. 3. Computed total activity of ^{64}Cu isotope depending on the thickness of the target made of natural nickel, irradiated by protons with an initial kinetic energy of 13 MeV (irradiation time was 3 h)

The computational results can be used to determine the activity of ^{64}Cu for a 300- μm -thick target irradiated for 3 hours with 13-MeV protons (beam current was 4 μA). The results indicate that the activity of ^{64}Cu amounted to 47 ± 3 MBq. It follows from statistical analysis of the measurement (30 ± 9 MBq) and the computation (47 ± 3 MBq) that the level achieved for the significance of the observed deviation between the computational and measurement results is 0.07 (7%). The achieved level of significance is the probability that the deviation between the computation and measurement due to statistical fluctuations reaches 7% for testing the null hypothesis. The hypothesis is that the observed difference between the computational and measurement data is associated with statistical fluctuations; the level of significance achieved should then be compared with the level of significance chosen in practice to be 0.05. Since the achieved significance level of 0.07 exceeds 0.05, the null hypothesis is confirmed, i.e., the observed difference is indeed associated with statistical fluctuations. Thus, the computed and measured results are in agreement at a significance level of 0.05. We can thus argue that the experimental data agree well with the computational results.

Conclusion

This paper describes the procedure for producing the ^{64}Cu isotope at the MGC-20 cyclotron. Three foils made of natural nickel were irradiated with a 13-MeV proton beam and subsequently subjected to radiochemical processing. The measured activity of the ^{64}Cu isotope was used to obtain the activity value at the end of irradiation, amounting to 30 ± 9 MBq. The computed activity of the ^{64}Cu isotope under conditions corresponding to the experimental ones amounted to 47 ± 3 MBq. The significance level achieved for the observed deviation of the computational result from the measurement was 0.07. Thus, we have established that the computed and measured results are in agreement at a significance level of 0.05, i.e., the agreement is good.

REFERENCES

1. **Gambhir S. S.**, Molecular imaging of cancer with positron emission tomography, *Nat. Rev. Cancer*. 2 (9) (2002) 683–693.
2. **Asabella A. N., Cascini G. L., Altini C., et al.**, The copper radioisotopes: A systematic review with special interest to ^{64}Cu , *BioMed Res. Int.* 2014 (May) (2014) 786463.
3. **Amiot M. N., Be M. M., Branger T., et al.**, Standardization of ^{64}Cu using an improved decay scheme, *Nucl. Instr. Meth. Phys. Res. A*. 684 (21 August) (2012) 97–104.
4. **Anderson C. J., Riccardo F.**, Copper-64 radiopharmaceuticals for PET imaging of cancer: Advances in preclinical and clinical research, *Cancer Biother. Radiopharm.* 24 (4) (2009) 379–393.
5. **Holland J. P., Riccardo F., Anderson C. J., Lewis J. S.**, Copper-64 radiopharmaceuticals for oncologic imaging, *PET Clinics*. 4 (1) (2009) 49–67.
6. **Zhou Y., Li J., Xu X., et al.**, ^{64}Cu -based radiopharmaceuticals in molecular imaging, *Technol. Cancer Res. Treat.* 18 (February 14) (2019) 1533033819830758.
7. **Boschi A., Martini P., Janevik-Ivanovska E., Duatti A.**, The emerging role of copper-64 radiopharmaceuticals as cancer theranostics, *Drug Discov. Today*. 23 (8) (2018) 1489–1501.
8. **Chakravarty R., Chakraborty S., Dash A.**, $^{64}\text{Cu}^{2+}$ ions as PET probe: An emerging paradigm in molecular imaging of cancer, *Molecul. Pharmaceut.* 13 (11) (2016) 3601–3612.
9. **Xie Q., Zhu H., Wang F., et al.**, Establishing reliable Cu-64 production process: From target plating to molecular specific tumor micro-PET imaging, *Molecules*. 22 (4) (2017) 641.
10. **Szűcs Z., Takács S., Alirezapour B.**, Development of cost-effective method for production of ^{64}Cu from ^{nat}Ni , *J. Radioanal. Nucl. Chem.* 302 (2) (2014) 1035–1038.
11. **Aslam M. N., Sudár S., Hussain M., et al.**, Charged particle induced reaction cross section data for production of the emerging medically important positron emitter ^{64}Cu : A comprehensive evaluation, *Radiochim. Acta*. 97 (12) (2009) 669–686.
12. **Tiba A., Berdnikov Ya. A.**, Optimization of the copper-64 isotope production from natural nickel target at a cyclotron, *St. Petersburg Polytechnical State University Journal. Physics and Mathematics*. 14 (2) (2021) 81–89.
13. **Rosman K. J. R., Taylor P. D. P.**, Isotopic compositions of the elements, *Pure Appl. Chem.* 70 (1) (1998) 217–235.

СПИСОК ЛИТЕРАТУРЫ

1. **Gambhir S. S.** Molecular imaging of cancer with positron emission tomography // *Nature Reviews Cancer*. 2002. Vol. 2. No. 9. Pp. 683–693.
2. **Asabella A. N., Cascini G. L., Altini C., Paparella D., Notaristefano A., Rubini G.** The copper radioisotopes: A systematic review with special interest to ^{64}Cu // *BioMed Research International*. 2014. Vol. 2014. May. P. 786463.
3. **Amiot M. N., Be M. M., Branger T., Cassette P., Lepy M. C., Menesguen Y., DaSilva I.** Standardization of ^{64}Cu using an improved decay scheme // *Nuclear Instruments and Methods in Physics Research A*. 2012. Vol. 684. 21 August. Pp. 97–104.
4. **Anderson C. J., Riccardo F.** Copper-64 radiopharmaceuticals for PET imaging of cancer: Advances in preclinical and clinical research // *Cancer Biotherapy and Radiopharmaceuticals*. 2009. Vol. 24. No. 4. Pp. 379–393.
5. **Holland J. P., Riccardo F., Anderson C. J., Lewis J. S.** Copper-64 radiopharmaceuticals for oncologic imaging // *PET Clinics*. 2009. Vol. 4. No. 1. Pp. 49–67.

6. Zhou Y., Li J., Xu X., Zhao M., Zhang B., Deng S., Wu Y. ^{64}Cu -based radiopharmaceuticals in molecular imaging // *Technology in Cancer Research & Treatment*. 2019. Vol. 18. February 14. P. 1533033819830758.
7. Boschi A., Martini P., Janevik-Ivanovska E., Duatti A. The emerging role of copper-64 radiopharmaceuticals as cancer theranostics // *Drug Discovery Today*. 2018. Vol. 23. No. 8. Pp. 1489–1501.
8. Chakravarty R., Chakraborty S., Dash A. $^{64}\text{Cu}^{2+}$ ions as PET probe: An emerging paradigm in molecular imaging of cancer // *Molecular Pharmaceutics*. 2016. Vol. 13. No. 11. Pp. 3601–3612.
9. Xie Q., Zhu H., Wang F., Meng X., Ren Q., Xia Ch., Yang Zh. Establishing reliable Cu-64 production process: From target plating to molecular specific tumor micro-PET imaging // *Molecules*. 2017. Vol. 22. No. 4. P. 641.
10. Szűcs Z., Takács S., Alirezapour B. Development of cost-effective method for production of ^{64}Cu from ^{nat}Ni // *Journal of Radioanalytical and Nuclear Chemistry*. 2014. Vol. 302. No. 2. Pp. 1035–1038.
11. Aslam M. N., Sudár S., Hussain M., Malik A. A., Shah H. A., Qaim S. M. Charged particle induced reaction cross section data for production of the emerging medically important positron emitter ^{64}Cu : A comprehensive evaluation // *Radiochimica Acta*. 2009. Vol. 97. No. 12. Pp. 669–686.
12. Тиба А., Бердников Я. А. Оптимизация получения изотопа меди-64 из природного никеля на циклотроне // *Научно-технические ведомости СПбГПУ. Физико-математические науки*. 2021. Т. 14. № 2. С. 81–89.
13. Rosman K. J. R., Taylor P. D. P. Isotopic compositions of the elements // *Pure and Applied Chemistry*. 1998. Vol. 70. No. 1. Pp. 217–235.

THE AUTHORS

TIBA Ali

Peter the Great St. Petersburg Polytechnic University
29 Politechnicheskaya St., St. Petersburg, 195251, Russia
alitiba1991@gmail.com
ORCID: 0000-0003-1320-6166

KARASEOV Platon A.

Peter the Great St. Petersburg Polytechnic University
29 Politechnicheskaya St., St. Petersburg, 195251, Russia
platon.karaseov@spbstu.ru
ORCID: 0000-0003-2511-0188

BERDNIKOV Yaroslav A.

Peter the Great St. Petersburg Polytechnic University
29 Politechnicheskaya St., St. Petersburg, 195251, Russia
berdnikov@spbstu.ru
ORCID: 0000-0003-0309-5917

EGOROV Anatoliy A.

Peter the Great St. Petersburg Polytechnic University
29 Politechnicheskaya St., St. Petersburg, 195251, Russia
egorov.a@spbstu.ru
ORCID: 0000-0003-4936-6962

MIRONOVA Svetlana Yu.

Peter the Great St. Petersburg Polytechnic University
29 Politechnicheskaya St., St. Petersburg, 195251, Russia
Scaremonger@yandex.ru
ORCID: 0000-0003-2114-716X



СВЕДЕНИЯ ОБ АВТОРАХ

ТИБА Али — аспирант Высшей инженерно-физической школы Санкт-Петербургского политехнического университета Петра Великого.

195251, Россия, г. Санкт-Петербург, Политехническая ул., 29

alitiba1991@gmail.com

ORCID: 0000-0003-1320-6166

КАРАСЕВ Платон Александрович — доктор физико-математических наук, профессор Высшей инженерно-физической школы Санкт-Петербургского политехнического университета Петра Великого.

195251, Россия, г. Санкт-Петербург, Политехническая ул., 29

platon.karaseov@spbstu.ru

ORCID: 0000-0003-2511-0188

БЕРДНИКОВ Ярослав Александрович — доктор физико-математических наук, профессор Высшей школы фундаментальных физических исследований Санкт-Петербургского политехнического университета Петра Великого.

195251, Россия, г. Санкт-Петербург, Политехническая ул., 29

berdnikov@spbstu.ru

ORCID: 0000-0003-0309-5917

ЕГОРОВ Анатолий Юрьевич — ассистент Высшей школы фундаментальных физических исследований Санкт-Петербургского политехнического университета Петра Великого.

195251, Россия, г. Санкт-Петербург, Политехническая ул., 29

egorov.a@spbstu.ru

ORCID: 0000-0003-4936-6962

МИРОНОВА Светлана Юрьевна — инженер Научно-технологического комплекса «Ядерная физика» Санкт-Петербургского политехнического университета Петра Великого.

195251, Россия, г. Санкт-Петербург, Политехническая ул., 29

Scaremonger@yandex.ru

ORCID: 0000-0003-2114-716X

Received 04.04.2022. Approved after reviewing 26.04.2022. Accepted 26.04.2022.

Статья поступила в редакцию 04.04.2022. Одобрена после рецензирования 26.04.2022. Принята 26.04.2022.

Original article

DOI: <https://doi.org/10.18721/JPM.15207>

ANALYSING THE EFFECT OF A CRANIUM THICKNESS ON A BRAGG PEAK RANGE IN THE PROTON THERAPY: A TRIM AND GEANT4 BASED STUDY

F. Ekinici¹✉, E. Bostanci², M. S. Güzel², Ö. Dağlı¹

¹ Gazi University, Ankara, Turkey,

² Ankara University, Ankara, Turkey

✉ fatih.ekinci2@gazi.edu.tr

Abstract. Cancer treatment with proton therapy, starting in 1946, continues with the treatment of 200,000 patients worldwide as of 2020. The energy release of protons in tissue and tissue equivalent (water) material is shown by Bragg curves. The main reason why proton beams are preferred in radiotherapy is that the proton beams continue on their way by giving maximum energy to the tissue to be treated and giving the least damage to the healthy tissue. In this study, with the help of Monte Carlo-based GEANT4 and TRIM simulation programs, Bragg peak positions in the 60 – 130 MeV energy range are given for water and brain by using the relativistic Bethe – Bloch equation. The difference between GEANT4 and TRIM was 7.4 % on average in the water phantom, while the difference was 7.6 % in the brain phantom. Bragg peak position was calculated for water and brain phantoms at 0.6, 0.8 and 1.0 cm thicknesses, which is suitable for the average thickness of the cortical bone in the skull. An average of 8.1 and 7.8 % deviations were detected between the two simulation systems in the cortical bony, water and brain phantoms with three different thicknesses. The values found were compared with the clinical studies available in the literature.

Keywords: Monte Carlo, GEANT4, TRIM, radiation therapy, proton therapy, LET

Citation: Ekinici F., Bostanci E., Güzel M. S., Dağlı Ö., Analysing the effect of a cranium thickness on a Bragg peak range in the proton therapy: a TRIM and GEANT4 based study, St. Petersburg State Polytechnical University Journal. Physics and Mathematics. 15 (2) (2022) 64–78. DOI: <https://doi.org/10.18721/JPM.15207>

This is an open access article under the CC BY-NC 4.0 license (<https://creativecommons.org/licenses/by-nc/4.0/>)



Научная статья

УДК 615.849.12

DOI: <https://doi.org/10.18721/JPM.15207>

АНАЛИЗ ВЛИЯНИЯ ТОЛЩИНЫ ТКАНЕЙ ЧЕЛОВЕЧЕСКОГО ЧЕРЕПА НА ДИАПАЗОН ПИКОВ БРЭГГА ПРИ ПРОТОННОЙ ТЕРАПИИ С ПОМОЩЬЮ ПРОГРАММ TRIM И GEANT4

Ф. Экинджи ^{1✉}, Э. Бостанджи ², М. С. Гузель ², О. Дагли ¹

¹ Университет Гази, г. Анкара, Турция;

² Университет Анкары, г. Анкара, Турция

✉ fatih.ekinci2@gazi.edu.tr

Аннотация. Лечение рака с помощью протонной терапии, начатое в 1946 году, продолжает развиваться по всему миру, и, например, в 2020 г. этот метод применяли у 200 тыс. пациентов. Энерговыведение протонов в человеческой ткани и тканевом эквиваленте (воде) контролируется кривыми Брэгга. Преимущество протонных лучей заключается в том, что они отдают максимальную энергию обрабатываемой ткани, проникая вглубь, и при этом наносят минимальный ущерб здоровым тканям. В данном исследовании представлены позиции пиков Брэгга в диапазоне энергий 60 – 130 МэВ для воды и мозга, полученные с помощью уравнения Бете – Блоха и программ моделирования GEANT4 и TRIM (основаны на методе Монте-Карло). Сравнение результатов, полученных через GEANT4 и TRIM, показало разницу в среднем 7,4 % для водного фантома и 7,6 % для мозгового. Положения пиков Брэгга были рассчитаны для фантомов воды и мозга при значениях толщины тканей 0,6, 0,8 и 1,0 см, что соответствует средней толщине коркового слоя черепной кости. Значения отклонений между двумя системами моделирования, составили в среднем 8,1 и 7,8 % для двух фантомов (три значения толщины тканей). Полученные в работе расчетные значения были сопоставлены с данными опубликованных клинических исследований.

Ключевые слова: метод Монте-Карло, GEANT4, TRIM, лучевая терапия, протонная терапия, LET

Для цитирования: Экинджи Ф., Бостанджи Э., Гузель М. С., Дагли О. Анализ влияния толщины тканей человеческого черепа на диапазон пиков Брэгга при протонной терапии с помощью программ TRIM и GEANT4 // Научно-технические ведомости СПбГПУ. Физико-математические науки. 2022. Т. 15. № 2. С. 64–78. DOI: <https://doi.org/10.18721/JPM.15207>

Статья открытого доступа, распространяемая по лицензии CC BY-NC 4.0 (<https://creativecommons.org/licenses/by-nc/4.0/>)

Introduction

Heavy ion beams have been the focus of radiation oncology for over 60 years due to their superior physical and biological properties compared to conventional high-energy photon beams [1]. Protons are currently used in more than 61 facilities worldwide [2], there are 16 centers in clinical operation in Europe, and many centers are under construction [3]. A single energy heavy ion beam releases most of its energy in a narrow depth range known as the Bragg peak, with the peak dose depth determined by the ion species and target properties [4]. Due to the narrow depth range of the Bragg peak, minimal lateral scattering [5, 6] combined with the high relative biological activity of heavy ions, heavy ion therapy provides a therapeutic dose that is well suited for the target volume, with an input dose much lower than it is possible with photon therapy [7]. Heavy-ion beams minimize damage to adjacent healthy tissues, which is particularly useful for treating deeply located tumors [4, 7]. However, due to large dose gradients, deviations between the treatment plan and the delivered dose distribution can have serious adverse effects on healthy tissue, especially if the treatment site is close to the organ at risk. Accurate, real-time measurement of dose distribution during irradiation minimizes errors between the treatment plan and the actual delivered dose [7]. The success of heavy ion therapy depends on accurate dose measurement and dosimetric accuracy obtained with the help of semi-analytical pencil beam algorithms [8].

Regarding the accuracy in dose measurement, general purpose Monte Carlo (MC) codes are considered the "gold standard" [9]. Different MC simulation codes are used in proton therapy centers to improve dose estimations over standard methods using analytical or semi-empirical dose algorithms [10 – 14]. Potentially adopting systematic and user-friendly use of general-purpose MC tools for quality assurance (QA) and research requires reliable as well as generally applicable interfaces for connecting MC tools and incorporating them into the radiation oncology workflow [15]. GEANT4 and TRIM MC simulation codes are used in proton therapy applications to compare energy distributions in simple water phantoms, phantoms with complex structures, and phantoms with voxelized geometry based on clinical CT data [16]. An advantage of using Geant4 and TRIM is that both are based on the MC method, which can yield the secondary knock-on atom (SKA) energy spectrum of a composite material or alloy, whereas the analytical INtegrated model for Competitiveness Assessment of SMRs (INCAS) code only describes cascades in pure metal [17]. Another advantage is that Geant4 and TRIM provide the spatial distribution of displacements [20]. In other words, the effect of neutron spectrum and dispersion or material shape on the distributions of defects and production rates can be simulated using this method [17].

In this study, the Bragg curves formed by the proton beam in both a homogeneous water phantom and a heterogeneous one such as the brain were confirmed by experimental and computational studies in the literature with the help of frequently used GEANT4 and TRIM MC simulation systems. The behavior of the therapeutic proton beam was found with the help of two simulation systems in the presence of 0.6, 0.8 and 1.0 cm thick cortical bone placed in front of both the water phantom and brain one. All the data from the two simulation systems were compared.

Materials and methods

Monte Carlo (MC) codes are a simulation technique developed for highly accurate solutions of analytically complex problems in dose measurements [9]. So the MC is capable of following and calculating all interactions of particles within the target [18]. One of these simulation systems is the TRIM (TRANsport of Ions in Matter) simulation program. Parameters such as the type of targeted particle beam, the particle number, energy, the structural and geometric properties of the target, the angle of incidence of the particle beam at the target and the probability number can be entered from the TRIM screen. TRIM saves and displays all calculation fields. TRIM calculates and tabulates all kinetic events related to the interaction processes of ions with the target, such as damage, scattering, ionization, phonon production and recoil [19]. The displacement of the target atoms caused by the collision cascades and the cavities occurring in the target crystal structure are calculated in detail. The number of displacement collisions of the target atoms indicates how many target atoms are activated at energies above the displacement energy. The spaces left behind when the recoil atom leaves its original region are called target spaces. A vacuum does not occur unless a moving atom hits the target's stationary atom and transfers enough energy to displace it [19, 20]. The "Detailed Calculation with Full Damage Cascades" type option was selected in the calculations from the display window of the TRIM program. The particle number of the heavy ion

beam was entered as 106 particles in the “Total Number of Ions” tab. Calculation outputs were declared in the "Output disk files" tab, and the ion range, recoils, sputtered atoms and collision details output files were selected. The phantom type was created in the "Compound Dictionary" tab and its geometry was created in the "Add New Layer" section.

The GEANT4 (GEometry ANd Tracking, version 4) is an MC-based simulation program, capable of simulating all interactions of the ions passing through the material in the target. GEANT4 consists of two user classes, “Mandatory Classes” and “Action Classes”, in simulation software [21]. In this study, mandatory classes G4V User Detector Construction, G4V User Primary Generator Action and G4V User Physics List were used. As for the action classes, G4 User Run Action, G4 User Event Action, G4 User Stacking Action, G4 User Tracking Action and G4 User Stepping Action classes were used. The simulation detector is designed as a cube-shaped ion chamber with an edge length of 1 cm and quenching gas Ar. The step range (Range cut) was taken as 0.01 cm.

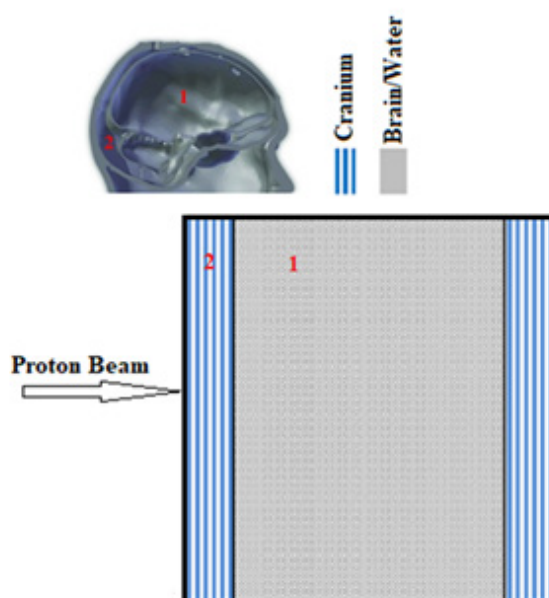


Fig. 1. The phantom cross-section geometry:
1 – water or brain, 2 – cranium; section 2 is removed only for brain and water measurements

Table 1

The main information about biomaterials used in the cross-section phantom [25, 26]

Biomaterial	Atomic percentage, %	Atomic density, 10^{22} atom/cm ³	Density, g/cm ³
Cranium	H 3.4; O 43.5; C 15.5; N 4.2; S 0.3; Ca 22.5; P 10.3; Mg 0.2	9.946	1.92
Brain	H 10.7; C 14.5; N 2.2; O 71.2; Cl 0.3; Na 0.2; P 0.4; S 0.2; K 0.2	8.879	1.04
Water	H 66.6; O 33.3	10.020	1.00

The most important problem for radiotherapy is whether the desired dose can be delivered to the target point correctly. To this end, attempts were made to determine and calibrate the correct dose using the water phantom before radiation therapy [19]. Since the basic component of the human body is water, it is the most important material frequently used in the field of medical physics. Reliability of dose and LET calculations for the water target and accurate calculation of their distribution are reliable for patient treatments. In this regard, the structure, shape and design of the phantom to be used are important. In the literature, some phantom types used in treatment planning for different regions and organs of the human body in radiotherapy applications are described [22]. Plate and cylindrical phantoms are actively used to investigate dose or LET distribution and the factors affecting them [23]. For this reason, the phantom of the skull was used in the study (see its cross-section in Fig. 1). First, a phantom consisting only of water and brain tissues was used. Next, we took a cranial section of 0.6, 0.8 and 1.0 cm thick in the horizontal direction from left to right, and then a head half section containing enough water and brain tissue to reach a total thickness of 15 cm. Densities and basic compositions of tissues are given in Table 1. The TRIM simulation program determined these percentages according to the ICRU-276 report [24]. In the Geant4 simulation program, it was obtained from the Geant4 library (such as G4_WATER, G4_BRAIN_ICRP) [21].

Table 2

**Bragg peaks for proton beams with different energies
in the water phantom: comparison with RPTC experimental data [36]**

Energy, MeV	TRIM (<i>a</i>)	GEANT (<i>b</i>)	RPTC (<i>c</i>)	Difference	
				(<i>a</i>) – (<i>c</i>)	(<i>b</i>) – (<i>c</i>)
90	6.21	5.65	5.50	0.71	0.15
100	7.26	6.98	6.83	0.43	0.15
110	9.00	8.70	8.28	0.72	0.42
120	10.50	10.18	9.80	0.70	0.38
130	12.00	11.65	11.45	0.55	0.20

Table 3

**Calculation results for Bragg peak points produced by proton beams
with different energies in the water phantom (using TRIM and GEANT4
simulation) and percentage differences**

Energy, MeV	TRIM (<i>a</i>)	GEANT (<i>b</i>)	Difference, % (<i>a</i>) – (<i>b</i>)
60	2.82	2.42	14.18
70	3.91	3.41	12.79
80	5.01	4.52	9.78
90	6.21	5.65	9.02
100	7.26	6.98	3.86
110	9.00	8.70	3.33
120	10.5	10.18	3.05
130	12.00	11.65	2.92

In this study, cross-section phantom was used. The main motivation for using this phantom was to explore the effect of ionization of the proton beam when its passing through different layers of biomaterials. It is very difficult to process this research data in two different simulation systems using the same input directory. An account must be taken of the facts that TRIM only allows a single or multi-layer structured phantom, creates difficulties for 3D computation, and finally, such a computation will not make a significant contribution to achieving the goal of the study. For this reason, calculations were made only in 1D single and multi-layer structures.

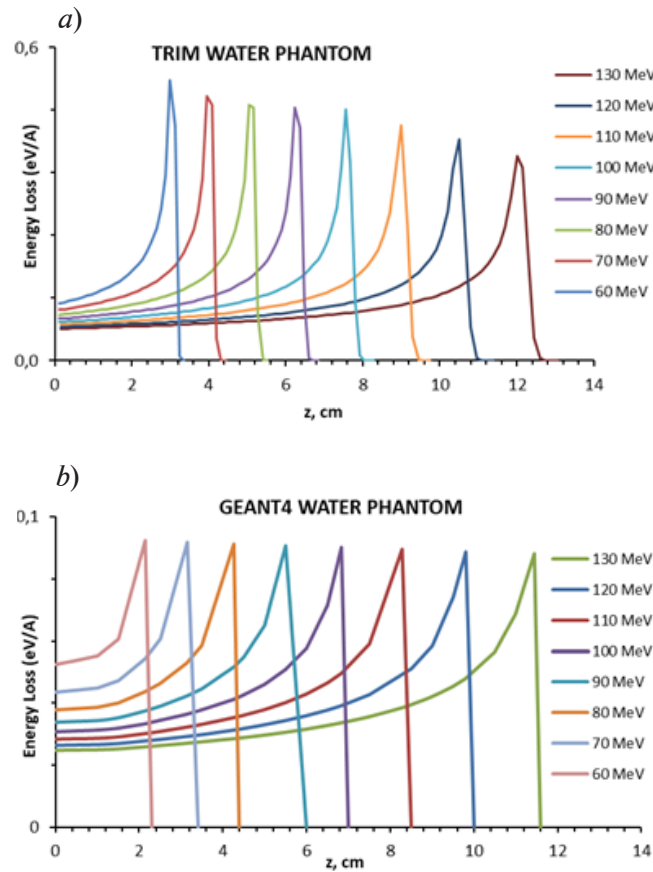


Fig. 2. Representation of Bragg curves for a 60 – 130 MeV proton beam in the water phantom from TRIM (a) and GEANT4 (b) simulation programs

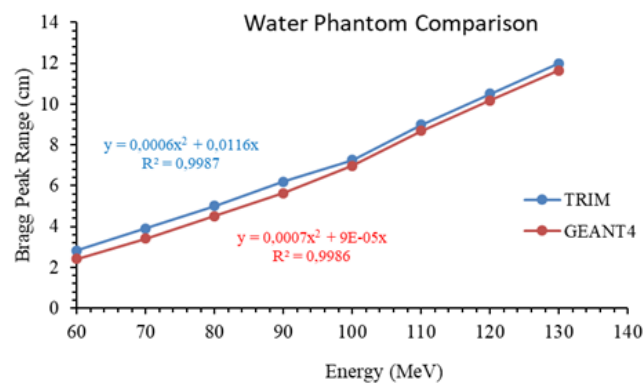


Fig. 3. Comparison of Bragg peaks for proton beams with different energies sent to the water phantom in two simulation systems

Table 4

Calculation results for Bragg peaks produced in the brain phantom by proton beams with different energies (TRIM and GEANT4 simulations were used) and percentage differences

Energy, MeV	TRIM (a)	GEANT (b)	Difference, % (a) – (b)
60	2.85	2.47	13.33
70	4.01	3.51	12.47
80	5.11	4.55	10.96
90	6.33	5.72	9.64
100	7.37	7.03	4.61
110	9.24	8.91	3.57
120	10.68	10.31	3.46
130	12.35	12.04	2.51

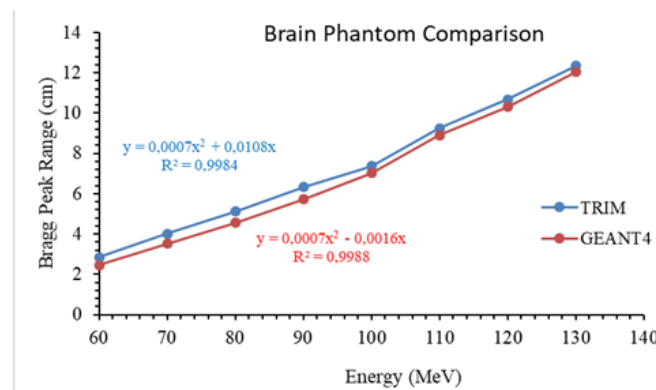


Fig. 4. Comparison of Bragg peaks produced in the brain phantom by proton beams with different energies (the two simulation codes were used)

Results

In this study, the effect of ionization interactions of protons passing through single or multiple layers on Bragg peak point was investigated for a cross-section phantom. The energy transferred per unit length of the proton beam to the layer or layers was taken into account. Therefore, the energy stored by the layer or layers per mass did not matter. In this connection, it was repeated in both simulation systems, taking into account the LET calculation. The Bragg peak positions (normalized to the maximum dose) for the water phantom irradiated by proton beams with different energies, in comparison with the experimental dose measurements of the Germany Rinecker Proton Therapy Center (RPTC) [27] are presented in Table 2. An average difference of 0.62 cm between RPTC and TRIM and that of 0.26 cm between RPTC and GEANT4 was found in the 90–130 MeV energy range.

Bragg peak points produced by the proton beams in the water phantom and obtained using TRIM and GEANT4 simulations are given in Table 3 and Figs. 2 and 3. As the energy of the proton beam increased, the difference between the Bragg peaks measured in the two simulation systems approached the difference ($\leq 5\%$) acceptable in medical physics. An average difference of 7.37 % difference was found for all proton beam energies between the two simulation systems.

The largest difference was observed for the proton beam of 60 MeV and the smallest one was for the proton beam of 130 MeV. It was established that there was an average difference of 0.4 cm between the two simulation systems. This result is considered to be reasonable and acceptable.

Table 4 and Fig. 4 present Bragg peak points produced by the proton beams in the brain



Table 5

Calculation results for Bragg peaks produced in the *water phantom* with different cortical bone thicknesses by proton beams (the two simulation systems were used) and their differences

W , MeV	Cortical bone thickness for water phantom						Difference		
	0.6 cm		0.8 cm		1.0 cm				
	TRIM (a)	GEANT4 (b)	TRIM (c)	GEANT4 (d)	TRIM (e)	GEANT4 (f)	(a)–(b)	(c)–(d)	(e)–(f)
60	2.65	2.28	2.53	2.19	2.38	2.06	$\frac{0.37}{13.96\%}$	$\frac{0.34}{13.44\%}$	$\frac{0.32}{13.45\%}$
70	3.59	3.12	3.48	3.04	3.36	2.93	$\frac{0.47}{13.09\%}$	$\frac{0.44}{12.64\%}$	$\frac{0.43}{12.80\%}$
80	4.68	4.21	4.58	4.09	4.48	3.97	$\frac{0.47}{10.04\%}$	$\frac{0.49}{10.70\%}$	$\frac{0.51}{11.38\%}$
90	5.93	5.34	5.85	5.26	5.58	5.02	$\frac{0.59}{9.95\%}$	$\frac{0.59}{10.09\%}$	$\frac{0.56}{10.04\%}$
100	7.18	6.53	7.11	6.41	6.88	6.24	$\frac{0.65}{9.05\%}$	$\frac{0.70}{9.85\%}$	$\frac{0.64}{9.30\%}$
110	8.58	8.24	8.53	8.18	8.32	8.02	$\frac{0.34}{3.96\%}$	$\frac{0.35}{4.10\%}$	$\frac{0.30}{3.61\%}$
120	10.14	9.85	9.95	9.65	9.79	9.48	$\frac{0.29}{2.86\%}$	$\frac{0.30}{3.02\%}$	$\frac{0.31}{3.17\%}$
130	11.71	11.51	11.53	11.45	11.36	11.28	$\frac{0.20}{1.71\%}$	$\frac{0.08}{0.69\%}$	$\frac{0.08}{0.70\%}$

Notation: W is the proton beam energy.

phantom. These results were obtained in accordance with the parameters given in Table 1 and by using the TRIM and GEANT4 simulations.

As the energy of the proton beam increased, the difference between the Bragg peaks measured in the two simulation systems approached the difference ($\leq 5\%$) acceptable in medical physics. An average difference of 7.57 % was found between the two simulation codes for all proton beam energies. The largest difference occurred in the proton beam of 60 MeV and the smallest one did in the proton beam of 130 MeV. An average difference of 0.43 cm between the two simulation systems was obtained. These results are considered to be reasonable and acceptable.

In the phantom geometry of the head section (see Fig. 1), the section I is water; the cranium 2 was selected in three different thicknesses: of 0.6, 0.8 and 1.0 cm. Using TRIM and GEANT4 simulations, the Bragg peak points produced by the proton beams in the phantom were calculated (Table 5).

An analysis of the obtained results makes possible to conclude that the difference between the two simulation programs decreased as the energy of the proton beam increased in all three cranium thicknesses. The Bragg peak difference between the two simulation codes was 8 % on average for all three cranium thicknesses. The average Bragg peak difference between the two simulation codes was 0.42 cm at 0.6 cm cranium thickness, 0.41 cm at 0.8 cm cranium thickness and 0.39 cm at 1.0 cm cranium thickness. For 0.6 cm cranium thickness, an average difference of 0.28 cm was found in TRIM between the Bragg peaks (see Tables 4 and 5), while a difference of 0.30 cm was found in GEANT4. Similarly, an average difference of 0.39 cm in TRIM and of 0.41 cm in GEANT4 were found for 0.8 cm cranium thickness, 0.57 cm in TRIM and 0.56 cm in GEANT4 for 1.0 cm cranium thickness. The differences found in the two simulation codes were considered to be at an acceptable level.

In the phantom cross-section (see Fig. 1 again), the section (I) is the brain tissue and the cranium (2) was selected in three different thicknesses: of 0.6, 0.8 and 1.0 cm. The Bragg peaks produced by the proton beams in the brain phantom are given in Table 6 (TRIM and GEANT4 simulations

Table 6

Calculation results for Bragg peaks produced in the *brain phantom* with different cortical bone thicknesses by proton beams (the two simulation systems were used) and their differences

W , MeV	Cortical bone thickness for brain phantom						Difference		
	0.6 cm		0.8 cm		1.0 cm				
	TRIM (a)	GEANT4 (b)	TRIM (c)	GEANT4 (d)	TRIM (e)	GEANT4 (f)	(a)–(b)	(c)–(d)	(e)–(f)
60	2.65	2.26	2.52	2.18	2.40	2.08	$\frac{0.39}{14.72\%}$	$\frac{0.34}{13.49\%}$	$\frac{0.32}{13.33\%}$
70	3.58	3.10	3.48	3.05	3.32	2.95	$\frac{0.48}{13.41\%}$	$\frac{0.43}{12.36\%}$	$\frac{0.37}{11.15\%}$
80	4.68	4.22	4.57	4.07	4.46	3.98	$\frac{0.46}{9.83\%}$	$\frac{0.50}{10.94\%}$	$\frac{0.48}{10.76\%}$
90	5.92	5.35	5.84	5.26	5.49	5.04	$\frac{0.57}{9.63\%}$	$\frac{0.58}{9.93\%}$	$\frac{0.45}{8.20\%}$
100	7.17	6.54	7.12	6.41	6.86	6.25	$\frac{0.63}{8.79\%}$	$\frac{0.71}{9.97\%}$	$\frac{0.61}{8.89\%}$
110	8.56	8.25	8.51	8.19	8.29	8.05	$\frac{0.31}{3.62\%}$	$\frac{0.32}{3.76\%}$	$\frac{0.24}{2.90\%}$
120	10.12	9.84	9.94	9.66	9.76	9.49	$\frac{0.28}{2.77\%}$	$\frac{0.28}{2.82\%}$	$\frac{0.27}{2.77\%}$
130	11.69	11.53	11.52	11.44	11.32	11.27	$\frac{0.16}{1.37\%}$	$\frac{0.08}{0.69\%}$	$\frac{0.05}{0.44\%}$

Notation: W is the proton beam energy.

were used). Analyzing this data, it was seen that the difference between the two simulation programs decreased as the energy of the proton beam increased in all three cranium thicknesses. The average Bragg peak difference between the two simulation codes was 0.41 cm for 0.6 cm cranium thickness, 0.41 cm for 0.8 cm cranium thickness and 0.35 cm for 1.0 cm cranium thickness.

Discussion

In the presented study, the Bragg curves obtained by the virtual proton beams in the phantoms both homogeneous (the water) and heterogeneous (the brain) were confirmed by experimental data. The results obtained in the two simulation systems were found to be in agreement with the experimental data. It has been observed that the Bragg peak position formed by the proton beam in the energy range of 60 – 130 MeV is different from the water and brain phantom. This difference averages 0.15 cm for TRIM and 0.13 cm for GEANT4. Thus, it was seen in both simulation systems that the Bragg peak position formed by the proton beam was deeper in the brain phantom. The difference between the Bragg peak positions of the proton beam and TRIM and GEANT4 simulations; it was found to be 7.4 % in the water phantom and 7.6 % in the brain one. We believe that the difference arises from atomic collisions, since brain tissue contains different atoms. Further studies are needed to cover the entire range of beam energies, target thicknesses and target materials, mainly, for therapeutic applications in this area.

Experimental measurements are also required to compare Monte Carlo codes [28 – 32]. In a different study, where microdosimetric measurements of monoenergetic and modulated Bragg peaks of 62 MeV therapeutic proton beam were performed with a synthetic single crystal diamond microdosimeter, it was seen that the data of GEANT4 and TRIM [33] were comparable, as it was in our study. In another study with GEANT4 and TRIM, the ionizations of proton beams on different targets were examined, and it was seen that the results were close to each other similar to our results [34, 35].



In order to understand the behavior of the Bragg peak in cortical bone, being denser than the water and brain, the same calculations were repeated and compared using the selected TRIM and GEANT4 simulation programs. Thus, the Bragg peak positions formed in the water phantom (made with TRIM) and the cortical bony water phantom of three different thicknesses were compared. Average differences of 0.28 cm for 0.6 cm thickness, 0.39 cm for 0.8 cm thickness and 0.57 cm for 1.0 cm thickness were found. Comparing the Bragg peak positions in the water phantom simulated in GEANT4 by a similar method and in the water phantom of a cortical bone with three different thicknesses, we determined an average difference of 0.30 cm for 0.6 cm thickness, 0.41 cm for 0.8 cm thickness and 0.56 cm for 1.0 cm thickness.

Comparing TRIM and GEANT4 in water phantom and the cortical bony water phantom with three different thicknesses by the same method, we found an average difference of 0.42 cm for 0.6 cm thickness, an average difference of 0.41 cm for 0.8 cm thickness, and an average difference of 0.39 cm for 1.0 cm thickness. Then the brain phantom and the one with three different thicknesses of cortical bones were compared. The difference in 0.6 cm thickness was found to be 0.41 cm on average, the difference in 0.8 cm thickness was 0.41 cm on average, and the difference in 1.0 cm thickness was 0.35 cm on average. These differences were found to be 8.0 % on average. The calculations used in our studies include a probability due to the properties of the Monte-Carlo computing. Therefore, the calculations from the two simulation programs were consistent.

The effect of materials of different densities and thicknesses on the proton beam is important for proton therapy [36]. For this reason, the proton beam passing through the cooling materials of different thicknesses was investigated in Geant4 and TRIM MC simulation codes. The results of the available simulations were also compared with the calculation results based on the NIST PSTAR and CSDA models, and the differences were presented in the same way as in this publication [37]. In similar studies, particularly in the study of demonstrating this effect with different simulation systems, the results obtained by Geant4 were compared with those obtained by TRIM [36, 38]. The change exhibited by the proton beam in the presence of cortical bone of different thickness used for both phantoms was compared with previous data and showed a good agreement [5, 6, 14]. In addition, considering the advantages of the two simulation systems, the recoil interactions of the proton beams within the target were investigated. The obtained results were also compared in the same way as in this study [39]. The ion spacing was estimated using the TRIM code and was found to be compatible with that obtained by GEANT4 [40].

In the literature, some authors tried to find Bragg peak positions performing calculations of Bragg curves given by proton beams with 100, 120 and 130 MeV energies while their passing through the water phantoms, using different MC-based simulation programs (FLUKA, GATE, MCNPX, PTRAN and PHITS). Then they tried to compare the results obtained (similar to the procedure taken in our study). Bragg peak positions obtained in the literature were compared with the values determined in this study. In this comparison, an average difference of 4.1 % in TRIM and 7.5 % in GEANT4 was found for a proton beam with 100 MeV energy [41–46]. An average difference of 1.4 % in TRIM and 1.7 % in GEANT4 was found in the 120 MeV energy proton beam [41, 47]. An average difference of 6.7 % in TRIM and 3.9% in GEANT4 was found in the proton beam with 130 MeV energy [44]. It has been seen that this difference is due to the features of MC simulation, calculation parameters and statistical reasons such as probability.

Summary

Since there is no experimental heavy ion beam line, it was decided to use MC TRIM and GEANT4 simulation programs in this study. In keeping with the current approach, a water phantom was used to validate patient radiotherapy plans for heavy ion therapy. We report on MC TRIM and GEANT4 data on LET values of four new proton beams in water and brain phantoms with energies ranging from 60 to 130 MeV/u in increments of 10 MeV and in cortical bony water and brain phantoms of different thicknesses (0.6, 0.8 and 1.0 cm). These values were compared with hospital data and other studies in the literature. It has been suggested to be repeated in Teflon, titanium alloys ($\text{Ti}_6\text{Al}_4\text{V}$ and Nital) and Al_2O_3 ceramic alloys [15], which give the closest results to bone among the biomaterials used instead of cortical bone. In these studies, recoil effects, besides ionization, were considered and compared using the TRIM and GEANT4 simulation system.

REFERENCES

1. **Durante M., Loeffler J. S.**, Charged particles in radiation oncology. *Nature Rev. Clin. Oncol.* 7 (1) (2010) 37–43.
2. Particle therapy co-operative group (PTCOG). An organization for those uninterested in proton, light ion and heavy charged particle radiotherapy. URL: <https://www.ptcog.ch/>. Accessed: 2019-10-10.
3. **Kozłowska W. S., Böhlen T. T., Cuccagna C., et al.**, FLUKA particle therapy tool for Monte Carlo independent calculation of scanned proton and carbon ion beam therapy, *Phys. Med. Biol.* 64 (7) (2019) 075012.
4. **Schardt D., Elsässer T., Schulz-Ertner D.**, Heavy-ion tumor therapy: Physical and radiobiological benefits, *Rev. Mod. Phys.* 82 (1) (2010) 383–425.
5. **Senirkentli G. B., Ekinci F., Bostanci E., Güzel M. et al.**, Proton therapy for mandibula plate phantom, *Healthcare.* 9 (2) (2021) 167.
6. **Ekinci F., Bostanci E., Dağlı Ö., Güzel M. S.**, Analysis of Bragg curve parameters and lateral straggle for proton and carbon beam, *Commun. Fac. Sci. Univ. Ank., Ser. A2–A3.* 63 (1) (2021) 32–41.
7. **Chacon A., Safavi-Naeini M., Bolst D., et al.**, Monte Carlo investigation of the characteristics of radioactive beams for heavy ion therapy, *Sci. Rep.* 9 (1) (2019) 6537.
8. **Hong L., Goitein M., Bucciolini M., et al.**, A pencil beam algorithm for proton dose calculations, *Phys. Med. Biol.* 41 (8) (1996) 1305–1330.
9. **Rogers D. W. O.**, Fifty years of Monte Carlo simulations for medical physics, *Phys. Med. Biol.* 51 (13) (2016) R287–R301.
10. **Baiocco G., Barbieri S., Babini G., et al.**, The origin of neutron biological effectiveness as a function of energy, *Sci. Rep.* 6 (September) (2016) 34033.
11. **Kajimoto T., Tanaka K., Endo S., et al.**, Double differential cross sections of neutron production by 135 and 180 MeV protons on A-150 tissue-equivalent plastic, *Nucl. Instr. Meth. Phys. Res. B.* 487 (2021) 38–44.
12. **Kurosu K., Das I. J., Moskvina V. P.**, Optimization of GATE and PHITS Monte Carlo code parameters for spot scanning proton beam based on simulation with FLUKA general-purpose code, *Nucl. Instr. Meth. Phys. Res. B.* 367 (2016) 14–25.
13. **Lund C. M., Famulari G., Montgomery L., Kildea J.**, A microdosimetric analysis of the interactions of mono energetic neutrons with human tissue, *Physica Medica.* 73 (May) (2020) 29–42.
14. **Ekinci F., Bölükdemir M. H.**, The effect of the second peak formed in biomaterials used in a slab head phantom on the proton Bragg peak, *J. Polytech.* 23 (1) (2019) 129–136.
15. **Augusto R. S., Bauer J., Bouhali O., et al.**, An overview of recent developments in FLUKA PET TOOLS, *Physica Medica.* 54 (October) (2018) 189–199.
16. **Titt U., Bednarz B., Paganetti H.**, Comparison of MCNPX and Geant4 proton energy deposition predictions for clinical use, *Phys. Med. Biol.* 57 (20) (2012) 6381–6393.
17. **Wu J.-C., Feng Q.-J., Liu X.-K., et al.**, A combination method for simulation of secondary knock-on atoms of boron carbide induced by neutron irradiation in SPRR-300, *Nucl. Instr. Meth. Phys. Res. B.* 368 (1 February) (2016) 1–4.
18. **Ogilvy C. S., Stieg Ph. E., Awad I., et al.**, Recommendations for the management of intracranial arteriovenous malformations, *Stroke.* 32 (6) (2001) 1458–1471.
19. **Shaller C., Schramm J., Huan D.**, Significance of factors contributing to surgical complications and to late outcome after elective surgery of cerebral arteriovenous malformations, *J. Neurol. Neurosurg. Psychiatr.* 65 (4) (1998) 547–554.
20. **Ogilvy C. S.**, Radiation therapy for arteriovenous malformations: a review, *Neurosurg.* 26 (5) (1990) 725–735.
21. Geant4. URL: <http://www.geant4.org/geant4/>, Son Erişim Tarihi: 20.04.2016.
22. **Jafar J. J., Davis A. J., Berenstein A., et al.**, The effect of embolization with N-butyl cyanoacrylate prior to surgical resection of cerebral arteriovenous malformations, *J. Neurosurg.* 78 (1) (1993) 60–69.
23. **Behrens R., Hupe O.**, Influence of the phantom shape (slab, cylinder or Alderson) on the performance of an Hp(3) eye dosimeter, *Rad. Protect. Dosim.* 168 (4) (2015) 441–449.
24. **Van Rooij W. J., Sluzewski M., Beute G. N.**, Brain AVM embolization with Onyx, *Am. J. Neurorad.* 28 (1) (2007) 172–178.
25. **Ziegler J. F.** SRIM – The stopping and range of ion in matter (2007). URL: <https://www.srim.org/> Accessed: 20.09.2019.



26. ICRU-1992: Photon, electron, proton and neutron interaction data for body tissues, Report 46 of The International Commission on Radiation Units and Measurements (ICRU), National Bureau of Standards, USA: US Department of Commerce, 1992.
27. Rinecker Proton Therapy Center (RPTC), Munich, Germany. URL: <https://www.rptc.de/en/home.html>. Son Ulaşım: 20 Aralık 2017.
28. **Battistoni G., Cerutti F., Fassò A., et al.**, The FLUKA code: description and benchmarking, AIP Conf. Proc. 896 (2007) 31–49.
29. **Mairani A.**, Nucleus-nucleus interaction modelling and applications in ion therapy treatment planning, PhD Thesis, Univesity of Pavia, Italy (2017).
30. **Böhlen T. T., Cerutti F., Chin M. P. W., et al.**, The FLUKA code: Developments and challenges for high energy and medical applications, Nucl. Data Sheets. 120 (June) (2014) 211–214.
31. **Dudouet J., Cussol D., Durand D., Labalme M.**, Benchmarking GEANT4 nuclear models for hadron therapy with 95 MeV/nucleon carbon ions, Phys. Rev. C. 89 (5) (2014) 054616.
32. **Aricò G., Gehrke T., Gallas R., et al.**, Investigation of single carbon ion fragmentation in water and PMMA for hadron therapy, Phys. Med. Biol. 64 (5) (2019) 055018.
33. **Verona C., Cirrone G. A. P., Magrin G., et al.**, Microdosimetric measurements of a monoenergetic and modulated Bragg peaks of 62 MeV therapeutic proton beam with a synthetic single crystal diamond microdosimeter, Med. Phys. 47 (11) (2020) 5791–5801.
34. **Wu Z., Chen S.**, Heavy ion, proton and neutron charge deposition analyses in several semiconductor materials, IEEE Trans. Nucl. Sci. 65 (8) (2018) 1791–1799.
35. **Du Q., Lin S. T., He H. T., et al.**, Response of gadolinium doped liquid scintillator to charged particles: measurement based on intrinsic U/Th contamination, J. Instrum. 13 (4) (2018) P04001.
36. **Mastromarco M., Digennaro A., Mazzone A., et al.**, Proton boron capture therapy: Dose calculations and a possible new measurement, RAD Conf. Proc. 4 (2020) 185–189.
37. **Yevseyeva O., de Assis J., Yevseev I., et al.**, Comparison of GEANT4 simulations with experimental data for thick Al absorbers, AIP Conf. Proc. 1139 (2009) 97–101.
38. **Liu T. Q., Lic D. Q., Caic C., et al.**, Heavy ion track straggling effect in single event effect numerical simulation of 3D stacked devices, Microelectr. Rel. 114 (November) (2020) 113853.
39. **Zheng Y., Zheng J., Wang X.**, Study on the applicability of neutron radiation damage method used for high-temperature superconducting tape based on Geant4 and SRIM, Sci. Technol. Nucl. Instal. (24 November) (2021) ID 2839746.
40. **Parida M. K., Prabakar K., Prasanna G., Sundari S. T.**, Efficiency of boric acid coated semiconductor neutron detector – A GEANT4 simulation study, In: Proc. The 14th IEEE India Council International Conference (INDICON), 2017. doi:10.1109/indicon.2017.8487978.
41. **Schwarz M.**, Treatment planning in proton therapy, Europ. Phys. J. Plus. 126 (7) (2011) 67.
42. **Jia X., Schümann, J., Paganetti, H., ve Jiang S. B.**, GPU-based fast Monte Carlo dose calculation for proton therapy, Phys. Med. Biol. 57 (23) (2012) 7783.
43. **Yang Z. Y., Tsai P. E., Lee S. C., et al.**, Inter-comparison of dose distributions calculated by FLUKA, GEANT4, MCNP, and PHITS for proton therapy, Europ. Phys. J., Web of Conf. 153 (2017) 04011.
44. **Jia S. B., Hadizadeh M. H., Mowlavi A. A., ve Loushab M. E.**, Evaluation of energy deposition and secondary particle production in proton therapy of brain using a slab head phantom, Rep. Pract. Oncol. Radiother. 19 (6) (2014) 376–384.
45. **Sterpin E., Sorriaux J., Vynckier S.**, Extension of PENELOPE to protons: Simulation of nuclear reactions and benchmark with Geant4, Med. Phys. 40 (11) (2013) 111705.
46. **Grimes D. R., Warren D. R., Partridge M.**, An approximate analytical solution of the Bethe equation for charged particles in the radiotherapeutic energy range, Sci. Rep. 7 (1) (2017) 9781.
47. **Almhagen E.**, Development and validation of a scanned proton beam model for dose distribution verification using Monte Carlo, Thesis for Master of Science in Medical Radiation Physics. (2015) 48–49.

СПИСОК ЛИТЕРАТУРЫ

1. **Durante M., Loeffler J. S.** Charged particles in radiation oncology // *Nature Reviews Clinical Oncology*. 2010. Vol. 7. No. 1. Pp. 37–43.
2. Particle therapy co-operative group (PTCOG). An organization for those uninterested in proton, light ion and heavy charged particle radiotherapy. URL: <https://www.ptcog.ch/>. Accessed: 2019-10-10.
3. **Kozłowska W. S., Böhlen T. T., Cuccagna C., Ferrari A., Fracchiolla F., Magro G., Mairani A., Schwarz M., Vlachoudis V., Georg D.** LUKA particle therapy tool for Monte Carlo independent calculation of scanned proton and carbon ion beam therapy // *Physics in Medicine & Biology*. 2019. Vol. 64. No. 7. P. 075012.
4. **Schardt D., Elsässer T., Schulz-Ertner D.** Heavy-ion tumor therapy: Physical and radiobiological benefits // *Review of the Modern Physics*. 2010. Vol. 82. No. 1. Pp. 383–425.
5. **Senirkentli G. B., Ekinci F., Bostanci E., Güzel M. S., Dağlı Ö., Karim A. M., Mishra A.** Proton therapy for mandibula plate phantom // *Healthcare*. 2021. Vol. 9. No. 2. P. 167.
6. **Ekinci F., Bostanci E., Dağlı Ö., Güzel M. S.** Analysis of Bragg curve parameters and lateral straggle for proton and carbon beam // *Communications Faculty of Sciences University of Ankara. Ser. A2–A3*. 2021. Vol. 63. No. 1. Pp. 32–41.
7. **Chacon A., Safavi-Naeini M., Bolst D., et al.** Monte Carlo investigation of the characteristics of radioactive beams for heavy ion therapy // *Scientific Reports*. 2019. Vol. 9. No. 1. P. 6537.
8. **Hong L., Goitein M., Bucciolini M., Comiskey R., Gottschalk B., Rosenthal S., Serago C., Urie M.** A pencil beam algorithm for proton dose calculations // *Physics in Medicine & Biology*. 1996. Vol. 41. No. 8. Pp. 1305–1330.
9. **Rogers D. W. O.** Fifty years of Monte Carlo simulations for medical physics // *Physics in Medicine & Biology*. 2006. Vol. 51. No. 13. Pp. R287–R301.
10. **Baiocco G., Barbieri S., Babini G., et al.** The origin of neutron biological effectiveness as a function of energy // *Scientific Reports*. 2016. Vol. 6. September. P. 34033.
11. **Kajimoto T., Tanaka K., Endo S., Kamada S., Tanaka H., Takada M., Hamano T.** Double differential cross sections of neutron production by 135 and 180 MeV protons on A-150 tissue-equivalent plastic // *Nuclear Instruments and Methods in Physics Research B: Beam Interactions with Materials and Atoms*. 2021. Vol. 487. Pp. 38–44.
12. **Kurosu K., Das I. J., Moskvina V. P.** Optimization of GATE and PHITS Monte Carlo code parameters for spot scanning proton beam based on simulation with FLUKA general-purpose code // *Nuclear Instruments and Methods in Physics Research B*. 2016. Vol. 367. Pp. 14–25.
13. **Lund C. M., Famulari G., Montgomery L., Kildea J.** A microdosimetric analysis of the interactions of mono energetic neutrons with human tissue // *Physica Medica*. 2020. Vol. 73. May. Pp. 29–42.
14. **Ekinci F., Bölükdemir M. H.** The effect of the second peak formed in biomaterials used in a slab head phantom on the proton Bragg peak // *Journal of Polytechnic*. 2019. Vol. 23. No. 1. Pp. 129–136.
15. **Augusto R. S., Bauer J., Bouhali O., et al.** An overview of recent developments in FLUKA PET TOOLS // *Physica Medica*. 2018. Vol. 54. October. Pp. 189–199.
16. **Titt U., Bednarz B., Paganetti H.** Comparison of MCNPX and Geant4 proton energy deposition predictions for clinical use // *Physics in Medicine and Biology*. 2012. Vol. 57. No. 20. Pp. 6381–6393.
17. **Wu J.-C., Feng Q.-J., Liu X.-K., Zhan C.-Y., Zou Y., Liu Y.-G.** A combination method for simulation of secondary knock-on atoms of boron carbide induced by neutron irradiation in SPRR-300 // *Nuclear Instruments and Methods in Physics Research B*. 2016. Vol. 368. 1 February. Pp. 1–4.
18. **Ogilvy C. S., Stieg Ph. E., Awad I., et al.** Recommendations for the management of intracranial arteriovenous malformations // *Stroke*. 2001. Vol. 32. No. 6. Pp. 1458–1471.
19. **Shaller C., Schramm J., Huan D.** Significance of factors contributing to surgical complications and to late outcome after elective surgery of cerebral arteriovenous malformations // *Journal of Neurology, Neurosurgery & Psychiatry*. 1998. Vol. 65. No. 4. Pp. 547–554.
20. **Ogilvy C. S.** Radiation therapy for arteriovenous malformations: a review, *Neurosurg.* 26 (5) (1990) 725–735.
21. Geant4. URL: <http://www.geant4.org/geant4/>, Son Erişim Tarihi: 20.04.2016.
22. **Jafar J. J., Davis A. J., Berenstein A., et al.** The effect of embolization with N-butyl cyanoacrylate prior to surgical resection of cerebral arteriovenous malformations, *J. Neurosurg.* 78 (1) (1993) 60–69.
23. **Behrens R., Hupe O.** Influence of the phantom shape (slab, cylinder or Alderson) on the performance of an Hp(3) eye dosimeter, *Rad. Protect. Dosim.* 168 (4) (2015) 441–449.



24. **Van Rooij W. J., Sluzewski M., Beute G. N.,** Brain AVM embolization with Onyx, *Am. J. Neurorad.* 28 (1) (2007) 172–178.
25. **Ziegler J. F.** SRIM – The stopping and range of ion in matter (2007). URL: <https://www.srim.org/> Accessed: 20.09.2019.
26. ICRU-1992: Photon, electron, proton and neutron interaction data for body tissues, Report 46 of The International Commission on Radiation Units and Measurements (ICRU), National Bureau of Standards, USA: US Department of Commerce, 1992.
27. Rinecker Proton Therapy Center (RPTC), Munich, Germany. URL: <https://www.rptc.de/en/home.html>. Son Ulaşım: 20 Aralık 2017.
28. **Battistoni G., Cerutti F., Fassò A., et al.,** The FLUKA code: description and benchmarking, *AIP Conf. Proc.* 896 (2007) 31–49.
29. **Mairani A.,** Nucleus-nucleus interaction modelling and applications in ion therapy treatment planning, PhD Thesis, Univesity of Pavia, Italy (2017).
30. **Böhlen T. T., Cerutti F., Chin M. P. W., et al.,** The FLUKA code: Developments and challenges for high energy and medical applications, *Nucl. Data Sheets.* 120 (June) (2014) 211–214.
31. **Dudouet J., Cussol D., Durand D., Labalme M.,** Benchmarking GEANT4 nuclear models for hadron therapy with 95 MeV/nucleon carbon ions, *Phys. Rev. C.* 89 (5) (2014) 054616.
32. **Aricò G., Gehrke T., Gallas R., et al.,** Investigation of single carbon ion fragmentation in water and PMMA for hadron therapy, *Phys. Med. Biol.* 64 (5) (2019) 055018.
33. **Verona C., Cirrone G. A. P., Magrin G., et al.,** Microdosimetric measurements of a monoenergetic and modulated Bragg peaks of 62 MeV therapeutic proton beam with a synthetic single crystal diamond microdosimeter, *Med. Phys.* 47 (11) (2020) 5791–5801.
34. **Wu Z., Chen S.,** Heavy ion, proton and neutron charge deposition analyses in several semiconductor materials, *IEEE Trans. Nucl. Sci.* 65 (8) (2018) 1791–1799.
35. **Du Q., Lin S. T., He H. T., et al.,** Response of gadolinium doped liquid scintillator to charged particles: measurement based on intrinsic U/Th contamination, *J. Instrum.* 13 (4) (2018) P04001.
36. **Mastromarco M., Digennaro A., Mazzone A., et al.,** Proton boron capture therapy: Dose calculations and a possible new measurement, *RAD Conf. Proc.* 4 (2020) 185–189.
37. **Yevseyeva O., de Assis J., Yevseev I., et al.,** Comparison of GEANT4 simulations with experimental data for thick Al absorbers, *AIP Conf. Proc.* 1139 (2009) 97–101.
38. **Liu T. Q., Lic D. Q., Caic C., et al.,** Heavy ion track straggling effect in single event effect numerical simulation of 3D stacked devices, *Microelectr. Rel.* 114 (November) (2020) 113853.
39. **Zheng Y., Zheng J., Wang X.,** Study on the applicability of neutron radiation damage method used for high-temperature superconducting tape based on Geant4 and SRIM, *Sci. Technol. Nucl. Instal.* (24 November) (2021) ID 2839746.
40. **Parida M. K., Prabakar K., Prasanna G., Sundari S. T.,** Efficiency of boric acid coated semiconductor neutron detector – A GEANT4 simulation study, In: *Proc. The 14th IEEE India Council International Conference (INDICON)*, 2017. doi:10.1109/indicon.2017.8487978.
41. **Schwarz M.,** Treatment planning in proton therapy, *Europ. Phys. J. Plus.* 126 (7) (2011) 67.
42. **Jia X., Schümann, J., Paganetti, H., ve Jiang S. B.,** GPU-based fast Monte Carlo dose calculation for proton therapy, *Phys. Med. Biol.* 57 (23) (2012) 7783.
43. **Yang Z. Y., Tsai P. E., Lee S. C., et al.,** Inter-comparison of dose distributions calculated by FLUKA, GEANT4, MCNP, and PHITS for proton therapy, *Europ. Phys. J., Web of Conf.* 153 (2017) 04011.
44. **Jia S. B., Hadizadeh M. H., Mowlavi A. A., ve Loushab M. E.,** Evaluation of energy deposition and secondary particle production in proton therapy of brain using a slab head phantom, *Rep. Pract. Oncol. Radiother.* 19 (6) (2014) 376–384.
45. **Sterpin E., Sorriaux J., Vynckier S.,** Extension of PENELOPE to protons: Simulation of nuclear reactions and benchmark with Geant4, *Med. Phys.* 40 (11) (2013) 111705.
46. **Grimes D. R., Warren D. R., Partridge M.,** An approximate analytical solution of the Bethe equation for charged particles in the radiotherapeutic energy range, *Sci. Rep.* 7 (1) (2017) 9781.
47. **Almhagen E.,** Development and validation of a scanned proton beam model for dose distribution verification using Monte Carlo, Thesis for Master of Science in Medical Radiation Physics. (2015) 48–49.

THE AUTHORS

EKINCI Fatih

Gazi University, Physics Department, Besevler, Ankara, Turkey
Emniyet Mahallesi Bandırma Caddesi No: 6/9 06500 Yenimahalle/ANKARA
fatih.ekinci2@gazi.edu.tr
ORCID: 0000-0002-1011-1105

BOSTANCI Erkan

Ankara University, Computer Engineering Department, Golbasi, Ankara, Turkey
ebostanci@ankara.edu.tr
ORCID: 0000-0001-8547-7569

GÜZEL Mehmet Serdar

Ankara University, Computer Engineering Department, Golbasi, Ankara, Turkey
mguzel@ankara.edu.tr
ORCID: 0000-0002-3408-0083

DAĞLI Özlem

Gazi University, Faculty of Medicine, Department of Neurosurgery Gamma Knife Unit, Ankara, Turkey
ozlemdagli@gazi.edu.tr
ORCID: 0000-0003-3798-8342

СВЕДЕНИЯ ОБ АВТОРАХ

ЭКИНДЖИ Фатих — доктор наук, профессор кафедры физики, факультета коммуникаций
Университета Гази, Бешевлер, г. Анкара, Турция.

Emniyet Mahallesi Bandırma Caddesi No: 6/9 06500 Yenimahalle/ANKARA
fatih.ekinci2@gazi.edu.tr
ORCID: 0000-0002-1011-1105

БОСТАНДЖИ Гази Эркан — кандидат наук, доцент кафедры вычислительной техники
Университета Анкары, Гельбаши, г. Анкара, Турция.

ebostanci@ankara.edu.tr
ORCID: 0000-0001-8547-7569

ГУЗЕЛЬ Мехмет Сердар — кандидат наук, доцент кафедры вычислительной техники
Университета Анкары, Гельбаши, г. Анкара, Турция.

mguzel@ankara.edu.tr
ORCID: 0000-0002-3408-0083

ДАГЛИ Озлем — сотрудница кафедры стереотоксической радиохирургии головного мозга
медицинского факультета Университета Гази, г. Анкара, Турция.

ozlemdagli@gazi.edu.tr
ORCID: 0000-0003-3798-8342

Received 01.03.2022. Approved after reviewing 25.04.2022. Accepted 25.04.2022.

*Статья поступила в редакцию 01.03.2022. Одобрена после рецензирования 25.04.2022.
Принята 25.04.2022.*

Original article

DOI: <https://doi.org/10.18721/JPM.15208>

RECONSTRUCTING QUINTESSENCE SCALAR FIELD MODEL FROM NEW HOLOGRAPHIC DARK ENERGY IN BIANCHI TYPE I UNIVERSE

C. R. Mahanta, M. P. Das ,

Gauhati University, India

 manashpratimdas22222@gmail.com

Abstract. In this paper, we investigate the cosmic evolution of a spatially homogeneous and anisotropic Bianchi type I universe filled with new holographic dark energy (NHDE) and cold dark matter (CDM) within the framework of General Relativity by considering both the components of the universe to be interacting with each other. To obtain the exact solutions of Einstein's field equations, we consider two expansion laws: an exponential expansion and a power-law volumetric expansion. The evolutions of some parameters of cosmological importance are studied for both the models corresponding to the exponential expansion and the power-law volumetric expansion. We observe that in both the models the anisotropy parameter decreases as time evolves and tends to zero at late times. The model corresponding to exponential expansion behaves like CDM model and the model corresponding to power-law volumetric expansion behaves like quintessence holographic dark energy model at late time. We also compare the equation of state (EoS) and energy density of our interacting NHDE model with that of quintessence scalar field and establish a correspondence between them. The quintessence potential is reconstructed which depicts the observed accelerated expansion of the universe.

Keywords: Bianchi type I universe, new holographic dark energy, quintessence, EoS parameter

Citation: Mahanta C. R., Das M. P. Reconstructing quintessence scalar field model from new holographic dark energy in Bianchi type I universe, St. Petersburg State Polytechnical University Journal. Physics and Mathematics. 15 (2) (2022) 79–92. DOI: <https://doi.org/10.18721/JPM.15208>

This is an open access article under the CC BY-NC 4.0 license (<https://creativecommons.org/licenses/by-nc/4.0/>)

Научная статья

УДК 530.12:517.988

DOI: <https://doi.org/10.18721/JPM.15208>

РЕКОНСТРУКЦИЯ МОДЕЛИ СКАЛЯРНОГО ПОЛЯ КВИНТЭССЕНЦИИ ДЛЯ НОВОЙ ГОЛОГРАФИЧЕСКОЙ МОДЕЛИ ТЕМНОЙ ЭНЕРГИИ ВО ВСЕЛЕННОЙ БИАНКИ ТИПА I

Ч. Р. Маханта, М. П. Дас ✉

Университет Гаухати, г. Гаухати, Индия

✉ manashpratimdas22222@gmail.com

Аннотация. В рамках общей теории относительности в работе исследована космическая эволюция однородной по пространству и анизотропной Вселенной Бианки типа I, заполненной новой голографической темной энергией (НГТЭ) и холодной темной материей (ХТМ); при этом сделано предположение, что оба компонента Вселенной взаимодействуют между собой. Чтобы получить точные решения полевых уравнений Эйнштейна, рассмотрены два закона расширения: экспоненциальное и степенное объемное. Для обоих случаев изучено изменение некоторых ключевых космологических параметров. Установлено, что для обеих моделей анизотропный параметр уменьшается со временем и в итоге стремится к нулю. Оказалось, что модель, соответствующая экспоненциальному расширению, ведет себя как модель ХТМ, а модель, соответствующая степенному объемному расширению, — как модель ГТЭ позднего периода. Проведено также сравнение уравнения состояния и плотности энергии взаимодействия в НГТЭ (наша модель) и в модели скалярного поля квинтэссенции и найдено соответствие между ними. Потенциал квинтэссенции реконструирован таким образом, чтобы он описывал наблюдаемое ускоренное расширение Вселенной.

Ключевые слова: Вселенная Бианки типа I, новая голографическая темная энергия, квинтэссенция, уравнение состояния

Для цитирования: Дас М. П., Маханта Ч. Р. Реконструкция модели скалярного поля квинтэссенции для новой голографической модели темной энергии во Вселенной Бианки типа I // Научно-технические ведомости СПбГПУ. Физико-математические науки. 2022. Т. 15. № 2. С. 79–92. DOI: <https://doi.org/10.18721/JPM.15208>

Статья открытого доступа, распространяемая по лицензии CC BY-NC 4.0 (<https://creativecommons.org/licenses/by-nc/4.0/>)



1. Introduction

Until the late 20th century, no consensus has been reached about the expansion rate of the universe. However, various cosmological and astrophysical observations such as Supernovae Type Ia (SN Ia) [1–3], Cosmic Microwave Background (CMB) [4, 8], Baryon Acoustic Oscillations (BAO) [9], Large Scale Structure (LSS) [10 – 12] and their cross relations make it clear that our universe is currently undergoing a phase of accelerated expansion. A strange kind of physical entity is supposed to be the cause of this late time cosmic acceleration which is termed as dark energy.

A dark energy candidate which can simply explain the late time cosmic acceleration is the so called cosmological constant Λ introduced by Einstein in his field equations. However, due to its non-evolving nature, it suffers from some theoretical challenges such as the fine-tuning and the cosmic coincidence problems. Therefore, quintessence [13–15], a minimally coupled homogeneous scalar field which provides a solution to the fine-tuning problem and also to the coincidence problem by means of tracker solutions, is considered as dark energy candidate. Different dynamical dark energy models such as phantom [16], k -essence [17], tachyon [18], dilatonic ghost condensate [19] and the interacting exotic fluid models such as Chaplygin gas models [20–23] etc. have also been investigated in the literature.

Holographic dark energy is another candidate of considerable interest which emerges from the Holographic Principle, first put forwarded by Gerard 't Hooft [24] in the context of black hole physics. This principle states that the number of degrees of freedom directly related to the entropy of a system scales with the enclosing surface area of the system and not with its volume. Based on the effective Quantum Field Theory, Cohen et al. [25] proposed a relationship between the ultraviolet (UV) cutoff and the infrared (IR) cutoff of a system due to the limit set by the formation of a black hole which in turn gives an upper bound on the zero-point energy of a system. When the whole universe is taken into account, this zero-point energy density has the same order of magnitude as the dark energy density which is referred to as the holographic dark energy.

In the cosmological context, a new version of the Holographic Principle was first proposed by Fischler and Susskind [26] which states that at any point during cosmological evolution the gravitational entropy within a closed surface should not exceed the particle entropy that passes through the past light-cone of that surface. Granda and Oliveros [27] proposed a new holographic dark energy density of the form

$$\rho_{\text{NHDE}} \approx \alpha H^2 + \beta \dot{H},$$

where H is the Hubble parameter, and the two constants α and β are to be determined so as to satisfy the restrictions entailed by the current observational data.

In Ref. [27], they showed that this new dark energy model can explain the current cosmic acceleration and being consistent with the observational data. In Ref. [28], these authors also established correspondence between quintessence, tachyon, k -essence and dilaton dark energy models with this new holographic dark energy in the flat Friedman – Robertson – Walker (FRW) universe. Many other researchers have since investigated several aspects of new holographic dark energy (NHDE) in an isotropic as well as in anisotropic background and studied the correspondence between the scalar fields such as quintessence, k -essence and NHDE models in cosmology [28–46].

The goal of this paper is to investigate a spatially homogeneous and anisotropic Bianchi type I universe filled with interacting cold dark matter and new holographic dark energy within the framework of General Relativity.

The reason why an anisotropic universe is considered in our investigation is that although our universe is homogeneous and isotropic at large scale, recent experimental tests like Wilkinson Microwave Anisotropy Probe (WMAP) [7, 8], Cosmic Background Explorers (COBE) [47] and Planck Collaboration results [48] support the existence of an anisotropic phase in the evolution of the universe that approaches an isotropic one.

The paper is organized as follows: In Section 2, we derive the field equations for the Bianchi type I line-element and find the expression for the equation-of-state (EoS) parameter for interacting cold dark matter and new holographic dark energy. In Section 3, we solve the Einstein field equations by considering two expansion laws viz. an exponential expansion and a volumetric expansion law. We construct two different models corresponding to these two expansion laws. In this section, we also obtain the expressions for some parameters of cosmological interest and discuss some physical and geometrical properties of both the models. In Section 4, we establish the correspondence between the quintessence and the new holographic dark energy for the model with volumetric expansion law. We conclude the paper with a brief discussion in Section 5.

2. Metric and field equations

A spatially homogeneous and anisotropic Bianchi type I universe is described by the line-element

$$ds^2 = -dt^2 + A^2 dx^2 + B^2 dy^2 + C^2 dz^2, \quad (1)$$

where A, B, C are functions of the cosmic time t alone.

We assume that the universe is filled with two interacting components: cold dark matter (CDM) and new holographic dark energy (NHDE).

In natural units ($8\pi G=1, c=1$), Einstein's field equations are

$$R_{ij} - \frac{1}{2} g_{ij} R = -(T_{ij} + \bar{T}_{ij}), \quad (2)$$

where R_{ij} is the Ricci tensor; R is the Ricci scalar; T_{ij} is the energy-momentum tensor for cold dark matter given by

$$T_{ij} = \rho_m u_i u_j, \quad (3)$$

and \bar{T}_{ij} is the energy-momentum tensor for new holographic dark energy given by

$$\bar{T}_{ij} = (\rho_{\text{NHDE}} + p_{\text{NHDE}}) u_i u_j + g_{ij} p_{\text{NHDE}}. \quad (4)$$

Here, ρ_m is the energy density of cold dark matter, ρ_{NHDE} and p_{NHDE} are respectively the energy density and the pressure of the new holographic dark energy.

In a comoving coordinate system, Eq. (2) with Eqs. (3) and (4) for the metric (1) lead to the following system of field equations:

$$\frac{\ddot{B}}{B} + \frac{\ddot{C}}{C} + \frac{\dot{B}\dot{C}}{BC} = -p_{\text{NHDE}}, \quad (5)$$

$$\frac{\ddot{C}}{C} + \frac{\ddot{A}}{A} + \frac{\dot{C}\dot{A}}{CA} = -p_{\text{NHDE}}, \quad (6)$$

$$\frac{\ddot{A}}{A} + \frac{\ddot{B}}{B} + \frac{\dot{A}\dot{B}}{AB} = -p_{\text{NHDE}}, \quad (7)$$

$$\frac{\dot{A}\dot{B}}{AB} + \frac{\dot{B}\dot{C}}{BC} + \frac{\dot{C}\dot{A}}{CA} = \rho_m + \rho_{\text{NHDE}}, \quad (8)$$

where an over dot denotes differentiation with respect to t .

Following Ref. [27], we consider the new holographic dark energy density as

$$\rho_{\text{NHDE}} = 3M_p^2(\alpha H^2 + \beta \dot{H}), \quad (9)$$

where $M_p^{-2} = 8\pi G = 1$; α, β are constants.

The pressure of the NHDE is given by

$$p_{\text{NHDE}} = \omega_{\text{NHDE}} \rho_{\text{NHDE}}, \quad (10)$$

where ω_{NHDE} is the EoS parameter of NHDE.

In a universe where dark matter and dark energy are interacting with each other, their energy densities do not conserve separately. So, when CDM and NHDE are interacting the continuity equations can be obtained as

$$\dot{\rho}_m + 3H\rho_m = Q, \quad (11)$$

$$\dot{\rho}_{\text{NHDE}} + 3H(\rho_{\text{NHDE}} + p_{\text{NHDE}}) = -Q, \quad (12)$$

where Q represents the interaction term between CDM and NHDE.

A natural choice for the interaction term available in the literature is $Q \propto H\rho_m$, $Q \propto H\rho_{\text{NHDE}}$ or a combination of these. We take

$$Q = 3H(\gamma\rho_{\text{NHDE}} + \delta\rho_m), \quad (13)$$

where γ, δ are coupling constants.

For $\gamma = 0$, we have $Q = 3H\delta\rho_m$, and for $\delta = 0$, we have $Q = 3H\gamma\rho_{\text{NHDE}}$. CDM and NHDE are non-interacting for $\gamma = 0 = \delta$.

From Eqs. (9), (10), (12) and (13), we obtain

$$\omega_{\text{NHDE}} = -1 - \frac{2\alpha H\dot{H} + \beta\ddot{H}}{3H(\alpha H^2 + \beta\dot{H})} - \left(\gamma + \frac{\delta\rho_m}{\rho_{\text{NHDE}}} \right). \quad (14)$$

3. Solutions of the field equations

From Eqs. (5) – (8), we derive

$$A(t) = a_1 V^{\frac{1}{3}} \exp(b_1 \int V^{-1} dt), \quad (15)$$

$$B(t) = a_2 V^{\frac{1}{3}} \exp(b_2 \int V^{-1} dt), \quad (16)$$

$$C(t) = a_3 V^{\frac{1}{3}} \exp(b_3 \int V^{-1} dt), \quad (17)$$

where $a_1 a_2 a_3 = 1$, $b_1 + b_2 + b_3 = 0$, and $V = ABC$ is the volume of the universe.

Now, as we have four equations in five unknown parameters A, B, C, ρ_m and ρ_{NHDE} , therefore, we need one extra condition to obtain an exact solution of the field equations. In view of Eqs. (15)–(17), we consider an exponential expansion law given by

$$V = ce^{3lt}, \quad (18)$$

and also a volumetric expansion law given by

$$V = ct^{3n}, \quad (19)$$

where c, l, n are positive constants.

A model for exponential expansion (Model 1). Using (18) in Eqs. (15) – (17), we get

$$A = a_1 c^{\frac{1}{3}} e^{lt} \exp\left[-\frac{b_1}{3cl} e^{-3lt}\right], \quad (20)$$

$$B = a_2 c^{\frac{1}{3}} e^{lt} \exp\left[-\frac{b_2}{3cl} e^{-3lt}\right], \quad (21)$$

$$C = a_3 c^{\frac{1}{3}} e^{lt} \exp\left[-\frac{b_3}{3cl} e^{-3lt}\right]. \quad (22)$$

For this model, the directional Hubble parameters H_i and the mean Hubble parameter H are obtained as

$$H_1 = \frac{\dot{A}}{A} = l + \frac{b_1}{c} e^{-3lt}, \quad (23)$$

$$H_2 = \frac{\dot{B}}{B} = l + \frac{b_2}{c} e^{-3lt}, \quad (24)$$

$$H_3 = \frac{\dot{C}}{C} = l + \frac{b_3}{c} e^{-3lt}, \quad (25)$$

$$H = l. \quad (26)$$

The scalar of expansion θ , the spatial volume V , the shear scalar σ^2 , the deceleration parameter q and the anisotropy parameter A_m for this model are obtained as

$$\theta = 3l, \quad (27)$$

$$\sigma^2 = \frac{M}{2c^2} e^{-6lt}, \quad (28)$$

$$q = -1, \quad (29)$$

$$A_m = \frac{M}{3l^2 c^2} e^{-6lt}, \quad (30)$$

where $M = b_1^2 + b_2^2 + b_3^2$.

From Eq. (9) we obtain

$$\rho_{\text{NHDE}} = 3\alpha l^2, \quad (31)$$

and from Eq. (11), using Eqs. (13) and (26), we get

$$\rho_m = \frac{3\alpha\gamma l^2}{1-\delta} + d e^{-3lt(1-\delta)}, \quad (32)$$

where d is an integrating constant and $\delta \neq 1$.

Therefore, for this model, the total energy density and the EoS parameter are given by

$$\Omega = \Omega_{\text{NHDE}} + \Omega_m = \frac{\rho_{\text{NHDE}}}{3H^2} + \frac{\rho_m}{3H^2} = \alpha + \frac{\alpha\gamma}{1-\delta} + \frac{d e^{-3lt(1-\delta)}}{3l^2}, \quad (33)$$

$$\omega_{\text{NHDE}} = -1 - \gamma - \delta \left(\frac{\gamma}{1-\delta} + \frac{d e^{-3lt(1-\delta)}}{3\alpha l^2} \right), \quad (34)$$

It is evident from the graphs in Fig. 1, that for small values of γ , our model approaches a flat isotropic universe in the course of time and behaves like a Λ CDM model. However, the model does not represent a flat isotropic universe for $\delta = 0$ and sufficiently large values of γ .

A model for volumetric expansion law (Model 2). Using Eq. (19) in Eqs. (15) – (17), we obtain

$$A(t) = a_1 c^{\frac{1}{3}} t^n \exp \left[\frac{b_1}{c(1-3n)} t^{-3n+1} \right], \quad (35)$$

$$B(t) = a_2 c^{\frac{1}{3}} t^n \exp \left[\frac{b_2}{c(1-3n)} t^{-3n+1} \right], \quad (36)$$

$$C(t) = a_3 c^{\frac{1}{3}} t^n \exp \left[\frac{b_3}{c(1-3n)} t^{-3n+1} \right], \quad (37)$$

where $n \neq 1/3$.

The directional Hubble parameters H_i and the mean Hubble parameter H for this model are obtained as

$$H_1 = nt^{-1} + \frac{b_1}{c} t^{-3n}, \quad (38)$$

$$H_2 = nt^{-1} + \frac{b_2}{c} t^{-3n}, \quad (39)$$

$$H_3 = nt^{-1} + \frac{b_3}{c} t^{-3n}, \quad (40)$$

$$H = \frac{n}{t}. \quad (41)$$

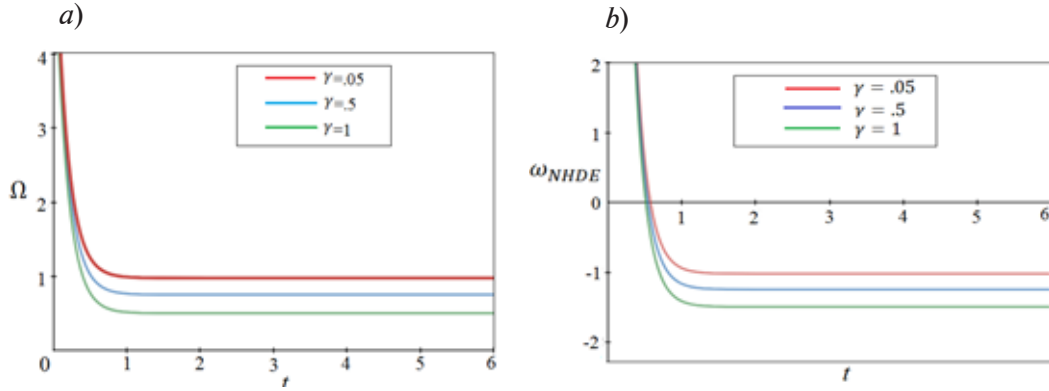


Fig. 1. Graphs of the total energy density Ω (a) and the EoS parameter (b) vs cosmic time t at different γ : 0.05 (red lines), 0.5 (blue ones) and 1.0 (green ones); $\alpha = 1, \delta = -1, d = 100, l = 1$

The scalar of expansion θ , the spatial volume V , the shear scalar σ^2 , the deceleration parameter q and the anisotropy parameter A_m are obtained as

$$\theta = \frac{3n}{t}, \quad (42)$$

$$\sigma^2 = \frac{1}{2c^2} M t^{-6n}, \quad (43)$$

$$q = -1 + \frac{1}{n}, \quad (44)$$

$$A_m = \frac{1}{3} \frac{M}{c^2 n^2 t^4} \quad (45)$$

where $M = b_1^2 + b_2^2 + b_3^2$.

The cosmological observations indicate that the value of the deceleration parameter lies in the range $-1 < q < 0$, so it is clear from Eq. (44) that for an accelerating expansion of the universe, we must take $n > 1$. Moreover, Eq. (45) reveals that the anisotropy parameter is a decreasing function of cosmic time and tends to zero in the course of time.

The NHDE density for this model is obtained from Eq. (9), as

$$\rho_{\text{NHDE}} = \frac{3(\alpha n^2 - \beta n)}{t^2}. \quad (46)$$

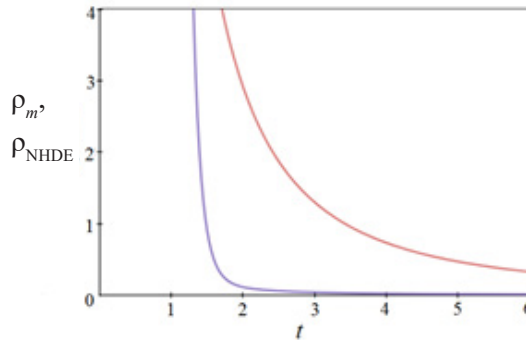


Fig. 2. Graphs of the new holographic dark energy density ρ_{NHDE} (the red line) and the cold dark matter density ρ_m (the blue one) vs cosmic time t ; $d = 100, \delta = -1, n = 2, \alpha = 1, \beta = 0.05, \gamma = 0.05$

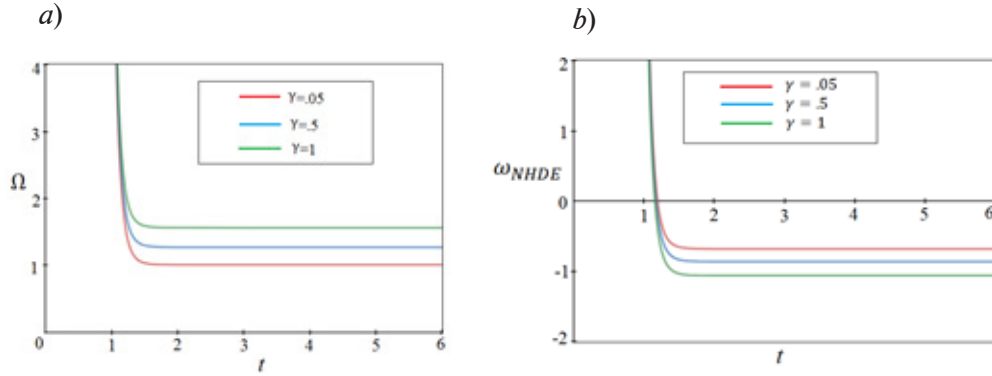


Fig. 3. Graphs of the total energy density Ω (a) and the EoS parameter ω_{NHDE} (b) vs cosmic time t at different γ : 0.05 (red lines), 0.5 (blue ones) and 1.0 (green ones); $n = 2$, $\alpha = 1$, $\beta = 0.05$, $\delta = -1$, $d = 100$

Using Eqs. (13) and (42) in Eq. (10), we obtain

$$\rho_m = \frac{9n\gamma(\alpha n^2 - \beta n)}{3n(1-\delta) - 2} t^{-2} + dt^{-3n(1-\delta)}, \quad (47)$$

where d is an integrating constant.

Therefore, for this model, the total energy density and the EoS parameters are given by

$$\Omega = \Omega_{\text{NHDE}} + \Omega_m = \frac{\rho_{\text{NHDE}}}{3H^2} + \frac{\rho_m}{3H^2} = \alpha - \frac{\beta}{n} + \frac{3\gamma(\alpha n - \beta)}{3n(1-\delta) - 2} + \frac{dt^{-3n(1-\delta)-2}}{3n^2}, \quad (48)$$

$$\omega_{\text{NHDE}} = -1 + \frac{2}{3n} - \left\{ \gamma + \delta \left(\frac{3n\gamma}{3n(1-\delta) - 2} + \frac{dt^{-3n(1-\delta)-2}}{3(\alpha n^2 - \beta n)} \right) \right\}. \quad (49)$$

It is clear from the graphs in Fig. 2 that both the CDM density ρ_m and the NHDE density ρ_{NHDE} are decreasing functions of cosmic time. The former tends to zero as time evolves while the latter is near to zero in the course of time. For $\gamma = 0$ and for sufficiently small values of γ this model approaches a flat universe and the EoS parameter enters into quintessence region $-1 < \omega_{\text{NHDE}} < -1/3$ at a later time (Fig. 3). The same as Model 1, this model fails to represent the current universe for sufficiently large values of γ and for $\delta = 0$.

Hence, to consider the interaction between NHDE and CDM, it suffices to take the coupling parameter δ as the interacting term and $\gamma = 0$. Thus, putting $\gamma = 0$ in Eq. (49), we obtain

$$\omega_{\text{NHDE}} = -1 + \frac{2}{3n} - \delta \frac{dt^{-3n(1-\delta)-2}}{3(\alpha n^2 - \beta n)}. \quad (50)$$

4. Correspondence between new holographic dark energy and quintessence scalar field model

Quintessence is described by an ordinary scalar field ϕ minimally coupled to gravity and self-interaction described by a potential $V(\phi)$ that leads to late time cosmic acceleration.

The action for the quintessence scalar field ϕ is given by an expression

$$S = \int d^4x \sqrt{-g} \left[-\frac{1}{2} g^{ij} \partial_i \phi \partial_j \phi - V(\phi) \right]. \quad (51)$$

The energy density and pressure of the scalar field are given by expression

$$\rho(\varphi) = \frac{1}{2}\dot{\varphi}^2 + V(\varphi), \quad (52)$$

$$p(\varphi) = \frac{1}{2}\dot{\varphi}^2 - V(\varphi). \quad (53)$$

Using Eqs. (52) and (53), the EoS for the quintessence scalar field is obtained as

$$\omega_\varphi = \frac{p(\varphi)}{\rho(\varphi)} = \frac{\dot{\varphi}^2 - 2V(\varphi)}{\dot{\varphi}^2 + 2V(\varphi)}. \quad (54)$$

In order to establish the correspondence between the new holographic dark energy and the quintessence scalar field model, we compare the EoS and the dark energy density for the interacting new holographic dark energy and quintessence dark energy models.

Thus, comparing Eqs. (50) and (54), we obtain

$$-1 + \frac{2}{3n} - \delta \frac{dt^{-3n(1-\delta)-2}}{3(\alpha n^2 - \beta n)} = \frac{\dot{\varphi}^2 - 2V(\varphi)}{\dot{\varphi}^2 + 2V(\varphi)}. \quad (55)$$

Also, comparing Eqs. (46) and (52), we obtain

$$\frac{3(\alpha n^2 - \beta n)}{t^2} = \frac{1}{2}\dot{\varphi}^2 + V(\varphi). \quad (56)$$

Again, from Eq. (55), we derive

$$\dot{\varphi}^2 = \frac{4(\alpha n - \beta) - 2\delta dt^{-3n(1-\delta)-2}}{6(\alpha n^2 - \beta n) - 2(\alpha n - \beta) + \delta dt^{-3n(1-\delta)-2}} V(\varphi). \quad (57)$$

Using Eq. (56) in Eq. (57), we obtain

$$V(\varphi) = \frac{3(\alpha n^2 - \beta n)}{t^2} \frac{6(\alpha n^2 - \beta n) - 2(\alpha n - \beta) + \delta dt^{-3n(1-\delta)-2}}{6(\alpha n^2 - \beta n) + 2(\alpha n - \beta) - \delta dt^{-3n(1-\delta)-2}}. \quad (58)$$

This type of potential can produce an accelerated expansion of the universe. Thus a correspondence between the interacting new holographic dark energy and quintessence scalar field model is established.

5. Conclusion

In this work, we study a spatially homogeneous and anisotropic Bianchi type I universe filled with interacting the new holographic dark energy and the cold dark matter by taking the coupling parameter Q as

$$Q = 3H(\gamma\rho_{\text{NHDE}} + \delta\rho_m).$$

To obtain the exact solutions of the Einstein field equations, we consider two expansion laws: an exponential expansion and a power-law volumetric one; they correspond to Models 1 and 2, respectively.

Considering Model 1, we find that the average Hubble parameter and the NHDE density are constant and the deceleration parameter equals -1 . The anisotropy parameter decreases as time evolves and tends to zero at late time. The total energy density for this model approaches 1 for $\gamma \rightarrow 0$. Thus, for small values of γ , this model approaches a flat, isotropic universe at late time and the EoS parameter approaches -1 showing thereby that the Model 1 behaves like a Λ CDM model.

In Model 2, the Hubble parameter, NHDE density and CDM one are decreasing functions of cosmic time. We also observe that the anisotropy parameter decreases as time evolves and tends to zero. Hence, we conclude that the anisotropy of our universe dies out in the course of the evolution to reach the present isotropic phase. It can be also seen from Fig. 3,*a* that the total energy density approaches 1, and from Fig. 3,*b* we see that the EoS parameter of this model lies in the quintessence region

$$-1 < \omega_{\text{NHDE}} < -1/3$$

for $\gamma \rightarrow 0$.

So, this model behaves like a quintessence holographic dark energy model.

In both the models we define the interaction between NHDE and CDM by taking

$$Q = 3H(\gamma\rho_{\text{NHDE}} + \delta\rho_m).$$

But the models represent current universe only for small values of γ . Therefore, we ignore γ while establishing correspondence between the new holographic dark energy model and the quintessence scalar field model. Quintessence potential is reconstructed which describes the accelerated phase of expansion of the universe.

REFERENCES

1. Riess A. G., Fillipenko A. V., Challis P., et al., Observational evidence from supernovae for an accelerating universe and a cosmological constant, *Astron. J.* 116 (3) (1998) 1009–1038.
2. Perlmutter S., Aldering G., Goldhaber G., et al., Measurements of Ω and Λ from 42 high-redshift supernovae, *Astrophys. J.* 517 (2) (1999) 565–586.
3. Perlmutter S., Aldering G., Valle M., et al., Discovery of a supernova explosion at half the age of the universe, *Nature*. 391 (6662) (1998) 51–54.
4. Miller A. D., Caldwell R., Devlin M. J., et al., A measurement of the angular power spectrum of the cosmic microwave background from $L = 100$ to 400, *Astrophys. J. Lett.* 524 (1) (1999) L1–L4.
5. De Bernardis P., Ade P., Bock J., et al., A flat universe from high-resolution maps of the cosmic microwave background radiation, *Nature*. 404 (6781) (2002) 955–959.
6. Halverson N. W., Leitch E. M., Prike C., et al., Degree angular scale interferometer first results: A measurement of the cosmic microwave background angular power spectrum, *Astrophys. J.* 568 (1) (2002) 38–45.
7. Bennett C. L., Halpern M., Hinshaw G., et al., First-year Wilkinson microwave anisotropy probe (WMAP)* observations: Preliminary maps and basic results, *Astrophys. J. Suppl. Ser.* 148 (1) (2003) 1–28.
8. Spergel D. N., Verde L., Peiris H. V., et al., First-year Wilkinson microwave anisotropy probe (WMAP)* observations: Determination of cosmological parameters, *Astrophys. J. Suppl. Ser.* 148 (1) (2003) 175–194.
9. Bassett B., Hlozek R., Baryon acoustic oscillations, In book: “Dark energy: Observational and theoretical approaches”. Ed. by P. Ruiz-Lapuente, Cambridge University Press, Cambridge (2010) 246–278.
10. Hawkins E., Maddox S., Cole S., et al., The 2dF galaxy redshift survey: correlation functions, peculiar velocities and the matter density of the universe, *Mon. Not. R. Astron. Soc.* 346 (1) (2003) 78–96.
11. Abazajian K., Adelman-McCarthy J. K., Agueros M. A., et al., The second data release of the Sloan Digital Sky Survey, *Astron. J.* 128 (1) (2004) 502–512.
12. Verde L., Heavens A. F., Persival W. J., et al., The 2dF galaxy redshift survey: the bias of galaxies and the density of the universe, *Mon. Not. R. Astron. Soc.* 335 (2) (2002) 432–440.
13. Wetterich C., Cosmology and the fate of dilatation symmetry, *Nucl. Phys. B.* 302 (4) (1988) 668–696.
14. Padmanabhan T., Dark energy and gravity, *Gen. Relativ. Gravit.* 40 (2–3) (2008) 529–564.
15. Sahni V., Starobinsky A., The case for a positive cosmological Λ -term, *Int. J. Mod. Phys. D.* 9 (4) (2000) 373–443.
16. Caldwell R. R., A phantom menace? Cosmological consequences of a dark energy component with super-negative equation of state, *Phys. Lett. B.* 545 (1–2) (2002) 23–29.



17. **Armendariz-Picon C., Mukhanov V., Steinhardt P. J.**, Essentials of k -essence, *Phys. Rev. D.* 63 (10) (2001) 103510.
18. **Sen A.**, Tachyon matter, *J. High Energy Phys.* 2002 (July) (2002), 07(2002)065. (arXiv:hep-th/0203265).
19. **Gasperini M., Piazza F., Veneziano G.**, Quintessence as a runaway dilaton, *Phys. Rev. D.* 65 (2) (2002) 023508.
20. **Srivastava S. K.**, Future universe with $w < -1$ without big smash, *Phys. Lett. B.* 619 (1–2) (2005) 1–4.
21. **Bertolami O., Sen A. A., Sen S., Silva P. T.**, Latest supernova data in the framework of the generalized Chaplygin gas model, *Mon. Not. R. Astron. Soc.* 353 (1) (2004) 329–337.
22. **Bento M. C., Bertolami O., Sen A. A.**, Generalized Chaplygin gas, accelerated expansion, and dark-energy-matter unification, *Phys. Rev. D.* 66 (4) (2002) 043507.
23. **Kamenshchik A., Moschella U., Pasquier V.**, An alternative to quintessence, *Phys. Lett. B.* 511 (2–4) (2001) 265–268.
24. **t' Hooft G.**, Dimensional reduction in quantum gravity, *Proc. Conf. on Highlights of Particle and Condensed Matter Physics (SALAMEST)*, 8 – 12 March 1993, Trieste, Italy; Report No. THU-93-26. *Conf. Proc. C* 930308 (1993) 284 – 296.
25. **Cohen A. G., Kaplan D. B., Nelson A. E.**, Effective field theory, black holes, and the cosmological constant, *Phys. Rev. Lett.* 82 (25) (1999) 4971–4974.
26. **Fischler W., Susskind L.**, Holography and cosmology, *J. High Energy Phys.* (June) (1998) arXiv: hep-th/9806039 (1998).
27. **Granda L. N., Oliveros A.**, Infrared cut-off proposal for the holographic density, *Phys. Lett. B.* 669 (5) (2008) 275–277.
28. **Granda L. N., Oliveros A.**, New infrared cut-off for the holographic scalar fields models of dark energy, *Phys. Lett. B.* 671 (2) (2009) 199–202.
29. **Chattopadhyay S., Debnath U.**, Holographic dark energy scenario and variable modified Chaplygin gas, *Astrophys. Space Sci.* 319 (2–4) (2009) 183–185.
30. **Farajollahi H., Sadeghi J., Pourali M.**, Stability analysis of holographic dark energy in Brans – Dicke cosmology, *Astrophys. Space Sci.* 341 (2) (2012) 695–700.
31. **Karami K., Fehri J.**, New holographic scalar field models of dark energy in non-flat universe, *Phys. Lett. B.* 684 (2–3) (2010) 61–68.
32. **Malekjani M.**, Generalized holographic dark energy model in the Hubble length, *Space Sci.* 347 (2) (2013) 405–410.
33. **Rao V. U. M., Santhi M. V., Aditya Y.**, Anisotropic Bianchi type- VI_h perfect fluid cosmological models in a modified theory of gravity, *Prespacetime J.* 6 (10) (2015) 947–960.
34. **Guberina B., Horvat R., Nikolić H.**, Generalized holographic dark energy and the IR cutoff problem, *Phys. Rev. D.* 72 (12) (2005) 125011.
35. **Mete V. G., Murade P. B., Bansod A. S.**, LRS Bianchi type I universe filled with interacting cold dark matter and holographic dark energy, *African Rev. Phys.* 12 (0017) (2017) 125–129.
36. **Ghaffari S.**, Holographic dark energy model in the DGP brane world with time varying holographic parameter, *New Astronomy.* 2019. Vol. 67 (February) (2019) 76–84.
37. **Rahman M. A., Ansari M.**, Interacting holographic polytropic gas model of dark energy with hybrid expansion law in Bianchi type- VI_0 space-time, *Astrophys. Space Sci.* 354 (2) (2014) 617–625.
38. **Saridakis N. E.**, Ricci–Gauss–Bonnet holographic dark energy, *Phys. Rev. D.* 97 (6) (2018) 064035.
39. **Srivastava S., Sharma U. K., Pradhan A.**, New holographic dark energy in Bianchi-III universe with k -essence, *New Astronomy.* 68 (April) (2019) 57–64.
40. **Katore S. D., Kapse D. V.**, Dynamics of Bianchi type VI_0 holographic dark energy models in general relativity and Lira’s geometry, *Pramana – J. Phys.* 88 (2) (2017) ID0030.
41. **Samanta G. C., Dhal S. N.**, Higher dimensional cosmological model filled with perfect fluid in $f(R, T)$ theory of gravity, *Int. J. Theor. Phys.* 52 (4) (2013) 1334–1344.
42. **Santhi M. V., Rao V. U. M., Gusu D. M., Aditya Y.**, Bianchi type-III holographic dark energy model with quintessence, *Int. J. Geom. Meth. Mod. Phys.* 15 (9) (2018) 1850161.
43. **Gusu D. M., Santhi M. V.**, Analysis of Bianchi type V holographic dark energy models in general relativity and Lira’s geometry, *Adv. High Energy Phys.* 2021 (January) (2021) ID 8818590.
44. **Kim R. G., Ri Ch. H.**, Generalized holographic dark energy and cosmic coincidence, *New Astronomy.* 84 (April) (2021) 101540.

45. **Pourojaghi S., Malekjani M.**, A new comparison between holographic dark energy and standard Λ -cosmology in the context of cosmography method, *Eur. Phys. J. C.* 81 (7) (2021) 575.
46. **Shaikh A. Y., Wankhade K. S.** Panorama behaviors of holographic dark energy models in modified gravity, *Found Phys.* 51 (3) (2021) 58.
47. **Smoot G. F., Bennett C. L., Kogyt A., et al.**, Structure in the COBE differential microwave radiometer first-year maps, *Astrophys. J.* 396 (September) (1992) L1–L5.
48. **Ade P. A. R., Aghanim N., Acrami Y., et al.** (Planck collaboration), Isotropy and statistics of the CMB, Planck 2015 results, *Astron. & Astrophys.* 594 (October) (2016) A16 (62 p.).

СПИСОК ЛИТЕРАТУРЫ

1. **Riess A. G., Fillipenko A. V., Challis P., et al.** Observational evidence from supernovae for an accelerating universe and a cosmological constant // *The Astronomical Journal*. 1998. Vol. 116. No. 3. Pp. 1009–1038.
2. **Perlmutter S., Aldering G., Goldhaber G., et al.** Measurements of Ω and Λ from 42 high-redshift supernovae // *The Astrophysical Journal*. 1999. Vol. 517. No. 2. Pp. 565–586.
3. **Perlmutter S., Aldering G., Valle M., et al.** Discovery of a supernova explosion at half the age of the universe // *Nature*. 1998. Vol. 391. No. 6662. Pp. 51–54.
4. **Miller A. D., Caldwell R., Devlin M. J., et al.** A measurement of the angular power spectrum of the cosmic microwave background from $L = 100$ to 400 // *The Astrophysical Journal Letters*. 1999. Vol. 524. No. 1. Pp. L1–L4.
5. **De Bernardis P., Ade P., Bock J., et al.** A flat universe from high-resolution maps of the cosmic microwave background radiation // *Nature*. 2002. Vol. 404. No. 6781. Pp. 955–959.
6. **Halverson N. W., Leitch E. M., Prike C., et al.** Degree angular scale interferometer first results: A measurement of the cosmic microwave background angular power spectrum // *The Astrophysical Journal*. 2002. Vol. 568. No. 1. Pp. 38–45.
7. **Bennett C. L., Halpern M., Hinshaw G., et al.** First-year Wilkinson microwave anisotropy probe (WMAP)* observations: Preliminary maps and basic results // *The Astrophysical Journal. Supplementary Series*. 2003. Vol. 148. No. 1. Pp. 1–28.
8. **Spergel D. N., Verde L., Peiris H. V., et al.** First-year Wilkinson microwave anisotropy probe (WMAP)* observations: Determination of cosmological parameters // *The Astrophysical Journal. Suppl. Ser.* 2003. Vol. 148. No. 1. Pp. 175–194.
9. **Bassett B., Hlozek R.** Baryon acoustic oscillations // *Dark energy: Observational and theoretical approaches*. Edited by P. Ruiz-Lapuente. Cambridge: Cambridge University Press, 2010. Pp. 246–278.
10. **Hawkins E., Maddox S., Cole S., et al.** The 2dF galaxy redshift survey: correlation functions, peculiar velocities and the matter density of the universe // *Monthly Notices of the Royal Astronomical Society*. 2003. Vol. 346. No. 1. Pp. 78–96.
11. **Abazajian K., Adelman-McCarthy J. K., Agueros M. A., et al.** The second data release of the Sloan Digital Sky Survey // *The Astronomical Journal*. 2004. Vol. 128. No. 1. Pp. 502–512.
12. **Verde L., Heavens A. F., Persival W. J., et al.** The 2dF galaxy redshift survey: the bias of galaxies and the density of the universe // *Monthly Notices of the Royal Astronomical Society*. 2002. Vol. 335. No. 2. Pp. 432–440.
13. **Wetterich C.** Cosmology and the fate of dilatation symmetry // *Nuclear Physics B*. 1988. Vol. 302. No. 4. Pp. 668–696.
14. **Padmanabhan T.** Dark energy and gravity // *General Relativity and Gravitation*. 2008. Vol. 40. No. 2–3. Pp. 529–564.
15. **Sahni V., Starobinsky A.** The case for a positive cosmological Λ -term // *International Journal of Modern Physics D*. 2000. Vol. 9. No. 4. Pp. 373–443.
16. **Caldwell R. R.** A phantom menace? Cosmological consequences of a dark energy component with super-negative equation of state // *Physics Letters B*. 2002. Vol. 545. No. 1–2. Pp. 23–29.
17. **Armendariz-Picon C., Mukhanov V., Steinhardt P. J.** Essentials of k -essence // *Physical Review D*. 2001. Vol. 63. No. 10. P. 103510.
18. **Sen A.** Tachyon matter // *Journal of High Energy Physics*. 2002. Vol. 2002. July. P. 07(2002)065. (arXiv:hep-th/0203265).
19. **Gasperini M., Piazza F., Veneziano G.** Quintessence as a runaway dilaton // *Physical Review D*. 2002. Vol. 65. No. 2. P. 023508.



20. **Srivastava S. K.** Future universe with $w < -1$ without big smash // *Physics Letters B*. 2005. Vol. 619. No. 1–2. Pp. 1–4.
21. **Bertolami O., Sen A. A., Sen S., Silva P. T.** Latest supernova data in the framework of the generalized Chaplygin gas model // *Monthly Notices of the Royal Astronomical Society*. 2004. Vol. 353. No. 1. Pp. 329–337.
22. **Bento M. C., Bertolami O., Sen A. A.** Generalized Chaplygin gas, accelerated expansion, and dark-energy-matter unification // *Physical Review D*. 2002. Vol. 66. No. 4. P. 043507.
23. **Kamenshchik A., Moschella U., Pasquier V.** An alternative to quintessence // *Physics Letters B*. 2001. Vol. 511. No. 2–4. Pp. 265–268.
24. **t' Hooft G.** Dimensional reduction in quantum gravity // *Proceedings of the Conference on Highlights of Particle and Condensed Matter Physics (SALAMEST)*, 8 – 12 March 1993. Trieste, Italy. Report No. THU-93-26. Conf. Proc. C 930308 (1993). Pp. 284 – 296.
25. **Cohen A. G., Kaplan D. B., Nelson A. E.** Effective field theory, black holes, and the cosmological constant // *Physical Review Letters*. 1999. Vol. 82. No. 25. Pp. 4971–4974.
26. **Fischler W., Susskind L.** Holography and cosmology // *Journal of High Energy Physics*. 1998. June (arXiv: hep-th/9806039 (1998)). 7 p.
27. **Granda L. N., Oliveros A.** Infrared cut-off proposal for the holographic density // *Physics Letters B*. 2008. Vol. 669. No. 5. Pp. 275–277.
28. **Granda L. N., Oliveros A.** New infrared cut-off for the holographic scalar fields models of dark energy // *Physics Letters B*. 2009. Vol. 671. No. 2. Pp. 199–202.
29. **Chattopadhyay S., Debnath U.** Holographic dark energy scenario and variable modified Chaplygin gas // *Astrophysics Space Science*. 2009. Vol. 319. No. 2–4. Pp. 183–185.
30. **Farajollahi H., Sadeghi J., Pourali M.** Stability analysis of holographic dark energy in Brans–Dicke cosmology // *Astrophysics and Space Science*. 2012. Vol. 341. No. 2. Pp. 695–700.
31. **Karami K., Fehri J.** New holographic scalar field models of dark energy in non-flat universe // *Physics Letters B*. 2010. Vol. 684. No. 2–3. Pp. 61–68.
32. **Malekjani M.** Generalized holographic dark energy model in the Hubble length // *Astrophysics and Space Science*. 2013. Vol. 347. No. 2. Pp. 405–410.
33. **Rao V. U. M., Santhi M. V., Aditya Y.** Anisotropic Bianchi type- VI_h perfect fluid cosmological models in a modified theory of gravity // *Prespacetime Journal*. 2015. Vol. 6. No. 10. Pp. 947–960.
34. **Guberina B., Horvat R., Nikolić H.** Generalized holographic dark energy and the IR cutoff problem // *Physical Review D*. 2005. Vol. 72. No. 12. P. 125011.
35. **Mete V. G., Murade P. B., Bansod A. S.** LRS Bianchi type I universe filled with interacting cold dark matter and holographic dark energy // *The African Review of Physics*. 2017. Vol. 12. No. 0017. Pp. 125–129.
36. **Ghaffari S.** Holographic dark energy model in the DGP brane world with time varying holographic parameter // *New Astronomy*. 2019. Vol. 67. February. Pp. 76–84.
37. **Rahman M. A., Ansari M.** Interacting holographic polytropic gas model of dark energy with hybrid expansion law in Bianchi type- VI_0 space-time // *Astrophysics and Space Science*. 2014. Vol. 354. No. 2. Pp. 617–625.
38. **Saridakis N. E.** Ricci – Gauss – Bonnet holographic dark energy // *Physical Review D*. 2018. Vol. 97. No. 6. P. 064035.
39. **Srivastava S., Sharma U. K., Pradhan A.** New holographic dark energy in Bianchi-III universe with k -essence // *New Astronomy*. 2019. Vol. 68. April. Pp. 57–64.
40. **Katore S. D., Kapse D. V.** Dynamics of Bianchi type VI_0 holographic dark energy models in general relativity and Lira's geometry // *Pramana – Journal of Physics*. 2017. Vol. 88. No. 2. P. ID0030.
41. **Samanta G. C., Dhal S. N.** Higher dimensional cosmological model filled with perfect fluid in $f(R, T)$ theory of gravity // *International Journal of Theoretical Physics*. 2013. Vol. 52. No. 4. Pp. 1334–1344.
42. **Santhi M. V., Rao V. U. M., Gusu D. M., Aditya Y.** Bianchi type-III holographic dark energy model with quintessence // *International Journal of Geometric Methods in Modern Physics*. 2018. Vol. 15. No. 9. P. 1850161.
43. **Gusu D. M., Santhi M. V.** Analysis of Bianchi type V holographic dark energy models in general relativity and Lira's geometry // *Advances in High Energy Physics*. 2021. Vol. 2021. January. P. ID 8818590.

44. Kim R. G., Ri Ch. H. Generalized holographic dark energy and cosmic coincidence // New Astronomy. 2021. Vol. 84. April. P. 101540.
45. Pourojaghi S., Malekjani M. A new comparison between holographic dark energy and standard Λ -cosmology in the context of cosmography method // The European Physical Journal C. 2021. Vol. 81. No. 7. P. 575.
46. Shaikh A. Y., Wankhade K. S. Panorama behaviors of holographic dark energy models in modified gravity // Foundations of Physics. 2021. Vol. 51. No. 3. P. 58.
47. Smoot G. F., Bennett C. L., Kogyt A., et al. Structure in the COBE differential microwave radiometer first-year maps // The Astrophysical Journal. 1992. Vol. 396. September. Pp. L1–L5.
48. Ade P. A. R., Aghanim N., Acrami Y., et al. (Planck collaboration). Isotropy and statistics of the CMB // Astronomy & Astrophysics. 2016. Vol. 594. October. Planck 2015 results. P. A16 (62 p.).

THE AUTHORS

MAHANTA Chandra Rekha

Gauhati University

Guwahati, Assam, 781014, India

crmahanta@gauhati.ac.in

ORCID: 0000-0002-8019-8824

DAS Manash Pratim

Gauhati University

Guwahati, Assam, 781014, India

manashpratimdas22222@gmail.com

ORCID: 0000-0002-1179-8068

СВЕДЕНИЯ ОБ АВТОРАХ

МАХАНТА Чандра Рекха — *MSc., Ph.D, доцент кафедры математики Университета Гаухати, г. Гаухати, Индия.*

Guwahati, Assam, India, 781014

crmahanta@gauhati.ac.in

ORCID: 0000-0002-8019-8824

ДАС Манаш Пратим — *ассистент кафедры математики Университета Гаухати, г. Гаухати, Индия.*

Guwahati, Assam, India, 781014

manashpratimdas22222@gmail.com

ORCID: 0000-0002-1179-8068

Received 01.08.2021. Approved after reviewing 21.03.2022. Accepted 21.03.2022.

Статья поступила в редакцию 01.08.2021. Одобрена после рецензирования 21.03.2022. Принята 21.03.2022.

Original article

DOI: <https://doi.org/10.18721/JPM.15209>

ON CONJUGACY CLASSES OF THE F_4 GROUP OVER A FIELD q WITH CHARACTERISTIC 2

N. V. Yurova ✉

Nizhni Novgorod State Technical University named after R. E. Alekseev,
Nizhni Novgorod, Russia

✉ yurova1980@yandex.ru

Abstract: This article continues a series of papers devoted to solving the problem by which a non-identity conjugacy class in a finite simple non-abelian group contains commuting elements. Previously, this statement was tested for sporadic, projective, alternating groups and some exceptional groups. In this article, the validity of the above-mentioned statement for the series exceptional groups ${}^2F_4(q)$ has been verified. After some basic definitions two theorems were proved. The former said about the content of commuting elements in the group, the latter did about the presence of conjugation of a semisimple element with its inverse. Then classes of unipotent and mixed elements were considered. The investigative techniques used were recommended for testing the general hypothesis when dealing with other groups.

Keywords: Chevalley group, conjugacy classes, finite simple group, commuting element

Citation: Yurova N. V., On conjugacy classes of the F_4 group over a field q with characteristic 2, St. Petersburg Polytechnical State University Journal. Physics and Mathematics. 15 (2) (2022) 93–101. DOI: <https://doi.org/10.18721/JPM.15209>

This is an open access article under the CC BY-NC 4.0 license (<https://creativecommons.org/licenses/by-nc/4.0/>)

Научная статья

УДК 512

DOI: <https://doi.org/10.18721/JPM.15209>

О КЛАССАХ СОПРЯЖЕННОСТИ В ГРУППЕ F_4 НАД ПОЛЕМ q С ХАРАКТЕРИСТИКОЙ 2

Н. В. Юрова 

Нижегородский государственный технический университет им. Р. Е. Алексеева,

г. Нижний Новгород, Россия

 yurova1980@yandex.ru

Аннотация. Данная статья продолжает цикл работ, посвященных решению проблемы, согласно которой неединичный класс сопряженности в конечной простой неабелевой группе содержит коммутирующие элементы. Ранее это утверждение было проверено для спорадических, проективных, знакопеременных групп и ряда исключительных групп. В этой работе проверяется справедливость вышеупомянутого утверждения для серии исключительных конечных простых групп ${}^2F_4(q)$. После основных определений доказываются две теоремы: о содержании в группе коммутирующих элементов и о наличии сопряжения полупростого элемента со своим обратным. Затем рассмотрены классы унитарных и смешанных элементов. Используемые в статье методы исследования рекомендовано применять для проверки общей гипотезы при рассмотрении других групп.

Ключевые слова: группа Шевалле, классы сопряженности, конечная простая группа, коммутирующий элемент

Для цитирования: Юрова Н. В. О классах сопряженности в группе F_4 над полем q с характеристикой 2 // Научно-технические ведомости СПбГПУ. Физико-математические науки. 2022. Т. 15. № 2. С. 93–101. DOI: <https://doi.org/10.18721/JPM.15209>

Статья открытого доступа, распространяемая по лицензии CC BY-NC 4.0 (<https://creativecommons.org/licenses/by-nc/4.0/>)

Introduction

Investigations of left distributive quasigroups, i.e., binary systems $G(\circ)$ with the left-distributivity identity

$$x \circ (y \circ z) = (x \circ y) \circ (x \circ z) \text{ for } x, y, z \in G(\circ),$$

have led to the problem that should be solved via calculations based on the theory of finite groups.

The left-distributivity identity is appealing because the mapping

$$L_a = (x \rightarrow a \circ x)$$

in the binary system $G(\circ)$ containing it, is clearly an endomorphism, or even an automorphism if $G(\circ)$ is a quasigroup.

This issue is thoroughly explored in [1]. Consideration of left distributive quasigroups is equivalent to consideration of homogeneous spaces, i.e., a set containing cosets of a subgroup T in group Π . Turning to groupoids and weakening the axiom of right divisibility $x \circ a = a \Rightarrow x = a$, it generally follows that a groupoid cannot be represented by a homogeneous space.

Left distributive groupoids are often found in applications, manifesting close relationships to groups. Symmetric spaces can be given in differential geometry, characterizing the nodes from a topological standpoint [2,3]. Representations of finite groups by homogeneous spaces have been described by Erofeeva in several studies [4–6]. Apparently, this statement is equivalent to the hypothesis borrowed from pure group theory, assuming that a union of two conjugacy classes in a finite group always contains commuting elements. An even stronger assertion is formulated in [7], arguing that a non-identity class in a finite non-Abelian group must contain commuting elements.

This study continues to verify the hypothesis put forward in [7] that a non-identity class of conjugate elements in a finite simple group contains commuting elements. We have earlier tested some exceptional Lie-type groups and simple groups $SP_4(q)$ in [8–11]. In this paper, we intend to test a series of exceptional groups ${}^2F_4(q)$.

Basic definitions

General information about Chevalley groups is assumed to be known. This is discussed in sufficient detail in the monograph by Robert Steinberg [12]. Specific results on the structure of groups $F_4(q)$ and ${}^2F_4(q)$ are primarily given in Ken-ichi Shinoda's studies [13, 14], as well as in [15].

Here we generally follow the notations adopted by Shinoda [13, 14]. Let us point out some differences. The main field in group $F_4(q)$ is a field of q -elements, $q = 2^{2n+1}$; conversely, Shinoda uses the letter l instead of q , while $q = \sqrt{l}$. Further, the author introduces the notation $x_{i \pm j}$ for $\alpha = e_i \pm e_j$ instead of $x_\alpha(t)$, writing $x_{1 \pm 2 \pm 3 \pm 4}$ for $\alpha = 1/2(e_1 \pm e_2 \pm e_3 \pm e_4)$.

Below we give the main definitions of groups $F_4(q)$ and ${}^2F_4(q)$. The type F_4 Dynkin diagram has the form shown in Fig. 1. The vertices 1, 2, 3, 4 of the graph in it correspond to the roots

$$e_2 - e_3; e_3 - e_4; e_4; \frac{1}{2}(e_1 - e_2 - e_3 - e_4),$$

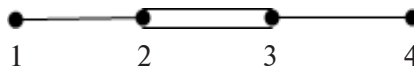


Fig. 1. Dynkin diagram:

graph vertices 1–4 correspond to the roots $e_2 - e_3, e_3 - e_4, e_4, (e_1 - e_2 - e_3 - e_4)/2$

where e_i ($i = 1, 2, 3, 4$) is a system of orthogonal unit vectors in R^4 .

The complete system of roots consists of vectors

$$\pm e_i; \pm e_i \pm e_j \ (i \neq j) \text{ and } \frac{1}{2}(\pm e_1 \pm e_2 \pm e_3 \pm e_4).$$

Group $F_4(q)$ is defined by the generators $x_\alpha(t)$, where α is the root, $t \in F_q$ is the finite field of q elements with certain ratios (see [12, p. 32]); notice the commuting form here:

$$(x_\alpha(t), x_\beta(t)) = \prod_{x_{\alpha+\beta}} (c_{ij} t^i u^j) (\alpha + \beta \neq 0),$$

where c_{ij} are some constants from the main field.

The 'twisted' group ${}^2F_4(q)$ is constructed as follows. The so-called automorphism σ is selected in the Dynkin diagram (see Fig. 1). $1 \leftrightarrow 4$; $2 \leftrightarrow 3$. Apparently, it can be continued until some permutation of all roots, where the long root is mapped onto the short one, and vice versa. The so-called field automorphism $\Theta: x \rightarrow x^{2^n}$, is selected in the field F_{q^2} . Now the automorphism σ over group $F_4(q)$ acts on the generators $x_\alpha(t)$ that are root subgroups in the following manner:

$$\sigma: x_\alpha(t) \rightarrow \begin{cases} x_{\sigma(\alpha)}(t^\Theta), & \text{if } \alpha \text{ is the long root,} \\ x_{\sigma(\alpha)}(t^{2\Theta}), & \text{if } \alpha \text{ is the short root.} \end{cases}$$

The subgroup of σ -fixed elements in group $F_4(q)$ is precisely the required group ${}^2F_4(q)$, which is simple at $n \geq 1$. A separate case is group ${}^2F_4(2)$, for which the field automorphism Θ is identical provided that $n = 0$. This group is not simple, but its commutator $({}^2F_4(2))'$ of index 2 in ${}^2F_4(2)$ is.

Analysis of the group ${}^2F_4(q)$

The following statements are crucial for subsequent consideration of group ${}^2F_4(q)$.

Statement 1. *The involution class in a finite simple group contains commuting elements.*

It is not necessary to prove this, since it follows from Glauberman's theorem from group theory (see [7] for more details).

Statement 2. *If the number of classes containing elements of this order n with centralizers of the same order is less than $\varphi(n)$, the class contains commuting elements.*

Here $\varphi(n)$ is the Euler function.

This statement can be assumed to be elementary; it is also proved in [7].

Let us now examine the corresponding group.

Theorem 1. *The non-identity conjugacy class in group ${}^2F_4(q)$ contains commuting elements.*

Proof. Consider the data in Table 1, where the element classes and their centralizers for group $({}^2F_4(2))'$ are given (the table is taken from Atlas [16]). For example, Table shows a representative of the conjugacy class $8A, 8B^{**}$; this means that there are two classes $8A$ and $8B^{**}$ containing 8^{th} -order elements with 32^{nd} -order centralizers of the corresponding elements. The presence of commuting elements in the involution class is guaranteed by virtue of Statement 1, assuming that this holds true for any finite simple group. Statement 2 is applied for the remaining classes.

The theorem is proved.

Let us now examine the classes of semisimple elements.

Theorem 2. *The semisimple element in group ${}^2F_4(q)$ is conjugate to its inverse.*

Proof. Notice that a semisimple element has an odd order, i.e., there are no involutions among semisimple elements. A semisimple element in the algebraic group \bar{G} , obtained from the group G by algebraic closure of the field F_q is conjugate to a Cartan element, i.e., an element of the form

Representatives of conjugacy classes
for group $({}^2F_4(2))'$

Element class	Centralizer
$2A$	10240
$2B$	1536
$3A$	102
$4A$	192
$4B$	128
$4C$	64
$5A$	50
$6A$	12
$8A, 8B^{**}$	32×2
$8C, 8D$	16×2
$10A$	10
$12A, 12B$	12×2
$13A, 13B^*$	13×2
$16A, 16B^{**},$ $16C^{*5}, 16D^{*5}$	16×4

$$h_{\alpha_1}(t_1)h_{\alpha_2}(t_2)\dots,$$

where $\alpha_1, \alpha_2, \alpha_3, \dots$ are simple roots.

We use ω to denote an element of the Weil group, which can be obtained by taking the product of reflections relative to four orthogonal roots, for example, relative to vectors e_1, e_2, e_3, e_4 . Conjugating the Cartan element using ω converts it into an equality

$$h_{w(\alpha_1)}(t_1)h_{w(\alpha_2)}(t_2)\dots = h_{-\alpha_1}(t_1)h_{-\alpha_2}(t_2)\dots$$

However, the element $h_{-\alpha}(t)h_{-\alpha}(t^{-1})$ commutes with elements of any root subgroup $x_{\beta}(u)$, and the center in the universal adjoint group of type F_4 is trivial [17]. Therefore, $h_{-\alpha}(t) = (h_{\alpha}(t))^{-1}$ is conjugate to $h_{\alpha}(t)$. Thus, a semisimple element is conjugate to the inverse in the algebraic group. Conjugacy in subgroup ${}^2F_4(q)$ of the algebraic group follows from the above observation on the triviality of the center [17, 18].

Further reasoning here is as follows. The algebraic group F_4 is simply connected, the centralizer of the semisimple element is connected (see [17, p. 192, sentence 3.9]). Making a transition from the algebraic group G to G_{σ} , there is no splitting of the class of semisimple elements, i.e., the element from the group G_{σ} conjugate in G is also conjugate in G_{σ} (see [17], p. 171, 3.4 (c)). Conjugacy of a semisimple element to the inverse in an algebraic group is discussed above.

The theorem is proved.

Next, we consider the class of unipotent elements.

There are 18 classes of unipotents in ${}^2F_4(q)$, listed in [13] together with the order of centralizers for the corresponding elements. Here we present a fragment of this table.

Selected classes of unipotent elements

u	$ Z(u) $	$u \sim x$
u_1	$q^{12}(q-1)(q^2+1)$	x_3
u_2	$q^{10}(q^2-1)$	x_4
u_3	$2q^7(q-1)(q^2+1)$	x_{10}
u_4	$2q^7(q-1)(q^2+1)$	x_{10}
u_{11}	$4q^4$	x_{28}
u_{12}	$4q^4$	x_{28}
u_{13}	$2q^3$	x_{29}
u_{14}	$2q^3$	x_{29}
u_{15}	$4q^4$	x_{34}
u_{16}	$4q^2$	x_{32}
u_{17}	$4q^2$	x_{34}
u_{18}	$4q^2$	x_{32}

Note: u_i, x_i are the class representatives in subgroups ${}^2F_4(q)$ and in $F_4(q)$, respectively, $|Z(u)|$ is the order of the centralizer $Z(u)$ of the corresponding element.

The table compiled by Shinoda [13] does not provide classes x_5-x_{10} because the corresponding representatives are conjugate to the inverse ones as the centralizer order has a single value.

The orders of class representatives x_i are given in [15]. In particular, the representatives of classes u_1 and u_2 are involutions (x_3, x_4 have the order equal to 2). Consequently, they contain commuting elements, by virtue of Statement 1. The orders of elements u_{11} and u_{12} , equal to the order of elements x_{28} , are equal to 8, so, according to Statement 1, both classes contain commuting elements. The same reasoning applies for classes u_{13} and u_{14} , whose orders of elements are equal to 8, and for classes $u_{15}-u_{18}$, whose orders of elements are equal to 16.

Now the remaining step is to consider classes with the representatives

$$u_3 = x_2(1)x_{1-2}(1)x_4(1)x_1(1)x_{1+2}(1) \text{ and } u_4 = x_2(1)x_{1-2}(1)x_4(1).$$

Both classes are inverse to each other, which is easy to verify using the commutation formula or, alternately, taking into account that both classes merge to $F_4(q)$. Thus, it is sufficient to consider one of them, for example x_4 .

We obtain the following equality:

$$u_4 = \alpha_5(1) = x_2(1)x_{1-2}(1)x_4(1).$$

This element lies in a subgroup generated by the root subgroups

$$x_{\pm 2}(t), x_{\pm(1-2)}(t), x_{\pm 1}(t).$$

This subgroup corresponds to the following Dynkin diagram in Fig. 2.

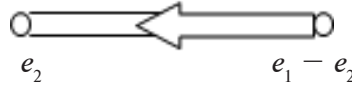


Fig. 2. Dynkin diagram:
 $e_2, (e_1 - e_2)$ are the roots of the graph vertices

The Dynkin diagram is constructed by the well-known technique, based on the scalar product of the vertex roots. A graphic automorphism represents the vertices, the field automorphism remains the same as in group $F_4(q)$.

The twisted variation leads to the Suzuki ${}^2B_2(q)$ group, for which the hypothesis put forward in [7] has already verified in [9]. Thus, the class of conjugate elements u_3 must contain commuting elements even in the subgroup ${}^2B_2(q) \subset {}^2F_4(q)$.

Let us now examine the class of mixed elements.

Shinoda [13] compiled information about mixed elements into a table, which is given below (Table 3).

Table 3 [13]

Classes of mixed elements

N	Class representative	Centralizer order
1	$t x_1(1) x_{1+2}(1)$	$q^2(q-1)$
2	$t x_{1-2}(1) x_2(1) x_1(1)$	$2q^2(q-1)$
3	$t x_{1-2}(1) x_2(1) x_{1+2}(1)$	$2q(q-1)$
4	$t x_{1+2+3+4}(1) x_{1-4}(1)$	$q(q-1)$
5	$t x_{1+2+3-4}(1) x_{1+4}(1)$	$q^3(q+1)$
6	$t x_{\alpha_1}(1) x_{\alpha_2}(1) x_{1+2+3-4}(\tau_0) x_{\beta_1}(1) x_{\beta_2}(1) x_{1+4}(\tau_0^{2\Theta})$	$3q^2$
7	$t x_{\alpha_1}(\eta) x_{\alpha_2}(\eta') x_{1+2+3-4}(\tau_1) x_{\beta_1}(\eta^{2\Theta}) x_{\beta_2}(\eta^{2\Theta'}) x_{1+4}(\tau_1^{2\Theta})$	$3q^2$
8	$t x_{\alpha_1}(\eta^2) x_{\alpha_2}(\eta^3) x_{1+2+3-4}(\tau_2) x_{\beta_1}(\eta^{4\Theta}) x_{\beta_2}(\eta^{4\Theta'}) x_{1+4}(\tau_2^{2\Theta})$	$3q^2$
9	$t x_{1+2+3-4}(1) x_{1+4}(1)$	$q(q+1)$
10	$t x_1(1) x_{1+2}(1)$	$q^2(q - \sqrt{2q} + 1)$
11	$t x_{1-2}(1) x_2(1) x_1(1)$	$2q(q - \sqrt{2q} + 1)$
12	$t x_{1-2}(1) x_2(1) x_{1+2}(1)$	$2q(q - \sqrt{2q} + 1)$
13	$t x_1(1) x_{1+2}(1)$	$q^2(q + \sqrt{2q} + 1)$
14	$t x_{1-2}(1) x_2(1) x_1(1)$	$2q(q + \sqrt{2q} + 1)$
15	$t x_{1-2}(1) x_2(1) x_{1+2}(1)$	$2q(q + \sqrt{2q} + 1)$

Table 4

Structure of centralizers for semisimple elements

t	Centralizer order	Structure
t_1	$(q-1)q^2(q-1)(q^2+1)$	$Z_{q-1} {}^2B_2(q)$
t_2	$(q-1)q(q-1)$	$Z_{q-1} SL_2(q)$
t_4	$3\frac{1}{3}q^3(q^2-1)(q^3+1)$	$Z_3 U_3(q)$
t_5	$(q+1)q(q^2-1)$	$Z_{q+1} SL_2(q)$
t_7	$(q-\sqrt{2q}+1)q^2(q-1)(q+1)$	$Z_{q-\sqrt{2q}+1} {}^2B_2(q)$
t_9	$(q+\sqrt{2q}+1)q^2(q-1)(q+1)$	$Z_{q+\sqrt{2q}+1} {}^2B_2(q)$

Conclusion

Here the representatives of the classes are written as a product of semisimple and unipotent factors, i.e., $x = x_u \cdot u_s$ is a decomposition of the mixed element into a product of a semisimple factor x_s and a unipotent u_s . The factors commute if the decomposition is of the Jordan type, but this requirement is not always satisfied in Table 3 for representatives of classes containing mixed elements. It follows from the existence of the Jordan-type decomposition of the mixed element that it lies in the centralizer of the semisimple factor. In turn, it is easy to determine the structure of the centralizers of semisimple factors. Each such centralizer $Z(t)$ contains powers of t and, being a reductive group, has a semisimple factor. It is not necessary to consider the elements $t_3, t_6, t_8, t_{10}, t_{11}, t_{12}$, since their centralizers do not contain unipotents of semisimple elements. Inspecting the centralizers $t_1, t_2, t_4, t_5, t_7, t_9$, we find that they have semisimple parts of the orders. The structure of the centralizers of the semisimple elements considered is given in Table 4, where the factor of type Z_m is a cyclic group consisting of the powers of t and included in the center of the centralizer t . The second factors ${}^2B_2(q), {}^2SL_2(q), U_3(q)$ represent a Suzuki group, a linear group and a unitary group, respectively. Notably, these factors are simple groups. The presence of commuting unipotent factors lying in the same class is proved in [7] for the Suzuki group ${}^2B_2(q)$ and the linear group ${}^{2SL}_2(q)$. The commutator of the Sylow r -subgroup for an identity group lies in its center. If the unipotent lies in the center, conjugating it to an element from the Cartan subgroup gives a commuting element from the same conjugacy class. If the unipotent u is not from the center of the Sylow p -subgroup, then there is another unipotent u' , not commuting with u . Elements u and $u'' = u' \cdot u \cdot (u')^{-1}$ lie in the same class and commute, since their commutator lies in the center of the Sylow p -subgroup. Elements x and $u' \cdot x \cdot (u')^{-1}$ clearly commute, lie in the same class, and are in fact different, since $u' \neq u''$. This concludes the consideration of mixed elements.

This study makes another step towards verifying the general hypothesis that a non-identity conjugacy class in a finite simple non-Abelian group contains commuting elements. We have described the methods for testing this hypothesis for the exceptional group ${}^2F_4(q)$.

The research methods used in the study can be directly applied to verifying the general hypothesis for analysis of other groups.

REFERENCES

1. Galkin V. M., Erofeeva L. N., Levodistributivnyye algebraicheskiye sistemy [Left-distribution algebraic systems], Publishing of Nizhni Novgorod State Technical University named after R. E. Alekseev, Nizhni Novgorod, 2018 (in Russian).
2. Helgason S., Differential geometry and symmetric spaces, 2nd edition, Amer. Mathematical Society, Providence, 2000.
3. Il'inykh A.P., Classification of finite groupoids with 2-transitive automorphism group, Sb. Math. 82 (1) (1995) 175–197.

4. Erofeeva L. N., K probleme tranzitivnosti L-gruppoidov [To the problem of groupoids' transitivity], Proceedings of the International Seminar on the Group Theory dedicated to 70-th anniversary of A. I. Starostin and 80-th anniversary of N. F. Sesekin; December 17–21, Ekaterinburg (2001) (in Russian).
5. Erofeeva L. N., Gruppya translyatsiy nekotorykh gruppoidov [Translation group of somegroupoids], Vestnik of Lobachevsky University of Nizhni Novgorod, Ser. Mathematics. (2) (2004) 96–100 (in Russian).
6. Erofeeva L. N., A class of groupoids, J. Math. Sci. 130 (3) (2005) 4720–4723.
7. Galkin V. M., Erofeeva L. N., Leshcheva S. V., Commuting elements in conjugacy class of finite groups, Russian Math. (Iz. VUZ). 60 (8) (2016) 9–16.
8. Erofeeva L. N., Leshcheva S. V., Mokhnina N. V., Yurova N. V., About simple group ${}^2G_2(q)$, Transactions of Nizhni Novgorod State Technical University n.a. R. Y. Alexeev. (3 (118)) (2017) 24–27 (in Russian).
9. Mokhnina N. V., Yurova N. V., Commuting elements in conjugacy classes in the group Suzuki, Transactions of Nizhni Novgorod State Technical University n.a. R. Y. Alexeev. (4 (119)) (2017) 45–50 (in Russian).
10. Leshcheva S. V., Yurova N. V., On conjugacy classes of the group ${}^3D_4(q)$, Transactions of Nizhni Novgorod State Technical University n.a. R. Y. Alexeev. (2 (125)) (2019) 53–60 (in Russian).
11. Yurova N. V., On conjugacy classes in the symplectic group $SP_4(q)$, Transactions of Nizhni Novgorod State Technical University n.a. R. Y. Alexeev. (4 (123)) (2018) 56–60 (in Russian).
12. Steinberg R., Lectures on Chevalley groups, Notes prepared by J. Faulkner and R. Wilson, Yale University, Department of Mathematics, New Haven, USA, 1967.
13. Shinoda K., Iwahori N., The conjugacy classes of the finite Ree groups of type (F_4) , J. Fac. Sci. Univ. Tokyo. Sec. 1A. Math. 22 (1975) 1–15.
14. Shinoda K., Iwahori N., The conjugacy classes of Chevalley groups of type (F_4) over finite fields of characteristic p_{ne2} , J. Fac. Sci. Univ. Tokyo. Sec. 1A. Math. 21 (1) (1974) 133–159.
15. Cao H. P., Chen C., Grechkoseeva M. A., et al., Recognition of the finite simple groups $F_4(2^m)$ by spectrum, Siberian Mathematical Journal. 45 (6) (2004) 1031–1035.
16. Conway I. H., Curtis R. T., Norton S. P., et al., Atlas of finite groups, Clarendon Press, Oxford, 1985.
17. Borel A., Carter R. W., Curtis Ch. W., et al., Seminar on algebraic groups and related finite groups: Held at the Institute for Advanced Study, Princeton, USA, 1968/1969 (Lecture Notes in Mathematics, Vol. 131), Springer, USA, 1970.
18. Gorenstein D., Finite simple groups, an introduction to their classification, Plenum Publishing Corporation, New York, London, 1982.

СПИСОК ЛИТЕРАТУРЫ

1. Галкин В. М., Ерофеева Л. Н. Леводистрибутивные алгебраические системы. Нижний Новгород: Нижегород. гос. техн. ун-т им. Р. Е. Алексеева, 2018. 158 с.
2. Хелгасон С. Дифференциальная геометрия и симметрические пространства. Пер. с англ. А. Л. Онищика. М.: Мир, 1964. 534с.
3. Ильиных А. П. Классификация конечных группOIDов с 2-транзитивной группой автоморфизма // Математический сборник. 1994. Т. 185. № 6. С. 51–78.
4. Ерофеева Л. Н. К проблеме транзитивности L-группOIDов // Международный семинар по теории групп, посвященный 70-летию А. И. Старостина и 80-летию Н. Ф. Сесекина; 17 – 21 декабря, г. Екатеринбург: Изд. Института математики и механики Уральского отделения РАН, 2001.
5. Ерофеева Л. Н. Группа трансляций некоторых группOIDов // Вестник Нижегородского университета им. Н. И. Лобачевского. Сер. Математика. 2004. № 2. С. 96–100.
6. Ерофеева Л. Н. Об одном классе группOIDов // Записки научных семинаров ПОМИ. 2003. Т. 305. С. 136–143.
7. Галкин В. М., Ерофеева Л. Н., Лещева С. В. Коммутирующие элементы в классе сопряженности конечных групп // Известия вузов. Математика. 2016. № 8. С. 12–20.
8. Ерофеева Л. Н., Лещева С. В., Мохнина Н. В., Юрова Н. В. О простой группе Ри ${}^2G_2(q)$ // Труды НГТУ им. Р. Е. Алексеева. 2017. № 3 (118). С. 24–27.

9. Мохнина Н. В., Юрова Н. В. Коммутирующие элементы в классах сопряженности в группе Сузуки ${}^2B_2(q)$ // Труды НГТУ им. Р. Е. Алексеева. 2017. № 4 (119). С. 45–50.
10. Лещева С. В., Юрова Н. В. О классах сопряженности в группе ${}^3D_4(q)$ // Труды НГТУ им. Р. Е. Алексеева. 2019. № 2 (125). С. 53–60.
11. Юрова Н. В. О классах сопряженности в симплектической группе $SP_4(q)$ // Труды НГТУ им. Р. Е. Алексеева. 2018. № 4 (123). С. 56–60.
12. Стейнберг Р. Лекции о группах Шевалле. Пер. с англ. И. Н. Бернштейна и Н. Н. Яковлева. М.: Мир, 1975. 263 с.
13. Shinoda K., Iwahori N. The conjugacy classes of the finite Ree groups of type (F_4) // Journal of the Faculty of Science, the University of Tokyo. Sec. 1A. Mathematics. 1975. Vol. 22. Pp. 1–15.
14. Shinoda K., Iwahori N. The conjugacy classes of Chevalley groups of type (F_4) over finite fields of characteristic p_{ne2} // Journal of the Faculty of Science, the University of Tokyo. Sec. 1A. Mathematics. 1974. Vol. 21. No. 1. Pp. 133–159.
15. Васильев А. В., Гречкосеева М. А., Мазуров В. Д., Чао Х. П., Чен Г. Ю., Ши В. Д. Распознавание конечных простых групп $F_4(2^m)$ по спектру // Сибирский математический журнал. 2004. Т. 45. № 6. С. 1256–1262.
16. Conway I. H., Curtis R. T., Norton S. P., Parker R. A., Wilson R. A. Atlas of finite groups. Oxford: Clarendon Press, 1985. 252 p.
17. Семинар по алгебраическим группам. Сборник статей (А. Борель, Ч. Кэтрис, Т. Спрингер и др.). Пер. с англ. С. И. Гельфанда. Ред. А. А. Кириллов. М.: Мир, 1973. 317 с.
18. Горенштейн Д. Конечные простые группы. Введение в их классификацию. Пер. с англ. В. И. Логинова. М.: Мир, 1985. 352 с.

THE AUTHOR

YUROVA Nadezhda V.

Nizhni Novgorod State Technical University named after R.E. Alekseev

24, Minin St., Nizhni Novgorod, 603950, Russia

yurova1980@yandex.ru

ORCID: 0000-0003-2355-2820

СВЕДЕНИЯ ОБ АВТОРЕ

ЮРОВА Надежда Вячеславовна — старший преподаватель Института транспортных систем Нижегородского государственного технического университета имени Р. Е. Алексеева.

603950, Россия, г. Нижний Новгород, ул. Минина, 24

yurova1980@yandex.ru

ORCID: 0000-0003-2355-2820

Received 29.03.2021. Approved after reviewing 19.03.2022. Accepted 19.03.2022.

Статья поступила в редакцию 29.03.2021. Одобрена после рецензирования 19.03.2022. Принята 19.03.2022.

Original article

DOI: <https://doi.org/10.18721/JPM.15210>

CALCULATION OF MIXED MODE STRESS INTENSITY FACTORS FOR ORTHOTROPIC MATERIALS IN THE PLANE STRESS STATE

A. V. Savikovskii , *A. S. Semenov*

Peter the Great St. Petersburg Polytechnic University, St. Petersburg, Russia

 savikovskij.av@edu.spbstu.ru

Abstract. In the article, stress intensity factors for a straight crack of a mixed-fracture mode in the orthotropic material and in its particular case, namely, in the material with cubic symmetry, have been calculated. The displacement and stress extrapolation method based on the Lekhnitskii formalism was used. For considered classes of materials, the explicit expressions for influence matrix elements were obtained through the elastic constants of the material in the cases of its planar-stressed state and given a non-zero angle between the material's anisotropy and the crack's axes. Influence matrix properties were analyzed systematically. The obtained results of verification of considered variants of the displacement and stress extrapolation method exhibited a good agreement between the numerical and analytical solutions (the difference did not exceed 0.8 %).

Keywords: Lekhnitskii formalism, orthotropic material, stress intensity factor, mixed-mode fracture

Citation: Savikovskii A. V., Semenov A. S., Calculation of mixed-mode stress intensity factors for orthotropic materials in the plane stress state, St. Petersburg Polytechnical State University Journal. Physics and Mathematics. 15 (2) (2022) 102–123. DOI: <https://doi.org/10.18721/JPM.15210>

This is an open access article under the CC BY-NC 4.0 license (<https://creativecommons.org/licenses/by-nc/4.0/>)



Научная статья

УДК 539.3, 539.42

DOI: <https://doi.org/10.18721/JPM.15210>

ВЫЧИСЛЕНИЕ КОЭФФИЦИЕНТОВ ИНТЕНСИВНОСТИ НАПРЯЖЕНИЙ В ОРТОТРОПНЫХ МАТЕРИАЛАХ ПРИ СМЕШАННОЙ МОДЕ РАЗРУШЕНИЯ В ПЛОСКОМ НАПРЯЖЕННОМ СОСТОЯНИИ

А. В. Савиковский , А. С. Семенов

Санкт-Петербургский политехнический университет Петра Великого, Санкт-Петербург, Россия

 savikovskij.av@edu.spbstu.ru

Аннотация. Статья посвящена вычислению коэффициентов интенсивности напряжений для прямолинейной трещины смешанной моды разрушения в ортотропном материале и его частном случае – материале с кубической симметрией. Использован метод экстраполяции перемещений и напряжений на основе формализма Лехницкого. Для рассмотренных классов материалов получены в явном виде выражения для элементов матрицы влияния через упругие константы материала в случаях его плосконапряженного состояния и наличия ненулевого угла между осями анизотропии материала и трещины. Систематически проанализированы свойства матрицы влияния. Полученные результаты верификации рассмотренных вариантов метода перемещений и напряжений показали хорошее согласие между численными и аналитическими решениями (отличие не превосходит 0.8%).

Ключевые слова: формализм Лехницкого, ортотропный материал, коэффициент интенсивности напряжений, смешанная мода разрушения

Для цитирования: Савиковский А. В., Семенов А. С. Вычисление коэффициентов интенсивности напряжений в ортотропных материалах при смешанной моде разрушения в плоском напряженном состоянии // Научно-технические ведомости СПбГПУ. Физико-математические науки. 2022. Т. 2 № .15. С. 102–123. DOI: <https://doi.org/10.18721/JPM.15210>

Статья открытого доступа, распространяемая по лицензии CC BY-NC 4.0 (<https://creativecommons.org/licenses/by-nc/4.0/>)

Introduction

Heat-resistant single-crystal nickel-based alloys [1–3] are widely used as a structural material for critical components (primarily blades) of gas turbine engines (GTE) [4–7] operating at temperatures above 1000 °C [8, 9]. Microstructurally, heat-resistant nickel alloys consist of an γ -phase (a Ni-based solid solution) and a strengthening γ' -phase [1, 4, 7]. Single-crystal nickel alloys have cubic symmetry of thermoelastic properties and can be regarded as a particular case of an orthotropic material with isotropic properties along the crystallographic axes [100], [010] and [001].

Cooled GTE blades made of heat-resistant nickel alloys are the most loaded elements in the engine [10–15], acted on by centrifugal forces and gas pressure, as well as unsteady and non-uniform temperature fields. Different kinds of combined variable loads induce fatigue, creep and thermal cracks in GTE blades [4, 16, 17].

The phenomena of thermal fatigue, initiation and propagation of cracks in single-crystal Ni alloys are often studied experimentally, for example, in hourglass specimens [4]. The initiation of a thermal fatigue crack in an hourglass specimen was simulated in [18, 19] by the finite element method (FEM). Evaluating crack resistance in nickel alloys and constructing approaches to calculating fracture parameters in the cases of cubic symmetry and orthotropic materials is a crucial challenge that is yet to be addressed conclusively.

We consider the stress intensity factors (SIFs) as the main fracture parameters in this study. In general, SIF calculations in anisotropic materials should be supported by analysis of mixed fracture modes.

The goal of this study consisted in obtaining explicit formulas for calculating the SIF in terms of crack edge displacements in the vicinity of the crack tip.

A numerical method is used for this purpose, extrapolating the displacements to the crack tip in a material with cubic symmetry and in an orthotropic material. A stress extrapolation method is also considered as an example.

The Lekhnitskii formalism is an effective technique used to achieve this [20]. We verified the proposed relations, testing the stress extrapolation method for isotropic and orthotropic materials, as well as for a material with cubic symmetry.

Constitutive equations

The constitutive equations for a linear elastic material take the following form [21, 22]:

$$\boldsymbol{\varepsilon} = {}^4\mathbf{S} \cdot \boldsymbol{\sigma}, \quad (1)$$

where $\boldsymbol{\varepsilon}$ is the strain tensor, $\boldsymbol{\sigma}$ is the stress tensor, ${}^4\mathbf{S}$ is the elastic compliance tensor of the material.

System of linear equations (1) can be conveniently rewritten in matrix form:

$$\{\boldsymbol{\varepsilon}\} = [\mathbf{S}]\{\boldsymbol{\sigma}\}, \quad (2)$$

where the notations for vector columns composed of tensor components are introduced:

$$\{\boldsymbol{\varepsilon}\} = \begin{Bmatrix} \varepsilon_{xx} \\ \varepsilon_{yy} \\ \varepsilon_{zz} \\ \gamma_{yz} \\ \gamma_{xz} \\ \gamma_{xy} \end{Bmatrix} \quad \text{and} \quad \{\boldsymbol{\sigma}\} = \begin{Bmatrix} \sigma_{xx} \\ \sigma_{yy} \\ \sigma_{zz} \\ \sigma_{yz} \\ \sigma_{xz} \\ \sigma_{xy} \end{Bmatrix}.$$

The order in which the components are listed corresponds to the Voigt notation.

The 6×6 elastic compliance matrix $[\mathbf{S}]$ corresponding to the compliance tensor ${}^4\mathbf{S}$ has a different form for materials with different structures.

Case of orthotropic material:

$$[\mathbf{S}] = \begin{pmatrix} \frac{1}{E_1} & -\frac{\nu_{12}}{E_1} & -\frac{\nu_{13}}{E_1} & 0 & 0 & 0 \\ -\frac{\nu_{12}}{E_1} & \frac{1}{E_2} & -\frac{\nu_{23}}{E_2} & 0 & 0 & 0 \\ -\frac{\nu_{13}}{E_1} & -\frac{\nu_{23}}{E_2} & \frac{1}{E_3} & 0 & 0 & 0 \\ 0 & 0 & 0 & \frac{1}{G_{23}} & 0 & 0 \\ 0 & 0 & 0 & 0 & \frac{1}{G_{13}} & 0 \\ 0 & 0 & 0 & 0 & 0 & \frac{1}{G_{12}} \end{pmatrix}, \quad (3)$$

where E_1, E_2, E_3 are Young's moduli; G_{23}, G_{13}, G_{12} are shear moduli; $\nu_{23}, \nu_{13}, \nu_{12}$ are Poisson's ratios.

Case of cubic symmetry:

$$[\mathbf{S}] = \begin{pmatrix} \frac{1}{E} & -\frac{\nu}{E} & -\frac{\nu}{E} & 0 & 0 & 0 \\ -\frac{\nu}{E} & \frac{1}{E} & -\frac{\nu}{E} & 0 & 0 & 0 \\ -\frac{\nu}{E} & -\frac{\nu}{E} & \frac{1}{E} & 0 & 0 & 0 \\ 0 & 0 & 0 & \frac{1}{G} & 0 & 0 \\ 0 & 0 & 0 & 0 & \frac{1}{G} & 0 \\ 0 & 0 & 0 & 0 & 0 & \frac{1}{G} \end{pmatrix}. \quad (4)$$

Case of isotropic material:

$$[\mathbf{S}] = \begin{pmatrix} \frac{1}{E} & -\frac{\nu}{E} & -\frac{\nu}{E} & 0 & 0 & 0 \\ -\frac{\nu}{E} & \frac{1}{E} & -\frac{\nu}{E} & 0 & 0 & 0 \\ -\frac{\nu}{E} & -\frac{\nu}{E} & \frac{1}{E} & 0 & 0 & 0 \\ 0 & 0 & 0 & \frac{2(1+\nu)}{E} & 0 & 0 \\ 0 & 0 & 0 & 0 & \frac{2(1+\nu)}{E} & 0 \\ 0 & 0 & 0 & 0 & 0 & \frac{2(1+\nu)}{E} \end{pmatrix}. \quad (5)$$

where E is Young's modulus, G is the shear modulus, ν is Poisson's ratio.

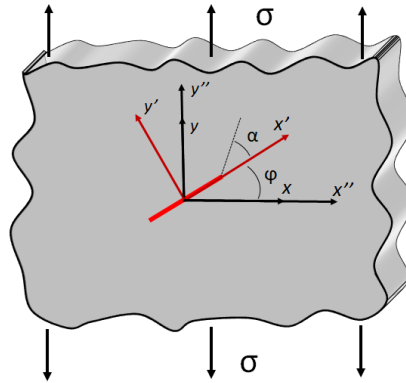


Fig. 1. Schematic diagram of uniaxial tension in the orthotropic plane with a single oblique straight crack (marked with a red line):

x, y are the axes of the global coordinate system; x', y' are the axes of the crack coordinate system; x'', y'' are the anisotropy axes of the material; φ is the crack orientation angle, α is the angle between the direction to the point and the crack axis; the arrows indicate the loading direction (σ is the uniaxial tensile stress)

Numerical methods for finding the SIF and the Lekhnitskii formalism

We consider the problem on uniaxial tension in an orthotropic plane (plate) with a single oblique straight crack assuming a plane stress state. The axes of the coordinate system introduced coincide with the anisotropy axes of the material and the loading direction. The orientation of the crack does not coincide with the anisotropy axes of the material and the loading direction (Fig. 1).

Asymptotic expressions for displacements in the vicinity of the crack tip in the general three-dimensional case for three fracture modes (non-zero values of the coefficients K_I , K_{II} , K_{III}) are represented for isotropic material by the relations given in monograph [22]. Similar expressions for anisotropic material are obtained using the Lekhnitskii formalism; they have the following form [23–25]:

$$\begin{aligned}
 u_x(r, \alpha) &= \frac{K_I \sqrt{2r}}{\sqrt{\pi}} \cdot \operatorname{Re} \left(\frac{1}{\mu'_1 - \mu'_2} \left(\mu'_1 p_2 \sqrt{\cos \alpha + \mu'_2 \sin \alpha} - \mu'_2 p_1 \sqrt{\cos \alpha + \mu'_1 \sin \alpha} \right) \right) + \\
 &+ \frac{K_{II} \sqrt{2r}}{\sqrt{\pi}} \cdot \operatorname{Re} \left(\frac{1}{\mu'_1 - \mu'_2} \left(p_2 \sqrt{\cos \alpha + \mu'_2 \sin \alpha} - p_1 \sqrt{\cos \alpha + \mu'_1 \sin \alpha} \right) \right), \\
 u_y(r, \alpha) &= \frac{K_I \sqrt{2r}}{\sqrt{\pi}} \cdot \operatorname{Re} \left(\frac{1}{\mu'_1 - \mu'_2} \left(\mu'_1 q_2 \sqrt{\cos \alpha + \mu'_2 \sin \alpha} - \mu'_2 q_1 \sqrt{\cos \alpha + \mu'_1 \sin \alpha} \right) \right) + \\
 &+ \frac{K_{II} \sqrt{2r}}{\sqrt{\pi}} \cdot \operatorname{Re} \left(\frac{1}{\mu'_1 - \mu'_2} \left(q_2 \sqrt{\cos \alpha + \mu'_2 \sin \alpha} - q_1 \sqrt{\cos \alpha + \mu'_1 \sin \alpha} \right) \right), \\
 u_z(r, \alpha) &= \frac{K_{III} \sqrt{2r}}{\sqrt{\pi}} \cdot \operatorname{Re} \left(\frac{\sqrt{\cos \alpha + \mu'_3 \sin \alpha}}{C'_{45} + \mu'_3 C'_{44}} \right),
 \end{aligned} \tag{6}$$

where $u_x(r, \alpha)$, $u_y(r, \alpha)$, $u_z(r, \alpha)$ are the axial displacements in the coordinate system of the crack; K_I , K_{II} , K_{III} are the SIFs for fracture modes I, II, III; G is the shear modulus; r is the distance from the crack tip to the given point; α is the angle between the direction to the point and the crack axis; ν is Poisson's ratio; C'_{ij} are the constants of the material's stiffness matrix in the coordinate system of the crack, $[C] = [S]^{-1}$; $p_i = S'_{11}\mu_i'^2 + S'_{12} - S'_{16}\mu_i'$, $q_i = S'_{12}\mu_i' + S'_{22}/\mu_i' - S'_{26}\mu_i'$ (S'_{ij} are the constants of the material's compliance matrix in the coordinate system of the crack); μ'_1 , μ'_2 are the roots of the 4th-order equation taking the form

$$S'_{11}\mu^4 - 2S'_{16}\mu^3 + (2S'_{12} + S'_{66})\mu^2 - 2S'_{26}\mu + S'_{22} = 0, \quad (7)$$

with a positive imaginary part; μ'_3 is the root of the equation

$$C'_{44}\mu^2 - 2C'_{45}\mu + C'_{55} = 0,$$

also with a positive imaginary part.

Displacements along the free edges of the crack are determined using the expressions presented in monograph [22], where the angle between the direction to the point and the crack axis α is taken equal to π . The obtained expressions can be used to find the SIF values in terms of crack edge displacements; if the material is isotropic, they take the form

$$\begin{aligned} K_I &= u_y(r, \pi) \sqrt{\frac{2\pi}{r}} \cdot \frac{2G}{1+\kappa}, \\ K_{II} &= u_x(r, \pi) \sqrt{\frac{2\pi}{r}} \cdot \frac{2G}{1+\kappa}, \\ K_{III} &= u_z(r, \pi) \sqrt{\frac{2\pi}{r}} \cdot G. \end{aligned} \quad (8)$$

If the material is anisotropic, substituting $\alpha = \pi$ in expression (6), we obtain an equation of the form

$$\{\mathbf{u}\} = \sqrt{\frac{2r}{\pi}} [\mathbf{B}] \cdot \{\mathbf{K}\}, \quad (9)$$

where $\{\mathbf{u}\} = \begin{Bmatrix} u_x(r, \pi) \\ u_y(r, \pi) \\ u_z(r, \pi) \end{Bmatrix}$, $\{\mathbf{K}\} = \begin{Bmatrix} K_I \\ K_{II} \\ K_{III} \end{Bmatrix}$;

$$[\mathbf{B}] = \begin{pmatrix} \operatorname{Re}\left(\frac{\mu'_1 p_2 - \mu'_2 p_1}{\mu'_1 - \mu'_2} i\right) & \operatorname{Re}\left(\frac{p_2 - p_1}{\mu'_1 - \mu'_2} i\right) & 0 \\ \operatorname{Re}\left(\frac{\mu'_1 q_2 - \mu'_2 q_1}{\mu'_1 - \mu'_2} i\right) & \operatorname{Re}\left(\frac{q_2 - q_1}{\mu'_1 - \mu'_2} i\right) & 0 \\ 0 & 0 & \frac{1}{\sqrt{C'_{44}C'_{55} - C'^2_{45}}} \end{pmatrix} \text{ is a } 3 \times 3 \text{ influence matrix for}$$

three components in the vector of the crack's relative edge displacement versus three SIFs.

Inverting Eq. (9) allows to calculate the SIF in terms of the edge displacements for the case of anisotropic material [26, 27]:

$$\{\mathbf{K}\} = \sqrt{\frac{\pi}{2r}} \cdot [\mathbf{B}]^{-1} \cdot \{\mathbf{u}\}, \quad (10)$$

$$\text{where } [\mathbf{B}]^{-1} = \begin{pmatrix} \frac{1}{\det[\mathbf{D}]} \operatorname{Re}\left(\frac{\mu'_1 p_2 - \mu'_2 p_1}{\mu'_1 - \mu'_2} i\right) & \frac{1}{\det[\mathbf{D}]} \operatorname{Re}\left(-\frac{p_2 - p_1}{\mu'_1 - \mu'_2} i\right) & 0 \\ \frac{1}{\det[\mathbf{D}]} \operatorname{Re}\left(-\frac{\mu'_1 q_2 - \mu'_2 q_1}{\mu'_1 - \mu'_2} i\right) & \frac{1}{\det[\mathbf{D}]} \operatorname{Re}\left(\frac{q_2 - q_1}{\mu'_1 - \mu'_2} i\right) & 0 \\ 0 & 0 & \sqrt{C'_{44}C'_{55} - C'^2_{45}} \end{pmatrix}, \quad (11)$$

$$\det[\mathbf{D}] = \begin{vmatrix} \operatorname{Re}\left(\frac{\mu'_1 p_2 - \mu'_2 p_1}{\mu'_1 - \mu'_2} i\right) & \operatorname{Re}\left(\frac{p_2 - p_1}{\mu'_1 - \mu'_2} i\right) \\ \operatorname{Re}\left(\frac{\mu'_1 q_2 - \mu'_2 q_1}{\mu'_1 - \mu'_2} i\right) & \operatorname{Re}\left(\frac{q_2 - q_1}{\mu'_1 - \mu'_2} i\right) \end{vmatrix}.$$

Notably, if the coordinate system of the crack does not coincide with the anisotropy axes of the material (which is what happens in mixed fracture mode), the constants of the compliance and stiffness matrices must be converted to the coordinate system of the crack, while the roots μ'_1, μ'_2 must be found from the 4th-order equation with compliance constants in the coordinate system of the crack.

If the coordinate system is rotated, the transition matrix from one coordinate system to the other for rotation in the plane by the angle φ has the form

$$Q = \begin{pmatrix} \cos \varphi & \sin \varphi & 0 \\ -\sin \varphi & \cos \varphi & 0 \\ 0 & 0 & 1 \end{pmatrix}$$

and the equation for transforming the elements of the elastic compliance tensor and 4th-order elastic moduli from the initial to the new coordinate system has the following form:

$$\begin{aligned} S'_{ijkl} &= Q_{im} \cdot Q_{jn} \cdot Q_{ko} \cdot Q_{lp} \cdot S_{mnop}, \\ C'_{ijkl} &= Q_{im} \cdot Q_{jn} \cdot Q_{ko} \cdot Q_{lp} \cdot C_{mnop}, \end{aligned} \quad (12)$$

where S_{mnop}, S'_{ijkl} are the elements of the compliance tensor in the initial and rotated (associated with the crack) coordinate systems, respectively; C_{mnop}, C'_{ijkl} are the elements of the stiffness tensor in the initial and rotated (associated with the crack) coordinate systems, respectively.

To use Eqs. (8) and (10), the displacements must also be converted from the global coordinate system to the coordinate system associated with the crack.

Rotating the plane at an angle φ for the case of an orthotropic material and transforming the tensors of elastic moduli, elastic compliances and rotation into 6×6 matrices (since $S_{16} = S_{26} = S_{45} = 0$ for the orthotropic material), then Eqs. (12) take the form given by Lekhnitskii [20, 28].

Thus, provided that the displacements of the crack edges and the elastic properties of the material are known, the SIF can be calculated by the displacement method.

Asymptotic expressions for stresses near the crack tip in the three-dimensional case, when the fracture modes I, II and III are observed, and the factors K_I, K_{II}, K_{III} are determined for the isotropic material by the relations [22, 29]. Considering the stresses on the path along which the crack grows in the vicinity of the crack tip, i.e., at $\alpha = 0$, and expressing the SIFs in terms of stresses, we obtain the following expressions for the isotropic material:

$$\begin{aligned} K_I &= \sigma_{yy}(r, 0) \cdot \sqrt{2\pi r}, \\ K_{II} &= \sigma_{xy}(r, 0) \cdot \sqrt{2\pi r}, \\ K_{III} &= \sigma_{yz}(r, 0) \cdot \sqrt{2\pi r}. \end{aligned} \quad (13)$$

Asymptotic expressions derived based on the Lekhnitskii formalism for stresses near the crack tip in the three-dimensional case take the following form for the anisotropic material [23–25, 30, 31]:

$$\begin{aligned}
 \sigma_{xx}(r, \alpha) &= \frac{K_I}{\sqrt{2\pi r}} \cdot \operatorname{Re} \left(\frac{\mu'_1 \mu'_2}{\mu'_1 - \mu'_2} \left(\frac{\mu'_2}{\sqrt{\cos \alpha + \mu'_2 \sin \alpha}} - \frac{\mu'_1}{\sqrt{\cos \alpha + \mu'_1 \sin \alpha}} \right) \right) + \\
 &\quad + \frac{K_{II}}{\sqrt{2\pi r}} \cdot \operatorname{Re} \left(\frac{1}{\mu'_1 - \mu'_2} \left(\frac{\mu'^2_2}{\sqrt{\cos \alpha + \mu'_2 \sin \alpha}} - \frac{\mu'^2_1}{\sqrt{\cos \alpha + \mu'_1 \sin \alpha}} \right) \right), \\
 \sigma_{yy}(r, \alpha) &= \frac{K_I}{\sqrt{2\pi r}} \cdot \operatorname{Re} \left(\frac{1}{\mu'_1 - \mu'_2} \left(\frac{\mu'_1}{\sqrt{\cos \alpha + \mu'_2 \sin \alpha}} - \frac{\mu'_2}{\sqrt{\cos \alpha + \mu'_1 \sin \alpha}} \right) \right) + \\
 &\quad + \frac{K_{II}}{\sqrt{2\pi r}} \cdot \operatorname{Re} \left(\frac{1}{\mu'_1 - \mu'_2} \left(\frac{1}{\sqrt{\cos \alpha + \mu'_2 \sin \alpha}} - \frac{1}{\sqrt{\cos \alpha + \mu'_1 \sin \alpha}} \right) \right), \\
 \sigma_{xy}(r, \alpha) &= \frac{K_I}{\sqrt{2\pi r}} \cdot \operatorname{Re} \left(\frac{\mu'_1 \mu'_2}{\mu'_1 - \mu'_2} \left(\frac{1}{\sqrt{\cos \alpha + \mu'_2 \sin \alpha}} - \frac{1}{\sqrt{\cos \alpha + \mu'_1 \sin \alpha}} \right) \right) + \\
 &\quad + \frac{K_{II}}{\sqrt{2\pi r}} \cdot \operatorname{Re} \left(\frac{1}{\mu'_1 - \mu'_2} \left(\frac{\mu'_1}{\sqrt{\cos \alpha + \mu'_2 \sin \alpha}} - \frac{\mu'_2}{\sqrt{\cos \alpha + \mu'_1 \sin \alpha}} \right) \right), \\
 \sigma_{xz}(r, \alpha) &= -\frac{K_{III}}{\sqrt{2\pi r}} \cdot \operatorname{Re} \left(\frac{\mu'_3}{\sqrt{\cos \alpha + \mu'_3 \sin \alpha}} \right), \quad \sigma_{yz}(r, \alpha) = \frac{K_{III}}{\sqrt{2\pi r}} \cdot \operatorname{Re} \left(\frac{\mu'_3}{\sqrt{\cos \alpha + \mu'_3 \sin \alpha}} \right),
 \end{aligned} \tag{14}$$

where $\sigma_{ij}(r, \alpha)$ are the components of the stress tensor in the coordinate system of the crack.

Considering expressions (14) at $\alpha = 0$ and expressing the SIFs in terms of stresses, we obtain the equations coinciding with the isotropic case for the anisotropic material:

$$\begin{aligned}
 K_I &= \sigma_{yy}(r, 0) \cdot \sqrt{2\pi r}, \\
 K_{II} &= \sigma_{xy}(r, 0) \cdot \sqrt{2\pi r}, \\
 K_{III} &= \sigma_{yz}(r, 0) \cdot \sqrt{2\pi r}.
 \end{aligned} \tag{15}$$

Thus, we can use the stresses in the vicinity of the crack tip to find the SIFs for both isotropic and anisotropic materials, so that the resulting expressions are the same. Notably, if Eqs. (13)–(15) are used, the stresses must be converted to the coordinate system of the crack.

Calculation of the matrix $[\mathbf{B}]^{-1}$ in terms of elastic moduli

We have established in the previous section that the SIF can be found from the displacements via Eq. (10) for the anisotropic material. Let us now obtain explicit expressions for the roots of the 4th-order equation and the matrix $[\mathbf{B}]^{-1}$ in terms of the elastic moduli of the orthotropic material in the case of a plane stress state, when the crack is in the plane xy . Consider first the 4th-order equation (7), when the coordinate system of the crack coincides with the coordinate system of the material:

$$S_{11}\mu^4 - 2S_{16}\mu^3 + (2S_{12} + S_{66})\mu^2 - 2S_{26}\mu + S_{22} = 0, \tag{16}$$

We substitute the coefficients S_{ij} for the case of the plane stress state and multiply by E_1 ; then, because Eq. (7) holds true, we obtain the equation:

$$\mu^4 + \left(\frac{E_1}{G_{12}} - 2\nu_{12} \right) \mu^2 + \frac{E_1}{E_2} = 0. \tag{17}$$

The roots of Eq. (17) depend on the elastic constants of the material. Thus, there are two cases for the roots of Eq. (17).

Case 1. If $\left(\frac{E_1}{G_{12}} - 2\nu_{12}\right)^2 - 4\frac{E_1}{E_2} < 0$, then the roots are expressed as follows:

$$\begin{aligned}\mu_1 &= A + iB, \\ \mu_2 &= -A + iB,\end{aligned}\tag{18}$$

$$\text{where } A = \frac{\sqrt{2\sqrt{\frac{E_1}{E_2}} - \left(\frac{E_1}{G_{12}} - 2\nu_{12}\right)}}{2}, \quad B = \frac{\sqrt{2\sqrt{\frac{E_1}{E_2}} + \left(\frac{E_1}{G_{12}} - 2\nu_{12}\right)}}{2}.$$

Case 2. If $\left(\frac{E_1}{G_{12}} - 2\nu_{12}\right)^2 - 4\frac{E_1}{E_2} \geq 0$, then the roots are expressed as follows:

$$\begin{aligned}\mu_1 &= i(b^* + a^*), \\ \mu_2 &= i(b^* - a^*),\end{aligned}\tag{19}$$

$$\text{where } b^* = \frac{\sqrt{\left(\frac{E_1}{G_{12}} - 2\nu_{12}\right) + 2\sqrt{\frac{E_1}{E_2}}}}{2}, \quad a^* = \frac{\sqrt{\left(\frac{E_1}{G_{12}} - 2\nu_{12}\right) - 2\sqrt{\frac{E_1}{E_2}}}}{2}.$$

To find the roots of the equation for the case when the coordinate system of the crack does not coincide with the coordinate system of the material, we should transform the roots obtained. If the coordinate system is rotated by the angle φ , the roots of the equation in the initial and rotated coordinate systems are related as follows [20]:

$$\begin{aligned}\mu'_1 &= \frac{\mu_1 \cos \varphi - \sin \varphi}{\cos \varphi + \mu_1 \sin \varphi}, \\ \mu'_2 &= \frac{\mu_2 \cos \varphi - \sin \varphi}{\cos \varphi + \mu_2 \sin \varphi}.\end{aligned}\tag{20}$$

Case 1. If $\left(\frac{E_1}{G_{12}} - 2\nu_{12}\right)^2 - 4\frac{E_1}{E_2} < 0$, then, substituting expression (18) into Eq. (20), we obtain after the transformations:

$$\begin{aligned}\mu'_1 &= \frac{A \cos 2\varphi + \frac{A^2 + B^2 - 1}{2} \sin 2\varphi}{\cos^2 \varphi + A \sin 2\varphi + (A^2 + B^2) \sin^2 \varphi} + i \frac{B}{\cos^2 \varphi + A \sin 2\varphi + (A^2 + B^2) \sin^2 \varphi}, \\ \mu'_2 &= \frac{-A \cos 2\varphi + \frac{A^2 + B^2 - 1}{2} \sin 2\varphi}{\cos^2 \varphi - A \sin 2\varphi + (A^2 + B^2) \sin^2 \varphi} + i \frac{B}{\cos^2 \varphi - A \sin 2\varphi + (A^2 + B^2) \sin^2 \varphi}.\end{aligned}\tag{21}$$

Case 2. If $\left(\frac{E_1}{G_{12}} - 2\nu_{12}\right)^2 - 4\frac{E_1}{E_2} \geq 0$, then, substituting expression (19) into Eq. (20), we obtain after the transformations:

$$\begin{aligned}\mu'_1 &= \frac{((b^* + a^*)^2 - 1) \sin \varphi \cos \varphi}{\cos^2 \varphi + (b^* + a^*)^2 \sin^2 \varphi} + i \frac{b^* + a^*}{\cos^2 \varphi + (b^* + a^*)^2 \sin^2 \varphi}, \\ \mu'_2 &= \frac{((b^* - a^*)^2 - 1) \sin \varphi \cos \varphi}{\cos^2 \varphi + (b^* - a^*)^2 \sin^2 \varphi} + i \frac{b^* - a^*}{\cos^2 \varphi + (b^* - a^*)^2 \sin^2 \varphi}.\end{aligned}\quad (22)$$

The matrix $[\mathbf{B}]^{-1}$ is defined by expression (11). Simplifying the expressions by which the elements of the matrix $[\mathbf{B}]^{-1}$ are calculated, we obtain:

$$\begin{aligned}\frac{p_2 - p_1}{(\mu'_1 - \mu'_2)} &= S'_{16} - S'_{11} \cdot (\mu'_1 + \mu'_2), \quad \frac{q_2 - q_1}{(\mu'_1 - \mu'_2)} = \frac{S'_{22}}{\mu'_1 \mu'_2} - S'_{12}, \\ \frac{\mu'_1 p_2 - \mu'_2 p_1}{(\mu'_1 - \mu'_2)} &= S'_{12} - S'_{11} \mu'_1 \mu'_2, \quad \frac{\mu'_1 q_2 - \mu'_2 q_1}{(\mu'_1 - \mu'_2)} = S'_{22} \frac{\mu'_1 + \mu'_2}{\mu'_1 \mu'_2} - S'_{26}.\end{aligned}\quad (23)$$

Substituting expressions (21) to (23) for the complex roots of the equation and given that

$$E_1 S'_{11} = 1 - A^2 \sin^2 2\varphi + \left(\sqrt{\frac{E_1}{E_2}} - 1\right)^2 \sin^4 \varphi + 2 \sin^2 \varphi \left(\sqrt{\frac{E_1}{E_2}} - 1\right),$$

we obtain the influence matrix $[\mathbf{B}]^{-1}$ explicitly:

$$[\mathbf{B}]^{-1} = \begin{pmatrix} \frac{\sqrt{E_1 E_2}}{4B} \left(1 - \sqrt{\frac{E_1}{E_2}}\right) \sin 2\varphi & \frac{\sqrt{E_1 E_2}}{2B} \left(\sqrt{\frac{E_1}{E_2}} \sin^2 \varphi + \cos^2 \varphi\right) & 0 \\ \frac{\sqrt{E_1 E_2}}{2B} \left(\sqrt{\frac{E_1}{E_2}} \cos^2 \varphi + \sin^2 \varphi\right) & \frac{\sqrt{E_1 E_2}}{4B} \left(1 - \sqrt{\frac{E_1}{E_2}}\right) \sin 2\varphi & 0 \\ 0 & 0 & \sqrt{G_{13} G_{23}} \end{pmatrix}, \quad (24)$$

where $B = \frac{\sqrt{2\sqrt{\frac{E_1}{E_2}} + \left(\frac{E_1}{G_{12}} - 2\nu_{12}\right)}}{2}$, φ is the rotation angle of the material's coordinate system

into the crack's coordinate system.

Substituting equalities (22) to (23) for the complex roots of Eq. (16) and given that

$$E_1 S'_{11} = (\cos^2 \varphi + B_1^2 \sin^2 \varphi)(\cos^2 \varphi + A_1^2 \sin^2 \varphi),$$

we obtain the expressions for the matrix $[\mathbf{B}]^{-1}$, which coincide with Eqs. (24).

Thus, the form of the matrix $[\mathbf{B}]^{-1}$ for Case 1 of roots (21) in Eq. (16) coincides with form (24) of the matrix $[\mathbf{B}]^{-1}$ for Case 2 of roots (22) in Eq. (16).

The SIF for the plane stress state in the orthotropic material is calculated from the displacements based on the following relations:

$$\begin{aligned}
 K_I &= \sqrt{\frac{\pi}{2r}} \left(\frac{\sqrt{E_1 E_2}}{4B} \left(1 - \sqrt{\frac{E_1}{E_2}} \right) \sin 2\varphi \cdot u_x + \frac{\sqrt{E_1 E_2}}{2B} \left(\sqrt{\frac{E_1}{E_2}} \sin^2 \varphi + \cos^2 \varphi \right) \cdot u_y \right), \\
 K_{II} &= \sqrt{\frac{\pi}{2r}} \left(\frac{\sqrt{E_1 E_2}}{2B} \left(\sqrt{\frac{E_1}{E_2}} \cos^2 \varphi + \sin^2 \varphi \right) \cdot u_x + \frac{\sqrt{E_1 E_2}}{4B} \left(1 - \sqrt{\frac{E_1}{E_2}} \right) \sin 2\varphi \cdot u_y \right), \\
 K_{III} &= \sqrt{\frac{\pi}{2r}} \cdot \sqrt{G_{13} G_{23}} \cdot u_z,
 \end{aligned} \quad (25)$$

where $B = \frac{\sqrt{2\sqrt{\frac{E_1}{E_2}} + \left(\frac{E_1}{G_{12}} - 2\nu_{12} \right)}}{2}$.

Thus, the matrix $[\mathbf{B}]^{-1}$ is the same for any values that the elastic parameters take in the orthotropic material. We should note that each SIF (K_I and K_{II}) in Eq. (25) depends on both displacement components u_x and u_y .

An important practical case concerns calculating the SIF for single-crystal blades of gas turbines, which have a cubic elasticity. In this case, Eqs. (25) are simplified as follows ($E_1 = E_2 = E$, $G_{12} = G_{13} = G_{23} = G$):

$$\begin{aligned}
 K_I &= \sqrt{\frac{\pi}{2r}} \cdot \frac{E}{\sqrt{2 + \left(\frac{E}{G} - 2\nu \right)}} \cdot u_y, \\
 K_{II} &= \sqrt{\frac{\pi}{2r}} \cdot \frac{E}{\sqrt{2 + \left(\frac{E}{G} - 2\nu \right)}} \cdot u_x, \\
 K_{III} &= \sqrt{\frac{\pi}{2r}} \cdot G \cdot u_z.
 \end{aligned} \quad (26)$$

Each SIF depends on only one displacement component, as opposed to the case of orthotropic material.

Consider the properties of the matrix $[\mathbf{B}]^{-1}$.

Property 1. It follows from the form of the matrix $[\mathbf{B}]^{-1}$ that mode separation is observed at $E_1 = E_2$ (for example, in the case of cubic symmetry), i.e., K_I depends only on u_y , K_{II} depends only on u_x , the same as in the case of isotropic material, but the expressions in the case of cubic symmetry are different from the isotropic material.

Property 2. Similarly, if $E_1 = E_2$ (for example, for cubic symmetry), the coefficients of the matrix $[\mathbf{B}]^{-1}$ are the same for any angle φ , i.e., they do not depend on it, as is the case for isotropic material.

Property 3. The matrix element $(\mathbf{B}^{-1})_{33}$ is constant and does not depend on the angle φ .

Property 4. In the cases of cubic symmetry and isotropic material, K_I linearly depends on u_y with the same proportionality factor as K_{II} depends on u_x .

Property 5. To analyze the degree to which u_x or u_y affect K_I and K_{II} for orthotropic material, consider the passes to the limit:

$$\lim_{\frac{E_1}{E_2} \rightarrow 0} \frac{(B^{-1})_{12}}{(B^{-1})_{11}} = \lim_{\frac{E_1}{E_2} \rightarrow 0} \frac{\sqrt{\frac{E_1}{E_2}} \sin^2 \varphi + \cos^2 \varphi}{\left(1 - \sqrt{\frac{E_1}{E_2}} \right) \sin \varphi \cos \varphi} = \operatorname{ctg} \varphi, \quad \lim_{\frac{E_1}{E_2} \rightarrow \infty} \frac{(B^{-1})_{12}}{(B^{-1})_{11}} = \lim_{\frac{E_1}{E_2} \rightarrow 0} \frac{\left(\sqrt{\frac{E_1}{E_2}} - 1 \right) \sin^2 \varphi + 1}{\left(1 - \sqrt{\frac{E_1}{E_2}} \right) \sin \varphi \cos \varphi} = -\operatorname{tg} \varphi,$$

$$\lim_{\frac{E_1}{E_2} \rightarrow 0} \frac{(B^{-1})_{21}}{(B^{-1})_{22}} = \lim_{\frac{E_1}{E_2} \rightarrow 0} \frac{\sqrt{\frac{E_1}{E_2}} \cos^2 \varphi + \sin^2 \varphi}{\left(1 - \sqrt{\frac{E_1}{E_2}}\right) \sin \varphi \cos \varphi} = \operatorname{tg} \varphi, \quad \lim_{\frac{E_1}{E_2} \rightarrow \infty} \frac{(B^{-1})_{21}}{(B^{-1})_{22}} = \lim_{\frac{E_1}{E_2} \rightarrow 0} \frac{\left(\sqrt{\frac{E_1}{E_2}} - 1\right) \cos^2 \varphi + 1}{\left(1 - \sqrt{\frac{E_1}{E_2}}\right) \sin \varphi \cos \varphi} = -\operatorname{ctg} \varphi.$$

The above results confirm that this effect of u_x or u_y on K_I and K_{II} depends on the ratio of Young's moduli E_1/E_2 and the rotation angle φ .

Property 6. As evident from expressions (25), the closer the root $\sqrt{E_1/E_2}$ to unity, the smaller the elements $(B^{-1})_{11}$, $(B^{-1})_{22}$ compared to the elements $(B^{-1})_{12}$, $(B^{-1})_{21}$. The value of K_I then largely depends on the value of u_y , and the value of K_{II} largely depends on u_x .

Analyzing the above relations, we can conclude that the degree of influence from either u_y or u_x depends on the value of the angle φ .

Property 7. Consider the determinant of the matrix $[\mathbf{B}]^{-1}$:

$$\begin{aligned} \det [\mathbf{B}]^{-1} &= \sqrt{G_{13}G_{23}} \cdot \frac{E_1E_2}{4B^2} \cdot \left(\left(1 + \frac{E_1}{E_2} - 2\sqrt{\frac{E_1}{E_2}}\right) \sin^2 \varphi \cos^2 \varphi - \frac{E_1}{E_2} \sin^2 \varphi \cos^2 \varphi - \right. \\ &\quad \left. - \sin^2 \varphi \cos^2 \varphi - \sqrt{\frac{E_1}{E_2}} \sin^4 \varphi - \sqrt{\frac{E_1}{E_2}} \cos^4 \varphi \right) = -\sqrt{G_{13}G_{23}} \frac{E_1\sqrt{E_1E_2}}{4B^2}. \end{aligned}$$

It follows from the form that the determinant of the matrix $[\mathbf{B}]^{-1}$ takes that the SIF cannot be explicitly calculated from the displacements, if

$$B = \frac{\sqrt{2\sqrt{\frac{E_1}{E_2}} + \left(\frac{E_1}{G_{12}} - 2\nu_{12}\right)}}{2} = 0.$$

$$2\sqrt{\frac{E_1}{E_2}} + \left(\frac{E_1}{G_{12}} - 2\nu_{12}\right) = 0, \quad \frac{E_1}{G_{12}} - 2\nu_{12} < 0, \quad \frac{E_1}{G_{12}} + 2\sqrt{\frac{E_1}{E_2}} < 1.$$

This corresponds to the case when the roots in the 4th-order equation take real values, which makes all elements of the matrix $[\mathbf{B}]^{-1}$ equal to zero; however, it was found in [15] that Eq. (16) cannot have real roots. On the other hand, if the ratio of elastic constants is such that

$$2\sqrt{\frac{E_1}{E_2}} + \left(\frac{E_1}{G_{12}} - 2\nu_{12}\right) \approx 0$$

or E_1 is sufficiently small, it may be problematic to numerically calculate the matrix $[\mathbf{B}]^{-1}$ or the SIF.

To illustrate other properties of the elements in the matrix $[\mathbf{B}]^{-1}$, we assume that the orthotropic material has the same properties as in Table 1, and plot the variations in the matrix elements depending on the crack's rotation angle φ (Fig. 2).

Property 8. Fig. 2 shows that all elements of the matrix $[\mathbf{B}]^{-1}$, except the constant $(B^{-1})_{33}$, vary with a period $T = \pi$.

The matrix elements $(B^{-1})_{11}$, $(B^{-1})_{22}$ become zero periodically, and the coefficient K_I depends only on u_y , while K_{II} depends only on u_x for the values of the angle $\varphi = 0, \pi/2, \pi, \dots$ for the orthotropic material (as well as for the cases of cubic symmetry and isotropic material).

The graphs of matrix elements $(B^{-1})_{12}$, $(B^{-1})_{21}$ are shifted relative to each other by $\varphi = \pi/2$.

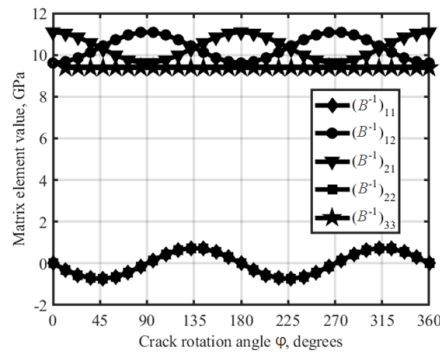


Fig. 2. Values of elements in matrix $[\mathbf{B}]^{-1}$ for orthotropic material as a function of the crack's rotation angle relative to its axes

Property 9. To analyze whether the matrix is definite, we calculate its main minors:

$$\text{minor } \Delta_1 = \frac{\sqrt{E_1 E_2}}{4B} \left(1 - \sqrt{\frac{E_1}{E_2}} \right) \sin 2\varphi$$

can be both greater or smaller than zero;

$$\text{minor } \Delta_2 = -\frac{E_1 \sqrt{E_1 E_2}}{4B^2} < 0, \quad \Delta_3 = -\sqrt{G_{13} G_{23}} \frac{E_1 \sqrt{E_1 E_2}}{4B^2} < 0.$$

Apparently, the matrix $[\mathbf{B}]^{-1}$ is neither positive-definite nor negative-definite.

Property 10. The eigenvalues of the matrix $[\mathbf{B}]^{-1}$ are defined as the roots of the equation

$$\begin{vmatrix} \frac{\sqrt{E_1 E_2}}{4B} \left(1 - \sqrt{\frac{E_1}{E_2}} \right) \sin 2\varphi - \lambda & \frac{\sqrt{E_1 E_2}}{2B} \left(\sqrt{\frac{E_1}{E_2}} \sin^2 \varphi + \cos^2 \varphi \right) & 0 \\ \frac{\sqrt{E_1 E_2}}{2B} \left(\sqrt{\frac{E_1}{E_2}} \cos^2 \varphi + \sin^2 \varphi \right) & \frac{\sqrt{E_1 E_2}}{4B} \left(1 - \sqrt{\frac{E_1}{E_2}} \right) \sin 2\varphi - \lambda & 0 \\ 0 & 0 & \sqrt{G_{13} G_{23}} - \lambda \end{vmatrix} = 0.$$

Table 1

Elastic properties of orthotropic material used in calculations

Modulus, MPa		Poisson's ratio
Young's ratio	Shear modulus	
$E_1 = 20,000$	$G_{12} = 13,000$	$\nu_{12} = 0.3$
$E_2 = 25,000$	$G_{23} = 11,000$	$\nu_{23} = 0.25$
$E_3 = 10,000$	$G_{31} = 8,000$	$\nu_{31} = 0.2$

Calculating the determinant, we obtain a cubic equation with respect to λ :

$$(\sqrt{G_{13}G_{23}} - \lambda) \cdot (\lambda^2 - \lambda \frac{\sqrt{E_1E_2}}{B} \left(1 - \sqrt{\frac{E_1}{E_2}}\right) \sin \varphi \cos \varphi - \frac{E_1 \sqrt{E_1E_2}}{4B^2}) = 0. \quad (27)$$

Separating the factors and calculating the discriminant, we find the roots of the equation:

$$\begin{aligned} \lambda_1 &= \frac{\sqrt{E_1E_2}}{2B} \left(\left(1 - \sqrt{\frac{E_1}{E_2}}\right) \sin \varphi \cos \varphi + \sqrt{\left(1 + \frac{E_1}{E_2}\right) \sin^2 \varphi \cos^2 \varphi + \frac{E_1}{E_2} (\sin^4 \varphi + \cos^4 \varphi)} \right), \\ \lambda_2 &= \frac{\sqrt{E_1E_2}}{2B} \left(\left(1 - \sqrt{\frac{E_1}{E_2}}\right) \sin \varphi \cos \varphi - \sqrt{\left(1 + \frac{E_1}{E_2}\right) \sin^2 \varphi \cos^2 \varphi + \frac{E_1}{E_2} (\sin^4 \varphi + \cos^4 \varphi)} \right), \\ \lambda_3 &= \sqrt{G_{13}G_{23}}. \end{aligned} \quad (28)$$

Thus, one eigenvalue of the matrix $[\mathbf{B}]^{-1}$ does not depend on the angle φ at all, and the other two are periodic functions of the angle φ with the period π .

Verification of the methods for calculating the SIF for cracks in anisotropic materials by the finite element method

The displacement method and the resulting expressions for matrix $[\mathbf{B}]^{-1}$ were tested based on the results of the FE solution for the boundary-value problem and SIF calculations for the case of a single oblique crack in the infinite plane for a mixed fracture mode (provided that modes K_I and K_{II} exist). We considered a single crack in the infinite plane at an angle φ to the anisotropy axis the material, normal to the direction in which the load was applied (Fig. 3). The problem was solved in a two-dimensional statement, assuming a plane stress state.

An analytical solution for SIF is known for this problem [23]:

$$\begin{aligned} K_I &= \sigma \sqrt{\pi a} \cdot \cos^2 \varphi, \\ K_{II} &= \sigma \sqrt{\pi a} \cdot \sin \varphi \cdot \cos \varphi. \end{aligned} \quad (29)$$

The analytical solution for the infinite plane does not depend on the type of anisotropy and the values taken by the elastic moduli of the material. The problem was solved in the PANTOCRATOR FE software [32], programmed to calculate the SIF for isotropic and anisotropic materials using the methods of displacements (see Eqs. (8), (10)) and stresses (see Eqs. (13) and (15)). Quadratic 8-node finite elements were used in the calculations.

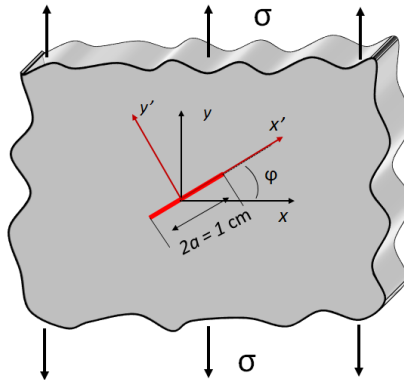


Fig. 3. Schematic for the statement of the problem on uniaxial tension of a plane with an oblique crack (highlighted in red).
The notations are the same as in Fig. 1

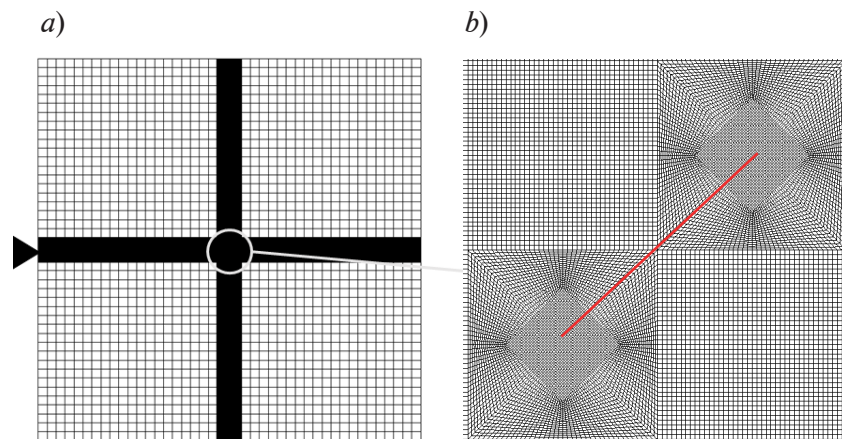


Fig. 4. Finite-element model of plate with oblique crack (a) and its central fragment (b)

FE models were constructed to compare the numerical solutions with analytical ones at different values of the angle φ (the crack's orientation angle relative to the material's orthotropy axes). Fig. 4 shows an example FE model with 126,000 degrees of freedom and 80 elements at the edge of the crack for the case of a square plate of finite dimensions and an inclination angle $\varphi = 45^\circ$.

The length and the width of the computational domain were taken to be 22 cm; the crack length was 1 cm, which is an approximation for modeling the crack's behavior in an infinite region. The plate was loaded on the upper edge with the stress $\sigma_{yy} = 100$ MPa and clamped at the lower edge (to exclude solid-state displacements). The elastic properties of the materials used in the calculations are given in Table 2.

Fig. 5 shows a comparison of numerical results for SIFs obtained by displacement and stress extrapolation with an analytical solution for three types of material: isotropic, orthotropic and cubic.

Table 2

Elastic properties of materials for three types of symmetry, used in FE calculations

Material	Modulus, MPa		Poisson's ratio
	Young's ratio	Shear modulus	
Isotropic	$E = 20,000$	$G = \frac{E}{2(1+\nu)} = 7692.3$	$\nu = 0.3$
With cubic symmetry	$E = 20,000$	$G = 11,000$	$\nu = 0.3$
Orthotropic	$E_1 = 20,000$	$G_{12} = 13,000$	$\nu_{12} = 0.3$
	$E_2 = 15,000$	$G_{23} = 11,000$	$\nu_{23} = 0.25$
	$E_3 = 10,000$	$G_{31} = 8,000$	$\nu_{31} = 0.2$

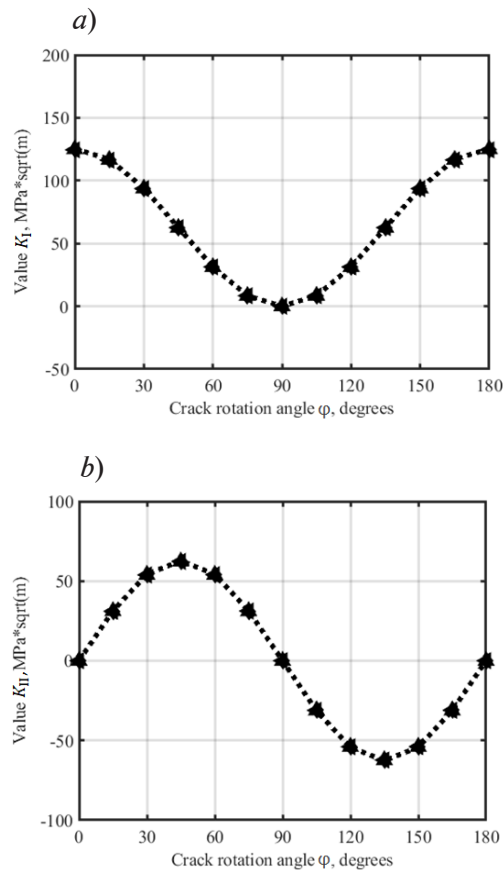


Fig. 5. Comparison of numerical solutions (symbols) for SIFs K_I (a) and K_{II} (b), obtained by the methods of displacements and stresses, with analytical solutions (dashes). The data are given for isotropic (▲) and orthotropic (◄) materials and for the material with cubic symmetry (◆)

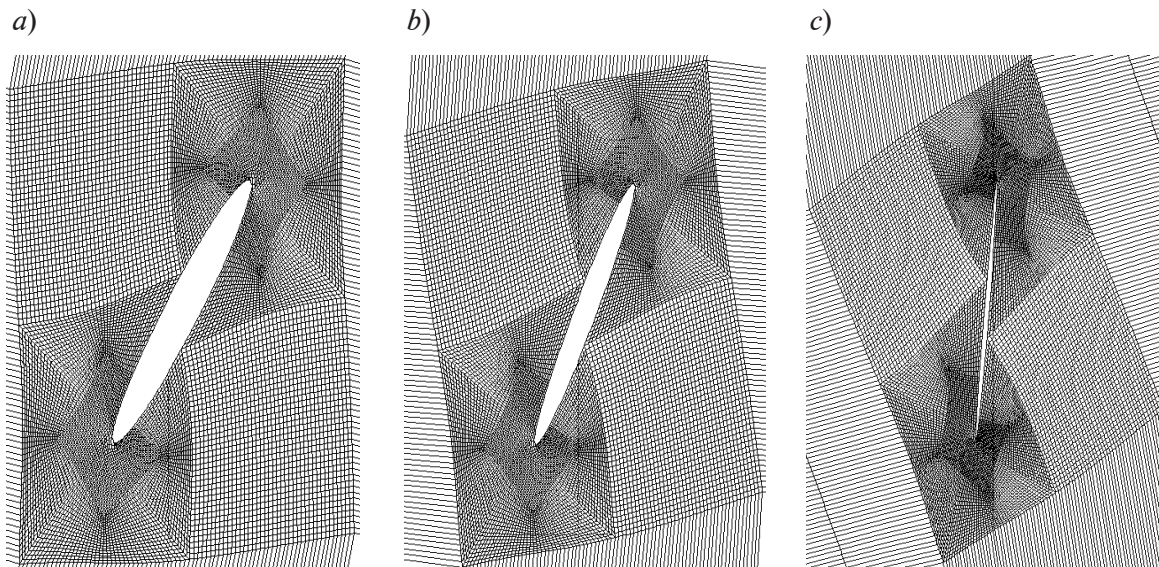


Fig. 6. Comparative results for FEM calculations of crack opening (initial inclination angle $\varphi = 60^\circ$) for materials with different symmetry of elastic properties: isotropic (a), cubic (b) and orthotropic (c). The scale of displacements is magnified by 60 times

Table 3 shows the values of K_I and K_{II} corresponding to Fig. 5. Notably, the maximum error δ_{\max} for the displacement method (0.79%) exceeds that for the stress method (0.42%); the error is minimal for the isotropic material and maximal for the orthotropic one. However, the error does not exceed 0.8% for all cases considered, confirming that both methods have a high accuracy.

Fig. 6 shows the differences in crack opening for different cases of material anisotropy with the crack inclination angle $\varphi = 60^\circ$.

FEM calculations performed for three cases of elastic symmetry in the material indicate that the crack opens to the maximum in the isotropic case, to the minimum in the orthotropic case, other conditions given by specific values of the elastic parameters being equal.

Table 3

**Comparison of analytical and numerical solutions
for three types of material**

$\varphi, ^\circ$	Analytical solution		Numerical solution by method of					
			displacements			stresses		
	K_I	K_{II}	K_I	K_{II}	δ_{\max}	K_I	K_{II}	δ_{\max}
	MPa·m ^{1/2}				%	MPa·m ^{1/2}		%
<i>For isotropic material</i>								
0	125.33	0	124.96	0.0005	0.29	125.05	0.0003	0.22
30	93.99	54.27	93.70	53.93	0.62	93.93	54.26	0.07
60	31.33	54.27	31.22	53.92	0.64	31.30	54.25	0.10
90	0	0	< 0.0001	0.0002	0.02	< 0.0001	< 0.0001	< 0.01
120	31.33	−54.27	31.22	−53.91	0.65	31.28	−54.23	0.15
150	93.99	−54.27	93.70	−53.93	0.62	93.93	−54.26	0.07
180	125.33	0	124.96	0.0005	0.29	125.05	0.0003	0.22
<i>For material with cubic symmetry</i>								
0	125.33	0	124.77	0.004	0.22	125.07	0.003	0.20
30	93.99	54.27	93.68	53.89	0.20	93.90	54.22	0.10
60	31.33	54.27	31.26	53.94	0.60	31.34	54.29	0.04
90	0	0	< 0.0001	0.0002	0.02	< 0.0001	< 0.0001	< 0.01
120	31.33	−54.27	31.25	−53.94	0.60	31.31	−54.29	0.07
150	93.99	−54.27	93.68	−53.89	0.70	93.90	−54.22	0.10
180	125.33	0	124.77	0.004	0.45	125.07	0.003	0.45
<i>For orthotropic material</i>								
0	125.33	0	124.50	0.006	0.66	124.80	0.007	0.42
30	93.99	54.27	93.61	53.84	0.79	93.83	54.23	0.18
60	31.33	54.27	31.31	53.95	0.58	31.40	54.30	0.20
90	0	0	< 0.0001	0.0002	0.02	< 0.0001	< 0.0001	< 0.01
120	31.33	−54.27	31.29	−53.95	0.58	31.35	−54.30	0.08
150	93.99	−54.27	93.61	−53.84	0.79	93.83	−54.23	0.18
180	125.33	0	124.50	0.006	0.66	124.80	0.0068	0.42

Notations: φ is the crack inclination angle to the axis x ; δ_{\max} is the maximum relative error of either of the two factors K_I and K_{II} (stress intensity factors for fracture modes I and II), taken relative to the result of the analytical solution.



Conclusions

Considering the case of a plane stress state, we have obtained explicit expressions for the roots of the equation of the 4th degree, defining the elements of the influence matrix accounting for three components of the relative displacement vector of the crack edges versus three stress intensity factors $[B]^{-1}$ in terms of the elastic constants of materials with orthotropic or cubic symmetry. We have carried out a systematic study of the properties of the influence matrix $[B]^{-1}$. The absence of mode mixing has been established for a material with cubic symmetry.

In addition, the SIF values were calculated for an oblique single crack in a plane stress state using two numerical methods: extrapolation of displacements and stresses to the tip of the crack for different orientations of the crack in the plane relative to the anisotropy axes of the material. The results of numerical solutions agree well with the analytical solution for the isotropic, cubic and orthotropic materials (the error did not exceed 0.8% in all cases). We have established that the method for calculating the SIF in terms of stress extrapolation to the tip of the crack has a higher accuracy than the method based on displacement extrapolation.

Finite element modeling of a plate with an oblique crack suggests that if the highest values of Young's modulus are equal, the crack edges open to the maximum extent in the isotropic material, and to the minimum in the orthotropic material.

The methods of displacement and stress extrapolation can be recommended for estimating the SIF in crack growth simulations and calculations of crack resistance in single-crystal blades of gas turbines.

REFERENCES

1. Shalin R. E., Svetlov I. L., Kachalov E. B., et al., Monokristally nikelovykh zharoprochnykh splavov [Single crystals of nickel heat-resistant alloys], Mashinostroyeniye, Moscow, 1997 (in Russian).
2. Wilson B. C., Hickman J. A., Fuchs G. E., The effect of solution heat treatment on a single-crystal Ni-based superalloy, JOM. 55 (3) (2003) 35–40.
3. Hodinev I. A., Monin S. A., Anisotropy of low cycle fatigue characteristics of single-crystal heat-resistant nickel alloys, Proceedings of VIAM. (10 (92)) (2020) 97–105 (in Russian).
4. Getsov L. B., Materialy i prochnost detaley gazovykh turbin [Materials and strength of gas turbine parts], in 2 Vols., Vol. 1, Gas Turbine Technologies Publishing, Rybinsk, 2010 (in Russian).
5. Getsov L. B., Semenov A. S., Ignatovich I. A., Thermal fatigue analysis of turbine discs on the base of deformation criterion, Int. J. Fatig. 97 (April) (2017) 88–97.
6. Wang R., Zhang B., Hu D., et al., A critical-plane-based thermomechanical fatigue lifetime prediction model and its application in nickel-based single-crystal turbine blades, Mater. High Temperat. 36 (4) (2019) 325–334.
7. Glotka A. A., Gayduk S. V., Prediction of the properties of single-crystal heat-resistance nickel alloys, Science & Progress of Transport. Bulletin of Dnepropetrovsk National University of Railway Transport. (2(80)) (2019) 91–100 (in Russian).
8. Bondarenko Yu. A., Kolodyazhny M. Yu., Echin A. B., Narskiy A. R., Directional solidification, structure and properties of natural composite based on eutectic Nb-Si at working temperatures up to 1350 °C for the blades of gas turbine engines, Proceedings of VIAM. (1 (61)) (2018) 3–14 (in Russian).
9. Bondarenko Yu. A., Trends in the development of high-temperature metal materials and technologies in the production of modern aircraft gas turbine engines, Aviation Materials and Technologies. (2 (55)) (2019) 3–11 (in Russian).
10. Semenov A. S., Grishchenko A. I., Kolotnikov M. E., Getsov L. B., Finite-element analysis of thermal fatigue of gas turbine blades, Part 1. Material models, fracture criteria, identification, Vestnik UGATU [USATU Bulletin]. 23 (1 (83)) (2019) 70–81 (in Russian).
11. Semenov A. S., Grishchenko A. I., Kolotnikov M. E., Getsov L. B., Finite-element analysis of thermal fatigue of gas turbine blades, Part 2. Results of computations, Vestnik UGATU [USATU Bulletin]. 23 (2 (84)) (2019) 61–74 (in Russian).
12. Getsov L. B., Semenov A. S., Besschetnov V. A., et al., Long-term strength determination for cooled blades made of monocrystalline superalloys, Therm. Eng. 64 (4) (2017) 280–287.
13. Getsov L. B., Mikhaylov V. E., Semenov A. S., et al., Raschetnoye opredeleniye resursa rabochikh i napravlyayushchikh lopatok GTU. Chast 1. Polikristallicheskiye materialy [Design determination of the work life of operating and guide blades of gas-turbine installations. Part 1. Polycrystalline materials], Gas Turbine Technologies. (7) (2011) 24–30 (in Russian).

14. **Getsov L. B., Mikhaylov V. E., Semenov A. S., et al.**, Raschetnoye opredeleniye resursa rabochikh i napravlyayushchikh lopatok GTU. Chast 2. Monokristallicheskiye materialy [Computational determination of the work life of operating and guide blades of gas-turbine units. Part 1. Monocrystalline materials], Gas Turbine Technologies. (8) (2011) 18–25 (in Russian).
15. **Kuzmina N. A., Pyankova L. A.**, Control of crystallographic orientation of monocrystalline nickel castings heat-resistant alloys by X-ray diffractometry, Proceedings of VIAM. (12 (84)) (2019) 11–19 (in Russian).
16. **Semenov A. S., Semenov S. G., Nazarenko A. A., Getsov L. B.**, Computer simulation of fatigue, creep and thermal fatigue cracks propagation in gas turbine blades, Mater. Technol. 46 (3) (2012) 197–203.
17. **Semenov A. S., Semenov S. G., Getsov L. B.**, Methods of computational determination of growth rates of fatigue, creep, and thermal fatigue cracks in poli- and monocrystalline blades of gas-turbine units, Strength Mater. 47 (2) (2015) 268–290.
18. **Savikovskii A. V., Semenov A. S., Getsov L. B.**, Coupled thermo-electro-mechanical modeling of thermal fatigue of single-crystal corset samples, Mater. Phys. Mech. 2019. Vol. 42 (3) (2019) 296–310.
19. **Savikovskii A. V., Semenov A. S., Getsov L. B.**, Crystallographic orientation, delay time and mechanical constants influence on thermal fatigue strength of single-crystal nickel superalloys, Mater. Phys. Mech. 44 (1) (2020) 125–136.
20. **Lekhnitsky S. G.**, Teoriya uprugosti anizotropnogo tela [Theory of elasticity of an anisotropic elastic body], Nauka, Moscow, 1977 (in Russian).
21. **Martynov N. I.**, Complex form of Hooke's law of anisotropic elastic body, Mechanics of Solids. 55 (4) (2020) 514–535.
22. **Kachanov M. L.**, Osnovy mekhaniki razrusheniya [Fundamentals of fracture mechanics]. Nauka, Moscow, 1974, Pp. 223–226 (in Russian).
23. **Sih G. C., Paris P. C., Irwin G. R.**, On cracks in rectilinearly anisotropic bodies, Int. J. Fract. 1 (3) (1965) 189–203.
24. **Judt P. O., Ricoeur A., Linek G.**, Crack path prediction in rolled aluminum plates with fracture toughness orthotropy and experimental validation, Eng. Fract. Mech. 138 (April) (2015) 33–48.
25. **Banks-Sills L., Hershkovitz I., Wawrzynek P. A., et al.**, Methods for calculating stress intensity factors in anisotropic materials: Part I: $z = 0$ is a symmetric plane, Eng. Fract. Mech. 72 (15) (2005) 2328–2358.
26. **Semenov S. G., Semenov A. S., Getsov L. B., et al.**, Application of linear and nonlinear fracture mechanics criteria for crack propagation analysis in single crystal bodies, Proc. XLI Int. Summer School–Conf. “Advanced Problems in Mechanics (APM-2013)” St. Petersburg, Russia, July 2–6 (2013) 75–82.
27. **Ranjan S., Arakere N. K.**, a fracture-mechanics-based methodology for fatigue life prediction of single crystal nickel-based superalloys, J. Eng. Gas Turbines Power. 2008 130 (3) (2008) 032501.
28. **Khansari N. M., Fakoor M., Berto F.**, Probabilistic micromechanical damage model for mixed-mode I/II fracture investigation of composite materials, Theor. Appl. Fract. Mech. 99 (February) (2019) 177–193.
29. **Cao J., Li F., Ma H., Sun Z.**, Study of anisotropic crack growth behavior for aluminum alloy 7050-T7451, Eng. Fract. Mech. 2018, Vol. 196 (1 June) (2018) 98–112.
30. **Fakoor M., Shavsavar S.**, The effect of T-stress on mixed mode I/II fracture of composite materials: Reinforcement isotropic solid model in combination with maximum shear stress theory, Int. J. Solids & Struct. 229 (15 October) (2021) 111145.
31. **Fakoor M., Farid H. M.**, Mixed-mode I/II fracture criterion for crack initiation assessment of composite materials, Acta Mechanica. 230 (1) (2019) 281–301.
32. **Semenov A. S.**, PANTOCRATOR – konechno-elementnyy programmnyy kompleks, oriyentirovanny na resheniye nelineynykh zadach mekhaniki [PANTOCRATOR – finite-element program specialized on the solution of non-linear problems of solid body mechanics], In: Proc. The V-th Int. Conf. “Scientific and engineering problems of reliability and service life of structures and methods of their decision”, St. Petersburg Polytechnical University Publishing, St. Petersburg (2003) 466–480.



СПИСОК ЛИТЕРАТУРЫ

1. Шалин Р. Е., Светлов И. Л., Качалов Е. Б., Толораия В. Н., Гаврилин В. С. Монокристаллы никелевых жаропрочных сплавов. М.: Машиностроение. 336 .1997 с.
2. Wilson B. C., Hickman J. A., Fuchs G. E. The effect of solution heat treatment on a single-crystal Ni-based superalloy // The Journal of the Minerals, Metals & Materials Society. 2003. Vol. 55. No. 3. Pp. 35–40.
3. Ходинев И. А., Монин С. А. Анизотропия характеристик малоциклового усталости монокристаллических жаропрочных никелевых сплавов // Труды ВИАМ (Всероссийский НИИ авиационных материалов). 92) 10 № .2020). С. 105–97.
4. Гецов Л. Б. Материалы и прочность деталей газовых турбин. В 2 тт. Т. 1. Рыбинск: Издат. дом «Газотурбинные технологии», 2010. 605 с.
5. Getsov L. B., Semenov A. S., Ignatovich I. A. Thermal fatigue analysis of turbine discs on the base of deformation criterion // International Journal of Fatigue. 2017. Vol. 97. April. Pp. 88–97.
6. Wang R., Zhang B., Hu D., Jiang K., Mao J., Jing F. A critical-plane-based thermomechanical fatigue lifetime prediction model and its application in nickel-based single-crystal turbine blades // Materials at High Temperatures. 2019. Vol. 36. No. 4. pp. 325–334.
7. Глотка А. А., Гайдук С. В. Прогнозирование свойств монокристаллических жаропрочных никелевых сплавов // Наука и прогресс транспорта. Вестник Днепропетровского национального университета железнодорожного транспорта. 80) 2 № .2019). С. 91–100.
8. Бондаренко Ю. А., Колодяжный М. Ю., Ечин А. Б., Нарский А. Р. Направленная кристаллизация, структура и свойства естественного композита на основе эвтектики Nb-Si на рабочие температуры до 1350 °С для лопаток ГТД // Труды ВИАМ. 2018. № 1 (61). С. 3–14.
9. Бондаренко Ю. А. Тенденция развития высокотемпературных металлических материалов и технологий при создании современных авиационных газотурбинных двигателей // Авиационные материалы и технологии. 55) 2 № .2019). С. 11–3.
10. Семенов А. С., Грищенко А. И., Колотников М. Е., Гецов Л. Б. Конечного-элементный анализ термоциклической прочности лопаток газовых турбин Ч. 1. Модели материала, критерии разрушения, идентификация параметров // Вестник УГАТУ (Уфимский государственный авиационный технический университет). 2019. Т. 83) 1 № .23). С. 70–81.
11. Семенов А. С., Грищенко А. И., Колотников М. Е., Гецов Л. Б. Конечного-элементный анализ термоциклической прочности лопаток газовых турбин. Ч. 2. Результаты расчетов // Вестник УГАТУ. 2019. Т. 23. № 2 (84). С. 61–74.
12. Гецов Л. Б., Семенов А. С., Бессчетнов В. А., Грищенко А. И., Семанов С. Г. Методика определения длительной прочности охлаждаемых лопаток из монокристаллических жаропрочных сплавов // Теплоэнергетика. 4 № .2017. С. 56–48.
13. Гецов Л. Б., Михайлов В. Е., Семенов А. С., Кривоносова В. В., Ножницкий Ю. А., Блинник Б. С., Магерамова Л. А. Расчетное определение ресурса рабочих и направляющих лопаток ГТУ. Ч. 1. Поликристаллические материалы // Газотурбинные технологии. 2011. № 7. С. 24–30.
14. Гецов Л. Б., Михайлов В. Е., Семенов А. С., Кривоносова В. В., Ножницкий Ю. А., Блинник Б. С., Магерамова Л. А. Расчетное определение ресурса рабочих и направляющих лопаток ГТУ. Ч. 2. Монокристаллические материалы // Газотурбинные технологии. 2011. № 8. С. 18–25.
15. Кузьмина Н. А., Пьянкова Л. А. Контроль кристаллографической ориентации монокристаллических отливок никелевых жаропрочных сплавов методом рентгеновской дифрактометрии // Труды ВИАМ. 2019. № 12 (84). С. 11–19.
16. Semenov A., Semenov S., Nazarenko A., Getsov L. Computer simulation of fatigue, creep and thermal-fatigue cracks propagation in gas-turbine blades // Materials and Technology. 2012. Vol. 46. No. 3. Pp. 197–203.
17. Семенов А. С., Семенов С. Г., Гецов Л. Б. Методы расчетного определения скорости роста трещин усталости, ползучести и термоусталости в поли- и монокристаллических лопатках ГТУ // Проблемы прочности. 2015. № 2. С. 61–87.
18. Savikovskii A. V., Semenov A. S., Getsov L. B. Coupled thermo-electro-mechanical modeling of thermal fatigue of single-crystal corset samples // Materials Physics and Mechanics. 2019. Vol. 42. No. 3. Pp. 296–310.

19. Savikovskii A. V., Semenov A. S., Getsov L. B. Crystallographic orientation, delay time and mechanical constants influence on thermal fatigue strength of single-crystal nickel superalloys // *Materials Physics and Mechanics*. 2020. Vol. 44. No. 1. Pp. 125–136.
20. Лехницкий С. Г. Теория упругости анизотропного тела. М.: Наука, 1977. 416 с.
21. Мартынов Н. И. Комплексная форма закона Гука анизотропного упругого тела // *Известия РАН. Механика твердого тела*. 4 №. 2020. С. 71–95.
22. Качанов Л. М. Основы механики разрушения. М.: Наука, 1974. С. 223–226.
23. Sih G. C., Paris P. C., Irwin G. R. On cracks in rectilinearly anisotropic bodies // *International Journal of Fracture Mechanics*. 1965. Vol. 1. No. 3. Pp. 189–203.
24. Judt P. O., Ricoeur A., Linek G. Crack path prediction in rolled aluminum plates with fracture toughness orthotropy and experimental validation // *Engineering Fracture Mechanics*. 2015. Vol. 138. April. Pp. 33–48.
25. Banks-Sills L., Hershkovitz I., Wawrzynek P. A., Eliasi R., Ingraffea A. R. Methods for calculating stress intensity factors in anisotropic materials: Part I: $z = 0$ is a symmetric plane // *Engineering Fracture Mechanics*. 2005. Vol. 72. No. 15. Pp. 2328–2358.
26. Semenov S. G., Semenov A. S., Getsov L. B., Melnikov B. E. Application of linear and nonlinear fracture mechanics criteria for crack propagation analysis in single crystal bodies // *Proceedings of XLI International Summer School –Conference “Advanced Problems in Mechanics (APM-2013)” Russia, St. Petersburg, July 2–6, 2013*. Pp. 75–82.
27. Ranjan S., Arakere N. K. A fracture-mechanics-based methodology for fatigue life prediction of single crystal nickel-based superalloys // *Journal of Engineering for Gas Turbines and Power*. 2008. Vol. 130. No. 3. P. 032501.
28. Khansari N. M., Fakoor M., Berto F. Probabilistic micromechanical damage model for mixed-mode I/II fracture investigation of composite materials // *Theoretical and Applied Fracture Mechanics*. 2019, Vol. 99. February. Pp. 177–193.
29. Cao J., Li F., Ma H., Sun Z. Study of anisotropic crack growth behavior for aluminum alloy 7050-T7451 // *Engineering Fracture Mechanics*. 2018. Vol. 196. 1 June. Pp. 98–112.
30. Fakoor M., Shavsavar S. The effect of T-stress on mixed mode I/II fracture of composite materials: Reinforcement isotropic solid model in combination with maximum shear stress theory // *International Journal of Solids and Structures*. 2021. Vol. 229. 15 October. P. 111145.
31. Fakoor M., Farid H. M. Mixed-mode I/II fracture criterion for crack initiation assessment of composite materials // *Acta Mechanica*. 2019. Vol. 230. No. 1. Pp. 281–301.
32. Семенов А. С. PANTOCRATOR – конечно-элементный программный комплекс, ориентированный на решение нелинейных задач механики // *Труды V-ой Международной конференции «Научно-технические проблемы прогнозирования надежности и долговечности конструкций»*. СПб.: Изд-во СПбГПУ, 2003. С. 466 –480.

THE AUTHORS

SAVIKOVSKII Artem V.

Peter the Great St. Petersburg Polytechnic University
 29 Politechnicheskaya St., St. Petersburg, 195251, Russia
 savikovskij.av@edu.spbstu.ru
 ORCID: 0000-0003-1710-1943

SEME NOV Artem S.

Peter the Great St. Petersburg Polytechnic University
 29 Politechnicheskaya St., St. Petersburg, 195251, Russia
 Semenov.Artem@googlemail.com
 ORCID: 0000-0002-8225-3487

СВЕДЕНИЯ ОБ АВТОРАХ

САВИКОВСКИЙ Артем Викторович — аспирант кафедры «Механика и процессы управления» Санкт-Петербургского политехнического университета Петра Великого.

195251, Россия, г. Санкт-Петербург, Политехническая ул., 29

savikovskij.av@edu.spbstu.ru

ORCID: 0000-0003-1710-1943

СЕМЕНОВ Артем Семенович — кандидат физико-математических наук, заведующий кафедрой сопротивления материалов Санкт-Петербургского политехнического университета Петра Великого.

195251, Россия, г. Санкт-Петербург, Политехническая ул., 29

Semenov.Artem@gmail.com

ORCID: 0000-0002-8225-3487

Received 20.01.2022. Approved after reviewing 22.04.2022. Accepted 22.04.2022.

Статья поступила в редакцию 20.01.2022. Одобрена после рецензирования 22.04.2022. Принята 22.04.2022.

Original article

DOI: <https://doi.org/10.18721/JPM.15211>

TWO-FACTOR OPTIMIZATION IN THE BRACHISTOCHRONE PROBLEM

A. S. Smirnov^{1,2✉}, *S. V. Suvorov*³

¹ Peter the Great St. Petersburg Polytechnic University, St. Petersburg, Russia;

² Institute of Problems of Mechanical Engineering of the Russian Academy of Sciences, St. Petersburg, Russia;

³ Central Design Bureau of Transport Engineering, Tver, Russia

✉ smirnov.alexey.1994@gmail.com

Abstract. The paper puts forward a new modification of the well-known brachistochrone problem. The joint account of minimizing the motion time and the trajectory length in their functional relationship has been introduced. A two-factor optimization criterion (TOC) was constructed in the form of a product of two particular criteria, which made it possible to find the best compromise between them. On the TOC basis a solution to the problem of a two-factor brachistochrone was obtained using a preliminary consideration of the auxiliary problem on a brachistochrone with a given length. A rational practical solution of the problem was proposed. It was characterized by a simpler geometry than the strictly optimal one: to adopt a circular arc with a central angle selected on the basis of the taken TOC.

Keywords: brachistochrone, optimization, motion time, trajectory length, two-factor criterion, rational solution

For citation: Smirnov A. S., Suvorov S. V., Two-factor optimization in the brachistochrone problem, St. Petersburg Polytechnical State University Journal. Physics and Mathematics. 15 (2) (2022) 124–139. DOI: <https://doi.org/10.18721/JPM.15211>

This is an open access article under the CC BY-NC 4.0 license (<https://creativecommons.org/licenses/by-nc/4.0/>)



Научная статья

УДК 531.332

DOI: <https://doi.org/10.18721/JPM.15211>

ДВУХФАКТОРНАЯ ОПТИМИЗАЦИЯ В ЗАДАЧЕ О БРАХИСТОХРОНЕ

А. С. Смирнов^{1,2✉}, С. В. Суворов³

¹Санкт-Петербургский политехнический университет Петра Великого, г. Санкт-Петербург, Россия;

²Институт проблем машиноведения Российской академии наук, г. Санкт-Петербург, Россия;

³Центральное конструкторское бюро транспортного машиностроения, г. Тверь, Россия

✉ smirnov.alexey.1994@gmail.com

Аннотация. В статье предлагается новая модификация известной задачи о брахистохроне. Введен совместный учет минимизаций времени движения и длины траектории в их функциональной взаимосвязи. Построен двухфакторный критерий оптимизации (ДКО) в виде произведения двух частных критериев, который позволил найти наилучший компромисс между ними; на основе ДКО получено решение задачи о двухфакторной брахистохроне с предварительным рассмотрением вспомогательной задачи о брахистохроне заданной длины. Предложено рациональное практическое решение задачи, обладающее более простой геометрией, чем строго оптимальное: принять дугу окружности с центральным углом, который подбирается на основе взятого ДКО.

Ключевые слова: брахистохрона, оптимизация, время движения, длина траектории, двухфакторный критерий, рациональное решение

Для цитирования: Смирнов А. С., Суворов С. В. Двухфакторная оптимизация в задаче о брахистохроне // Научно-технические ведомости СПбГПУ. Физико-математические науки. 2022. Т. 2 № 15. С. 124–139. DOI: <https://doi.org/10.18721/JPM.15211>

Статья открытого доступа, распространяемая по лицензии CC BY-NC 4.0 (<https://creativecommons.org/licenses/by-nc/4.0/>)

Introduction

The problem of the brachistochrone was first formulated by Johann Bernoulli in 1696 (published in *Acta Eruditorum* under the title *Problema novum ad cujus solutionem Mathematici invitantur* [A new problem to whose solution mathematicians are invited]).

The problem was posed as follows:

Given in a vertical plane two points A and B , assign to the moving [body] M , the path AMB , by means of which — descending by its own weight and beginning to be moved [by gravity] from point A — it would arrive at the other point B in the shortest time.

This problem was successfully solved by such great scientists as Gottfried Leibniz, Johann Bernoulli, Guillaume de l'Hôpital and Isaac Newton [1]. Even though the solutions presented were different, the final answers turned out to be the same: the trajectory that is sought is a cycloidal arc. Importantly, the solution proposed by Bernoulli was the first step towards a new field in mathematical analysis, coming to be known as calculus of variations. Exploration of the brachistochrone problem has extended to modern times. In particular, the obtained solution has long been known for its practical applications in construction in tropical countries, where fast runoff of water from the roof considerably affects the building's durability throughout the rainfall season. For instance, the roofs of Buddhist pagodas are distinctly similar in shape to the cycloidal arc.

The classical problem of the brachistochrone is interesting both from an educational and a research perspective; it has been formulated as multiple generalizations, useful for wider practical applications. The first (but far from only) generalization was the problem of the brachistochrone in a resisting medium considered by Leonhard Euler. This direction has been continued in a series of modern studies [2–5], adopting models of both viscous and Coulomb friction. It is also intriguing to explore the problem of the brachistochrone for a rolling disk [6–8] and its different spatial configurations [9, 10], as well as some other generalizations (a detailed list is given in [11]).

Problem statement

Suppose that the start and end points A and B lie on the same horizontal level and are located at a distance l from each other (Fig. 1).

The problem of the brachistochrone can be interpreted as that on optimal design of an underground tunnel, whose classical statement only minimizes a single factor that is the motion time T of a point particle along the curve $y(x)$. Meanwhile, the length L of this curve turns out to be sufficiently large, which can be inconvenient for generating such a trajectory in practice. Moreover, it is often impossible to construct a tunnel precisely along the cycloid if there are underground rivers, so this configuration should be discarded in favor of other options. Finally, minimization of the path length is directly related to such economic metrics as the costs for building and subsequently maintaining a tunnel whose path is simulated by the required trajectory.

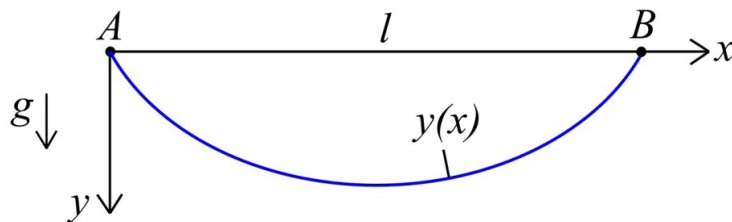


Fig. 1. Statement of the classical brachistochrone problem:

body M , acted on by its own gravity, should pass the trajectory $y(x)$ from point A to point B in the shortest possible time (g is the acceleration of gravity)

It follows from the above that it is crucial to minimize the trajectory length L from a practical standpoint. However, simultaneously minimizing the two quantities T and L is meaningless, since they are determined by the known expressions

$$T = \int_0^l \sqrt{\frac{1+y'^2}{2gy}} dx, \quad L = \int_0^l \sqrt{1+y'^2} dx, \quad (1)$$

(the prime indicates a derivative with respect to the coordinate x), clearly taking their minimum values at different extremals $y(x)$ (cycloid and straight line, respectively).

Nevertheless, the problem on finding the best compromise between these two factors, achievable by constructing and analyzing an adequate two-factor optimization criterion, turns out to be fairly meaningful. Evidently, to obtain a trajectory with maximum efficiency, it seems reasonable to strive for the best relative compromise between the quantities T and L , taking into account their functional relationship. It is easy to understand that for this purpose it is advisable to synthesize a multiplicative optimization criterion in the form of the following composition of the particular criteria T and L :

$$J = T \cdot L = \min. \quad (2)$$

A similar criterion was successfully applied in other multicriterial mechanical problems [12, 13], where it proved to be effective, gaining major practical significance. Criterion (2) allows to estimate the degree to which the motion time T should be increased for the trajectory length L to decrease to the greatest extent compared to the increase in time. This is precisely what is meant by the best relative compromise between these factors.

The primary goal of this study is to analyze the two-factor optimization criterion (2) and find the optimal trajectory with respect to this criterion.

Determining the brachistochrone of the given length

Before we can focus on criterion (2), let us discuss in detail the auxiliary problem on finding a brachistochrone of a given length, which is mathematically formulated as follows [14]:

$$T = \min, \quad L = \text{fix}, \quad (3)$$

where expressions (1) should be taken into account.

Problem (3) is an isoperimetric problem of variational calculus that should be solved by composing a function

$$H = \sqrt{\frac{1+y'^2}{2gy}} + \lambda \sqrt{1+y'^2} = H(y, y'), \quad (4)$$

where λ is a constant.

Next, we should consider the problem on the extremals of a functional with the integrand $H(y, y')$. As in the classical brachistochrone problem, this function does not explicitly depend on x , so we solve it using the first integral of the Euler–Lagrange equation:

$$H - y' \frac{\partial H}{\partial y'} = \left(\frac{1}{\sqrt{2gy}} + \lambda \right) \frac{1}{\sqrt{1+y'^2}} = C, \quad (5)$$

where C is a constant.

Let us introduce a standard substitution $y' = \text{ctg } \varphi$ in this equation, so that after some simplifications we obtain:

$$y = \frac{a \sin^2 \varphi}{2(1 - b \sin \varphi)^2}, \quad a = \frac{1}{gC^2}, \quad b = \frac{\lambda}{C}, \quad (6)$$

where a, b are the new constants related to C and λ .

Next, calculating y' by expression (6) and taking into account that $y' = \text{ctg } \varphi$, we obtain the following equation:

$$y' = \frac{a \sin \varphi \cos \varphi}{(1 - b \sin \varphi)^3} \varphi' = \text{ctg } \varphi. \quad (7)$$

Separating the variables in it, we obtain:

$$\frac{a \sin^2 \varphi}{(1 - b \sin \varphi)^3} d\varphi = dx, \quad x = a \int \frac{\sin^2 \varphi}{(1 - b \sin \varphi)^3} d\varphi. \quad (8)$$

To calculate the resulting integral, we use the following trigonometric substitution:

$$z = \operatorname{tg} \frac{\varphi}{2}, \quad \varphi = 2 \operatorname{arctg} z, \quad d\varphi = \frac{2dz}{1+z^2}, \quad \sin \varphi = \frac{2z}{1+z^2}. \quad (9)$$

As a result, after the transformations, we proceed to calculate the integral of the rational function:

$$\int \frac{\sin^2 \varphi}{(1 - b \sin \varphi)^3} d\varphi = 8 \int \frac{z^2}{(z^2 - 2bz + 1)^3} dz. \quad (10)$$

Let us use tables of integrals from [15] for this purpose. It is clear from the tables that the integral has different representations at $|b| < 1$ and $|b| > 1$. This is because the roots of the quadratic trinomial $z^2 - 2bz + 1$ are complex conjugate in the first case, and real in the second case.

Representations of integral (10). Let us consider the first case when $|b| < 1$. The integral of rational function (10) is in this case

$$\begin{aligned} \int \frac{z^2}{(z^2 - 2bz + 1)^3} dz = & \frac{1}{4(1-b^2)} \left[\frac{(2b^2 - 1)z - b}{(z^2 - 2bz + 1)^2} + \right. \\ & \left. + \frac{2b^2 + 1}{2(1-b^2)} \left(\frac{z - b}{z^2 - 2bz + 1} + \frac{1}{\sqrt{1-b^2}} \operatorname{arctg} \frac{z - b}{\sqrt{1-b^2}} \right) \right]. \end{aligned} \quad (11)$$

Returning to the initial variable φ , we obtain from equality (10) for $x(\varphi)$:

$$x = \frac{a}{(1-b^2)^2} \left[\frac{2b^2 + 1}{\sqrt{1-b^2}} \operatorname{arctg} \frac{\operatorname{tg} \frac{\varphi}{2} - b}{\sqrt{1-b^2}} + \frac{\cos \varphi ((4b^2 - 1) \sin \varphi - 3b)}{2(1 - b \sin \varphi)^2} \right] + x_0, \quad (12)$$

where x_0 is the integration constant.

As the problem is formulated so that the points A and B lie on the same horizontal at a distance l away from each other, then $y(0) = 0$, $y(l) = 0$. As evident from expression (6), these points correspond to the parameter values $\varphi = 0$ and $\pi = 0$. The constant x_0 is defined from the condition $x = 0$ at $\varphi = \pi$:

$$x_0 = \frac{a}{(1-b^2)^2} \left(\frac{2b^2 + 1}{\sqrt{1-b^2}} \operatorname{arctg} \frac{b}{\sqrt{1-b^2}} + \frac{3b}{2} \right). \quad (13)$$

In turn, the constant a is found from the condition $x = l$ at $\varphi = \pi$:

$$a = \frac{l(1-b^2)^2}{\frac{2b^2 + 1}{\sqrt{1-b^2}} \left(\frac{\pi}{2} + \operatorname{arctg} \frac{b}{\sqrt{1-b^2}} \right) + 3b}. \quad (14)$$

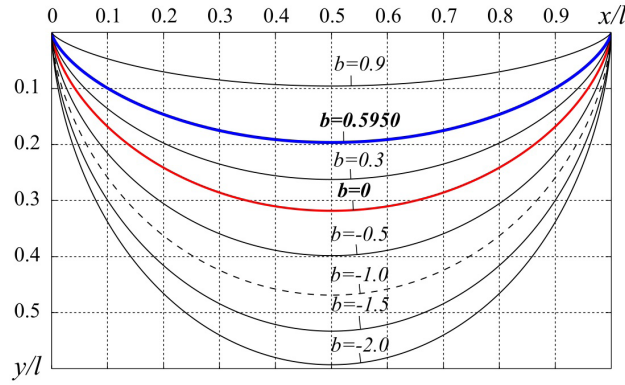


Fig. 2. Family of brachistochrones with different lengths (constructed in dimensionless coordinates)
 See Eq. (15), case $0 < |b| < 1$; Eq. (16), case $b = 0$ (curve highlighted in red);
 Eq. (26), case $b < -1$, and Eq. (32), case $b = -1$ (dashed curve).
 The optimal trajectory with respect to the two-factor criterion (2) is highlighted in blue

As a result, the solution of problem (3) for the case $|b| < 1$ takes the form:

$$\left\{ \begin{aligned} x &= \frac{a}{(1-b^2)^2} \left[\frac{2b^2+1}{\sqrt{1-b^2}} \left(\operatorname{arctg} \frac{\operatorname{tg} \frac{\varphi}{2} - b}{\sqrt{1-b^2}} + \operatorname{arctg} \frac{b}{\sqrt{1-b^2}} \right) + \right. \\ &\quad \left. + \frac{\cos \varphi ((4b^2-1)\sin \varphi - 3b)}{2(1-b\sin \varphi)^2} + \frac{3b}{2} \right], \\ y &= \frac{a \sin^2 \varphi}{2(1-b\sin \varphi)^2} \end{aligned} \right. , \quad (15)$$

where the quantity a is defined by Eq. (14).

Thus, parametric solution (15) can be used to construct a family of brachistochrones corresponding to different values of the parameter b provided that $|b| < 1$. These trajectories are shown in Fig. 2, where the dimensionless coordinates x/l and y/l are plotted along the axes for convenience.

We should note that the value $b = 0$ corresponds to a cycloidal trajectory. Indeed, the equation for the cycloid follows directly from expressions (15):

$$\left\{ \begin{aligned} x &= \frac{a}{4} (2\varphi - \sin 2\varphi) = r(\psi - \sin \psi) \\ y &= \frac{a}{4} (1 - \cos 2\varphi) = r(1 - \cos \psi) \end{aligned} \right. , \quad (16)$$

where $r = a/4$ is the radius of the rolling circle; $\psi = 2\varphi$ is its rotation angle, varying from 0 to 2π .

The values $0 < b < 1$ correspond to the trajectories lying above the cycloid, and the values $-1 < b < 0$ correspond to the trajectories below it. Evidently, the dimensionless parameter b uniquely corresponds to the length L of the curve, which is defined by the second formula in (1).

To establish this correspondence, we substitute the expression $y' = \operatorname{ctg} \varphi$ into the given formula, consequently obtaining:

$$L = a \int_0^{\pi} \frac{\sin \varphi}{(1 - b \sin \varphi)^3} d\varphi = 4a \int_0^{\infty} \frac{z(1 + z^2)}{(z^2 - 2bz + 1)^3} dz, \quad (17)$$

where the same substitution as above is performed for the variable (9).

Again, using the tables of integrals from [15], we find:

$$L = \frac{a}{(1 - b^2)^2} \left[\frac{3b}{\sqrt{1 - b^2}} \left(\frac{\pi}{2} + \operatorname{arctg} \frac{b}{\sqrt{1 - b^2}} \right) + 2 + b^2 \right]. \quad (18)$$

Substituting the value of a here, in accordance with Eq. (14) and introducing the dimensionless quantity $\delta = l/L$, which lies within $0 < \delta < 1$ based on the physical meaning of the problem, we obtain:

$$\delta = \frac{\left(\frac{\pi}{2} + \operatorname{arctg} \frac{b}{\sqrt{1 - b^2}} \right) \frac{2b^2 + 1}{\sqrt{1 - b^2}} + 3b}{\left(\frac{\pi}{2} + \operatorname{arctg} \frac{b}{\sqrt{1 - b^2}} \right) \frac{3b}{\sqrt{1 - b^2}} + 2 + b^2}. \quad (19)$$

This formula can be used to plot the dependence $\delta(b)$ over the interval $-1 < b < 1$ (Fig. 3). Notably, the value $b = 1$ corresponds to a straight line when $\delta = 1$, and the value $b = 0$ corresponds to a cycloid when $\delta = \pi/4 \approx 0.7854$.

Finally, let us express the time of motion along the optimal trajectory according to the first formula in (1), performing the substitution $y' = \operatorname{ctg} \varphi$ in it and using expressions (6) and (8):

$$T = \sqrt{\frac{a}{g}} \int_0^{\pi} \frac{d\varphi}{(1 - b \sin \varphi)^2} = 2 \sqrt{\frac{a}{g}} \int_0^{\infty} \frac{1 + z^2}{(z^2 - 2bz + 1)^2} dz. \quad (20)$$

Again, using the tables of integrals from [15], we find:

$$T = 2 \sqrt{\frac{a}{g}} \frac{1}{1 - b^2} \left[\frac{1}{\sqrt{1 - b^2}} \left(\frac{\pi}{2} + \operatorname{arctg} \frac{b}{\sqrt{1 - b^2}} \right) + b \right], \quad (21)$$

where it should be borne in mind that the quantity a is determined by Eq. (14).

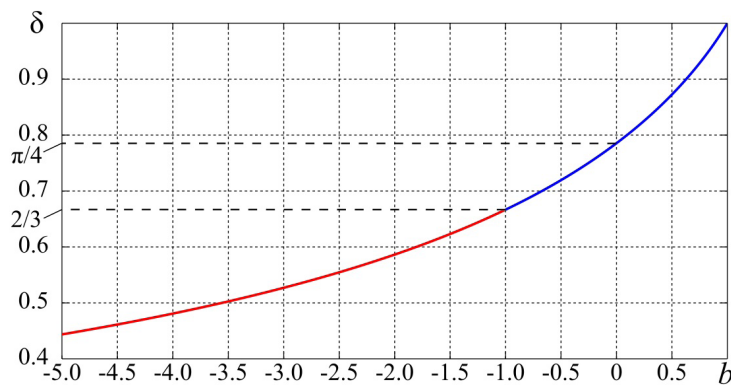


Fig. 3. Quantity δ as a function of the parameter b over the interval $-1 < b < 1$ (curve highlighted in blue) and at $b \leq -1$ (curve highlighted in red)

Let us now consider the second case, when $|b| > 1$. Using the tables of integrals from [15], we confirm that integral (10) takes the form:

$$\int \frac{z^2}{(z^2 - 2bz + 1)^3} dz = \frac{1}{4(1-b^2)} \left[\frac{(2b^2-1)z-b}{(z^2-2bz+1)^2} + \right. \\ \left. + \frac{2b^2+1}{2(1-b^2)} \left(\frac{z-b}{z^2-2bz+1} + \frac{1}{2\sqrt{b^2-1}} \ln \left| \frac{z-b-\sqrt{b^2-1}}{z-b+\sqrt{b^2-1}} \right| \right) \right]. \quad (22)$$

Returning to the initial variable φ , we obtain the function $x(\varphi)$ in accordance with Eq. (10):

$$x = \frac{a}{(1-b^2)^2} \left[\frac{2b^2+1}{2\sqrt{b^2-1}} \ln \left| \frac{\operatorname{tg} \frac{\varphi}{2} - b - \sqrt{b^2-1}}{\operatorname{tg} \frac{\varphi}{2} - b + \sqrt{b^2-1}} \right| + \frac{\cos \varphi ((4b^2-1)\sin \varphi - 3b)}{2(1-b\sin \varphi)^2} \right] + x_0. \quad (23)$$

As before, we define the constant x_0 from the condition $x = 0$ at $\varphi = 0$:

$$x_0 = \frac{a}{(1-b^2)^2} \left(\frac{3b}{2} - \frac{2b^2+1}{2\sqrt{b^2-1}} \ln \left| \frac{b+\sqrt{b^2-1}}{b-\sqrt{b^2-1}} \right| \right). \quad (24)$$

Then we find the constant a from the condition $x = l$ at $\varphi = \pi$:

$$a = \frac{l(1-b^2)^2}{\frac{2b^2+1}{2\sqrt{b^2-1}} \ln \left| \frac{b-\sqrt{b^2-1}}{b+\sqrt{b^2-1}} \right| + 3b}. \quad (25)$$

As a result, the solution of the problem for the case $|b| > 1$ takes final form:

$$\left\{ \begin{aligned} x &= \frac{a}{(1-b^2)^2} \left[\frac{2b^2+1}{2\sqrt{b^2-1}} \ln \left| \frac{\left(\operatorname{tg} \frac{\varphi}{2} - b - \sqrt{b^2-1} \right) (b - \sqrt{b^2+1})}{\left(\operatorname{tg} \frac{\varphi}{2} - b + \sqrt{b^2-1} \right) (b + \sqrt{b^2+1})} \right| + \right. \\ &\quad \left. + \frac{\cos \varphi ((4b^2-1)\sin \varphi - 3b)}{2(1-b\sin \varphi)^2} + \frac{3b}{2} \right], \\ y &= \frac{a \sin^2 \varphi}{2(1-b\sin \varphi)^2} \end{aligned} \right., \quad (26)$$

where a is found from Eq. (25).

Parametric solution (26) can be used to construct the optimal trajectories corresponding to the values of the parameter b from the interval $b < -1$, which (see Fig. 2) continue the family of trajectories previously constructed for the values $-1 < b < 1$. As for the values $b > 1$, they are physically impossible, i.e., they do not correspond to the optimal trajectories. This can be better observed by expressing the curve length L by the second formula in (1):

$$L = \frac{a}{(1-b^2)^2} \left(-\frac{3b}{2\sqrt{b^2-1}} \ln \left| \frac{b+\sqrt{b^2-1}}{b-\sqrt{b^2-1}} \right| + 2+b^2 \right). \quad (27)$$

Substituting expression (25) here, we express the value of the dimensionless quantity $\delta = l/L$:

$$\delta = \frac{\frac{2b^2+1}{2\sqrt{b^2-1}} \ln \left| \frac{b-\sqrt{b^2-1}}{b+\sqrt{b^2-1}} \right| + 3b}{-\frac{3b}{2\sqrt{b^2-1}} \ln \left| \frac{b+\sqrt{b^2-1}}{b-\sqrt{b^2-1}} \right| + 2+b^2}, \quad (28)$$

which, provided that $b > 1$, corresponds to negative values of the quantity δ , which cannot be the case in reality if we adopt the representation of δ as a ratio of lengths. Dependence (28) for the values $b < -1$ is also shown in Fig. 3.

The remaining step is to express the time of motion along the optimal trajectory in accordance with the first formula in (1) for the case under consideration:

$$T = 2\sqrt{\frac{a}{g}} \frac{1}{1-b^2} \left[-\frac{1}{2\sqrt{1-b^2}} \ln \left| \frac{b+\sqrt{b^2-1}}{b-\sqrt{b^2-1}} \right| + b \right], \quad (29)$$

where it should be borne in mind that the quantity a is determined by Eq. (25).

Notably, if $b \rightarrow 1$, we obtain, in accordance with Eq. (28), that $\delta \rightarrow 1$, (i.e., $L \rightarrow l$), while in accordance with Eq. (29), we obtain that $T \rightarrow \infty$, so that the case $b = 1$ is a limiting one.

To complete the picture, let us separately focus on the case when $b = -1$. This case is intermediate between the cases $-1 < b < 1$ and $b < -1$ analyzed above. Here, we obtain the following:

$$\int \frac{z^2}{(z^2 - 2bz + 1)^3} dz = \int \frac{z^2}{(z+1)^6} dz = -\frac{10z^2 + 5z + 1}{30(z+1)^5}. \quad (30)$$

Returning to the initial variable φ , we obtain in accordance with Eq. (10):

$$x = -\frac{4a \left(10 \operatorname{tg}^2 \frac{\varphi}{2} + 5 \operatorname{tg} \frac{\varphi}{2} + 1 \right)}{15 \left(\operatorname{tg} \frac{\varphi}{2} + 1 \right)^5} + x_0. \quad (31)$$

Given that $x = 0$ at $\varphi = 0$, and $x = l$ at $\varphi = \pi$, we find, in accordance with expression (31), that $x_0 = 4a/15$, and $a = 15l/4$, so in this case we obtain $x_0 = l$.

Thus, the solution for the case $b = -1$ can be written as

$$\begin{cases} x = \frac{4a}{15} \left[1 - \frac{10 \operatorname{tg}^2 \frac{\varphi}{2} + 5 \operatorname{tg} \frac{\varphi}{2} + 1}{\left(\operatorname{tg} \frac{\varphi}{2} + 1 \right)^5} \right] \\ y = \frac{a \sin^2 \varphi}{2(1 - b \sin \varphi)^2} \end{cases} \quad (32)$$

This trajectory is shown in Fig. 2 by a dashed line. Finally, let us express the quantities L and T corresponding to this trajectory:

$$L = 4a \int_0^\infty \frac{z(1+z^2)}{(z+1)^6} dz = \frac{2a}{5}, \quad T = 2\sqrt{\frac{a}{g}} \int_0^\infty \frac{1+z^2}{(z+1)^4} dz = \frac{4}{3} \sqrt{\frac{a}{g}}. \quad (33)$$

It follows then that if $b = -1$, we obtain the value $\delta = l/L = 2/3 \approx 0.6667$, which is fully consistent with the graph shown in Fig. 3.

Thus, the problem on finding a brachistochrone with a given length can be considered solved.

Determining the optimal solution with respect to the two-factor criterion

Let us now proceed to search for the optimal solution by the multiplicative criterion (2). Apparently, in this case it is sufficient to use the solution to the above problem about the brachistochrone with the given length, where, provided that the value of L was known, a curve with the minimum possible motion T along it was found. This is because all other curves, yielding a larger result with respect to time for the given L , are also clearly worse with respect to the criterion (2), so they can be ignored performing the two-factor optimization procedure.

Thus, since we previously completed the first stage of optimization, we now consider criterion (2) only for the curves with the minimum motion time at the given length. Therefore, the problem is no longer variational but rather a conventional algebraic one on finding the minimum point of a single-variable function.

Considering the limiting cases, it is easy to see that criterion (2) indeed allows finding a specific optimal trajectory. As a matter of fact, we obtain for the first limiting case when the trajectory profile is close to rectilinear ($b \rightarrow 1$): $T \rightarrow \infty$, $L \rightarrow l$, i.e., $J \rightarrow \infty$. Conversely, if the trajectory has a deep profile ($b \rightarrow -\infty$), then $T \rightarrow \infty$, $L \rightarrow \infty$, so we once more obtain $J \rightarrow \infty$. This means that the criterion J , convenient to be considered as a function of the parameter b , should have an internal extremum, specifically, a minimum, in the interval $b < 1$. Recall that the time T is given by Eqs. (21) and (29) for cases $-1 < b < 1$ and $b < -1$, respectively, the length L is determined by expressions (18) and (27), and the parameter a included in these expressions is found from relations (14) and (25).

We introduce the dimensionless quantity I , proportional to the criterion J and related to it by the following formula:

$$I = \frac{J}{l} \sqrt{\frac{g}{l}}. \quad (34)$$

Because the representations for T and L are rather cumbersome, it is the easiest to determine the minimum point of function (34) by plotting its dependence on the parameter b (Fig. 4).

We can determine from the graph in Fig. 4 that the required minimum corresponds to the value $b_* = 0.5950$. We should note that its location in the interval $0 < b < 1$ can be also identified from general considerations. Indeed, the value $b = 0$ corresponds to the cycloidal profile, and the relative compromise for criterion (2) can only be reached by moving upwards from the cycloid, increasing the motion time T and decreasing the trajectory length L . It then becomes apparent what the values of T and L are equal to for motion along a trajectory that is optimal with respect to the two-factor criterion, as well as the value of the criterion J itself. If we substitute the value of b_* found into Eqs. (21) and (18), then, by virtue of (14) bearing in mind that $I_* = 2.9430$ (see Fig. 4), and using Eq. (34), we obtain:

$$T_* = 2.6265\sqrt{\frac{l}{g}}, L_* = 1.1205l, J_* = I_*l\sqrt{\frac{l}{g}} = 2.9430l\sqrt{\frac{l}{g}}. \quad (35)$$

At the same time, we obtain for the cycloidal trajectory at $b = 0$:

$$T_c = \sqrt{2\pi}\sqrt{\frac{l}{g}} \approx 2.5066\sqrt{\frac{l}{g}}, L_c = \frac{4l}{\pi} \approx 1.2732l. \quad (36)$$

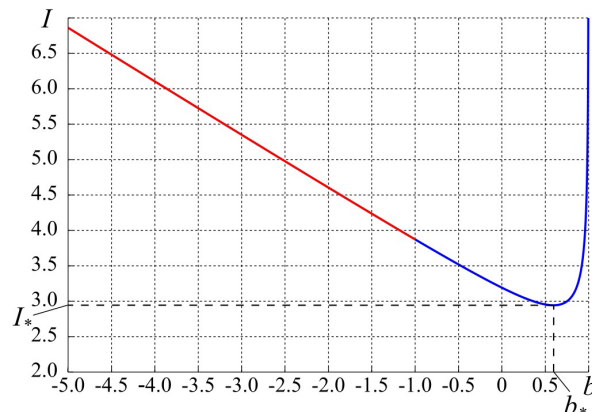


Fig. 4. Two-factor criterion I as a function of the parameter b in the interval $-1 < b < 1$ (curve highlighted in blue) and at $b \leq -1$ (curve highlighted in red). The minimum on the curve $I_* = 2.9430$ at $b_* = 0.5950$ is shown

Comparing the corresponding values of (35) and (36), we can conclude that the motion time for the optimal trajectory with respect to criterion (2) is 4.8% longer than that for the cycloid, and the length of this trajectory is smaller than that of the cycloid by 12%.

The obtained results clearly demonstrate the required best relative compromise between the two criteria T and L and prove that a fairly small increase in the motion time can yield a much greater decrease in the trajectory length. Based on the values obtained, we can once again recommend the criteria of form (2) for solving multicriterial problems in different areas of mechanics. Notice that the optimal trajectory found is also shown in Fig. 2 ($b = 0.5950$).

Constructing a rational solution

The solutions to most optimization problems in mechanics are optimal only in a formal (i.e., purely mathematical) sense, since their geometry is rather complex. Naturally, their practical implementations remain challenging. A related issue is to construct a solution that is not strictly optimal but has a simpler geometry and is more convenient for specific practical purposes. This solution can be called quasi-optimal, or rational; it is not optimal in general but rather in a class of functions characterizing the simplified geometry of the problem [16].

It is preferable to adopt a circular profile in the brachistochrone problem considered, that is, to consider trajectories in the form of a circular arc. Interestingly, Galileo proved that the shortest path is not always the fastest by comparing the motion time over a straight line with the motion time over a circular arc [11]. Thus, the problem on finding a rational solution is posed as follows:

Considering all the circles passing through the two given points A and B lying on the same horizontal (in our presentation), we are going to choose the one such that motion along it affords an extremum value to the given optimization criterion.

The formulated problem statement is illustrated graphically in Fig. 5.

We consider both the minimization for the motion time only and the two-factor criterion (2). If comparing the parameters of these circular trajectories with the characteristics of the solutions discussed above reveals sufficiently small differences, these rational solutions can be recommended for practical applications instead of the initial, strictly optimal solutions.

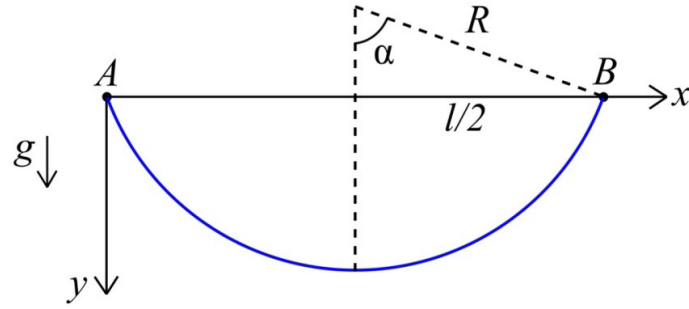


Fig. 5. Problem statement for the rational solution based on the circular profile with the radius R (2α is the central angle)

It is well known that the oscillation half-period of a mathematical pendulum, equal to the time of motion along the circumference from point A to point B , is found by Eq. [17]:

$$T = 2\sqrt{\frac{R}{g}}K\left(\sin\frac{\alpha}{2}\right), \quad (37)$$

where R is the circle radius, α is the oscillation amplitude, $K(\kappa)$ is the complete elliptic first-kind integral with the modulus κ .

It is clear that the quantities R , α and l are related in the following manner (see Fig. 5):

$$R = \frac{l}{2\sin\alpha}. \quad (38)$$

Substituting expression (38) into Eq. (37), we obtain the final expression for the motion time along a circular arc with the central angle of 2α :

$$T = \sqrt{\frac{2l}{g}} \frac{1}{\sqrt{\sin\alpha}} K\left(\sin\frac{\alpha}{2}\right) = T(\alpha). \quad (39)$$

Let us first consider the problem on minimizing the motion time. For this purpose, we differentiate function (39) with respect to the variable α , taking into account the rules for calculating derivatives of elliptical integrals, and equate the resulting expression to zero. As a result, the following equation can be obtained after the transformations:

$$(1 + 2\cos\alpha)K\left(\sin\frac{\alpha}{2}\right) = 2E\left(\sin\frac{\alpha}{2}\right), \quad (40)$$

where $E(\kappa)$ is a complete elliptic second-kind integral with the modulus κ .

The only root of equation (40) that corresponds to the meaning of the problem is $\alpha_{*1} = 1.2433$, while the motion time corresponding to it, found from Eq. (39), and the trajectory length, found by the formula $L = 2\alpha R = \alpha l / \sin\alpha$ and necessary for further comparisons, are equal to, respectively:

$$T_{*1} = 2.5233\sqrt{\frac{l}{g}}, L_{*1} = 1.3131l. \quad (41)$$

Evidently, the time T_{*1} exceeds the motion time along the cycloid, found by the first formula in (36), by only 0.7%. This means that the found circular arc with the central angle $2\alpha_{*1} = 2.4866$ (or 142.47°) is largely equivalent to the cycloid with respect to the time factor, so it can be recommended for practical applications.

Now, proceeding to find the best parameter of the circular trajectory with respect to the two-factor criterion (2), let us compose for it an expression accounting for Eq. (39) and bearing in mind that $L = \alpha l / \sin \alpha$:

$$J = l \sqrt{\frac{2l}{g}} \frac{\alpha}{\sin^{3/2} \alpha} K\left(\sin \frac{\alpha}{2}\right) = J(\alpha). \quad (42)$$

Differentiating this function with respect to α and the resulting expression equating to zero, we obtain the following equation after simplifications:

$$[\alpha(1 + 4 \cos \alpha) - 2 \sin \alpha] K\left(\sin \frac{\alpha}{2}\right) = 2\alpha E\left(\sin \frac{\alpha}{2}\right), \quad (43)$$

whose only root consistent with the meaning of the problem is $\alpha_{*2} = 0.8720$. The motion time, trajectory length and two-factor criterion value corresponding to this root then take the following form:

$$T_{*2} = 2.6650 \sqrt{\frac{l}{g}}, \quad L_{*2} = 1.1390l, \quad J_{*2} = 3.0354l \sqrt{\frac{l}{g}}. \quad (44)$$

Clearly, the motion time increased by 5.6% compared to Eqs. (41), while the trajectory length decreased by 13.3%. These values also illustrate the best compromise reached between these factors for the case when optimization is carried out for a class of circular arcs. The last stage is to compare the found expressions (44) with similar values for the strictly optimal solution previously obtained with respect to the two-factor criterion, which are given by Eqs. (35).

For example, the time T_{*2} is only 1.5% larger than T_* , the length L_{*2} is only 1.7% larger than L_* , and finally, the value of the two-factor criterion J_{*2} is only 3.1% larger than J_* , which can be considered excellent results. Therefore, if a two-factor optimization criterion has to be used, the optimal trajectory with respect to this criterion, found above, can be replaced with acceptable accuracy by a circular arc with the central angle $2\alpha_{*2} = 1.7440$ (or 99.92°), which has much simpler geometry. The circular profiles found, which are optimal with respect to the above criteria $T = \min$ and $J = \min$, are shown in Fig. 6 by dashed lines together with the corresponding trajectories that are generally optimal with respect to the same criteria, represented by solid lines.

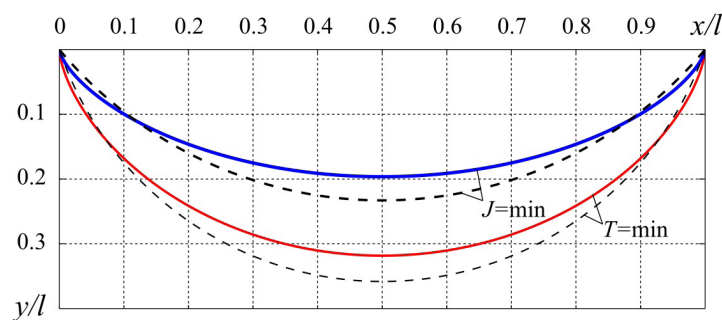


Fig. 6. Comparison of optimal profiles (solid lines) with rational ones (dashes); T, J are optimization criteria (the motion time of a point particle along the curve and the multiplicative criterion, respectively)



Conclusion

We have proposed a modification of the classical brachistochrone problem, allowing for minimizing the length of trajectory in addition to minimizing the time of motion. The problem was solved by constructing a two-factor multiplicative optimization criterion. As we analyzed the problem posed, we have considered in detail the problem on the brachistochrone of a given length; the results provided the simplest way to finding the optimal trajectory with respect to the two-factor criterion adopted. The numerical values presented in the paper and the comparisons drawn lead us to conclude that such multiplicative criteria are satisfactory, so they can be used for solving other problems on optimization of mechanical systems, where a relatively optimal balance between several factors should be reached.

Furthermore, we have constructed a rational solution which is characterized by simplified geometry and is easy to use.

We have established that the circular profile is virtually equivalent to the strictly optimal solution if the profile's parameters are selected properly based on the optimization criterion adopted. For this reason, we also recommend to construct similar rational solutions for many other problems.

REFERENCES

1. **Yakovlev V. I.** The beginnings of analytical mechanics, Institute of Computer Sciences, Moscow, Izhevsk, 2002 (in Russian).
2. **Golubev Yu. F.**, Brachistochrone with friction, *Journal of Computer and Systems Sciences*. 49 (5) (2010) 719–730.
3. **Zarodnyuk A. V., Cherkasov O. Yu.**, Brachistochrone with linear viscous friction, *Moscow University Mechanics Bulletin*. 70 (3) (2015) 70–74.
4. **Sumbatov A. S.**, Brachistochrone with Coulomb friction as the solution of an isoperimetrical variational problem, *Intern. J. Non-Linear Mech.* 88 (January) (2017) 135–141.
5. **Wensrich C. M.**, Evolutionary solutions to the brachistochrone problem with Coulomb friction, *Mech. Res. Commun.* 31 (2) (2004) 151–159.
6. **Legeza V. P.**, Brachistochrone for a rolling cylinder. *Mechanics of Solids*. 45 (1) (2010) 27–33.
7. **Akulenko L. D.**, An analog of the classical brachistochrone for a disk, *Doklady Physics*. 53 (3) (2008) 156–159.
8. **Sumbatov A. S.**, Problem of the brachistochronic motion of a heavy disk with dry friction, *Intern. J. Non-Linear Mech.* 99 (March) (2018) 295–301.
9. **Legeza V. P.**, Brachistochronic motion of a material point on a transcendental surface, *Intern. Appl. Mech.* 56 (3) (2020) 358–366.
10. **Gladkov S. O., Bogdanova S. B.**, The theory of a space brachistochrone, *Tomsk State University Journal of Mathematics and Mechanics*. 68 (2020) 53–60 (in Russian).
11. **Sumbatov A. S.**, The problem on a brachistochrone (classification of generalizations and some recent results), *Trudy MFTI [Transactions of Moscow Institute of Physics and Technology]*. 9 (3) (2017) 66–75 (in Russian).
12. **Smolnikov B. A., Smirnov A. S.**, Novyy kriteriy optimizatsii v zadache Gomana [A new optimization criterion in the Hohmann problem], In book: XII Vserossiyskiy Syezd po fundamentalnym problemam teoreticheskoy i prikladnoy mekhaniki. Sbornik trudov. V 4-kh tomakh. T. 1. Obshchaya i prikladnaya mekhanika [Transactions of “The 12-th All-Russian Congress on Fundamental Problems of Theoretical and Applied Mechanics”, Aug. 19–24, 2019, Ufa, Republic of Bashkortostan, Russia. The collection of works in 4 Vols., Vol. 1: General and Applied Mechanics, Bash. State Univ. Reg. Inf. Center, Ufa (2019) 266–268 (in Russian).
13. **Smirnov A. S., Smolnikov B. A.**, Catenary optimization, In book: *Trudy seminarov «Kompyuternyye metody v mekhanike sploshnoy sredy» [Transactions of the seminar “Computer Methods in Continuum Mechanics”]*, 2019–2020, Saint-Petersburg University Publishing, St. Petersburg (2020) 35–50 (in Russian).
14. **Gladkov S. O., Bogdanova S. B.**, Analytical and numerical solution of the problem on brachistochrones in some general cases, *J. Math. Sci.* 245 (4) (2020) 528–537.
15. **Gradshteyn I. S., Ryzhik I. M.**, Table of integrals, series and products, Translated from Russian, Seventh Edition, Eds. Jeffrey A., Zwillinger D., Elsevier Inc., Amsterdam, Boston, Heidelberg, etc., 2007.

16. **Suvorov S. V., Smirnov A. S.**, Otsenka effektivnosti optimalnykh balochnykh konstruksiy [Performance evaluation of the optimal beam structures], Nedelya nauki SPbPU: materialy nauchnoy konferentsii s mezhdunarodnym uchastiyem. Institut prikladnoy matematiki i mekhaniki [Proceedings of the scientific conference “Science Week at SPbPU” with international participation. The Institute of Applied Mathematics and Mechanics], November 18–23, 2019, St. Petersburg Polytechnic University Publishing, St. Petersburg (2019) 102–104 (in Russian).

17. **Sikorskiy Yu. S.**, Elementy teorii ellipticheskikh funktsiy s prilozheniyami k mekhanike [Elements of the theory of elliptic functions with applications to mechanics]. KomKniga, Moscow, 2006 (in Russian).

СПИСОК ЛИТЕРАТУРЫ

1. **Яковлев В. И.** Начала аналитической механики. М., Ижевск: Институт компьютерных исследований, 2002. 352 с.

2. **Голубев Ю. Ф.** Брахистохрона с трением // Известия Российской академии наук. Теория и системы управления. 2010. № 5. С. 41–52.

3. **Зароднюк А. В., Черкасов О. Ю.** К задаче о брахистохроне с линейным вязким трением // Вестник Московского университета. Сер. 1: Математика. Механика. 2015. № 3. С. 65–69.

4. **Sumbatov A. S.** Brachistochrone with Coulomb friction as the solution of an isoperimetrical variational problem // International Journal of Non-Linear Mechanics. 2017. Vol. 88. January. Pp. 135–141.

5. **Wensrich C. M.** Evolutionary solutions to the brachistochrone problem with Coulomb friction // Mechanics Research Communications. 2004. Vol. 31. No. 2. Pp. 151–159.

6. **Лережа В. П.** Брахистохрона для катящегося цилиндра // Известия Российской академии наук. Механика твердого тела. 2010. № 1. С. 34–41.

7. **Акуленко Л. Д.** Аналог классической брахистохроны для диска // Доклады Академии наук. 2008. Т. 419. № 2. С. 193–196.

8. **Sumbatov A. S.** Problem of the brachistochronic motion of a heavy disk with dry friction // International Journal of Non-Linear Mechanics. 2018. Vol. 99. March. Pp. 295–301.

9. **Legeza V. P.** Brachistochronic motion of a material point on a transcendental surface // International Applied Mechanics. 2020. Vol. 56. No. 3. Pp. 358–366.

10. **Гладков С. О., Богданова С. Б.** К теории пространственной брахистохроны // Вестник Томского государственного университета. Математика и механика. 2020. № 68. С. 53–60.

11. **Сумбатов А. С.** Задача о брахистохроне (классификация обобщений и некоторые новые результаты) // Труды МФТИ. 2017. Т. 9. № 3. С. 66–75.

12. **Смольников Б. А., Смирнов А. С.** Новый критерий оптимизации в задаче Гомана // XII Всероссийский съезд по фундаментальным проблемам теоретической и прикладной механики. 19–24 августа 2019 г., г. Уфа, Республика Башкортостан, Россия. Сборник трудов в 4-х тт. Т. 1. Общая и прикладная механика. Уфа: РИЦ БашГУ, 2019. С. 266–268.

13. **Смирнов А. С., Смольников Б. А.** Оптимизация цепной линии // Труды семинара «Компьютерные методы в механике сплошной среды» 2019–2020. СПб.: Изд-во Санкт-Петербургского университета, 2020. С. 35–50.

14. **Гладков С. О., Богданова С. Б.** Аналитическое и численное решение задачи о брахистохроне в некоторых общих случаях // Итоги науки и техники. Серия «Современная математика и ее приложения». Тематические обзоры. 2018. Т. 145. С. 114 – 122.

15. **Градштейн И. С., Рыжик И. М.** Таблицы интегралов, рядов и произведений. СПб.: БХВ-Петербург, 2011. 1232 с.

16. **Суворов С. В., Смирнов А. С.** Оценка эффективности оптимальных балочных конструкций // Неделя науки СПбПУ: материалы научной конференции с международным участием. Институт прикладной математики и механики. 18 – 23 ноября 2019 г., Санкт-Петербургский политехнический университет. СПб.: Изд-во Политехнического университета, 2019. С. 102–104.

17. **Сикорский Ю. С.** Элементы теории эллиптических функций с приложениями к механике. М.: КомКнига, 2006. 366 с.

THE AUTHORS

SMIRNOV Alexey S.

Peter the Great St. Petersburg Polytechnic University

Institute of Problems of Mechanical Engineering of the Russian Academy of Sciences

29 Politechnicheskaya St., St. Petersburg, 195251, Russia

smirnov.alexey.1994@gmail.com

ORCID: 0000-0002-6148-0322

SUVOROV Sergei V.

Central Design Bureau of Transport Engineering

45v, Peterburgskoe HWY, Tver, 170003, Russia

suvorovsv96@gmail.com

ORCID: 0000-0002-7461-2742

СВЕДЕНИЯ ОБ АВТОРАХ

СМИРНОВ Алексей Сергеевич — ассистент Высшей школы механики и процессов управления Санкт-Петербургского политехнического университета Петра Великого, Санкт-Петербург, Россия; стажер-исследователь Института проблем машиноведения Российской академии наук.

195251, Россия, г. Санкт-Петербург, Политехническая ул., 29

smirnov.alexey.1994@gmail.com

ORCID: 0000-0002-6148-0322

СУВОРОВ Сергей Викторович — инженер по испытаниям 3-й категории Центрального конструкторского бюро транспортного машиностроения.

170003, Россия, г. Тверь, Петербургское шоссе, 45в

suvorovsv96@gmail.com

ORCID: 0000-0002-7461-2742

Received 25.01.2022. Approved after reviewing 23.03.2022. Accepted 23.03.2022.

Статья поступила в редакцию 25.01.2022. Одобрена после рецензирования 23.03.2022. Принята 23.03.2022.

Original article

DOI: <https://doi.org/10.18721/JPM.15212>

THE RESPONSE OF A ROUND PLATE AND A CYLINDRICAL WATER-FILLED VOLUME UNDERNEATH TO A POINT LOAD MOVING PERIODICALLY

Yu. A. Lavrov ✉

Peter the Great St. Petersburg Polytechnic University, St. Petersburg, Russia

✉ lyamm06@rambler.ru

Abstract. The two-dimensional problem of determining the steady-state field of enforced joint gravitational motions of incompressible fluid and a round elastic plate covering its surface has been considered. The motions are caused by a point load moving periodically along the outer surface of the plate, and refer to enforced harmonic oscillations in the system. A procedure for constructing an exact analytical representation of the vibrational field of the plate's bending displacements was proposed. The unwanted mechanical resonance conditions were formulated. The results obtained make it possible to find bending moments and shear forces, if need be, in assessment of the strength of a plate. Moreover, they may be useful, for instance, in organizing safe regular movement of vehicles on a layer of ice covering a body of water.

Keywords: cylindrical reservoir, gravitational fluid motion, elastic plate, moving load, harmonic oscillations

For citation: Lavrov Yu. A., The response of a round plate and a cylindrical water-filled volume underneath to a point load moving periodically, St. Petersburg Polytechnical State University Journal. Physics and Mathematics. 15 (2) (2022) 140–147. DOI: <https://doi.org/10.18721/JPM.15212>

This is an open access article under the CC BY-NC 4.0 license (<https://creativecommons.org/licenses/by-nc/4.0/>)

Научная статья

УДК 517.947:534.414

DOI: <https://doi.org/10.18721/JPM.15212>

ДЕЙСТВИЕ ПЕРИОДИЧЕСКИ ДВИЖУЩЕЙСЯ ТОЧЕЧНОЙ НАГРУЗКИ НА КРУГЛУЮ ПЛАСТИНУ И НАХОДЯЩИЙСЯ ПОД НЕЙ ЦИЛИНДРИЧЕСКИЙ ВОДОЗАПОЛНЕННЫЙ ОБЪЕМ

Ю. А. Лавров ✉

Санкт-Петербургский политехнический университет Петра Великого, Санкт-Петербург, Россия

✉ lyamm06@rambler.ru

Аннотация. В работе рассмотрена задача определения стационарного поля вынужденных совместных гравитационных движений несжимаемой жидкости в цилиндрическом водоеме и круглой упругой пластины, покрывающей его поверхность. Указанные движения вызываются точечной нагрузкой, совершающей периодические перемещения по внешней поверхности пластины, и представляют собой вынужденные гармонические колебания. Предложена процедура построения аналитического представления для вибрационного поля изгибных смещений пластины. Сформулированы условия возникновения нежелательных механических резонансов.



Полученные результаты позволяют находить величины изгибающих моментов и сдвиговых сил при необходимости оценки прочности пластины, а полезны, например, при организации безопасного регулярного движения автомобильного транспорта по слою льда, покрывающего водоем.

Ключевые слова: цилиндрический водоем, гравитационное движение жидкости, упругая пластина, движущаяся нагрузка, гармонические колебания

Для цитирования: Лавров Ю. А. Действие периодически движущейся точечной нагрузки на круглую пластину и находящийся под ней цилиндрический водозаполненный объем // Научно-технические ведомости СПбГПУ. Физико-математические науки. 2022. Т. 15. № 2. С. 140–147. DOI: <https://doi.org/10.18721/JPM.15212>

Статья открытого доступа, распространяемая по лицензии CC BY-NC 4.0 (<https://creativecommons.org/licenses/by-nc/4.0/>)

Introduction

Organizing safe regular traffic over ice layers covering water bodies requires an adequate mathematical model and preliminary numerical experiments. Early calculations on the problem, carried out in the first half of the 20th century, were constructed by a simplified scheme assuming that an ice layer rests on a Winkler foundation. This approach proved fully valid in the case of the *Road of Life* organized on the ice of Lake Ladoga. On the other hand, the model assuming a locally elastic surface of the medium under the ice layer can considerably deviate from the real-life scenario at high loads on the ice (vertical, produced by the vehicle weight, and horizontal, produced by the winds).

As a rule, ice roads are intended for periodic traffic of automotive vehicles. The traffic frequency is generally far below the lowest natural frequency of the ice-water system and cannot trigger resonance accidents. However, the oscillation pattern of the vehicle's drivetrain can approach the natural frequency of the system, and the dangerous near-resonance increase in oscillation amplitudes should be prevented.

Problems on gravitational oscillations in aqueous media under ice, discussed in the literature over fifty years ago, generally considered two media: an ideal incompressible fluid and an elastic ice plate. An increasing focus has been directed over the recent years towards systems accounting for the influence of additional structures moving along the surface of the plate.

The plate was considered infinite in [1–3], semi-infinite in [4, 5], limited in size in [6, 7]. The thin plate acting as ice cover of an infinitely long waterway is considered in [8, 9]. The influence of a crack in the plate on mechanical processes is described in [3, 10]. Refs. [7, 11] examined how moving loads, particularly those induced by air-cushion vehicles, can be exploited for breaking the ice cover. Further circumstances complicating the problem statement are outlined in [2] (irregular surface of the plate) and [12] (weakly nonlinear model). The problems posed are solved via numerical methods in [1, 3, 7, 11]. Ref. [13] presents an extensive review of the literature, tracing the approaches to solving the problem and analyzing the results obtained for the interactions between ice, water and structures [13]. The review confirms that the problems assuming the volume of the aqueous medium to be finite have yet to receive proper attention.

Even though numerical methods are fairly versatile, they have two drawbacks: specifically, they consume large computational resources and it is difficult to estimate the error of the results obtained. The first drawback can only be mitigated through advances in computer technology, independent of the specific researcher. The second drawback can be controlled by the researcher if the errors of universal numerical methods are estimated by comparison with the results obtained by solving particular benchmark problems allowing for analytical methods.

This study introduces an analytical solution to the problem of oscillations in a water body of limited size, covered with an ice plate, under the action of a periodically moving point load.

Problem statement

The ideal incompressible fluid fills a cylindrical volume of radius R and height H , where it is reasonable to prefer a cylindrical coordinate system (r, φ, z) :

$$0 \leq r < R, \quad -\pi \leq \varphi < \pi, \quad 0 < z < H.$$

The round elastic plate, covering the surface of the fluid lying along the plane $z = H$, is only capable of bending vibrations.

The force p , varying harmonically with time, is acting on the plate in the negative direction of the axis O_z ; this force is represented in the form

$$p(r, \varphi, t) = \sum_{k=-\infty}^{+\infty} e^{i\omega_k t} \sum_{m=-\infty}^{+\infty} e^{im\varphi} \sum_{n=n_m}^{+\infty} p_{kmn} f_{mn}(r),$$

where t is the time; ω_k is the circular frequency, $\omega_k = 2\pi k/T$ (T is the period when the load is applied); p_{kmn} are the given constant coefficients; $f_{mn}(r) = J_m(q_{mn}r)/J_m(j_{mn})$ ($J_m(x)$ is the Bessel function, $q_{mn} = j_{mn}/R$, j_{mn} is the root of the equation $J'_m(j) = 0$; $j_{00} = 0$; $n_0 = 0$, $n_m = 1$ for $m \neq 0$).

The plate's bending displacement field $w(r, \varphi, t)$ and the function $\psi(r, \varphi, z, t)$, such that $\frac{\partial \psi(r, \varphi, z, t)}{\partial t}$ is the potential of velocities in the fluid, are found in the form

$$w(r, \varphi, t) = \sum_{k=-\infty}^{+\infty} e^{i\omega_k t} \sum_{m=-\infty}^{+\infty} e^{im\varphi} \cdot W_{km}(r),$$

$$\psi(r, \varphi, z, t) = \sum_{k=-\infty}^{+\infty} e^{i\omega_k t} \sum_{m=-\infty}^{+\infty} e^{im\varphi} \cdot \Psi_{km}(r, z).$$

The function $\Psi_{km}(r, z)$ satisfies the equation

$$\Delta_1 \Psi_{km}(r, z) = 0, \quad (1)$$

$$\Delta_1 = \frac{\partial^2}{\partial r^2} + \frac{1}{r} \cdot \frac{\partial}{\partial r} - \frac{m^2}{r^2}.$$

The lower ($z = 0$) and lateral ($r = R$) boundaries of the volume are perfectly rigid, i.e.,

$$\left. \frac{\partial \Psi_{km}(r, z)}{\partial z} \right|_{z=0} = 0, \quad (2)$$

$$\left. \frac{\partial \Psi_{km}(r, z)}{\partial r} \right|_{r=R} = 0. \quad (3)$$

The function $W_{km}(r)$ obeys the requirement

$$(\Delta_1^2 - \mu_k^4) W_{km}(r) = \nu_k \Psi_{km}(r, H) - \frac{1}{D_1} \sum_{n=0}^{+\infty} p_{kmn} f_{mn}(r), \quad (4)$$

where $m_k^4 = (\rho_1 h_1 \omega_k^2 - \rho_0 g) / (\rho_1$ is the plate material density, h_1 is the plate thickness, ρ_0 is the fluid density, g is the acceleration of gravity); D_1 is the cylindrical stiffness, $D_1 = E_1 H_1^3 / 12(1 - \sigma_1^2)$ (E_1 , σ_1 , respectively, are Young's modulus and Poisson's ratio of the plate material); $v_k = \rho_0 \omega_k^2 / D_1$.

The condition for continuous displacements of the plate and the fluid surface perturbations has the form

$$W_{km}(r) = \frac{\partial \Psi_{km}(r, z)}{\partial z} \Big|_{z=H}. \quad (5)$$

The edges of the elastic plate are rigidly clamped, so that

$$\frac{dW_{km}(r)}{dr} \Big|_{r=R} = 0, \quad (6)$$

$$W_{km}(R) = 0. \quad (7)$$

Construction of the solution

The required functions should be represented as

$$\Psi_{km}(r, z) = \sum_{n=n_m}^{+\infty} \psi_{kmn} f_{mn}(r) \frac{\cosh(q_{mn} z)}{\cosh(q_{mn} H)}, \quad (8)$$

$$W_{km}(r) = W_{km0}(r) + W_{km1}(r), \quad (9)$$

$$W_{km1}(r) = \sum_{n=0}^{+\infty} w_{km1n} f_{mn}(r), \quad (10)$$

$$W_{km0}(r) = C_{km} \frac{R}{4\mu_k^3} \left(\frac{J_m(\mu_k r)}{J'_m(\mu_k R)} - \frac{I_m(\mu_k r)}{I_m(\mu_k R)} \right), \quad (11)$$

$$W_{km0}(r) = C_{km} \sum_{n=n_m}^{+\infty} \frac{\eta_{mn}}{q_{mn}^4 - \mu_k^4} f_{mn}(r), \quad (12)$$

where $\eta_{0n} = 1$, $\eta_{mn} = j_{mn}^2 / (j_{mn}^2 - m^2)$ with $m \neq 0$; ψ_{kmn} , w_{km1n} , C_{km} are the yet unknown coefficients.

The function $W_{km1}(r)$ is assigned the role of a partial solution to the inhomogeneous differential equation (4), while the function $W_{km0}(r)$ is a general solution to the homogeneous differential equation corresponding to requirement (4).

Representations (8)–(12) meet the requirements (1)–(3), (6).

The right-hand side of expression (12) is constructed by decomposing the right-hand side of (11) into a series of functions $f_{mn}(r)$, and is equivalent to it, $\forall r \in [0, R]$.

Because the expansion in basis functions $f_{mn}(r)$ is unique, requirements (4), (5) correspond to a system of equations relative to the coefficients ψ_{kmn} and w_{km1n} . Expression (11) should be substituted to Eq. (4), while the expression (12) is substituted to Eq. (5).

Solution of the system allows to obtain the following formulas:

$$\psi_{kmn} = C_{km} \frac{\eta_{mn}}{\xi_{kmn}} - \frac{p_{kmn}}{\xi_{kmn} D_1}, \quad (13)$$

$$w_{kmn} = C_{km} \eta_{mn} \left(\frac{1}{\xi_{kmn}} - \frac{1}{q_{mn}^4 - \mu_k^4} \right) - \frac{p_{kmn}}{\xi_{kmn} D_1}, \quad (14)$$

$$\xi_{kmn} = q_{mn} \tanh(q_{mn} H) (q_{mn}^4 - \mu_k^4) - \nu_k.$$

It follows from expression (14) that

$$W_{km}(r) = \sum_{n=1}^{+\infty} \left(C_{km} \eta_{mn} - \frac{p_{kmn}}{D_1} \right) \frac{q_{mn} \tanh(q_{mn} H)}{\xi_{kmn}} f_{mn}(r). \quad (15)$$

The term $n = 0$ is absent in Eq. (15) because the fluid in the water body is incompressible. Condition (7) of the problem statement allows expressing the last of the required coefficients:

$$C_{km} = \frac{1}{D_1} \cdot \left(\sum_{n=1}^{+\infty} \eta_{mn} \frac{q_{mn} \tanh(q_{mn} H)}{\xi_{kmn}} \right)^{-1} \cdot \sum_{n=1}^{+\infty} p_{kmn} \frac{q_{mn} \tanh(q_{mn} H)}{\xi_{kmn}}. \quad (16)$$

The equation

$$\sum_{n=1}^{+\infty} \eta_{mn} \frac{q_{mn} \tanh(q_{mn} H)}{\xi_{kmn}} = 0 \quad (17)$$

serves to search for the natural frequencies of the oscillatory system comprising the water body and the ice plate [14, 15].

The oscillation amplitudes grow infinitely over time for processes excited at natural frequencies, which can bring about failure in the plate.

Numerical experiment

The path of a single-point load moving counterclockwise relative to the center of the plate is given by the relations

$$\begin{cases} r = \alpha(t) \\ \varphi = \beta(t) \end{cases},$$

where $\alpha(t)$, $\beta(t)$ are periodic functions, with the period T , continuous at $t \in (-T/2, T/2)$, such that

$$\lim_{t \rightarrow -T/2+0} \alpha(t) = \lim_{t \rightarrow T/2-0} \alpha(t) = R,$$

$$-\lim_{t \rightarrow -T/2+0} \beta(t) = \lim_{t \rightarrow T/2-0} \beta(t) = \varphi_0,$$

$$0 < \varphi_0 < \pi,$$

where $-\varphi_0$ is the polar angle of the load entry point to the plate and φ_0 is the polar angle of the load exit point.

The pressure applied to the plate by the moving point load takes the form

$$p(r, \varphi, t) = F \cdot \delta(r - \alpha(t)) \cdot \delta(\varphi - \beta(t)),$$

where F is the force applied by the load; $\delta(x)$ is the Dirac delta function, therefore,

$$p_{kmn} = F \cdot \left(2\pi TR \int_0^R j_{mn} J_m^2(j_{mn}) \cdot dr \right)^{-1} \cdot \int_{-T/2}^{T/2} e^{-i\omega_k t} \cdot e^{-im\beta(t)} \cdot \alpha(t) J_m(q_{mn} \alpha(t)) \cdot dt.$$

The pressure applied to the plate by several moving point loads, whose number is equal to S , can be regarded as the sum of single-point pressures, for example, in the form

$$p(r, \varphi, t) = \sum_{s=0}^{S-1} F \cdot \delta(r - \alpha(t - sT/S)) \cdot \delta(\varphi - \beta(t - sT/S)).$$

The calculation is carried out for the case of a load moving uniformly along the plate chord perpendicular to the direction $\varphi = 0$, at a distance $r = A$ from its center,

$$\alpha(t) = \sqrt{A^2 + (2Bt/T)^2}, \quad \beta(t) = \arctan(2Bt/(AT)), \quad B = \sqrt{R^2 - A^2}.$$

The selected values of geometric and physical parameters are as follows:

$$R = 1000 \text{ m}, H = 10 \text{ m}, A = 500 \text{ m}, h_1 = 0.2 \text{ m};$$

$$T = 1000 \text{ s}, F = 1 \text{ N}, E_1 = 3 \cdot 10^{10} \text{ N/m}^2;$$

$$\sigma_1 = 0.3, \rho_1 = 919.4 \text{ kg/m}^3, \rho_0 = 1000 \text{ kg/m}^3.$$

The figure shows the shapes of the bending displacements in the plate. The Cartesian coordinate system Oxy is aligned with the polar coordinate system $Or\varphi$ in a standard manner. The arrows directed vertically downward indicate the points where the moving load is applied.

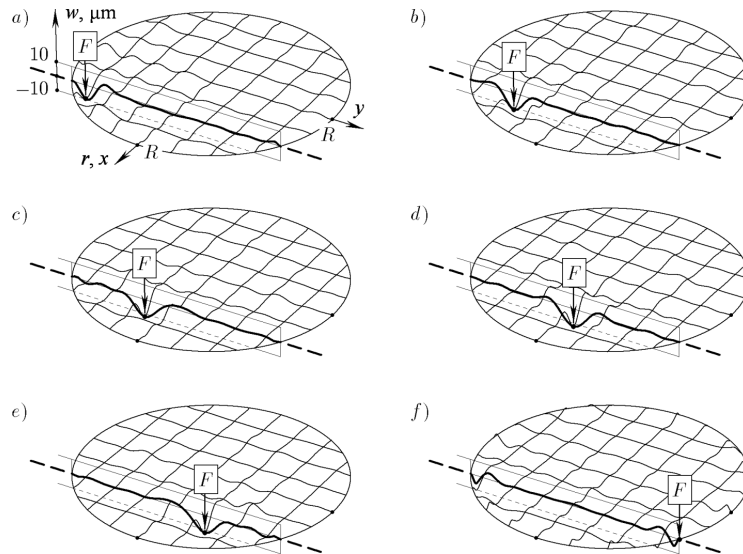


Fig. 1. Shape evolution of bending displacements w for the plate of radius R at instants $t = -3\Delta t$ (a), $-2\Delta t$ (b), $-\Delta t$ (c), 0 (d), Δt (e), $T/2$ (f), where $\Delta t = T/(4\sqrt{3})$

Conclusions

An analytical solution to the problem on determining the vibrational field $w(r, \varphi, t)$ of bending displacements in a plate subjected to a point load periodically moving over the plate. The resulting representation for the field allows (if it is required to estimate the strength of the plate) finding the bending moments and shear forces.

REFERENCES

1. **Chen K., Tong, X. F.**, Numerical solution of dynamic responses of moving load on ice sheet, *Appl. Mech. Mater.* 138–139 (2011) 44–49.
2. **Chatterjee M., Chattopadhyay A.**, Effect of moving load due to irregularity in ice sheet floating on water, *Acta Mech.* 228 (5) (2017) 1749–1765.
3. **Xue Y. Z., Zeng L. D., Ni B. Y., et al.**, Hydroelastic response of an ice sheet with a lead to a moving load, *Phys. Fluids.* 33 (3) (2021) 037109.
4. **Kouзов D. P.**, Rasseyaniye gravitatsionnoy volny na kromke plavayushchey plastiny [Scattering of a gravitational wave at the edge of a floating plate], *Transactions of the 25-th – 26-th Summer Schools «Analysis and synthesis of nonlinear mechanical oscillatory systems»*, 1998. Institute of Problems of Mechanical Engineering, RAS, St. Petersburg; Vol. 2 (1998) 356–364 (in Russian).
5. **Sturova I. V.**, Action of periodic surface pressure on an ice cover in the vicinity of a vertical wall, *J. Appl. Mech. Techn. Phys.* 58 (1) (2017) 80–88.
6. **Sturova I. V.**, The effect of periodic surface pressure on a rectangular elastic plate floating on shallow water, *J. Appl. Math. Mech.* 70 (3) (2006) 378–386.
7. **Zhestkaya V. D., Dzhabrailov M. R.**, Numerical solution of the problem of motion of a load on a cracked ice sheet, *J. Appl. Mech. Techn. Phys.* 49 (3) (2008) 473–477.
8. **Shishmarev K., Khabakhpasheva T., Korobkin A.**, The response of ice cover to a load moving along a frozen channel, *Appl. Ocean Res.* 59 (September) (2016) 313–326.
9. **Khabakhpasheva T., Shishmarev K., Korobkin A.**, Large-time response of ice cover to a load moving along a frozen channel, *Appl. Ocean Res.* 86 (May) (2019) 154–165.
10. **Marchenko A. V.**, Surface wave diffraction at a crack in sheet ice, *Fluid Dynamics.* 28 (2) (1993) 230–237.
11. **Li Y., Liu J., Hu M., Zhang Z.**, Numerical modeling of ice-water system response based on Rankine source method and finite difference method, *Ocean Engineering.* 138 (1 July) (2017) 1–8.
12. **Dinvay E., Kalisch H., Părau E. I.**, Fully dispersive models for moving loads on ice sheets, *J. Fluid Mechanics.* 876 (10 October) (2019) 122–149.
13. **Ni B., Han D., Di S., Xue Y.**, On the development of ice-water-structure interaction, *J. Hydrodyn.* 32 (4) (2020) 629–652.
14. **Lavrov Yu. A.**, O svobodnykh gravitatsionnykh kolebaniyakh zhidkosti, zapolnyayushchey pryamougolnyy konteyner s zhestkimi stenkami i uprugoy kryshkoy [On free gravitational vibrations of liquid filling a rectangular container with rigid walls and an elastic cover], *Transactions of the 25-th – 26-th Summer Schools «Analysis and synthesis of nonlinear mechanical oscillatory systems»*, 1998, Institute of Problems of Mechanical Engineering, RAS, St. Petersburg; Vol. 2 (1998) 348–355 (in Russian).
15. **Lavrov Yu. A.**, O gravitatsionnykh kolebaniyakh zhidkosti, zapolnyayushchey tsilindricheskiy konteyner s uprugoy kryshkoy [On gravitational oscillations of liquid filling a cylindrical container with an elastic cover], *Transactions of the International Conference «Numerical and Analytical Methods for Structures Design»*, Samara State Academy of Architecture and Civil Engineering, Samara (1998) 104–108 (in Russian).

СПИСОК ЛИТЕРАТУРЫ

1. **Chen K., Tong, X. F.** Numerical solution of dynamic responses of moving load on ice sheet // *Applied Mechanics and Materials*. 2011. Vol. 138–139. November. Pp. 44–49.
2. **Chatterjee M., Chattopadhyay A.** Effect of moving load due to irregularity in ice sheet floating on water // *Acta Mechanica*. 2017. Vol. 228. No. 5. Pp. 1749–1765.
3. **Xue Y. Z., Zeng L. D., Ni B. Y., Korobkin A. A., Khabakhpasheva T. I.** Hydroelastic response of an ice sheet with a lead to a moving load // *Physics of Fluids*. 2021. Vol. 33. No. 3. P. 037109.
4. **Коузов Д. П.** Рассеяние гравитационной волны на кромке плавающей пластины // *Труды XXV–XXVI летних школ «Анализ и синтез нелинейных механических колебательных систем»*. Т. 2. 1998. СПб.: Ин-т проблем машиноведения РАН. С. 356–364.
5. **Стурова И. В.** Действие периодического поверхностного давления на ледовый покров в окрестности вертикальной стенки // *Прикладная механика и техническая физика*. 2017. Т. 58. № 1. С. 92–101.

6. Стурова И. В. Влияние периодического поверхностного давления на прямоугольную упругую пластину, плавающую на мелководье // Прикладная математика и механика. 2006. Т. 70. № 3. С. 417–426.
7. Жесткая В. Д., Джабраилов М. Р. Численное решение задачи о движении нагрузки по ледяному покрову с трещиной // Прикладная механика и техническая физика. 2008. Т. 49. № 3 (289). С. 473–477.
8. Shishmarev K., Khabakhpasheva T., Korobkin A. The response of ice cover to a load moving along a frozen channel // Applied Ocean Research. 2016. Vol. 59. September. Pp. 313–326.
9. Khabakhpasheva T., Shishmarev K., Korobkin A. Large-time response of ice cover to a load moving along a frozen channel // Applied Ocean Research. 2019. Vol. 86. May. Pp. 154–165.
10. Марченко А. В. Дифракция поверхностных волн на трещине в ледяном покрове // Известия РАН. Механика жидкости и газа. 1993. № 2. С. 93–102.
11. Li Y., Liu J., Hu M., Zhang Z. Numerical modeling of ice-water system response based on Rankine source method and finite difference method // Ocean Engineering. 2017. Vol. 138. 1 July. 1. Pp. 1–8.
12. Dinvay E., Kalisch H., Părau E. I. Fully dispersive models for moving loads on ice sheets // Journal of Fluid Mechanics. 2019. Vol. 876. 10 October. Pp. 122–149.
13. Ni B., Han, D., Di, S., Xue Y. On the development of ice-water-structure interaction // Journal of Hydrodynamics. 2020. Vol. 32. No. 4. Pp. 629–652.
14. Лавров Ю. А. О свободных гравитационных колебаниях жидкости, заполняющей прямоугольный контейнер с жесткими стенками и упругой крышкой // Труды XXV–XXVI летних школ «Анализ и синтез нелинейных механических колебательных систем». Т. 2. 1998. СПб.: Ин-т проблем машиноведения РАН. С. 348–355.
15. Лавров Ю. А. О гравитационных колебаниях жидкости, заполняющей цилиндрический контейнер с упругой крышкой // Труды международной конференции «Численные и аналитические методы расчета конструкций». Самара: Самарская государственная академия строительства и архитектуры, 1998. С. 104–108.

THE AUTHOR

LAVROV Yury A.

Peter the Great St. Petersburg Polytechnic University

29 Politechnicheskaya St., St. Petersburg, 195251, Russia

lyamm06@rambler.ru

ORCID: 0000-0001-9626-0461

СВЕДЕНИЯ ОБ АВТОРЕ

ЛАВРОВ Юрий Аркадьевич — доктор физико-математических наук, профессор кафедры высшей математики Санкт-Петербургского политехнического университета Петра Великого.

195251, Россия, г. Санкт-Петербург, Политехническая ул., 29

lyamm06@rambler.ru

ORCID: 0000-0001-9626-0461

Received 20.03.2022. Approved after reviewing 12.04.2022. Accepted 12.04.2022.

Статья поступила в редакцию 20.03.2022. Одобрена после рецензирования 12.04.2022. Принята 12.04.2022.